

# **An Experimental Assessment of Computational Fluid Dynamics Predictive Accuracy for Electronic Component Operational Temperature**

Author

**Valérie C. Eveloy, M.Sc.**

A Thesis submitted to Dublin City University in fulfilment of  
the requirement for the degree of Doctor of Philosophy

Supervisors

**Professor M. S. J. Hashmi, Ph.D., D.Sc.**

School of Mechanical and Manufacturing Engineering,  
Dublin City University, Ireland

**Peter Rodgers, Ph.D.**

Electronics Thermal management Ltd., Ireland

August 2003

## Declaration

I hereby certify that this material, which I now submit for assessment on the programme of study leading to the award of *Doctor of Philosophy* is entirely my own work and has not been taken from the work of others save and to the extent that such work has been cited and acknowledged within the text of my work.

Signed:

V. Seby  
Valérie C. Eveloy, ID: 52175995  
(Candidate)

Date:

September 21, 2003

## **Acknowledgements**

First and foremost I wish to sincerely thank my supervisor, Professor M.S.J. Hashmi, for giving me the opportunity to undertake my doctoral study within the School of Mechanical and Manufacturing Engineering. His support on all matters was invaluable and much appreciated.

Also sincere thanks to Dr. Peter Rodgers, Electronics Thermal Management, Ltd., for his technical guidance and co-ordinating the research with the CFD companies and research institutes involved with this work.

The numerical analyses presented in this Thesis were undertaken using the computational facilities of Electronics Thermal Management, Ltd., who financially funded the research.

Flomerics, UK, and Fluent Europe, UK are gratefully acknowledged for the use of Flotherm and Icepak / Fluent software respectively, and their technical support.

The PQFP 160 test vehicles were built and thermally characterised at the Stokes Research Institute (SRI), University of Limerick. Dr. John Lohan, Galway-Mayo Institute of Technology (GMIT), is gratefully acknowledged for providing clarification on the published measurements, supplying supporting surface temperature measurement data, and providing the opportunity to undertake the experimental flow visualisations at GMIT.

Thanks to Professor Mark Davies, SRI, for his permission to undertake destructive testing on the actual PQFP 160 test components. Component cross sectioning was undertaken at the Departments of Mechanical/Industrial Engineering and Physical Sciences, GMIT. X-Ray analysis and Surface Acoustic Microscopy (SAM) of component internal architecture were performed at Analog Devices B.V., Limerick, with supporting SAM undertaken at Materials Ireland, University of Limerick. Dr. Tom Moore, Analog Devices B.V., and Dr. Paul Butler, Materials Ireland, are gratefully acknowledged for their assistance.

The SO8 and PQFP 208 test vehicles were thermally characterised at the Nokia Research Centre, Finland, where I was previously employed. Destructive and non-destructive analyses of component internal architecture were also undertaken at Nokia.

The component compact thermal model resistor networks used in this study were generated by Professor Alfonso Ortega and Mr. Jason DeVoe, Department of Aerospace and Mechanical Engineering and The Center for Electronic Packaging Research, The University of Arizona, USA.

# An Experimental Assessment of Computational Fluid Dynamics Predictive Accuracy for Electronic Component Operational Temperature

Valérie C. Eveloy, M.Sc.

## Abstract

Ever-rising Integrated Circuit (IC) power dissipation, combined with reducing product development cycles times, have placed increasing reliance on the use of Computational Fluid Dynamics (CFD) software for the thermal analysis of electronic equipment. In this study, predictive accuracy is assessed for board-mounted electronic component heat transfer using both a CFD code dedicated to the thermal analysis of electronics, Flotherm, and a general-purpose CFD code, Fluent.

Using Flotherm, turbulent flow modelling approaches typically employed for the analysis of electronics cooling, namely algebraic mixing length and two-equation high-Reynolds number  $k-\epsilon$  models, are assessed. As shown, such models are not specific for the analysis of forced airflows over populated electronic boards, which are typically classified as low-Reynolds number flows. The potential for improved predictive accuracy is evaluated using candidate turbulent flow models more suited to such flows, namely a one-equation Spalart-Allmaras model, two-layer zonal model and two-equation SST  $k-\omega$  model, all implemented in Fluent.

Numerical predictions are compared with experimental benchmark data for a range of component-board topologies generating different airflow phenomena and varying degrees of component thermal interaction. Test case complexity is incremented in controlled steps, from single board-mounted components in free convection, to forced air-cooled, multi-component board configurations. Apart from the prediction of component operational temperature, the application of CFD analysis to the design of electronic component reliability screens and convective solder reflow temperature profiles is also investigated. Benchmark criteria are based on component junction temperature and component-board surface temperature profiles, measured using thermal test chips and infrared thermography respectively. This data is supplemented by experimental visualisations of the forced airflows over the boards, which are used to help assess predictive accuracy.

Component numerical modelling is based on nominal package dimensions and material thermal properties. To eliminate potential numerical modelling uncertainties, both the test component geometry and structural integrity are assessed using destructive and non-destructive testing. While detailed component modelling provides the *à priori* junction temperature predictions, the capability of compact thermal models to predict multi-mode component heat transfer is also assessed.

In free convection, component junction temperature predictions for an in-line array of fifteen board-mounted components are within  $\pm 5^\circ\text{C}$  or 7% of measurement. Predictive accuracy decays up to  $\pm 20^\circ\text{C}$  or 35% in forced airflows using the  $k-\epsilon$  flow model. Furthermore, neither the laminar or  $k-\epsilon$  turbulent flow model accurately resolve the complete flow fields over the boards, suggesting the need for a turbulence model capable of modelling transition. Using a  $k-\omega$  model, significant improvements in junction temperature prediction accuracy are obtained, which are associated with improved prediction of both board leading edge heat transfer and component thermal interaction. Whereas with the  $k-\epsilon$  flow model, prediction accuracy would only be sufficient for the early to intermediate phase of a thermal design process, the use of the  $k-\omega$  model would enable parametric analysis of product thermal performance to be undertaken with greater confidence. Such models would also permit the generation of more accurate temperature boundary conditions for use in Physics-of-Failure (PoF) based component reliability prediction methods.

The case is therefore made for vendors of CFD codes dedicated to the thermal analysis of electronics to consider the adoption of eddy viscosity turbulence models more suited to the analysis of component heat transfer. While this study ultimately highlights that electronic component operational temperature needs to be experimentally measured to qualify product thermal performance and reliability, the use of such flow models would help reduce the current dependency on experimental prototyping. This would not only enhance the potential of CFD as a design tool, but also its capability to provide detailed insight into complex multi-mode heat transfer, that would otherwise be difficult to characterise experimentally.

# Table of Contents

	<b>Page</b>
<b>Acknowledgements</b>	iii
<b>Abstract</b>	iv
<b>List of Figures</b>	ix
<b>List of Tables</b>	xiv
<b>Nomenclature</b>	xviii
<b>Chapter 1 Introduction</b>	
1.1 Electronics Thermal Management	1
1.2 Application of CFD Analysis to Electronics Thermal Design	4
1.2.1 Prediction of Electronic Component Operational Temperature	5
1.2.2 Numerical Analysis of Electronic Component Transient Heat Transfer	9
1.3 Proposed Area of Study and Outline of Thesis	10
<b>Chapter 2 Literature Review and Benchmark Strategy</b>	
2.1 Introduction	13
2.2 Experimental Characterisation of Air-Cooled Electronic Component Heat Transfer	13
2.3 Experimental Flow Visualisation	15
2.4 CFD Predictive Accuracy	16
2.4.1 Prediction of Electronic Component Heat Transfer	17
2.5 Summary of Literature Survey	21
2.6 Benchmark Strategy	22
2.6.1 CFD Code Selection	24
2.7 Summary	25
<b>Chapter 3 Benchmark Test Configurations</b>	
3.1 Introduction	26
3.2 Electronic Packaging	26
3.2.1 Component Architecture	27
3.2.2 Printed Circuit Board Construction	30
3.2.3 Characterisation of Electronic Component Thermal Performance	30
3.3 Multi-Component Board Heat Transfer Configurations	33
3.3.1 Test Components	34
3.3.2 Test Printed Circuit Boards	35
3.3.3 Experimental Thermal Characterisation	37
3.3.3.1 Characterisation Methods	38
3.3.3.2 Uncertainty in Experimental Measurements	43
3.3.3.3 Thermal Characterisation Data	46
3.3.3.3.1 Populated Board	46
3.3.3.3.2 SEMI Standard PCB	53

3.3.3.3	Assessment of the Experimental Data for Benchmark Purposes	55
3.3.4	Component Structural Analysis	57
3.3.5	Experimental Airflow Visualisation	67
3.3.5.1	Experimental Methods	67
3.3.5.2	Visualised Flows	70
3.4	Transient Component Heat Transfer Configurations	78
3.4.1	Characterisation Methods	78
3.4.2	Characterisation Data	80
3.5	Component Compact Thermal Modelling Configurations	83
3.5.1	SO8 Component Configurations	83
3.5.2	PQFP 208 Component Configurations	88
3.6	Summary	91
<b>Chapter 4</b>	<b>Numerical Models</b>	
4.1	Introduction	92
4.2	Fluid Flow Modelling	92
4.3	Numerical Software	95
4.3.1	Flotherm	96
4.3.2	Fluent	97
4.4	Numerical Modelling Strategy	100
4.5	Component and PCB Modelling	103
4.5.1	Component Modelling	103
4.5.1.1	Detailed Component Modelling	104
4.5.1.2	Component Compact Thermal Modelling	110
4.5.2	PCB Modelling	119
4.6	Numerical Models	122
4.6.1	Populated Board Test Configurations	122
4.6.1.1	Free Convection	122
4.6.1.2	Forced Convection	127
4.6.2	SEMI PCB Test Configurations	140
4.6.3	Compact Component Thermal Modelling Test Configurations	144
4.7	Summary	150
<b>Chapter 5</b>	<b>Numerical Predictive Accuracy: Single Component Board Heat Transfer</b>	
5.1	Introduction	151
5.2	Validation of the PQFP 160 Component-PCB Numerical Models	151
5.2.1	Junction Temperature Predictions	152
5.2.2	Component-Board Surface Temperature Profiles	154
5.2.3	Energy Balance Analyses of Component Heat Transfer	158
5.3	Transient Component Heat Transfer	159
5.3.1	Numerical Model Validation	160
5.3.2	Reliability Testing	161
5.3.3	Convective Solder Reflow	166
5.3.4	Summary of Results	167
5.4	Component Compact Thermal Modelling	168

5.4.1	Detailed Component Modelling	168
5.4.2	Compact Thermal Model Predictive Accuracy	170
5.4.2.1	SO8 Component	170
5.4.2.2	PQFP 208 Component	173
5.4.3	Summary of Results	179
5.5	Summary of Chapter 5	179
<b>Chapter 6</b>	<b>Numerical Predictive Accuracy: Multi-Component Board Heat Transfer in Free Convection</b>	
6.1	Introduction	181
6.2	Individually Powered Component Configurations	181
6.2	Simultaneously Powered Component Configuration	182
6.3	Energy Balance Analyses of Component Heat Transfer	187
6.4	Summary	188
<b>Chapter 7</b>	<b>Numerical Predictive Accuracy: Multi-Component Board Heat Transfer in Forced Convection</b>	
7.1	Introduction	189
7.2	Standard Flow Modelling	189
7.2.1	Stage 2, Component H Individually Powered	190
7.2.2	Stage 3, Individually Powered Components	192
7.2.3	Stage 3, Simultaneously Powered Components	194
7.2.4	Summary of Results	200
7.3	Alternative Flow Modelling Strategies	200
7.3.1	Stage 1 PCB	201
7.3.2	Non-insulated Stage 3, Individually Powered Components	202
7.3.3	Non-insulated Stage 3, Simultaneously Powered Components	203
7.4	Summary	206
<b>Chapter 8</b>	<b>Conclusions and Recommendations</b>	
8.1	Conclusions	207
8.1.1	Experimental Benchmarks	207
8.1.2	Component Steady-State Heat Transfer	207
8.1.3	Component Transient Heat Transfer	210
8.1.4	Numerical Modelling	210
8.2	Recommendations	211
	<b>References</b>	214
<b>Appendix A</b>	<b>Thermal Test Components</b>	
A.1	External Component Geometry	234
A.2	Thermal Test Die	236
A.3	Scanning Acoustic Microscopy	238
<b>Appendix B</b>	<b>Uncertainty Analysis</b>	
B.1	Uncertainty in Measured Component Junction Temperature	239

<b>Appendix C</b>	<b>Fluid Flow Modelling</b>	
C.1	Time-Averaged Conservation Equations	241
C.2	Eddy Viscosity Turbulence Models	242
C.2.1	LVEL Model	242
C.2.2	Standard High-Reynolds Number k- $\epsilon$ Model	243
C.2.3	Spalart-Allmaras Model	247
C.2.4	Two-Layer Zonal Model	250
C.2.5	Shear Stress Transport (SST) k- $\omega$ Model	252
<b>Appendix D</b>	<b>Publication Work</b>	
D.1	Conference Proceedings	257
D.2	Journals	257



## List of Figures

Figure	Title	Page
1.1	Historical power trend for Intel's CPUs	2
1.2	Heat density trends for data processing, computer systems and telecommunication equipment	2
1.3	Thermal analysis chain of an electronic system, from IC to data centre	3
3.1	An example of a populated printed circuit board	27
3.2	Evolution of IC packaging	28
3.3	Typical architectures of a leaded IC package	29
3.4	Internal architecture of a standard Quad Flat Pack, with epoxy moulding compound partially cut away	29
3.5	Schematic cross sections of typical PCB constructions	30
3.6	Populated PCB, shown for the Stage 3 topology	34
3.7	160-lead PQFP external geometry (28 x 28 mm)	35
3.8	Layout of surface copper tracking pattern on the populated PCB	36
3.9	PQFP 160 test Printed Circuit Board conforming to SEMI G42-88	37
3.10	Forced convection characterisation of the populated board at the outlet of the wind tunnel	39
3.11	Still-air enclosure for free convection characterisation, with the Stage 3 PCB shown in vertical orientation	40
3.12	Measurement of component surface temperature on the Stage 3 PCB, using miniature thermistors mounted onto the package heat slugs	41
3.13	Cumulative uncertainties in component junction and surface temperature measurement for the populated board characterisation	43
3.14	Surface temperature infrared thermographs for component H individually powered on the Stage 1 PCB in free convection	47
3.15	Surface temperature infrared thermographs for the simultaneously powered non-insulated PCB Stage 3 configuration in free convection	48
3.16	Surface temperature infrared thermographs for component H individually powered on the Stage 2 PCB in forced convection	49
3.17	Surface temperature infrared thermographs for the simultaneously powered non-insulated Stage 3 configuration in a 4 m/s airflow	50
3.18	Surface temperature infrared thermographs for the simultaneously powered insulated Stage 3 PCB in forced convection, board component side	52
3.19	Definition of component-board infrared surface temperature profile analysis planes on the populated board, used to assess numerical predictive accuracy	52
3.20	Surface temperature infrared thermographs for package design II on the SEMI standard PCB	54
3.21	Definition of component-board infrared surface temperature profile analysis planes on the SEMI standard PCB, used to assess numerical predictive accuracy	55
3.22	160-lead PQFP component geometry, package design I	60
3.23	160-lead PQFP component geometry, package design II	61
3.24	160-lead PQFP component geometry, package design III	62

3.25	Scanning Acoustic Microscopy (SAM) analysis for the 160-lead PQFP component geometry	65
3.26	Magnified view of the die - paddle interface for package design I, showing delamination	65
3.27	Impact of measured die attach delamination on component thermal resistance for a 208-lead PowerQuad2 package	66
3.28	Stage 3 PCB mounted vertically within the wind tunnel test section for smoke-flow visualisation	68
3.29	Wind tunnel used for paint-film evaporation and smoke-flow visualisation	68
3.30	Smoke-flow visualisation over the Stage 1 PCB at 2 m/s	71
3.31	Paint-film evaporation sequence from the Stage 1 PCB at 2 m/s using an ethanol paint film	72
3.32	Interpretations of oil-streak patterns on the SEMI standard PCB, obtained in 2 and 4 m/s airflows	73
3.33	Smoke-flow visualisation over the non-insulated Stage 2 PCB at 2 m/s	74
3.34	Smoke-flow visualisation over the non-insulated Stage 3 PCB at 2 m/s	75
3.35	Experimentally visualised flow field on the insulated Stage 3 PCB at 2 m/s	76
3.36	Paint-film evaporation from the insulated Stage 3 PCB at 2 m/s using Ethanol	77
3.37	Variable speed heated wind tunnel	79
3.38	Measured transient component junction temperature rise for a continuous power dissipation of 3W in a quiescent air at 20°C, Test I	81
3.39	Measured component junction temperature rise for both continuous and pulsed 3W component power dissipation in a 1 m/s airflow at 20°C, Test II	81
3.40	Measured passive component junction temperature in dynamic ambient air temperature conditions (15°C/min ramp, 300s dwell time), in a 1 m/s airflow, Test III	81
3.41	Measured passive component junction temperature in dynamic ambient air temperature conditions (25°C/min ramp, 300s dwell time), in a 1 m/s airflow, Test IV	81
3.42	Measured passive component junction temperature in dynamic ambient air temperature conditions (5°C/min ramp, 60s dwell time), in a 2.25 m/s airflow, Test V	81
3.43	Measured passive component junction temperature in dynamic ambient air temperature conditions (15°C/min ramp, 60s dwell time), in a 2.25 m/s airflow, Test VI	81
3.44	Measured passive component junction temperature in dynamic air temperature conditions (25°C/min ramp, 60s dwell time), in a 2.25 m/s airflow, Test VII	82
3.45	Measured passive component junction temperature in dynamic ambient air temperature conditions (15°C/min ramp, 120s dwell time), in a 4 m/s airflow, Test VIII	82
3.46	Measured transient component junction temperature rise for a pulsed 3W component power dissipation in dynamic ambient air temperature conditions (15°C/min ramp, 60s dwell time), in a 1 m/s airflow, Test IX	82
3.47	Measured transient component junction temperature rise for a pulsed 3W component power dissipation in dynamic ambient air temperature conditions (15°C/min ramp, 60s dwell time), in a 2.25 m/s airflow, Test X	82

3.48	Measured passive component junction temperature in dynamic ambient air temperature conditions representative of those in a standard convective reflow soldering process	82
3.49	Cross sectional analysis and X-Ray imaging of an SO8 package	84
3.50	SO8 test PCB constructions	85
3.51	Measured component-PCB surface temperature profiles in the direction of package width for a single SO8 component in natural convection, as a function of PCB construction, Figure 3.49(b)	87
3.52	Measured component-PCB surface temperature profiles in the direction of package length for a single SO8 component mounted on FR4#2 PCB in natural convection	87
3.53	PQFP 208 component internal architecture	89
3.54	PQFP 208 test PCB	89
3.55	Measured component-PCB surface temperature profiles for a single board-mounted PQFP208 component in a 2 m/s airflow	90
4.1	PQFP 160 numerical model, package design I	107
4.2	PQFP 160 numerical model, package design II	108
4.3	PQFP 160 numerical model, package design III	108
4.4	Detailed SO8 numerical model	109
4.5	Detailed PQFP 208 numerical model (quarter geometry)	109
4.6	Nomenclature for package prime lumped surfaces (quarter geometry)	111
4.7	Illustrations of standard resistor network topologies for component compact thermal models. (a) two-node, (b) star-shaped, (c) shunted, and (d) shunted with floating node	111
4.8	Default geometry implementation of a resistor network-based CTM for a leaded package in Flotherm, using the code's Compact Component SmartPart	117
4.9	Modified CTM implementation, shown for the SO8 component	117
4.10	SO8 component compact thermal model	118
4.11	PQFP 208 component compact thermal models	118
4.12	Numerical modelling of single-component PCBs copper tracking	120
4.13	Numerical modelling of populated PCB copper tracking	121
4.14	Non-insulated Stage 1 and 3 free convection numerical models	125
4.15	Computational domain discretization grid applied for the free convection, non-insulated Stage 1 and 3 numerical models shown in Figure 4.14	126
4.16	Numerically predicted flow unsteadiness in the stream-wise direction above component G on the insulated Stage 3 PCB in a 2 m/s airflow	129
4.17	Stages 1 and 2 forced convection numerical models	132
4.18	Stage 3 forced convection numerical models	133
4.19	Computational domain discretization grids applied to the Stage 3 forced convection numerical models shown in Figure 4.18	134
4.20	Stage 1 forced convection numerical model (half geometry)	138
4.21	Non-insulated Stage 3 forced convection numerical model (Central stream-wise component row, F - J)	139
4.22	Free convection numerical model for the single board-mounted PQFP 160 component	142
4.23	Forced convection numerical model for the single board-mounted PQFP 160 component	143
4.24	Free convection numerical models for the single board-mounted SO8 component	147

4.25	Computational domain discretization grids applied to the free convection single board-mounted SO8 component numerical models shown in Figure 4.24	147
4.26	Forced convection numerical models for the single board-mounted SO8 component	148
4.27	Computational domain discretization grids applied to the forced convection single board-mounted SO8 component numerical models shown in Figure 4.26	148
4.28	Forced convection numerical models for the single board-mounted PQFP 208 component	149
4.29	Computational domain discretization grids applied to the forced convection single board-mounted PQFP 208 component numerical models shown in Figure 4.28	149
5.1	Comparison of measured and predicted component-PCB surface temperature profiles on the Stage 1 PCB for a single board-mounted PQFP 160 component, package design I, at position H in free convection	155
5.2	Comparison of measured and predicted component-PCB surface temperature profiles on the SEMI PCB for a single board-mounted PQFP 160 component, package design II, in free and forced convection	157
5.3	Comparison of measured and predicted transient component junction temperature rise for a continuous power dissipation of 3W in a quiescent air at 20°C, Test I	160
5.4	Comparison of measured and predicted transient component junction temperature rise for both continuous and pulsed 3W component power dissipation in a 1 m/s airflow at 20°C, Test II	160
5.5	Comparison of measured and predicted passive component junction temperature in dynamic ambient air temperature conditions, in a 1 m/s airflow, Test IV	162
5.6	Comparison of measured and predicted passive component junction temperature in dynamic ambient air temperature conditions, in a 2.25 m/s airflow	163
5.7	Comparison of measured and predicted passive component junction temperature in dynamic ambient air temperature conditions (15°C/min ramp, 120s dwell time), in a 4 m/s airflow, Test VIII	164
5.8	Comparison of measured and predicted transient component junction temperature rise for a pulsed 3W component power dissipation in dynamic ambient air temperature conditions	165
5.9	Comparison of measured and predicted passive component junction temperature in dynamic ambient air temperature conditions representative of those in a standard convective reflow soldering process	167
5.10	Comparison of measured and predicted component-PCB surface temperature profiles in the direction of package width for a single SO8 component in natural convection, as a function of PCB construction, Figure 3.31(b)	172
5.11	Comparison of measured and predicted component-PCB surface temperature profiles in the direction of package length for a single SO8 component mounted on FR4#2 PCB in natural convection	172
5.12	Comparison of measured and predicted component-PCB surface temperature profiles for a single board-mounted PQFP208 component in a 2 m/s airflow	176
5.13	Comparison of measured and predicted component-PCB surface temperature profiles for a single board-mounted PQFP208 component in a 2 m/s airflow as a function of CTM lead node modelling	177

5.14	Numerically predicted temperature distribution in the plane of PCB surface copper tracking for a single board-mounted PQFP 208 component in a 2 m/s airflow	178
6.1	Comparison of measured and predicted component-PCB surface temperature profiles on the board non-component side, for the simultaneously powered PCB in free convection	185
6.2	Comparison of measured and predicted component-PCB surface temperature profiles on the board component side, for the simultaneously powered PCB in free convection	186
7.1	Comparison of measured and predicted component-PCB surface temperature profiles for component H individually powered on the Stage 2 PCB in forced convection	191
7.2	Comparison of measured and predicted component junction temperature rise between the individually- and simultaneously powered configurations for the central stream-wise row components (F - J) on the Stage 3 PCB in forced convection	198
7.3	Comparison of measured and predicted component-PCB surface temperature profiles in the stream-wise airflow direction on the Stage 3 PCB in forced convection	199
7.4	Predicted flow field vectors at the leading edge of Stage 3 PCB, taken along the board central stream-wise axis (Plane X-X, Figure 3.19)	203
7.5	Comparison of measured and predicted component junction temperature rises between the individually- and simultaneously powered configurations for the central stream-wise row components (F - J) on the Stage 3 PCB	204
A.1	160-lead PQFP (Amkor) package body geometry details	234
A.2	SO8 (Infineon) package body geometry details	235
A.3	PQFP 208 (ST microelectronics) package body geometry details	236
A.4	Thermal test die layouts	237
A.5	Scanning Acoustic Microscopy (SAM) analysis of the die-paddle interface for the 160-lead PQFP component, package design I	238

## List of Tables

Table	Title	Page
3.1	Measured quantities and estimated uncertainties for characterisation of the PQFP 160 component on the populated board and SEMI PCB	45
3.2	Measured component junction and surface temperatures for a single-board mounted component at position H (Stage 1) in free convection	46
3.3	Measured component junction and surface temperatures for individually powered component configurations on the non-insulated Stage 3 PCB in free convection	47
3.4	Measured component junction and surface temperatures for the simultaneously powered non-insulated Stage 3 configuration in free convection	47
3.5	Measured component junction and surface temperatures for component H individually powered on the Stage 1 and 2 PCBs in forced convection	48
3.6	Measured component junction and surface temperatures for individually powered component configurations on the non-insulated Stage 3 PCB in a 2 m/s airflow	49
3.7	Measured component junction and surface temperatures for individually powered component configurations on the non-insulated Stage 3 PCB in a 4 m/s airflow	49
3.8	Measured component junction and surface temperatures for the simultaneously powered non-insulated Stage 3 configuration in a 4 m/s airflow	50
3.9	Measured component junction and surface temperatures for individually powered component configurations on the insulated Stage 3 PCB in a 2 m/s airflow	50
3.10	Measured component junction and surface temperatures for individually powered component configurations on the insulated Stage 3 PCB in a 4 m/s airflow	51
3.11	Measured component junction and surface temperatures for the simultaneously powered insulated Stage 3 configuration in a 2 m/s airflow	51
3.12	Measured component junction and surface temperatures for the simultaneously powered insulated Stage 3 configuration in a 4 m/s airflow	51
3.13	Measured steady-state PQFP 160 component junction and surface temperatures for package designs II and III mounted on the SEMI PCB	53
3.14	Component dynamic power dissipation in fixed ambient conditions	80
3.15	Passive component operation in dynamic ambient air temperature conditions	80
3.16	Combined component dynamic power dissipation in varying ambient air temperature conditions	80
3.17	Typical convective solder reflow thermal profile in a 4 m/s airflow	80
3.18	Measured quantities and estimated uncertainties for both free and forced convection thermal characterisation of the SO8 component	86
3.19	Measured steady-state component junction temperatures (°C) for a single board-mounted SO8 component in free and forced convection	86

3.20	Measured quantities and estimated uncertainties for characterisation of the PQFP208 component	88
3.21	Measured component junction temperature for a single board-mounted PQFP 208 in a 2 m/s airflow	90
4.1	Vendor specified thermo-physical properties for component constituent elements	104
4.2	Effective thermo-physical properties values for the modelled leadframe and leads elements for the SO8, PQFP 208 and PQFP 160 packages	106
4.3	Prime lumped surface areas for the SO8 and PQFP 208 packages (quarter package geometry), Figure 4.6	110
4.4	Imposed set of thermal Boundary Conditions used to generate detailed component model thermal response data for five prime lumped surfaces, Figure 4.6	113
4.5	SO8 detailed model thermal response data to the Boundary Conditions defined in Table 4.4	113
4.6	PQFP 208 detailed model thermal response data to the Boundary Conditions defined in Table 4.4	113
4.7	Optimised values of resistors for SO8 CTM shunted network, Figure 4.10(a)	113
4.8	Optimised values of resistors for PQFP 208 CTM star-shaped network, Figure 4.11(a)	114
4.9	Optimised values of resistors for PQFP 208 CTM shunted network, Figure 4.11(b)	114
4.10	Optimised values of resistors for PQFP 208 CTM shunted network having a floating node, Figure 4.11(c)	114
4.11	SO8 CTM resistor network accuracy versus detailed model for the imposed set of thermal Boundary Conditions defined in Table 4.4	115
4.12	PQFP208 CTM star-shaped resistor network accuracy versus detailed model for the imposed set of thermal Boundary Conditions defined in Table 4.4	115
4.13	PQFP208 CTM shunted resistor network accuracy versus detailed model for the imposed set of thermal Boundary Conditions defined in Table 4.4.	115
4.14	PQFP208 CTM shunted resistor network with floating node accuracy versus detailed model for the imposed set of thermal Boundary Conditions defined in Table 4.4	116
4.15	Geometric construction of CTM implementation in the CFD model	117
4.16	Nominal material thermal property values for PCB constituent elements	120
4.17	Location of applied artificial boundary conditions relative to the PCB for the Stage 1 and Stage 3 free convection numerical models, Figure 4.14	124
4.18	Computational domain size and grid discretization details for the Stage 1 and non-insulated Stage 3 free convection numerical models	124
4.19	Location of applied artificial boundary conditions relative to the PCB for the forced convection Stages 1, 2 and non-insulated 3 numerical models, Figures 4.17 and 4.18	131
4.20	Computational domain size and grid discretization details for the forced convection Stages 1, 2 and 3 numerical models	131
4.21	Location of applied artificial boundary conditions relative to the PCB for the Stages 1 and 3 forced convection numerical models, Figures 4.20 and 4.21	137

4.22	Computational domain size and grid discretization details for the Stages 1 and 3 forced convection numerical models	137
4.23	Computational domain size and grid discretization details for the SEMI PCB free and forced convection numerical models, Figures 4.22 and 4.23	141
4.24	Location of applied artificial boundary conditions relative to the PCB for the SO8 free convection numerical models, Figure 4.24	145
4.25	Computational domain size and grid discretization details for the SO8 free convection numerical models	145
4.26	Location of applied artificial boundary conditions relative to the PCB for the SO8 forced convection numerical models, Figure 4.26	145
4.27	Computational domain size and grid discretization details for the SO8 forced convection numerical models	145
4.28	Location of applied artificial boundary conditions relative to the PCB for the PQFP 208 forced convection numerical model, Figure 4.28	146
4.29	Computational domain size and grid discretization details for the PQFP 208 forced convection numerical models	146
5.1	Comparison of measured and predicted component steady-state junction temperatures for the PQFP 160 package design I, characterised on the Stage 1 PCB	152
5.2	Comparison of measured and predicted component steady-state junction temperatures for the PQFP 160 package designs II and III, characterised on the SEMI standard PCB	152
5.3	Numerical component energy balance (%) for the PQFP 160 component on the SEMI PCB	159
5.4	Numerical component energy balance (%) for the PQFP 160, package design I, on the Stage 1 PCB	159
5.5	Comparison of measured and predicted component junction temperatures for a single board-mounted SO8 component	169
5.6	Comparison of measured and predicted component junction temperatures for a single board-mounted PQFP 208 in a 2 m/s airflow	170
5.7	Comparison of measured and predicted component junction temperatures for a single board-mounted SO8 component	171
5.8	Compact versus detailed model junction temperature predictions for a single board-mounted SO8 component	171
5.9	Comparison of compact and detailed model predictions of component heat transfer energy balance (%) for a single board-mounted SO8 component in natural convection	173
5.10	Comparison of compact and detailed model predictions of component energy balance (%) for a single board-mounted SO8 component in a 2 m/s airflow	173
5.11	Comparison of measured and predicted component junction temperatures for a single board-mounted PQFP 208 in a 2 m/s airflow	174
5.12	Compact versus detailed model component junction temperature predictions for a single board-mounted PQFP208 in a 2 m/s airflow	174
5.13	Comparison of compact and detailed model predictions of component energy balance (%) for a single board-mounted PQFP208 in a 2 m/s airflow	174
6.1	Comparison of measured and predicted junction temperatures for individually powered components on the non-insulated Stage 3 PCB in free convection	182
6.2	Comparison of measured and predicted component junction temperatures on simultaneously powered, non-insulated Stage 3 PCB in free convection	183



6.3	Comparison of measured and predicted component junction temperature rise between the individually and simultaneously powered component configurations on the non-insulated Stage 3 PCB in free convection	183
6.4	Numerical component energy balances for individually and simultaneously powered components on the non-insulated Stage 3 PCB in free convection	187
7.1	Comparison of measured and predicted component junction temperatures for component H individually powered on the Stage 2 PCB in forced convection	190
7.2	Comparison of measured and predicted component junction temperatures for individually powered components on the non-insulated Stage 3 PCB in a 2 m/s airflow	193
7.3	Comparison of measured and predicted component junction temperatures for individually powered components on the non-insulated Stage 3 PCB in a 4 m/s airflow	193
7.4	Comparison of measured and predicted component junction temperatures for individually powered components on the insulated Stage 3 PCB in a 2 m/s airflow	194
7.5	Comparison of measured and predicted component junction temperatures for individually powered components on the insulated Stage 3 PCB in a 4 m/s airflow.	194
7.6	Comparison of measured and predicted component junction temperatures for simultaneously powered components on the non-insulated Stage 3 PCB in a 4 m/s airflow	195
7.7	Comparison of measured and predicted component junction temperatures for simultaneously powered components on the insulated Stage 3 PCB in a 2 m/s airflow	197
7.8	Comparison of measured and predicted component junction temperatures for simultaneously powered components on the insulated Stage 3 PCB in a 4 m/s airflow	197
7.9	Comparison of measured and predicted component junction temperatures for the Stage 1 PCB in a 4 m/s airflow	201
7.10	Comparison of measured and predicted component junction temperatures for individually powered components on the Stage 3 PCB in a 4 m/s airflow	202
7.11	Comparison of measured and predicted component junction temperatures for simultaneously powered components on the Stage 3 PCB in a 4 m/s airflow	204
7.12	Numerical component energy balances on the simultaneously powered non-insulated Stage 3 PCB in a 4 m/s airflow	205
B.1	Measured parameters and estimated uncertainties	240
C.1	Model constants for the high-Reynolds number k- $\epsilon$ model implemented in Flotherm [69] and Fluent [70]	245
C.2	Model constants for the Spalart-Allmaras model implemented in Fluent [70]	249
C.3	Model constants for the SST k- $\omega$ model implemented in Fluent [70]	255

## Nomenclature

Symbol	Description	Unit
A	Surface area	m <sup>2</sup>
BI	Bottom_inner package prime lumped surface	---
BO	Bottom_outer package prime lumped surface	---
C	Turbulent flow model constant	---
C <sub>p</sub>	Specific heat capacity	J/kg.K
f	Damping function	
G	Generation rate	
Gr	Grashof number, $g \beta (T_s - T_a) L^3 / \nu^2$	---
g	Gravitational acceleration	m/s <sup>2</sup>
h	Heat transfer coefficient	W/m <sup>2</sup> .K
I	Electrical current	A
K	Linear coefficient for diode forward voltage change with temperature (K factor)	K/V
k	Thermal conductivity	W/m.K
	Turbulent kinetic energy	m <sup>2</sup> /s <sup>2</sup>
L	Characteristic length	m
	Lead foot package prime lumped surface	---
Nu	Nusselt number, $h L / k$	---
Pr	Prandtl number, $\mu C_p / k$	---
Q <sub>diss</sub>	Component power dissipation	W
q''	Heat flux	W/m <sup>2</sup>
R	Measured quantity	
Re	Reynolds number, $u L / \nu$	---
S	Source term	
	Strain tensor	
St	Stanton number, $h / \rho u C_p$	---
T	Temperature	K
TI	Top_inner package prime lumped surface	---
TO	Top_outer package prime lumped surface	---
$\Delta T$	Temperature difference	K
U <sub>i</sub> , U <sub>j</sub> , U <sub>k</sub>	Mean fluid velocity component	m/s
u <sub>i</sub> , u <sub>j</sub> , u <sub>k</sub>	Fluid velocity components	m/s
u <sub><math>\tau</math></sub>	Friction velocity, $(\tau_w / \rho)^{1/2}$	m/s
V	Voltage	V
V <sub>f</sub>	Diode forward voltage	V
x	Individual measurement or parameter	
x,y,z	Cartesian co-ordinates	m
Y	Destruction rate	
y	Distance from the wall	m
y <sup>+</sup>	Non-dimensional wall co-ordinate, $u_\tau y / \nu$	---
y <sub>s</sub>	Distance from the wall equivalent to $y^+ \approx 11.5$	m

## Greek

$\beta$	Volumetric thermal expansion coefficient	$K^{-1}$
$\Gamma$	Diffusivity	$m^2/s$
$\delta$	Hydrodynamic / thermal boundary layer thickness	$m$
$\varepsilon$	Surface emissivity	---
	Rate of dissipated turbulent energy	$m^2/s^3$
$\kappa$	Von Karman's constant	---
$\lambda$	Blending function	
$\theta$	Thermal resistance, $(T - T_{ref})/Q_{diss}$	$K/W$
$\mu$	Dynamic viscosity	$N.s/m^2$
$\nu$	Kinematic viscosity	$m^2/s$
$\hat{\nu}$	Modified turbulent eddy viscosity, Spalart-Allmaras model	$m^2/s$
$\rho$	Mass density	$kg/m^3$
$\sigma$	Stefan-Boltzmann constant	$W/m^2.K^4$
	Turbulent Prandtl number for $k, \varepsilon, \omega$	
$\tau$	Shear stress	$N/m^2$
$\Phi$	General dependent variable	
$\omega$	Specific dissipation rate	$s^{-1}$
$\Omega$	Rotation tensor	---

## Subscript

a	Ambient
c	Component surface (case)
eff	Effective
f	Fluid
j	Component junction
ja	Component junction-to-ambient
jc	Component junction-to-case
L	Characteristic length
nw	Near-wall
ref	Reference
s	Surface
t	Turbulent
w	Wall
y	Distance from the wall

## Superscript

'	Fluctuating quantity
+	Non-dimensional

## 1.0 Introduction

In this introductory chapter, background is provided on electronics thermal management. The application of Computational Fluid Dynamics (CFD) analysis to the thermal design of electronic equipment, and the challenges posed for the prediction of electronic component operating temperature in air-cooled electronic systems are described. The need to assess CFD predictive accuracy for electronics cooling is outlined. Finally, the subject of the proposed research is defined, with the outline of the thesis given.

### 1.1 Electronics Thermal Management

In today's society, electronic products span an ever-increasing spectrum of applications such as aerospace, automotive, communications, computing, medical and entertainment. In the telecommunications sector alone, products range from cellular phones, personal digital assistants (PDAs), multimedia to network computers [1]. Developing sectors such as the biomedical are anticipated to further boost the growth of the electronics industry, by driving the development of a multitude of new electronic devices. With worldwide electronic equipment revenues forecast to exceed \$2 trillion by 2007 [2], the electronics industry acts as a driving engine for science, technology, and manufacturing.

To satisfy consumer demands for more compact and sophisticated electronic devices, advances of semiconductor technology have achieved increased Integrated Circuit (IC) functionality and miniaturisation. This progress is still described by Moore's law, which states that "the number of transistors per chip will double every eighteen months" [3]. However, rising transistor density and switching speed of microprocessors have been accompanied by drastic increases in die heat flux and power dissipation, which are on the exponential rise at all levels of electronic packaging, irrespective of market segment and clock frequency [4]. The continuous rise in IC power dissipation is well documented [5,6] and illustrated in Figure 1.1, which shows the history of Intel's CPU power dissipation. The impact of such trends at system level, as forecasted by the world's leading Information Technology (IT) manufacturers [7], is illustrated in Figure 1.2 for data processing, computer systems and telecommunication equipment. These projections suggest a dramatic increase in system heat flux. In this context, rising IC heat densities, combined with even more stringent performance and reliability constraints in the future [8], pose challenges that will make thermal management a key enabling technology in the development of microelectronic systems in the next decade [9].

Many IC packaging failure mechanisms have been found to be dependent upon spatial temperature gradients, temperature cycle magnitude, rate of temperature change, rather than absolute temperature [10], while semiconductor die circuit electrical performance can

be highly sensitive to operating temperature [11]. While no simple, generic relationship exists that relates electronic component and Printed Circuit Board (PCB) reliability with these variables [10], it is notable, however, that reducing the operational temperature will almost invariably reduce temperature gradients, all other things being equal [12]. It is therefore accepted that temperature must be controlled to meet both performance and reliability requirements, with electronics thermal design generally aiming at reducing component junction temperature.

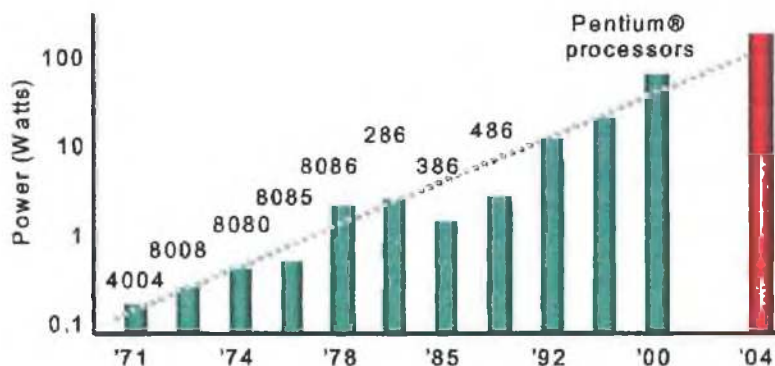


Figure 1.1 Historical power trend for Intel's CPUs [13].

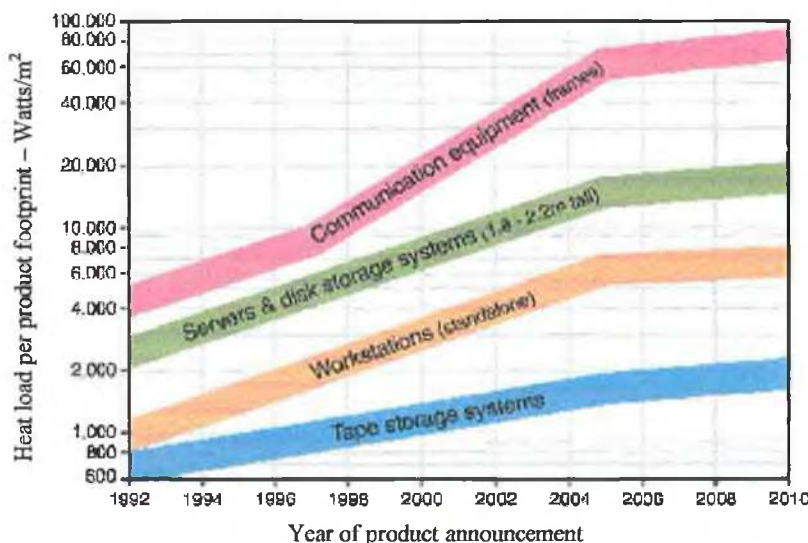


Figure 1.2 Heat density trends for data processing, computer systems and telecommunication equipment [14].

Over the last decade, thermal design practices within the electronics industry have progressed from basic analytical and semi-empirical calculations, applicable to simple systems in tandem with extensive physical prototype characterisation, to a high reliance on virtual prototyping using numerical predictive techniques. This evolution has been driven by ever-reducing product development cycle times, preventing extensive

prototyping, and has been enabled by increases in computational power. Realistically the conjugate heat transfer problems typically encountered in today's more complex electronic equipment can only be accurately represented by Computational Fluids Dynamics (CFD)-based methods, which simultaneously solves the appropriate governing equations for the solid and fluid domains, and couple both at the solid-fluid interface [15]. The potential of this technique as a design tool, to generate and quickly assess solutions, has been demonstrated by Prakash [16] and Lee et al. [17]. CFD analysis is now widely-used within the electronics industry for predicting electronic equipment thermal performance. Such predictions then form critical boundary conditions for electrical and thermo-mechanical performance analyses, component life and reliability calculations.

An efficient thermal design needs to focus on the complete heat transfer chain of an electronic system, Figure 1.3, from the heat dissipating components acting as thermal source, to the environment external to the system enclosure, as sink. Thus effective thermal analysis typically addresses four distinct hierarchical levels [18], namely: die, component, PCB, and system, with each step ultimately increasing the complexity of the problem posed for CFD analysis. Within this categorisation, the present study is concerned with the prediction of PCB-mounted component operational temperature in air-cooled electronic systems. As will be shown, such sub-systems can form an appropriate benchmark level for assessing CFD predictive accuracy, while the prediction of component junction temperature is of relevance to many current reliability prediction methods. The merits of such reliability assessment methods are not discussed in this study as they are outside its scope, but the related contentious issues are highlighted, for example, by Pecht et al. [19] and Das and Pecht [20].



**Figure 1.3** Thermal analysis chain of an electronic system, from IC to data centre [21].

## 1.2 Application of CFD Analysis to Electronics Thermal Design

Although current CFD software are capable of solving with reasonable accuracy the Navier-Stokes equations for laminar steady flows [22], for turbulent conditions, Reynolds-Averaged Navier-Stokes (RANS)-based computations are typically constrained to modelling the Reynolds stresses by the Boussinesq hypothesis. It is likely that this approach will continue to be utilised for the analysis of electronics cooling in the foreseeable future [23,24]. At present, higher-order turbulence closure models such as Reynolds Stress Models (RSM), or time-accurate simulations using Large Eddy Simulation (LES) or Direct Numerical Simulation (DNS) techniques place excessive demands on computational resources for practical engineering analyses. In this study, discussion therefore focuses on the application of eddy viscosity turbulence models to predict airflow and heat transfer in electronic systems.

CFD analysis is generally applied with different strategies and objectives throughout the design cycle of electronic equipment. The benefits of CFD analysis as a virtual prototyping tool are undisputed in the early to intermediate design phase, where the aim is to select a cooling strategy and refine a thermal design by parametric analysis. In this phase, the productivity of design analysis is considered to be more critical than predictive accuracy [25-28]. This is on the premise that qualitative predictions can be relied upon, an assumption that should be considered on a case-by-case basis. A number of methods to automate parametric design synthesis [29,30], deal with uncertainties in boundary conditions during the design process [31], or employ CFD codes as diagnostic tools [32] have been recently proposed. Considering the potential computational expense incurred with CFD modelling, alternative design methods, such as semi-empirical analysis and flow network modelling have also been advocated [33], which are of value in providing an initial design to be refined by CFD analysis. Generally therefore, modern thermal design methodologies rely, to varying extents, upon the ability of CFD analysis to produce realistic temperature predictions.

Responding to the demand for improved design productivity, vendors of CFD codes dedicated to the thermal analysis of electronics over the last five years have focused on enhancing code pre- and post-processing capabilities, with comparatively less efforts on improving calculation strategies and turbulent flow modelling. However, the suitability of CFD analysis for generating critical temperature boundary conditions used in subsequent product performance and reliability analyses, hence strategic product design decisions, has been questioned [34,35]. This concern is based on a number of factors impacting on predictive accuracy, including computational constraints, uncertainties in physical boundary conditions, and the capability of the CFD code to predict complex airflow

phenomena and their impact on heat transfer. While there is no consensus in the literature on maximum permissible prediction error for component junction temperature, the following guidelines have been proposed. Whereas in the early to intermediate design phase, an accuracy of  $\pm 10^{\circ}\text{C}$  or 20% to  $\pm 5^{\circ}\text{C}$  or 10% is generally sufficient [35,36], for temperature predictions to be applied as boundary conditions in component Physics-of-Failure (PoF) based reliability prediction methods [10,37-40], which rely on the accurate determination of electronic component operating parameters, a criterion of  $\pm 3^{\circ}\text{C}$  or 5% applies [41]. PoF reliability prediction methods are based on root cause analyses of underlying electronic component failure processes, and are used to proactively predict distributions of Time to Failure (TTF). This is achieved by developing failure models through experimental studies of the critical materials and by developing computer-assisted stress models of the intended product, whereby CFD analysis would provide the thermal boundary conditions. The merits of PoF approaches over traditional statistical empirical reliability assurance approaches are discussed by Dasgupta [40].

To date, the predictive accuracy of CFD codes dedicated to the thermal analysis of electronic equipment has not been comprehensively validated. Typically, simplified and limited studies have been undertaken by CFD vendors prior to market release and the premise that this work is sufficient to merit accurate analysis of complex thermofluid problems, such as encountered in electronics cooling applications, without the need for extensive experimental validation is weak. This fundamental limitation has been well recognised in the technical literature, with the result that numerous benchmark studies have been published [42]. However despite the importance of this combined effort, these studies collectively do not constitute a comprehensive assessment of CFD analysis to the whole field of electronics cooling [34]. On this basis, numerical analysis without supporting experimentation still remains an unreliable design strategy [23,34]. Experimentation is required to validate numerical models and qualify a final design, which can effectively prolong the product development cycle time, and thus undermine the potential of CFD analysis to improve the efficiency of design analysis.

In this context, the present work aims to provide a perspective on the potential of CFD analysis as a design tool, to provide critical temperature predictions used for strategic product design decisions or reliability calculations. This is achieved based on a systematic assessment of CFD predictive accuracy for PCB-mounted electronic component heat transfer.

### **1.2.1 Prediction of Electronic Component Operational Temperature**

It is worth reflecting on the constraints imposed on CFD analysis for the prediction of



component operating temperature in a typical forced-air cooled rack-mounted electronic system, and therefore the challenges posed. Despite increases in computational power, discretization constraints still prohibit the explicit modelling of length scales from micron to meter at component to cabinet level respectively within a single numerical model. The large grids/meshes required to resolve these disparities result in computational times that would be excessive in a design environment.

In such instances, an alternative two-tier analysis strategy is typically employed [43], whereby (i) coarse computations of temperature distributions and global flow field features are performed using a system level model and (ii) the sub-system of interest, such as PCB, is analysed in isolation using a detailed model to predict component operating temperature, from which performance, life and reliability estimates are to be calculated. System level boundary conditions, which are extracted from a control volume enclosing the region of interest, are applied at the domain boundaries of the sub-system model. However, computational limitations may still be prohibitive for sub-system analysis, as will be shown in this study. Furthermore, considerable uncertainties in both physical and applied numerical boundary conditions at system level, are propagated through the prescribed boundary conditions. Physical uncertainties include, for example, power dissipation for the various system units, and grilles and vents pressure loss coefficients [34]. In addition, the capability of the CFD code to predict complex flow phenomena, such as fan-induced, and their impact on heat transfer needs to be considered [24,44,45]. This is often compounded by the fact that in the early design phase, the CFD user may have little or no *à priori* knowledge of the flow regime, whether laminar, transitional, turbulent, and whether steady or unsteady. Such an uncertainty typically arises from the absence of a physical prototype, and the difficulty in defining a characteristic dimension, hence transition Reynolds number, that adequately describes the heat transfer characteristics over the PCB or sub-system considered. In spite of this difficulty, the onus is on the CFD user to select an appropriate flow modelling strategy. These factors combined highlight considerable difficulties in undertaking meaningful system level analysis at present.

To further ease discretization constraints, so-called component 'compact' thermal modelling (CTM) methodologies have been widely advocated [46-55]. Such approaches eliminate the need for detailed component geometry modelling, whereby both the mechanical architecture and thermo-physical properties of the component constituent elements are explicitly represented, with conduction solved within the component solid domain. CTMs permit steady-state component thermal behaviour to be modelled using simplified few parameter-based representations of the package conductive domain, typically consisting of thermal resistor networks as illustrated in Section 4.5.1.2. Once

incorporated into a rack- or system level numerical model, such representations are intended to provide estimates of electronic component operating temperature at a reduced computational expense. CTMs could also help overcome other issues associated with detailed component modelling, such as uncertainties in packaging material thermo-physical properties, and proprietary package architecture. This approach, however, may be far from satisfactory, as computational constraints still have to be overcome for adequately resolving the impact of local flow field features on component heat transfer. In addition, the capability of CTMs to predict complex multi-mode component heat transfer in real electronic systems has not yet been comprehensively evaluated. As will be outlined in Section 2.4.1, several issues are still to be resolved before CTMs can be routinely adopted for the prediction of component operating temperature in electronic systems. The impact of some of these issues on prediction accuracy will be investigated in this study.

Electronic systems contain complex geometries, numerous length scales, buoyancy forces and the fluid flow is often transitional [56,57] with complex flow phenomena [58]. Such phenomena are generated by cooling fans or intricate geometries such as EMC screens, vents, and populated circuit boards [59]. Fan-generated flows contain swirling flow patterns [44], while screen holes will produce jets downstream [24,45]. Such flow disturbances can generate unsteady or transitional flow conditions over electronic circuit boards, with attaching, separating and recirculating flow features [60]. In addition, the component topology often generates multi-dimensional flow phenomena that include pulsating and vortical structures [60,61]. Airflows over component-boards are usually classified as low-Reynolds number flows due to the small velocities and geometric length scales encountered [62]. In addition to free-stream turbulence generated by system elements, turbulence may also be generated locally by the components. Depending on the local Reynolds number, it may then decay locally or persist until the next downstream protrusion where it may be enhanced.

While the nature of fluid flow may therefore vary considerably throughout an electronic system, and although a multitude of turbulence models has been developed, no universal model exists yet that performs superiorly and reliably for all classes of flows. Saulnier [63] notes that each model embody intrinsic limitations associated with the physical geometry from which they were developed. The application of eddy viscosity turbulence models is thus an act of approximation that requires verification [64]. In the absence of a universal model, the development of improved turbulence models specifically intended for distinct categories of flows is being actively pursued [65]. Consequently, an extensive need for benchmarking exists to evaluate the capabilities of various turbulence models for different thermofluid problems. A review of published CFD benchmark studies is presented in

Chapter 2, focusing on electronics cooling applications, from which areas of weakness to be addressed in this study will be identified.

To date, the majority of CFD computations performed on electronic equipment have been undertaken using commercial CFD codes dedicated to such applications. “Dedicated” refers to tailored pre-processing, permitting numerical models to be quickly generated. However, the turbulent flow modelling approaches employed are typically confined to an algebraic model and a standard two-equation high-Reynolds number  $k-\epsilon$  model, used in conjunction with standard “law-of-the-wall” wall functions. Such models meet the criteria of robustness, i.e. promote stable convergence, and to some extent, universality, which make them popular for practical engineering calculations [66]. As the application of two-equation models can be computationally prohibitive for system-level turbulent flow analysis, the algebraic models are typically employed for coarse grid computations of global flow and temperature distributions. The two-equation standard  $k-\epsilon$  model is subsequently used for refined sub-system analysis, such as for PCB assemblies. However, this strategy has been shown to fail to yield accurate predictions of component operating temperature in air-cooled PCBs [35], as neither a laminar or standard high-Reynolds number  $k-\epsilon$  flow model are specific for such flows.

For turbulent flow calculations the use of “law-of-the-wall” wall functions to calculate the surface heat transfer coefficient is justified for boundary layer type flows, but is inadequate for separating, reattaching or recirculating flow conditions. Ferziger and Peric [67] caution on the applicability of wall functions when such flow features exist over a large portion of the wall boundaries, which is typical of populated PCBs [68]. Therefore, using a standard  $k-\epsilon$  turbulence model and wall functions, prediction accuracy for the component/board convective heat transfer coefficient will depend both on how far the flow conditions deviate from boundary layer flow, and on the sensitivity of heat transfer to these conditions. In addition, wall functions become less reliable in situations where low-Reynolds number or near-wall effects are pervasive in the flow domain, and the hypotheses underlying the wall functions cease to be valid [65].

The impact of these limitations on the prediction of electronic component heat transfer will be quantified in this study using a software dedicated to the thermal analysis of electronic equipment, Flotherm [69]. In addition, the potential for improved predictive accuracy will be evaluated using a range of candidate, turbulent flow modelling approaches that may be more suited to the analysis of forced airflows over populated electronic boards. This will be performed using a general-purpose engineering code, having a wider range of turbulence modelling capabilities, Fluent [70].

### 1.2.2 Numerical Analysis of Electronic Component Transient Heat Transfer

While many electronic parts are subjected to transient operating conditions in the course of their life, due to dynamic power operation or varying ambient conditions, Parry et al. [71] note that over 90% of numerically-based thermal analyses performed on electronic equipment in recent years have been steady-state. This is essentially attributed to previous reliability prediction methods, such as MIL-HDBK-217F [72], focusing on steady-state temperature, as well as design for continuous operation and prohibitive computational requirements for transient analysis.

The need for accurate transient analysis is now also motivated by Physics-of-Failure reliability prediction methods, which require the knowledge of component transient operating temperature for assessing electrical and thermo-mechanical performance. Lasance [73] outlines that progress in reliability prediction is considerably hampered by the lack of methods to accurately predict spatial and temporal temperature gradients, from component to system level. Despite increases in computational power, a fully coupled thermal and mechanical analysis is not yet feasible [74] and instead, sequential approaches are employed. With short development cycle times prohibiting separate detailed thermal analysis, thermo-mechanical analysis is generally constrained to approximating convective heat transfer at the solid boundary using prescribed boundary conditions, derived from semi-empirical correlations, or to applying fixed temperature boundary conditions within the solid domain. The potential shortcomings of such approximations are highlighted by Wakil and Ho [75], who found that isothermal loading may lead to significant modelling errors for the prediction of the strain distribution within a heat dissipating PQFP component. They concluded by stressing the need for accurate modelling of the temperature distribution within the component body. As highlighted in Chapter 2, this can only be realistically predicted using CFD methods.

Apart from the prediction of transient component operating temperature, a potential application area of CFD analysis could be the design of both optimum reliability testing conditions and assembly processes. Electronic circuit board assembly processes and reliability testing techniques expose electronic components to severe transient thermal environments early in their lifetime [76]. Whereas high junction temperatures and large thermal gradients are discouraged during the assembly process, they are encouraged for reliability testing so that any latent manufacturing defects can be identified. The success of either process depends on a thorough understanding of the components' thermal response to such transient environments [77].

To date, the electronics industry has relied on experimental testing and the acquisition of field experience to optimise component reliability tests and assembly processes. However,

with ever-reducing product development cycle times preventing both extensive prototyping and the acquisition of field experience in the use of both new packaging technologies and assembly processes, numerical predictive techniques will need to be increasingly relied upon.

Reliability tests typically consist of power cycling, air temperature cycling, or a combination of both, in environments that approximate the real use conditions. Their objectives are to detect latent manufacturing defects or predict component reliability and performance during operation. Physics-of-Failure-based reliability prediction methods rely on the accurate determination of testing parameters, which must accelerate the same failure mechanisms as those taking place in the application environment. Warner et al. [74] point out that it is difficult to include, for example, the temperature difference within the package and board in an experimental accelerated environment, and that to accelerate this temperature difference requires the knowledge of the application environment. In such instances, and on the premise that sufficient predictive accuracy can be obtained, numerical analysis could provide the necessary boundary conditions.

Reflow soldering is a process where electronic components are assembled onto PCBs. This process involves the use of infrared heating, convection heating, or a combination of both in an oven to bond the parts. Heating and cooling of the assembly must be carefully controlled both to minimise soldering defects and the impact of elevated temperature or temperature gradients on device reliability. The introduction of lead-free solders, imposed by recent European Union directives [78], will require extensive re-qualification of such processes, partly resulting from higher reflow temperatures [79]. Typical methods which use thermocouples for thermally characterising PCB assemblies during reflow soldering are known to be prone to error [79]. In this context, numerical analysis could both contribute to accelerate process re-qualification, and possibly enable accurate characterisation.

As the heat transfer processes involved in either component reliability testing or surface-mount assembly are typically highly conjugate, realistic heat transfer predictions can only be obtained using CFD-based methods.

### **1.3 Proposed Area of Study and Outline of Thesis**

This study aims to provide a perspective on the capability of CFD analysis to predict air-cooled PCB-mounted electronic component heat transfer, and thus its potential as a design tool, to provide critical temperature predictions required for strategic product design decisions. This is achieved based on a systematic assessment of numerical predictive accuracy against experimental benchmarks.

The benchmarks will involve a range of PCB test vehicles incorporating different

electronic component types, thermally characterised in free- and forced-air convective environments. These configurations generate different airflow phenomena and varying degrees of component thermal interaction, representing different levels of complexity for CFD analysis. Both the prediction of steady-state and transient component heat transfer will be investigated. The suitability of modelling methodologies for component-PCB heat transfer will also be assessed for use in a design environment. Apart from the prediction of component operational temperature in electronic equipment, the application of CFD analysis to the design of component reliability tests and convective solder reflow temperature profiles will be investigated. Future work programs will also be identified to improve the accuracy of numerical predictions.

The thesis is structured as follows.

In Chapter 2, a review of previous experimental studies on characterising electronic component heat transfer is presented, revealing the complexity of the thermofluid phenomena involved and thus the challenge posed for numerical prediction. Previously published CFD benchmark studies, focusing on component-circuit board heat transfer, are then reviewed which highlight areas of weakness that will be addressed in the current work. From this combined literature review, experimental studies providing accurate characterisation data for electronic component heat transfer are identified, which will be used in this study to assess CFD predictive accuracy. The strategy employed to assess predictive accuracy is outlined, which will permit both the numerical modelling methodology and CFD solver capability to be carefully evaluated.

In Chapter 3, the benchmark test configurations employed for assessing numerical predictive accuracy are described. Details of the component architectures, circuit board layouts, characterisation environments and characterisation methods are provided. Component geometry and structural integrity are investigated using destructive and non-destructive testing techniques, so as to eliminate potential numerical modelling uncertainties. The experimental characterisation data generated in previous studies, comprising of component junction temperature and component-board surface temperature, is presented. This data is augmented in this study by experimental visualisations of the forced airflows over the populated boards, undertaken using two complimentary flow visualisation techniques. Combined, the documentation of the test vehicles, characterisation methods and experimental measurement data in this thesis, form standalone benchmarks that could be re-used in the future to evaluate CFD advancements in terms of predictive accuracy.

In Chapter 4, features of the two CFD codes employed in the study, that are of relevance to the analysis of air-cooled PCB-mounted component heat transfer are reviewed. The potential

shortcomings of the turbulence modelling used in CFD software dedicated to the analysis of electronics cooling are outlined. Alternative candidate turbulence flow models available in the general-purpose CFD code, which may be more suited to the analysis of electronic component heat transfer, are selected for evaluation. Numerical modelling methodologies are developed and applied to the respective test configurations presented in Chapter 3.

The component-board numerical modelling methodology is validated in Chapter 5. CFD predictive accuracy is then assessed for transient component heat transfer in operating conditions of relevance to electronic equipment application environments and component reliability screening. The capability of component compact thermal models to predict multi-mode component heat transfer is also assessed.

In Chapter 6, CFD predictive accuracy for multi-component board heat transfer in free convection is assessed. To both build confidence in the modelling methodology and investigate potential sources of prediction error, the test case complexity is incremented in controlled steps from single- to multi-component board conjugate heat transfer.

The natural convection benchmark analysis methodology is reproduced for forced convection in Chapter 7, where a range of turbulent flow models are evaluated. The impact of aerodynamic and thermal factors on component operating temperature predictive accuracy are quantified. The validated numerical models are used to extract energy balance analyses of component heat transfer, which are used to help link junction temperature prediction errors to flow field prediction errors.

Conclusions on the major findings of this thesis and recommendations for future work are given in Chapter 8.

It is intended that this study will not only increase the understanding of the thermofluids processes involved in component-PCB heat transfer, but also help develop confidence in the numerical modelling methodologies applied, and begin to establish the capability of CFD design analysis both now and in the foreseeable future.

## **2.0 Literature Review and Benchmark Strategy**

### **2.1 Introduction**

In this chapter, a review of published studies on experimental characterisation and numerical prediction of electronic component-board heat transfer is presented. The former studies reveal the complexity of component-PCB thermofluids and thus the challenge posed for numerical prediction. From the numerical studies cited, potential areas of weakness are identified that will be addressed by the present study. Finally, a benchmark strategy for component-PCB heat transfer is outlined, to enable both the numerical modelling methodologies and solver capability to be carefully evaluated.

### **2.2 Experimental Characterisation of Air-Cooled Electronic Component Heat Transfer**

While forced air-cooling is no longer sufficient for many high-power dissipating applications [80], it still remains a popular solution and is likely to play a key role in the development of future electronic systems [4,81]. Although higher-performance cooling technologies, such as liquid cooling or refrigeration are under active development, because of perceived stringent cost constraints, reliability concerns and technological packaging challenges, Azar [4] outlines that many thermal management strategies will remain confined to air-cooling for the foreseeable future.

Direct air-cooling of PCB mounted electronic components is well described in the literature, with numerous experimental and numerical studies being reported [82,83]. Recognising the complexity of the flow phenomena [58,84-86] and conjugate heat transfer processes associated with real PCBs [87,88], experimental studies sought to simplify the representation of the populated PCB geometry and the associated heat transfer processes. The best approximations of component geometry typically consisted of three-dimensional, cubical or low-profile, solid metal blocks that were tested either in isolation or arranged in arrays [89-94]. Less realistic representations employed two-dimensional ribs or flush mounted heat sources [95-98]. These idealised component replicas were typically exposed to channel airflows generated by a wind tunnel.

Simplifications to the thermal boundary conditions imposed included: i) the use of aluminium or copper metal blocks that allowed both active and passive array elements to be considered as isothermal, ii) polished metal surfaces that enabled radiation to be neglected, and iii) non-conducting substrates that limited heat loss from the module's base to typically less than 15%.

These experimental studies sought to: i) develop Nusselt-Reynolds number correlations



so that convective heat transfer coefficients could be defined for individual modules, ii) highlight the sensitivity of component heat transfer to module position relative to the PCB's leading edge, iii) quantify the effect of introducing channel flow disturbances on module temperature, and iv) measure the adiabatic temperature rise<sup>1</sup> of passive neighbouring or downstream modules for different PCB configurations and air velocities [99].

While these idealised PCB configurations have generated excellent data for benchmarking current Computational Fluid Dynamics (CFD) codes, which incidentally was not the intended objective, it is disappointing to note that little agreement exists between the various Nusselt-Reynolds correlations that have been developed [100,101]. This results, in part, from the difficulty of defining a dominant characteristic dimension for component shape and PCB configuration, and the lack of a consistent method of characterising the reference fluid temperature. As a result, Anderson and Moffat [100] proposed a more robust correlation that relates module heat transfer coefficients to channel pressure drop, and promising results were reported for a range of module shapes and PCB configurations.

However, the absence of conductive heat transfer between the block base and the substrate limits the applicability of these correlations for design. The importance of this omission became obvious when later studies, using real components, showed that base conduction accounted for as much as 70% of the total heat dissipation [77,102,103]. As a result, more recent experimental studies by Arabzadeh et al. [94], Nakayama and Park [104] and Tang and Ghajar [105] have addressed this issue by changing either the conductive resistance between the module base and substrate, or altering the substrate thermal conductivity to allow significant heat loss through the base. These studies highlighted that substrate conduction has a significant impact on module operating temperature, its thermal footprint size and substrate temperature gradients. This highlights the need for more complex, yet realistic studies, that allow the combined effects of flow disturbance and substrate conduction to be evaluated simultaneously [83].

One study of this nature has been published [12,99,106,107]. It describes the extent of span-wise and stream-wise component thermal interaction between fifteen functional Plastic Quad Flat Packs (PQFPs), surface mounted in a symmetrical, in-line array on a FR-4 conducting circuit board. Influence factors were used to describe the effects of local aerodynamic and thermal conditions on component thermal resistance, as a function of

---

<sup>1</sup> Module equilibrium temperature rise above free-stream fluid temperature without self-heating.

free-stream velocity. Based on this experimental data, a novel forced air-cooling thermal design methodology was proposed [107]. It was based upon the adjustment, using the above factors, of components' standard junction-to-ambient thermal resistances derived from single board-mounted components, characterised in standardised convective environments [108-110]. The method utilised numerical predictions for system level flow characterisation, and the adjusted thermal characteristics for board- and component level modelling. However, the premise is that system level flow fields predicted by CFD analysis can be relied upon to provide boundary conditions for board level analysis. This study served to highlight the complexity of actual PCB heat transfer, which is too difficult to describe in a generic way using empirical correlations. The test configurations experimentally characterised in [106] will be used in the present study to assess CFD predictive accuracy for electronic component heat transfer.

While the foregoing studies were confined to steady-state component heat transfer, due to a past perception that absolute temperature was the dominant stress parameter influencing electronics reliability (Section 1.2.2), little experimental work has been published on characterising dynamic board-mounted component thermal behaviour. Studies have been primarily confined to characterising component thermal impedance in conductive environments [111,112], one of the objectives being to support the development of dynamic component compact thermal modelling methodologies [113,114]. Davies et al. [115] and Lohan and Davies [77] are the only studies reported on conjugate heat transfer. They measured the spatial and temporal gradients on a board-mounted component exposed to power- and air temperature cycling conditions. These measurements will be used in the current study to investigate the capability of CFD analysis to predict transient component heat transfer. The accurate prediction of dynamic component thermal behaviour is critical for Physics-of-Failure (PoF) analysis of failure processes influenced by temporal temperature gradients.

### **2.3 Experimental Flow Visualisation**

The three-dimensional shape and irregular nature of electronic component topologies on air-cooled PCBs give rise to complex airflow patterns that have been well documented [58,59]. Numerous flow visualisation studies have been undertaken to help develop an understanding of such flow phenomena, and their impact on the underlying convective heat transfer processes involved, which have been well summarised by Garimella [68].

These studies provide excellent descriptions of the flow phenomena about classical geometries such as two-dimensional ribs [95] and cubical elements [62,116,117,91], or the flat pack geometries considered in this study [61,84,118]. The link between flow

phenomena and convective heat transfer has also been investigated using various techniques, including mass transfer techniques such as naphthalene sublimation [119,120], interferometry [95,121,122], Particle Image Velocimetry (PIV) [121,123,124,125], heat flux sensors [126], and surface temperature contour maps measured using infrared thermography [58,62,123,127].

Whereas the foregoing studies employed flow visualisation to develop a physical understanding of PCB thermofluids, Evely et al. [128] applied such methods to qualitatively interpret numerical prediction errors in component heat transfer. A similar approach will be taken in this study, whereby the value of flow visualisation methods in aiding the CFD prediction of component heat transfer in a design environment will be demonstrated.

## **2.4 CFD Predictive Accuracy**

The need to assess CFD predictive accuracy for electronics cooling was outlined in Chapter 1. Ideally, good benchmark tests for assessing CFD predictive accuracy should exhibit complex thermofluid phenomena that can be accurately characterised by experimental analysis. A number of fundamental benchmark test cases exist against which CFD codes have been evaluated and though not explicitly derived for electronics cooling applications, these are of relevance to this area due to both the geometries and heat transfer processes involved. Typical examples include flow over a blunt flat plate or around an obstacle, backward facing step, and channel flows by Ota and Kon [129], Fokkelman et al. [130], Abe et al. [131,132], Freitas [133], Cokljat et al. [134]. An extensive validation study was presented by Freitas [133], who summarised the performance of commercial CFD codes for the prediction of flow around two- and three-dimensional obstacles, and the backward-facing step. This study highlighted the limitations of currently available two-equation eddy viscosity models for predicting such flow phenomena. These limitations were further exposed at the 6<sup>th</sup> ERCOFTAC/IAHR/COST Workshop [135], where an investigation of flow around a three-dimensional cubical element array revealed that reasonable predictions of the benchmark data could only be achieved using Direct Numerical Simulation (DNS) techniques.

While such studies are useful for assessing turbulence model capability, it is difficult to translate their findings to the analysis of the more complex, discrete, three-dimensional, non-isothermal components in air-cooled electronic systems, where the aim is to predict the internal operating junction temperature. Therefore, a need exists to better understand the capabilities and limitations of current CFD based software tools for the analysis of such systems.

Before reviewing previous CFD evaluations focusing on PCB-mounted component heat transfer, it is worth tempering the forthcoming discussion with the advice of Azar and Manno [136] who cautioned researchers to seek a balanced combination of both experimental and numerical effort. To facilitate the comparison between both approaches, Rhee and Moffat [137] outline the critical factors that enable one to distinguish between measurement uncertainty and numerical prediction inaccuracy. In addition to accuracy, Ghosh [138] outlines criterion that should be considered in the selection of numerical tools to ensure their appropriateness for a given electronic cooling application. Tucker [42] provides a review study of the technical capabilities of commercial CFD codes for electronic cooling with overviews given by Holt et al. [139] and Remsburg [140]. Apart from proposing a system level benchmark test case, Linton and Agonafer [141] listed various features of electronic systems that could serve as practical benchmark test cases.

#### **2.4.1 Prediction of Electronic Component Heat Transfer**

As highlighted in Section 1.2.2, limited work has been carried out on the numerical prediction of transient conjugate component heat transfer, as a result of reliability prediction methods focusing on steady-state temperature and computational constraints. Previously reported numerical studies on transient component heat transfer have been confined to the analysis of conduction-cooled high-power modules, such as IGBT devices [142-145]. The cooling configuration permitted these analyses to be confined to the modelling of conduction, with either a fixed temperature boundary condition or effective heat transfer coefficient prescribed at the domain boundary. Though justified in such applications, this modelling approach would not be appropriate for the majority of air-cooled, board-mounted components, from which heat transfer is highly conjugate. To the author's knowledge, no corresponding studies involving CFD analysis have been published. The following review is therefore confined to the CFD prediction of component steady-state heat transfer.

The majority of studies in this area have focused on either single-board mounted components or replicas of operational multi-component PCBs consisting of either heat-dissipating metal cuboid blocks, ribs or flush mounted elements on a low thermal conductivity substrate.

Studies that have focused on single-board mounted components in laminar free convection include Rosten et al. [103], Adams et al. [146], Ramakrishna et al. [147], Zahn [148], Eveloy et al. [128], Lohan et al. [149], Peng and Ishizuka [150]. These studies provide an insight to modelling methodology and prediction accuracy, which was within 10% of measurements for junction-to-ambient thermal resistance. Approximations of

multi-component PCBs were studied by Kim et al. [151], Di Perna et al. [152], Heindel et al. [153,154], Wang et al. [155], Drabbels [156], and Behnia and Nakayama [157]. The former studies have shown that steady-state, single-component PCB heat transfer can be predicted with good accuracy ( $\pm 5\%$ ), providing that the geometries, material thermal properties and boundary conditions are accurately known, and appropriate modelling methodologies are employed. However, the requirement to model turbulence was absent. The objective of the second category of studies was essentially to investigate the influence of characteristic parameters on the velocity and thermal fields, with the solution procedure validated against either experimental or other numerical data.

For forced convection, studies that have analysed single-component PCBs in forced airflows include Rosten and Viswanath [158] and Teng et al. [159] who both modelled the component with and without a pin-fin heat sink. Junction-to-ambient thermal resistance ( $\theta_{ja}$ ) was predicted to within 4% and 10% of the measured values respectively, with the error coming from an overprediction of the heat transfer rate. When the heat sink was attached, prediction error increased to a worst case of 18% at approximately 1 m/s in both studies. Rosten and Viswanath [158] attributed this error to either the heat sink modelling methodology employed or the limitations of the algebraic turbulence model. Unfortunately Teng et al. [159] did not document which turbulence model was employed in their study, but an experimental parametric study suggested that component internal conductive resistance was modelled correctly. These heat sink studies reflect current trends towards the introduction of more complex geometries at PCB level, which demand the application of appropriate modelling methodologies and a correct flow model. Similar levels of predictive accuracy (within 10%) were reported by Ramakrishna et al. [147], Adams et al. [160], Chiriac and Lee [161] and Ramakrishna and Lee [162], who focused on the development of component modelling methodologies for new packaging technologies.

However, it is notable that these studies almost invariably used a single metric, component junction temperature, for evaluating predictive accuracy. Addressing this point, Rodgers et al. [35] proposed a dual approach, based upon the metrics of measured component junction temperature and component-PCB surface temperature for validating the component-board numerical model. Predictive accuracy was assessed for two different single component-boards in a 2 m/s airflow, incorporating SO16 and PQFP 208 devices. Component junction temperature prediction accuracy was overall within 3°C of measurement. The predicted board surface temperature distributions were also in good agreement with measurement in both the span-wise airflow direction, and upstream of the component in the stream-wise direction, indicating that PCB heat spread was well captured. However, discrepancies were clearly identified downstream of either

component, which were attributed to inaccurate prediction of the advected air temperature adjacent to the board in this region. This suggested the need to assess component temperature prediction accuracy for more realistic, multi-component board topologies, generating more complex flows. The authors addressed this and their findings are summarised later in this section.

As an important step from the modelling of single component-boards, Anderson [163] analysed an idealised, populated PCB consisting of an 8 x 6 array of low profile, rectangular aluminium blocks in forced convection. Significant errors in the prediction of downstream module adiabatic temperature rise were highlighted. These errors were attributed to incorrect prediction of downstream fluid flow mixing, as good agreement between predicted and measured adiabatic heat transfer coefficient was found. These findings therefore indicated a weakness of the turbulence modelling approach employed by the CFD code to deal with these more complex flows, suggesting that the flow phenomena generated by the simple, single-component PCB topologies only posed a moderate challenge to CFD analysis. However, the test vehicle employed did not permit to translate the full implications of these findings to the analysis of multiple, non-isothermal PCB-mounted components, for which heat transfer is highly conjugate.

Addressing this weakness, Rodgers et al. [35,164] analysed for the first time a populated board incorporating real electronic components (SO16, TSOP 48 and PQFP 208), in a 2 m/s wind tunnel airflow. Using a CFD code dedicated to the thermal analysis of electronic equipment, component junction temperature prediction accuracy was found to be within  $\pm 5^{\circ}\text{C}$  or 10%. It was detected that component thermal interaction was not fully captured, and anticipated that this limitation could lead to more significant prediction errors on densely packed PCBs, having a high degree of component thermal interaction. It was also found that neither the laminar or turbulent flow model used (standard high-Reynolds number k- $\epsilon$ ) were able to resolve the complete flow field over the populated board, while the variation between flow model predictions was proportional to the amount of flow disturbance introduced in the flow field upstream of the component. The greatest prediction errors and variations between flow models (up to  $10^{\circ}\text{C}$ ) occurred in regions identified as aerodynamically sensitive by both experimental measurement and flow visualisation. The results suggested that ultimately a transitional flow model may be required to predict the complete flow field over populated PCBs, hence yield best predictive accuracy for all components. Overall, prediction accuracy was only found to be sufficient for the intermediate design phase. This study served to highlight the potential shortcomings of the turbulence modelling typically employed by CFD codes dedicated to the analysis of electronics cooling, which are discussed in Section 4.2. However, to

generalise these findings to the prediction of board-mounted component heat transfer using such CFD codes, the following aspects need to be addressed. The study was confined to one multi-component PCB topology, which did not generate a sufficient degree of component thermal interaction for the prediction of this variable to be fully assessed. In addition, the forced convection analyses were limited to 2 m/s airflow velocity. Finally, the impact of aerodynamic disturbance generated by system level elements on predictive accuracy was not investigated.

A limited number of studies have applied turbulence models intended for the prediction of low-Reynolds number flows to the analysis of idealised electronic boards, consisting of multiple wall-mounted isothermal modules. Deb and Majumdar [165] considered an array of modules mounted on an adiabatic wall, exposed to 1 m/s channel airflow. They assessed predictive accuracy for a standard high-Reynolds number  $k-\epsilon$  model used in conjunction with standard wall functions, and a low-Reynolds number  $k-\epsilon$  model. The latter model was found to yield more accurate Nusselt number predictions for individually powered modules in the channel entrance region, where strong flow separation existed. A more extensive evaluation was reported at the Eighth ERCOFTAC workshop [166] for a matrix of low-conductivity substrate-mounted isothermal cubes in 3.86 m/s channel airflow. Several two-equation eddy viscosity turbulence models, Reynolds Stress Model (RSM), and both Large Eddy Simulation (LES) and Direct Numerical Simulation (DNS) techniques were evaluated. The two-equations models were a high-Reynolds number  $k-\epsilon$  in conjunction with standard wall functions, a low-Reynolds number  $k-\epsilon$ , and two variants of the  $k-\omega$  model. LES and DNS were shown to yield more accurate flow field predictions than the steady-state RANS-based computations, particularly for cross-flow. The full Reynolds-stress model seemed to predict cross-flow better than the eddy viscosity turbulence models. Overall, the  $k-\omega$  models predicted the velocity profiles better than the other eddy viscosity models. Accurate board-module surface temperature distributions could only be obtained using LES or DNS. The organisers concluded that there was a critical need for benchmarks and thus benchmark data, to gain a proper perspective of CFD predictive accuracy and flow model performance for a wide range of applications, generating different flow phenomena. However, neither Deb and Majumdar [165] or the ERCOFTAC workshop [166] evaluated the prediction of module adiabatic temperature, hence thermal interaction.

While the foregoing discussion focused on detailed component modelling, whereby both the mechanical architecture and thermo-physical properties of the component constituent elements are explicitly represented (Section 1.2.1), component compact thermal modelling (CTM) has received significant attention in recent years. The development of CTMs has

been studied, for example, in the frame of the European-funded DELPHI project [46,167], and industrially implemented through the European-funded SEED [168] project. Component manufacturers and end users were encouraged to share the responsibility for thermal design, whereby the component manufacturers generate Boundary Condition Independent (BCI) CTMs, to be implemented into CFD models. However, CTM assessment to date for the prediction of conjugate component heat transfer has been limited to single board-mounted components [169-174]. These studies have found CTM accuracy to be generally within 10% of the detailed component model predictions for both junction temperature and heat flows from the package external surfaces. However, two critical aspects have been highlighted: CTM prediction sensitivity to the board thermal conductivity [175,176], and modelling of the thermal wake flow emanating from the component [171,174]. Such errors and their implications at system level have not yet been systematically quantified. This will be addressed in the current study.

## **2.5 Summary of Literature Survey**

From the foregoing literature cited and described, the following points can be noted.

1. The experimental studies highlighted the complexity of component-board thermofluids, thereby demonstrating both the potential of this area to test CFD accuracy, and the need for confidence in CFD predictions. Experimental studies providing accurate characterisation data for multi-component board heat transfer were identified, which will be used in this study to assess CFD predictive accuracy.

2. The majority of numerical studies on component heat transfer have focused on steady-state heat transfer, for either single-board mounted components or idealised multi-component boards. It is therefore difficult to translate their findings to practical PCB applications. The former studies reported good prediction accuracy. The second category studies highlighted shortcomings of the turbulence modelling employed in CFD codes dedicated to the thermal analysis of electronic equipment, for the analysis of more complex flows over populated board topologies.

3. The impact of these limitations for the prediction of actual, multi-component board heat transfer was highlighted by Rodgers et al. [35,164]. However, the scope of the study was not sufficient to provide a full perspective on the limitations of the turbulence modelling employed in CFD codes dedicated to the thermal analysis of electronic equipment.

4. Studies that have assessed CFD predictive accuracy for idealised multi-component boards using turbulence models more suited to the modelling of airflows over such boards, have reported improved accuracy relative to the turbulence modelling used in dedicated



electronics cooling CFD codes. However, such studies have not assessed the prediction of component thermal interaction.

5. No study has been published on the prediction of conjugate transient component heat transfer using CFD analysis, which would be of relevance for both the prediction of component operational temperature or the determination of reliability testing environments.

6. The capability of CTMs to predict complex multi-mode component heat transfer in real electronic systems has not yet been comprehensively evaluated.

This study seeks to address weaknesses highlighted above and the strategy employed is described in the next section.

## **2.6 Benchmark Strategy**

The accuracy of the numerical predictions and ultimately their applicability, are dependent upon the modelling methodology employed, material properties specification and the ability of the CFD code to predict the associated thermofluids. With these variables in mind, experimental benchmarks were derived for component and PCB heat transfer. A superior approach to assessing the predictive accuracy of a code solely on the basis of discrepancies with measurements, is to discuss the discrepancies in the context of the assumptions inherent in the code. This approach is taken here and described in Chapter 4.

To evaluate the modelling methodologies applied and solver capability, CFD accuracy should be evaluated for a range of different thermofluid systems spanning the complete heat transfer chain of an electronic system. Ideally, good benchmark tests should exhibit complex thermofluids phenomena that can be accurately characterised by experimental analysis. Thus, the discrepancy between prediction and measurement needs to be distinguished from the experimental error. This may be difficult to achieve for system level analysis as considerable uncertainties may exist in both the physical quantities being measured and the numerical boundary conditions applied. Such uncertainties are coupled with computational discretization constraints prohibiting the explicit modelling of geometric length scales from micron to meter at component to cabinet level respectively within a single numerical model. By contrast, sub-systems or units, such as populated PCBs, represent an appropriate benchmark level, where the thermofluids can be experimentally characterised accurately and modelled using well-defined boundary conditions. Although such an analysis represents a simplification compared to that of a complete electronic system, the complexity of component-PCB thermofluids (Section 2.2) still poses a significant challenge for CFD analysis. In addition to forming good benchmarks, the analysis of component heat transfer is also of relevance to the majority of electronics reliability prediction methods, which require the specification of component

operating temperature. In the absence of a working prototype in the design phase, component temperature can only be realistically estimated using CFD analysis.

Such a strategy is used in this study. Eliminating system level uncertainties, numerical predictive accuracy is assessed for PCB-mounted component heat transfer, in a still-air enclosure and wind tunnel for free and forced convection cooling respectively. Both types of convective environments are considered to reflect the nature of cooling airflows in commercial products, which may vary considerably from quiescent to highly agitated. Highly disturbed flows increase the complexity of numerical analysis as the impact of fluid turbulence on heat transfer requires to be modelled. As previously highlighted (Section 1.2.1), turbulence modelling is a vulnerable area of CFD analysis and therefore one aim of this study is to assess the effect of turbulence modelling on the prediction of component junction temperature.

A methodical approach is employed to permit both the modelling methodology applied and solver capability to be carefully evaluated. Test case complexity is incremented in controlled steps from; i) single board-mounted components, to ii) individually powered components on populated boards and iii) simultaneously powered configurations, where all components are powered. The single board-mounted component cases serve to validate the component and PCB modelling methodology. The step from cases i) to ii) enables the impact of aerodynamic conditions on junction temperature prediction accuracy to be quantified, while stepping from ii) to iii) permits the ability of the code to predict component thermal interaction to be assessed.

The test vehicles are firstly analysed in laminar free convection conditions, thereby eliminating the variable of turbulence modelling on predictive accuracy. In forced-air, both uniform flow conditions, and highly disturbed conditions upstream of the boards are studied.

To assess the prediction of transient component heat transfer, three types of operating conditions are considered, namely (i) component dynamic power dissipation in fixed ambient conditions, (ii) passive component operation in dynamic ambient conditions, and (iii) combined component dynamic power dissipation in varying ambient conditions. Such environments are representative of industry-standard electronic component reliability testing. Before analysing such conditions, predictive accuracy is firstly assessed for steady-state heat transfer, whereby the variable of modelling thermal capacitance is eliminated.

Benchmark criteria are based on component junction and component-board surface temperatures, measured using thermal test dies and infrared thermography respectively. While junction temperature is used as the primary criterion, component/board surface temperature distributions serve to validate the component and PCB modelling

methodologies. In addition, supporting experimental visualisations of the forced airflows over the boards are used to help assess predictive accuracy.

Reflecting the constraints imposed on a thermal designer in an industrial environment, a pragmatic approach is adopted for detailed component and PCB modelling, whereby all geometry dimensions and constituent material thermo-physical properties correspond to nominal vendor specifications. In this approach therefore, no calibration is made to the numerical models in a possible attempt to improve predictive accuracy. This work therefore also permits the suitability of the pragmatic modelling strategy employed to be assessed for use in a design environment. To establish confidence in the data supplied by component manufacturers, component internal geometry and structural integrity were verified using destructive and non-destructive testing techniques. In addition, the use of component compact thermal modelling is also evaluated for the analysis of board-mounted electronic component heat transfer.

Acknowledging the difficulties in defining a characteristic dimension, hence transition Reynolds number, that adequately describes the fluid flow regime in non-dimensional form over populated boards [177], no meaningful Reynolds number, based on either component length or board length, can be used for the *à priori* selection of a laminar or turbulence model. Consequently, the fluid domain for the forced convection configurations was solved using both laminar and a range of turbulent flow models. This will include both standard turbulence models available in CFD codes dedicated to the thermal analysis of electronic equipment, and candidate turbulence models that may be more suited to the analysis of forced airflows over populated electronic boards but not currently available in such codes. Such an evaluation will therefore permit perspective to be given on the capabilities of dedicated CFD codes for the prediction of electronic component heat transfer, and the potential for improved predictive accuracy. The potential accuracy of temperature prediction, hence component life prediction, is ultimately evaluated.

Numerical predictive accuracy for component operating temperature is categorised based on the guidelines identified in Section 1.2 for the various phases of the thermal design cycle. These accuracy requirements are typically  $\pm 10^{\circ}\text{C}$  or 20%,  $\pm 5^{\circ}\text{C}$  or 10% and  $\pm 3^{\circ}\text{C}$  or 5% of measurement for the early, intermediate and final design phases respectively.

Finally, the use of validated numerical models to provide an insight into the physics of component heat transfer will be illustrated.

### **2.6.1 CFD Code Selection**

Two CFD codes are employed, Flotherm [69] and Fluent [70], from Flomerics and Fluent respectively. Flotherm is a software dedicated to the thermal analysis of electronic

equipment having tailored pre- and post-processing features, but limited flow modelling capabilities. Fluent is a general-purpose engineering code, having a suite of turbulence models and near-wall treatment approaches, some of which may be more suited to the analysis of forced airflows over populated electronic boards. The turbulence modelling capabilities of both codes are described in Section 4.2. Using Flotherm, industry perspective will be provided on the capabilities of dedicated CFD codes for the analysis of electronic component heat transfer. Assessment of alternative turbulent flow modelling approaches in Fluent will permit the potential for improved predictive accuracy to be evaluated.

These CFD codes were selected as they both are market leaders in their field. Based on a survey of commercial CFD software revenues [178], Fluent holds the dominant world market share at 31%, while Flomerics' share is at 10%. Whereas Fluent's market encompasses a variety of engineering sectors, Flotherm is confined to the electronics cooling sector. In this market sector, although there is no independent market research to justify the vendor claim, a commissioned market surveys by Flomerics indicates that Flotherm had the dominant market share at 85% [179] at the commencement of this research, and currently at 70% [180]. This, together with the fact that the majority of previously published benchmark studies for electronics cooling [42] were undertaken using Flotherm, forms the justification for only considering this dedicated CFD software in this study.

## **2.7 Summary**

A review of published studies highlighted the complexity of component-PCB thermofluids.

The limitations of the turbulence models employed in CFD codes dedicated to the thermal analysis of electronic equipment for the prediction of component operational temperature were highlighted. The need to more comprehensively quantify the impact of these limitations on prediction accuracy, and evaluate the potential for improved accuracy using alternative turbulence models was outlined.

The benchmark strategy employed to achieve these objectives was described, to enable both the numerical modelling methodologies and solver capability to be carefully evaluated.

## **3.0 Benchmark Test Configurations**

### **3.1 Introduction**

In this chapter, a set of experimental benchmarks is proposed to assess Computational Fluids Dynamics (CFD) predictive accuracy for electronic component heat transfer. Both the prediction of steady-state and transient heat transfer are considered. Apart from populated board applications, the test configurations also involve thermal environments representative of electronic component reliability screening and assembly processes. Benchmarks are also presented to evaluate the predictive performance of component compact thermal modelling implemented in CFD models.

The benchmark data, comprising of component junction temperature and component-board surface temperature measurements, are assembled from a number of previously published experimental studies. To demonstrate the suitability of this data to serve as benchmarks, the characterisation methods employed are described, and the accuracy of the measurements assessed. Details of the test vehicles and characterisation environments are given for numerical modelling.

The thermal characterisation data is augmented by experimental visualisations of the forced airflows over the populated boards used, undertaken in this study using two complimentary flow visualisation techniques. These flow visualisations will be used to help assess predictive accuracy qualitatively. In addition, both test component geometry and structural integrity are assessed using destructive and non-destructive testing, so as to eliminate potential numerical modelling uncertainties.

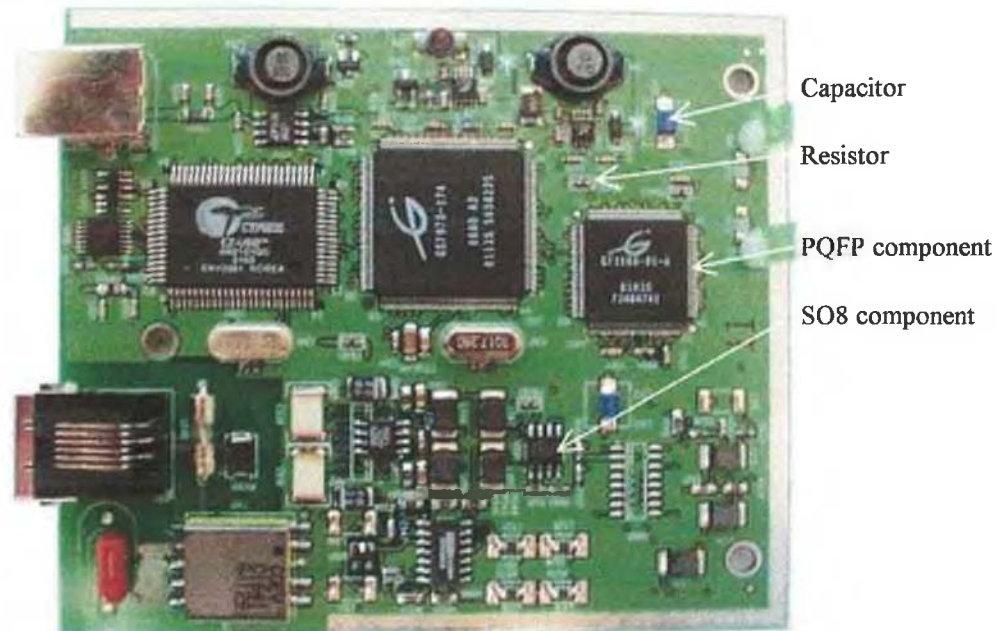
Apart from serving to assess CFD predictive accuracy in the present work, the benchmarks documented may be re-used in subsequent studies to evaluate future developments in CFD modelling, or new component-board modelling methodologies for the prediction of electronic component heat transfer.

Before describing the benchmarks, a brief overview of electronic component packaging and thermal characterisation is given.

### **3.2 Electronic Packaging**

Electronic systems are typically made of diverse components assembled onto PCBs. Packaging refers to hardware that mechanically and electrically interconnects electronic components, and protects them from external stresses. An example of a populated PCB assembly is shown in Figure 3.1, identifying several Integrated Circuit (IC) component types and discrete components such as resistors and capacitors. The numerical prediction of board-mounted IC component thermal behaviour is the subject of this research.

Typical IC packaging architectures and PCB constructions are described in the following sections.



**Figure 3.1** An example of a populated printed circuit board<sup>2</sup>.

### 3.2.1 Component Architecture

The mechanical structure which encapsulates the IC and electrically interconnects it to the PCB is commonly termed a package. Responding to diverse electrical, mechanical, miniaturisation or reliability requirements, a variety of IC package families exist. Common package families and their evolution are illustrated in Figure 3.2. At present, plastic Surface Mount Technology (SMT) devices are the most widely used for cost effectiveness, size, weight, and availability [56]. Although area array packages such as Ball Grid Arrays (BGAs), introduced in the 1990's [181,182], can offer improved miniaturisation, peripheral (leaded) devices remain predominant, with the Small-Outline (SO) and Quad Flat Pack (QFP) being still the workhorses of the IC packaging industry [183]. Both package types are used as test components in this study, namely 160- and 208-lead QFPs, and 8-lead SO. It should be noted however that the selection of a specific package type was not a critical aspect for this study, as the findings in terms of CFD predictive accuracy would translate to other package types. In addition, the component modelling methodologies employed herein are generically applicable to other package families, as will be shown in Chapter 4.

<sup>2</sup> Fujitsu FDX310 ADSL USB Integrated Modem.

Typical architectures for leaded IC packages are illustrated in Figure 3.3. For a standard construction such as shown in Figure 3.3(a), the IC die is attached to a metal support (die paddle) and wire bonded to a metal leadframe, Figure 3.4, for electrical connection to the external leads and thus the PCB. The structure is encapsulated by an epoxy resin which forms the component body. As the package also acts as a thermal dissipator of the heat generated by the IC, it may contain a highly-thermally conductive metal part, referred to as “heat slug”, for enhanced thermal performance [184], Figures 3(b) and 3(c). In this instance, a paddle is not required for die attachment, which can be directly to the heat slug. In Figures 3(b) and 3(c), the heat slug is exposed either at the base or top of the package body respectively. Package geometry and materials are controlled by international standards set by the JEDEC [185] and SEMI [186] organisations.

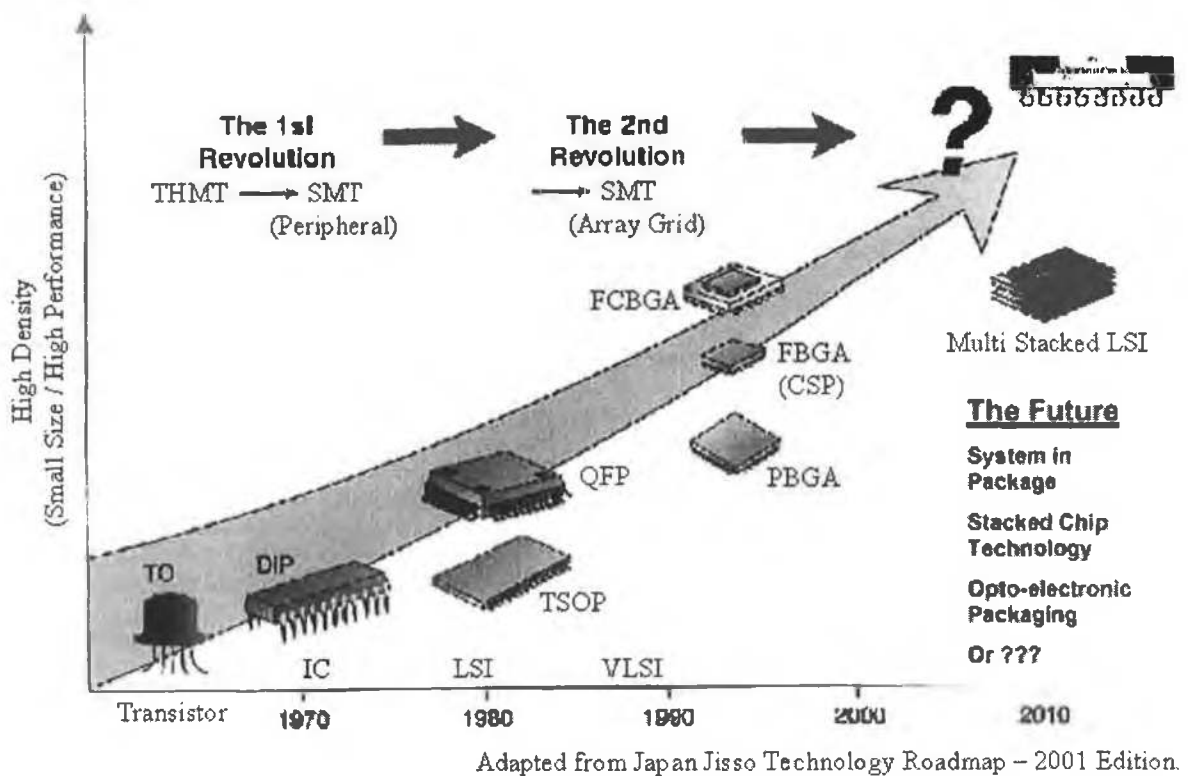
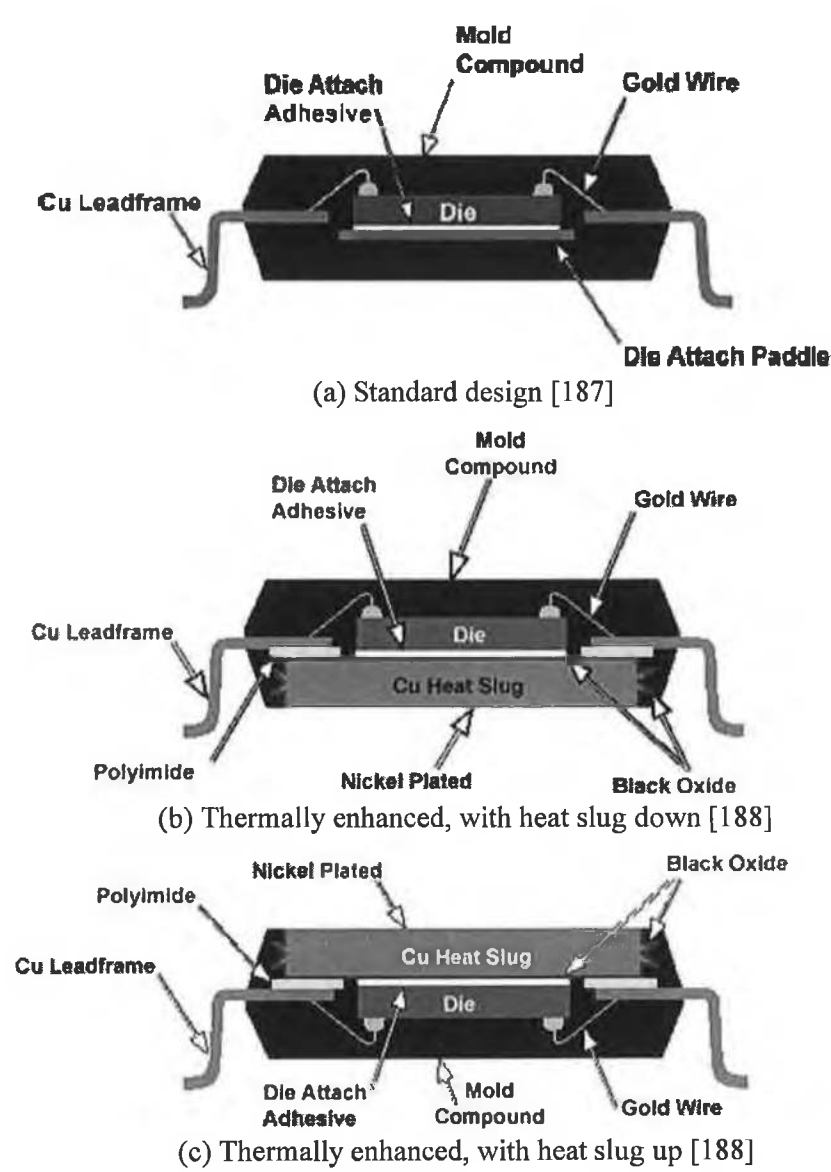
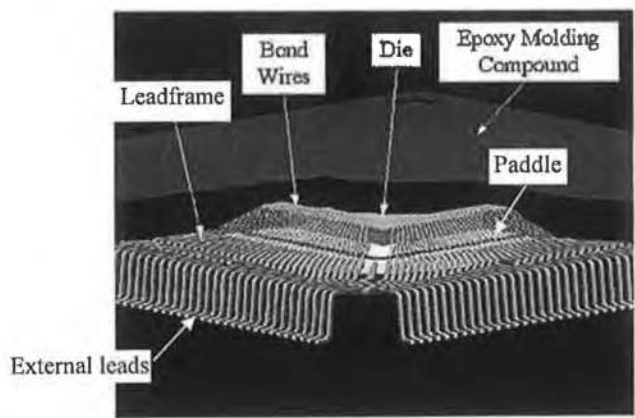


Figure 3.2 Evolution of IC packaging [183].



**Figure 3.3** Typical architectures of a leaded IC package.

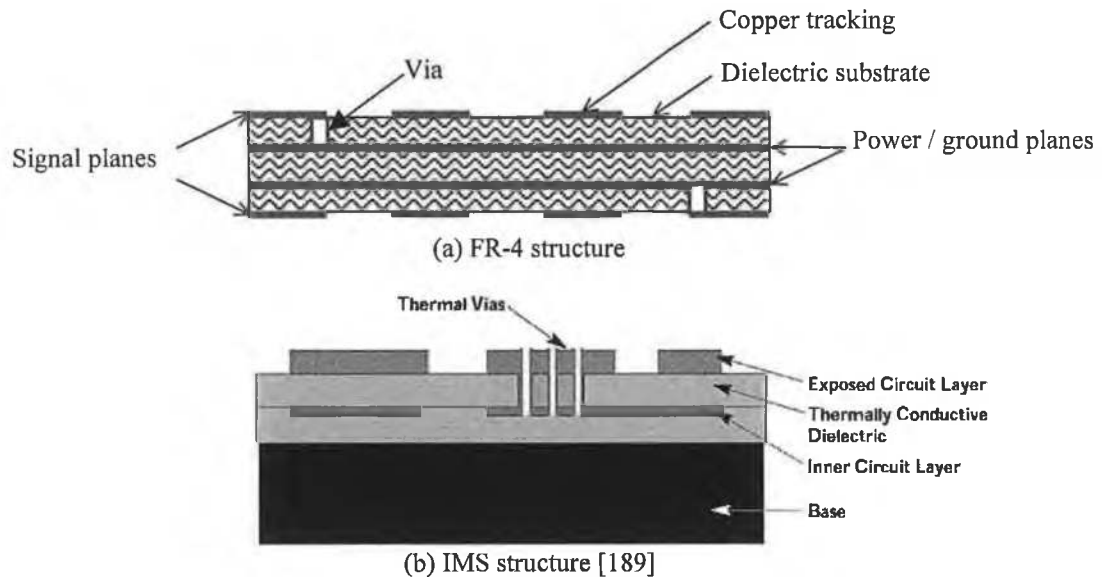


**Figure 3.4** Internal architecture of a standard Quad Flat Pack, with epoxy moulding compound partially cut away [184].



### 3.2.2 Printed Circuit Board Construction

A standard PCB construction typically comprises of several layers of copper conductors, commonly termed tracking, which are laminated onto a dielectric substrate. A commonly-employed dielectric is FR-4, a glass-reinforced resin. Copper layers are electrically interconnected by metal-plated holes, referred to as “vias”. A typical PCB structure is illustrated in Figure 3.5. The PCB layer build-up is commonly categorised as  $N_1S/N_2P$ , where  $N_1$  and  $N_2$  denote the number of signal (S) and power/ground (P) planes respectively.



**Figure 3.5** Schematic cross sections of typical PCB constructions.

The extent of conductive heat spread in PCBs is dominated by the presence of nearly or fully complete power and ground copper layers, producing much larger in-plane thermal conductivity values than in the normal or through-plane direction [190,191]. A common approach to enhance the PCB’s heat spreading properties therefore is to increase the number of internal continuous copper planes. An alternative is Insulated Metal Substrate (IMS) technology [189], which combines a thick copper- or aluminium base with a thermally enhanced dielectric material, Figure 3.5(b). The test vehicles used in this study were FR-4 based PCBs of construction 2S/0P, 2S/2P and copper-based 1S/1P IMS PCB.

### 3.2.3 Characterisation of Electronic Component Thermal Performance

The characterisation of IC packaging thermal performance is governed by international standards [185,186], set with the objective of allowing repeatable and reproducible characterisation. Component thermal performance is typically characterised by single-

valued junction-to-reference thermal resistance parameters, measured in idealised conditions defined by the appropriate standards. The concept of thermal resistance is based upon the analogy between electrical and heat conduction. Applying the heat transfer analogy of Ohm's law, component thermal resistance is defined as:

$$\theta_{j-ref} = (T_j - T_{ref})/Q_{diss} \quad (3.1)$$

where:  $\theta_{j-ref}$  is the thermal resistance between junction and reference point (K/W);  $T_j$ ,  $T_{ref}$  are the temperatures of the diode junction and reference points respectively (K), and  $Q_{diss}$  is the power dissipated by the IC (W). Typical reference points are the component surface (case) temperature or ambient air temperature.

The component is tested individually mounted on a PCB, in a still-air enclosure or wind tunnel for free- and forced-air characterisation respectively. Component junction temperature is measured using an electrical method, whereby a Temperature Sensitive Parameter (TSP) on the die, typically the voltage drop across a forward-biased diode, is used as a thermometer. As IC complexity may be prohibitive for junction temperature measurement [192], package thermal characterisation is generally performed with a thermal test die, rather than the application die. Thermal test dies contain both heat dissipating elements to simulate active device power dissipation, and one or more temperature sensitive diodes to permit junction temperature measurement. This permits power dissipation and junction temperature sensing, via the TSP, to be performed simultaneously. The heat dissipating elements are distributed uniformly on the die surface, covering at least 85% of its area. For temperature sensing, electrically isolated diodes are located at the centre of the die surface. The design and layout of thermal test chips are controlled by international standards [193,194].

The functionality of thermal test dies for the measurement of component junction temperature is described in detail by Motta [195]. Based on the linear relationship (K factor) between diode forward voltage, excited as a constant current, and temperature rise, junction temperature is calculated by the following expression:

$$\Delta T_j = K (V_{f1} - V_{f2}) \quad (3.2)$$

where:  $\Delta T_j$  is the diode temperature rise above reference conditions,  $V_{f1}$  and  $V_{f2}$  are the diode forward voltages for the die unpowered and powered conditions respectively, and  $K$  is the linear coefficient for forward voltage change with temperature.

To minimise ohmic heating of the diode, the exciting current level is kept as low as possible, but sufficient to generate a voltage drop that can be accurately measured.

All junction temperature measurements used to assess numerical predictive accuracy in this study were performed using thermal test dies embedded in each test component. Test die functionality conformed to SEMI standard G32-94 [193]. Component power dissipation was provided by a diffused resistor for all test dies, with centrally located temperature sensitive diodes used for junction temperature measurement. The thermal test die patterns are shown in Appendix A for each test component used.

Although not specified by component characterisation standards, component-board surface temperature measurements were made simultaneously with junction temperature measurements, and are used in this study as an additional metric to assess the numerical prediction of component heat transfer (Section 2.6). Component surface temperature, however, is commonly-used in industry to estimate operating temperature, as the measurement of junction temperature requires a more complex electrical method for application dies [192]. Component surface temperature data is most applicable for packages having a low internal thermal resistance.

Historically, component thermal resistances have been used over the years as figure of merits for comparing the thermal performance of similar devices from different vendors. More contentiously, their application has been extended to predicting the junction temperature of functional devices in application environments. The limitations of this approach have been well documented, for example by Lasance [196]. These limitations arise from the aerodynamic and thermal factors influencing component thermal resistance [12] generally differing significantly between characterisation and application environments.

To overcome these limitations, it has been proposed that knowledge of the junction temperature in an application may be derived by factoring the standard thermal resistance value [107] (Section 2.2).

Another alternative is the DELPHI methodology for the characterisation of electronic parts, popularised by the European-funded DELPHI project [46,167] (Section 2.4.1). Rather than component manufacturers supplying single valued junction-to-reference thermal resistances, they are encouraged to generate Boundary Condition Independent (BCI) component compact thermal models (CTMs) for use in CFD modelling. This approach forms a radical change in philosophy, since it replaces the single-valued junction-to-ambient thermal resistance by a set of BCI parameters consisting of a thermal resistor network. The adoption of CTMs for characterising component thermal performance by component vendors is currently the focus of a forthcoming international standard [197]. However, limitations are also associated with this approach for predicting component operational temperature, as will be shown in this study.

### 3.3 Multi-Component Board Heat Transfer Configurations

The test vehicle used to assess the numerical prediction of multi-component board heat transfer is shown in Figure 3.6. This PCB was thermally characterised in wind tunnel airflows from 0 to 10 m/s, by Lohan and Davies [106], who undertook an extensive experimental investigation into component thermal interaction on this board. The experimental data, consisting of component junction temperature and component-PCB surface temperature measurements, is presented in Section 3.3.3.3. This quantitative data is supplemented by supporting experimental visualisations of the forced-air flows over the board, undertaken in this study and presented in Section 3.3.5.

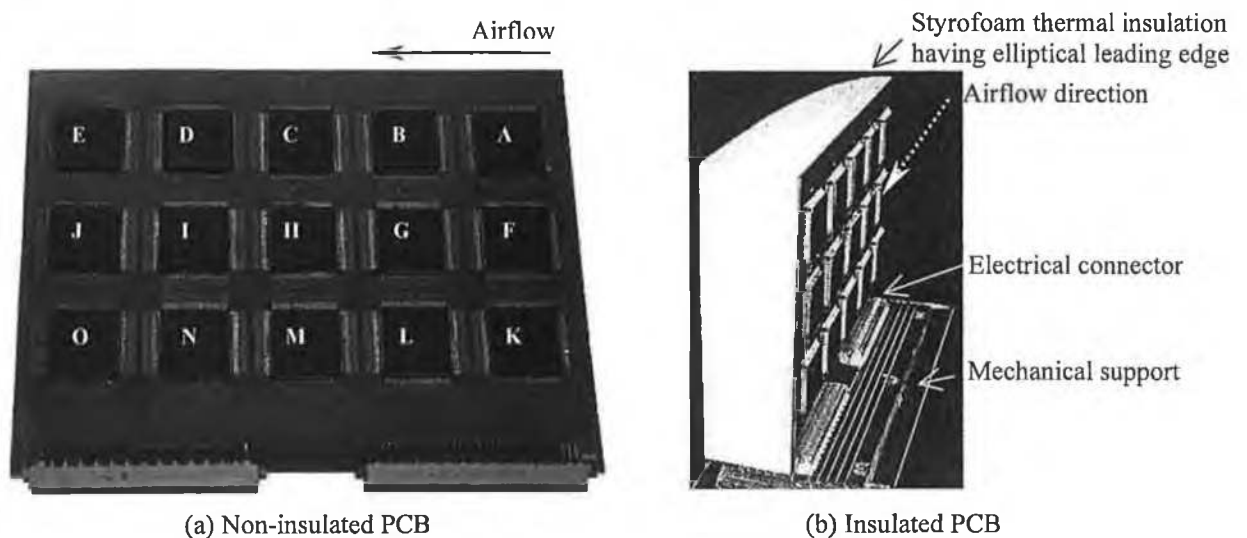
The present study uses the thermal characterisation data for passive and forced-air cooling at 2 and 4 m/s. These forced-air conditions represent the mid- to higher-range of velocities employed for cooling electronics. Such cooling airflows are typically confined to the 0 to 5 m/s range, both to minimise acoustic emissions and due to component thermal resistance reaching an asymptotic limit at higher velocities [198]. 2 m/s was found to exceed the region where PCB heat transfer is buoyancy-aided for the powering configurations under analysis [106].

The PCB shown in Figure 3.6 was populated in incremental steps with one, seven and fifteen 28 mm square 160-lead Plastic Quad Flat Pack (PQFP 160) packages described in Section 3.3.1. These PCB topologies are referred to as Stages 1, 2 and 3 respectively. Component location on the PCB is identified by the lettering A to O, Figure 3.6(a). Stage 1 consists of the centrally located component (H), while Stage 2 also incorporates the three leading (A,F,K) and trailing edge (E,J,O) devices. Stage 3 corresponds to the symmetrical in-line array shown in Figure 3.6. These topologies are used to assess predictive accuracy for different aerodynamic conditions and varying degrees of component thermal interaction.

In addition for Stage 3, flow disturbance mimicking more realistic system level flow conditions than wind tunnel conditions, was introduced upstream by attaching a 50 mm-thick layer of Styrofoam thermal insulation on the board non-component side, Figure 3.6(b). While in the experimental study [106], the primary purpose of this insulating layer was to generate a high degree of component thermal interaction, present in double-sided PCB applications, in this study it also acts as a controlled flow disturbance, having a similar influence on the flow and heat transfer as that generated by structural supports and ancillary electronic equipment, such as power supplies and transformers, in real systems. The extent of flow separation was controlled, however, by having this insulating block contoured with an elliptical profile at its leading edge, as indicated in Figure 3.6(b). Although presenting an additional level of complexity compared to wind tunnel conditions for numerical analysis, this test configuration retained well-defined boundary conditions for numerical modelling.

In addition to the Stage 1-3 configurations, the PQFP 160 component was also individually characterised on a single-component board shown in Figure 3.9, both in free-air, and forced airflows from 1 to 5.5 m/s. These measurements were undertaken by Davies et al. [115] and Lohan and Davies [77] for free and forced convection respectively. The present study uses the thermal characterisation data for both passive- and forced-air cooling at 1, 2 and 4 m/s. These test configurations will be used as supporting analysis to validate the component-board numerical modelling methodologies.

Component internal architectures, PCB layouts, characterisation environments and experimental benchmark data are presented in the Sections 3.3.1 to 3.3.4.



**Note:** PCB size = 233 x 178 x 1.6 mm. The position of each component on the PCB is identified by the lettering, A to O. A, F and K are leading edge components in forced convection. “Insulated PCB” and “non-insulated PCB” refer to Styrofoam thermal insulation being attached and not attached to the board non-component side respectively. Package design I, Figure 3.7(b,i), is mounted at board locations (A,F,K) and (G to I). Package design II, Figure 3.7(b,ii), is positioned at location J. The outer row components (B to E) and (L to O) are package design III, Figure 3.7(b,iii).

**Figure 3.6** Populated PCB, shown for the Stage 3 topology.

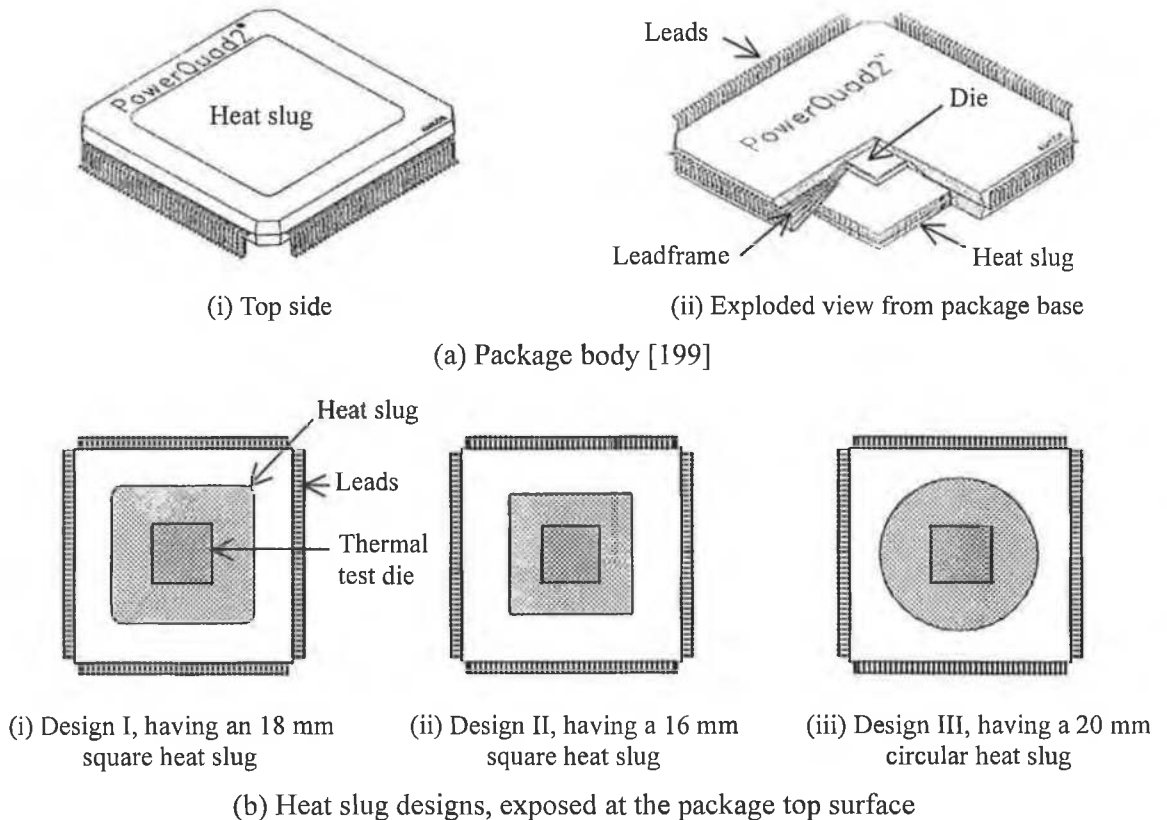
### 3.3.1 Test Components

The test component was a thermally enhanced PQFP 160 from Amkor, whose external geometry is shown in Figure 3.7. This design is patented as the PowerQuad 2 [188], a packaging solution widely-used for power microprocessors, Application-Specific Integrated Circuits (ASICs) and Digital Signal Processors (DSPs).

The component internal architecture corresponds to the thermally enhanced design illustrated in Figure 3.3(c), having an embedded heat slug exposed at the package top. Three variants of the PQFP 160 were used, denoted herein as designs I, II and III, which only differed by the heat slug design, Figure 3.7(b). Component internal architecture and

mechanical integrity are analysed in Section 3.3.4. The vendor supplied package external geometry details are given in Figure A.1. Package designs I and II had the same junction-to-ambient thermal resistance, while package design III's was on order 10% lower.

Each component contained an embedded 7.5 mm square thermal test die with functionality that conformed to SEMI standard G32-94 [193]. The test die layout is given in Figure A.4(a). The die required six active leads, namely two for both diode constant current supply and voltage measurement, and two for resistor power supply.

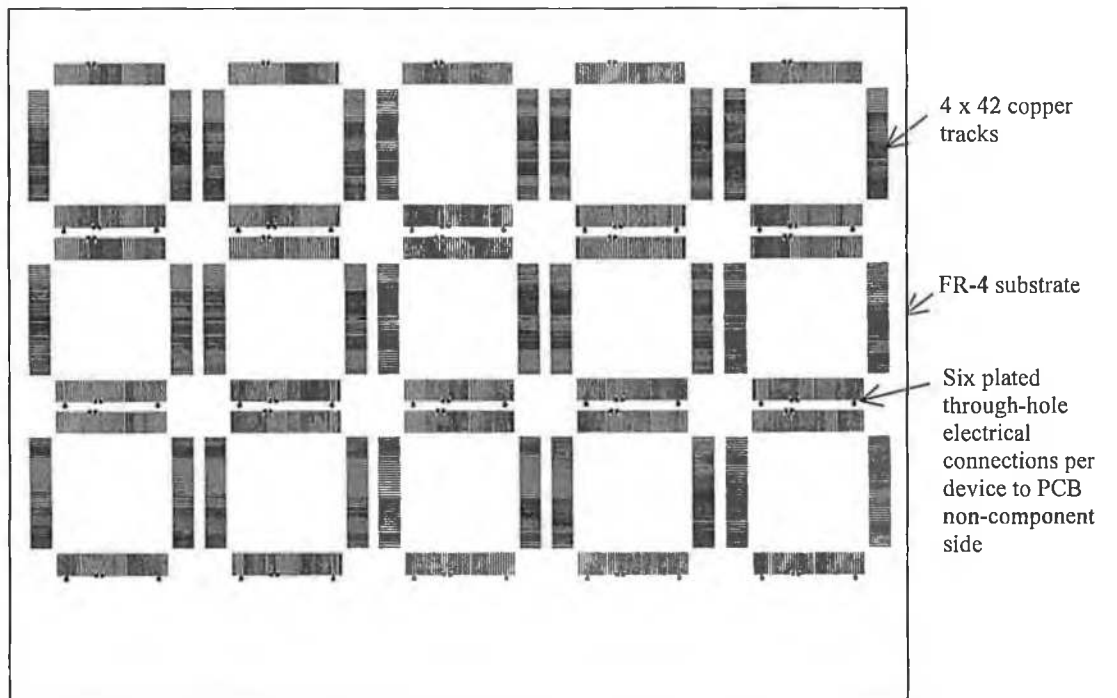


**Figure 3.7** 160-lead PQFP external geometry (28 x 28 mm).

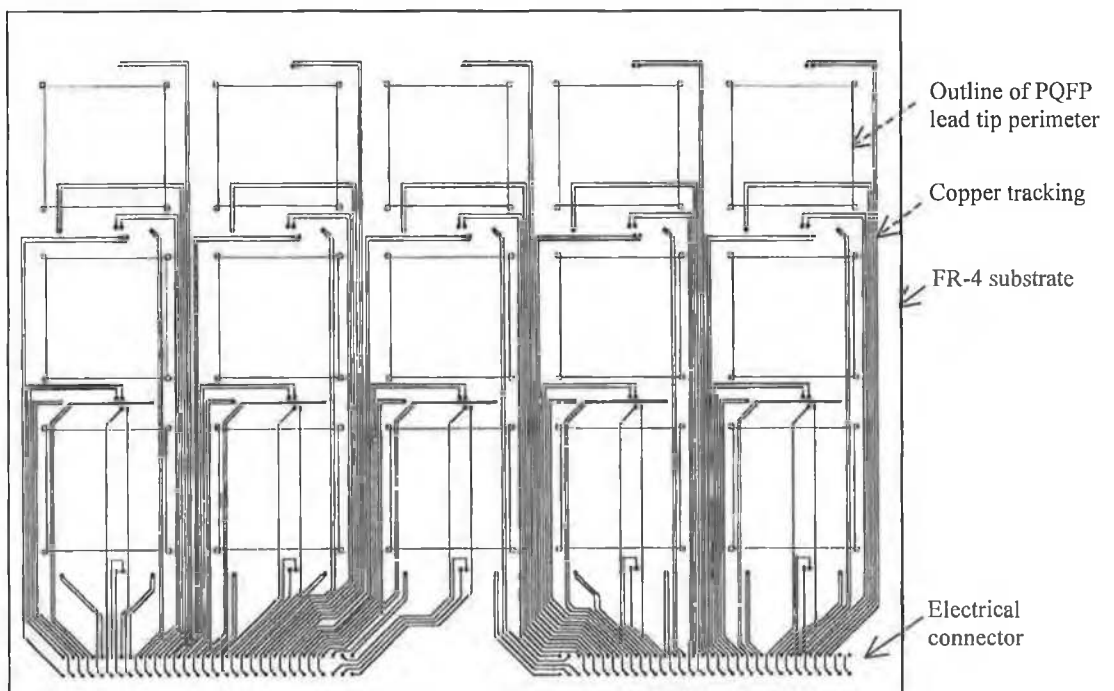
### 3.3.2 Test Printed Circuit Boards

*Populated Board.* The test components were surface-mounted onto the PCB shown in Figure 3.6, whose layout is given in Figure 3.8. This board was a 1.6 mm thick FR-4 design of industrial standard size 233 mm x 160 mm, with 35  $\mu\text{m}$  thick copper tracking on both sides. This PCB had no embedded copper planes. Component spacing was uniform across the Stage 3 array, and approximately half package size. The copper tracking on the board component side acted as a mounting surface, whereas tracking on the non-component side were signal connections. As illustrated in Figure 3.8, all six active leads on each component were connected to the board's non-component side via plated through-holes, which in turn were connected to 64-pin DIN 41612 connectors at the base of the PCB, Figure 3.8(b). Two

additional sense lines were routed from each component to these 64-pin connectors, enabling the power dissipation level to be accurately calibrated before testing [106].



(a) Component side



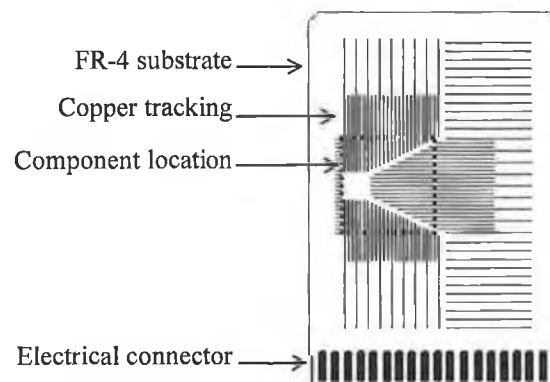
(b) Non-component side

Note: PCB size = 233 x 178 x 1.6 mm. All dimensions in millimetres. Copper signal traces are 35  $\mu$ m thick.

Figure 3.8 Layout of surface copper tracking pattern on the populated PCB.

Package design I was mounted at board locations (A,F,K) and (G to I), Figure 3.6(a). Package design II was positioned at location J. The outer row components (B to E) and (L to O) were design III. While this heterogeneous population resulted from a limited supply of one package type, component layout on the PCB was primarily designed for characterising component thermal interaction in forced convection conditions [106]. Thus the array was constructed to be symmetrical about the central stream-wise component row (F to J) in forced convection. The purpose of the outer rows was only to generate both symmetrical flow phenomena and conductive and convective interaction with the centre row devices in forced airflows. Thus the most important conclusions of the experimental study in forced convection were drawn from the thermal behaviour of both the central row (F to I) and leading edge (A,F,K) components, which all had the same heat slug design [106]. This will also be the case in the present work.

*SEMI Standard PCB.* The single-component board used to validate the component and board numerical modelling methodologies conformed to the SEMI standard SEMI G42-88 [200]. This test board was a 1.6 mm thick FR4 design of size 116 mm x 78 mm, having the same copper tracking layout on both sides as shown in Figure 3.9. The copper tracking was 35  $\mu\text{m}$  thick. Package designs II and III were individually characterised on this PCB, but corresponding characterisation was not performed for design I.



Note: PCB size = 116 x 78 x 1.6 mm. Copper signal traces are 35  $\mu\text{m}$  thick.

**Figure 3.9** PQFP 160 test Printed Circuit Board conforming to SEMI G42-88 [200].

### 3.3.3 Experimental Thermal Characterisation

This section outlines the thermal characterisation of both the populated board performed by Lohan and Davies [106], and of the SEMI PCB by both Davies et al. [115] and Lohan and Davies [77]. Whereas these studies reported junction-to-ambient thermal resistance data, the actual junction temperature measurements are presented here, which are the direct metric used to assess numerical predictive accuracy.



Although not presented in [106], corresponding component-board surface temperature measurements were also recorded for the populated board using both infrared thermography and miniature thermistors as reported by the authors. This data was subsequently presented in Davies et al. [12] in the format of aerodynamic and thermal influence factors. The actual surface temperature measurements are presented in this section. In addition, visualisations of the flow fields over the populated boards, undertaken in this study, are also presented.

### 3.3.3.1 Characterisation Methods

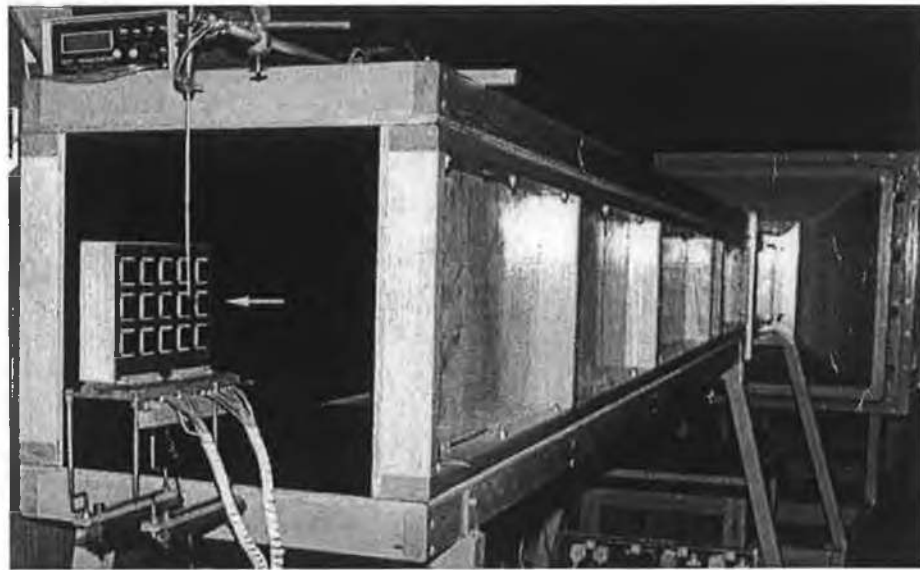
*Populated Board.* The test vehicles were thermally characterised at the outlet of a wind tunnel diffuser section shown in Figure 3.10, having internal dimensions 490 x 490 mm. This characterisation facility enabled optical access for infrared thermography. The experimental set-up employed for free and forced convection characterisation is illustrated in Figure 3.10(b). In forced airflows, the free-stream velocity profiles at this location both in the span-wise airflow direction along the test assembly's leading edge, and in the transverse direction normal to the board, were measured to be uniform with less than 3% variation. Hot-wire anemometry measurements of turbulence intensity yielded an average value of 2% at the test location for the velocity range of interest [77].

When extending the forced-air characterisation data set of Lohan and Davies [106] to additional test configurations [107], Cole [201] undertook reproducibility tests at a different facility, with the test vehicle mounted centrally within a wind tunnel test section of cross sectional area 200 x 100 mm, and length 300 mm. Component junction temperature measurements were found to be within the bounds of repeatability reported by Lohan and Davies [106]. This provided further confidence in the suitability of the characterisation environment shown in Figure 3.10.

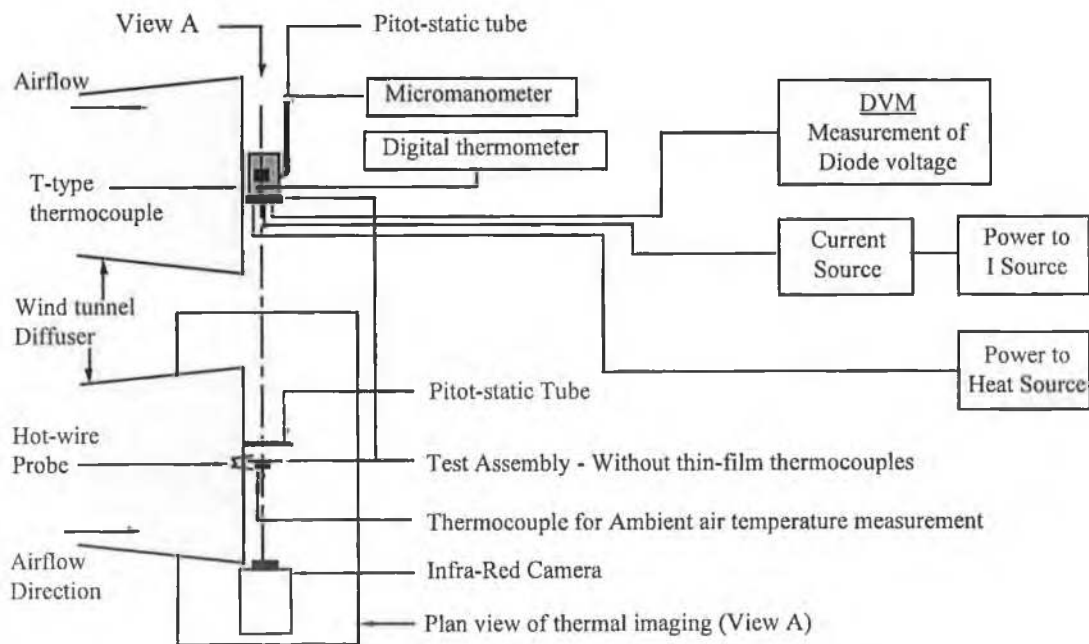
Despite obtaining good repeatability and reproducibility for the free convection measurements, Lohan et al. [99] cautioned on the repeatability of the data at other facilities, as draft-free test chambers are recommended for standard still-air testing to eliminate potential laboratory air currents enhancing component heat transfer. Lohan and Davies [106] ensured that such effects were minimised by sealing the laboratory for external drafts. To assess the reproducibility of the free-air characterisation data, Cole [201] repeated a series of the tests in a Perspex still-air enclosure, shown in Figure 3.11. Cole reported that the data matched almost perfectly that of Lohan and Davies [106], showing that the results found at the diffuser outlet were accurate.

All free convection measurements were taken with the boards vertically oriented, with component locations (A to E) defining the top span-wise component row. For forced

convection, devices (A,F,K) were leading edge components.



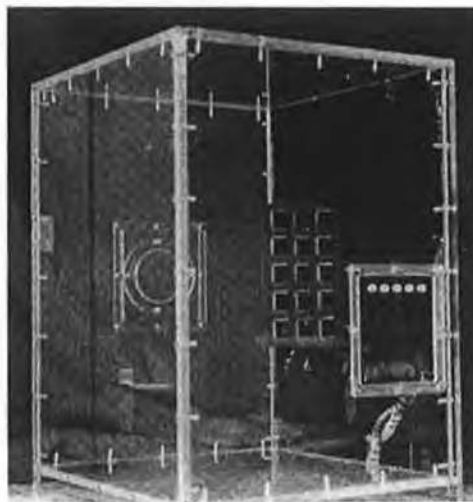
(a) Characterisation of the insulated Stage 3 PCB at the outlet of the wind tunnel [Courtesy of the Stokes Research Institute, University of Limerick, Ireland].



(b) Forced convection testing and thermal imaging of PCB at wind tunnel outlet in (a) [106]

**Note:** Diffuser outlet internal dimensions = 490 mm square.

**Figure 3.10** Forced convection characterisation of the populated board at the outlet of the wind tunnel.



**Note:** Enclosure internal dimensions for height, width, and depth are 630 x 462 x 457 mm respectively  
**Figure 3.11** Still-air enclosure for free convection characterisation, with the Stage 3 PCB shown in vertical orientation [201].

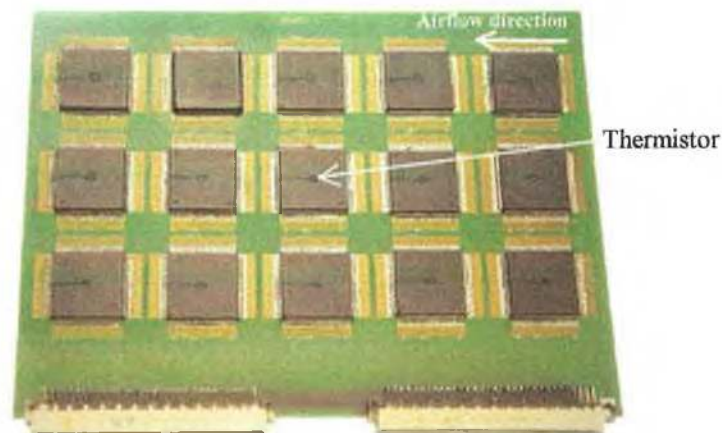
A control unit was used for powering both the thermal test dies heat dissipating elements and temperature sensitive diodes. A standard data acquisition system was used to record the sensed output voltage from the thermal test dies and thermistors, and converting each measurement to its associated temperature. This involved Analog-to-Digital (ADC) conversion and signal conditioning. Junction temperatures were recorded by stepping the free-stream air velocity generated by the wind tunnel from 0 to 10 m/s, while maintaining component power dissipation at a fixed level of 3 W. Measurements for a given airflow velocity were made once steady-state conditions were reached.

Component junction temperature measurements conformed to the SEMI standard G38-87 [108], with the thermal test dies calibrated to an accuracy of  $\pm 0.4^{\circ}\text{C}$ . Corresponding component-board surface temperature measurements were recorded using both infrared thermography and miniature thermistors. Miniature 79  $\mu\text{m}$  diameter thermistors were used [202], placed centrally on the heat slug surface of each component, and aligned in the stream-wise direction in forced air, Figure 3.12. It was verified that their attachment did not adversely impact on component thermal resistance. These thermistors had a worst-case calibration error of  $\pm 0.4^{\circ}\text{C}$  over the temperature range considered, 10 to  $100^{\circ}\text{C}$  [202].

Component and board surface temperatures were measured using an AGEMA infrared Thermovision 880 system, operating in the 8 to 12  $\mu\text{m}$  spectral range, having a specified accuracy of  $\pm 2^{\circ}\text{C}$  or 2%. Measurement geometric resolution was approximately 0.86 mm, while spatial temperature resolution was estimated at 2.9 mm, that is approximately 3.4 times the geometric resolution based on a rule-of-thumb given by the camera vendor. Thermographic measurements for the non-insulated PCB were taken from both the board

component- and non-component sides. Measurements were only taken from the component side on the insulated PCB.

For uniform emissivity, the top surface of each test component was sprayed with a uniform layer of matt black paint having an emissivity estimated at 0.96. The PCB surface was left untreated since its measured emissivity was also estimated at 0.96 [106]. It is suspected however that this emissivity value is apparent, as the experimental procedure used to derive it was effectively an in-situ calibration of the infrared system. Although not detailed in [106], the FR-4 substrate and paint emissivity were estimated by comparing the surface temperature of a heated isothermal FR-4 sample, either bare or sprayed, against a Type-T thermocouple measurement over the temperature range 30 – 100°C. The camera emissivity setting was varied until the measured surface temperature matched that of the thermocouple reading over the above temperature range. The estimated surface emissivity was taken as that of the corresponding camera emissivity setting. However, hemispherical FR-4 emissivity measurements have been subsequently documented, by for example Järvinen [203], who report an actual emissivity of 0.92. While the above procedure permitted to accurately calibrate the infrared system, for numerical analysis the board and component surface emissivity was specified as 0.92.



**Figure 3.12** Measurement of component surface temperature on the Stage 3 PCB, using miniature thermistors mounted onto the package heat slugs.

Component junction and component-board surface temperature measurements were referenced to the quiescent ambient air temperature in free convection, or the free-stream air temperature measured upstream of the PCB in forced convection. The reference ambient air temperature was measured using a thermistor accurate to within  $\pm 0.2^\circ\text{C}$  over the range of ambient temperatures considered.

Component power dissipation was measured to an accuracy of  $\pm 0.2\%$ , with a worst-case

2% deviation across the entire Stage 3 component array.

Free-stream airflow velocity was measured using a 2 mm diameter Pitot static tube, located 50 mm from the test assembly's non-component side and connected to a digital micro-manometer. Air velocity measurement accuracy was in excess of 99% for all airflow velocities under analysis.

*SEMI Standard PCB.* Free convection characterisation of the single-board mounted components on the SEMI standard PCB was performed in a still-air cubical enclosure of volume  $0.02832 \text{ m}^3$  [115], conforming to the SEMI standard G38-87 [108]. The objective of Davies et al. [115] was to assess the impact of both board orientation and component lead contact to the board, on component thermal resistance. The junction temperature measurement of relevance to this study is for a vertical board orientation, referred to as "Orientation 5" by the authors, having all component leads soldered to the board, and a component power dissipation of 3 W. Although undertaken in the course of the study, this data point was not reported in Davies et al. [115], who only present the free convection component junction temperature and component-board surface temperature for this board orientation, with only 6 component leads soldered and a power dissipation of 2.5W.

Forced convection characterisation was performed at the outlet of the same wind tunnel used for characterising the populated board, shown in Figure 3.10(a), to enable surface temperature measurements by infrared thermography [77]. Reproducibility tests were undertaken at a different facility, with the test vehicle mounted centrally within a wind tunnel test section of cross-sectional dimensions of 125 x 125 mm and length 200 mm, Figure 3.36. Component junction temperature measurements were found to be within the bounds of repeatability. This provided further confidence in the suitability of the characterisation environment shown in Figure 3.10(a).

Component junction temperature measurements conformed to the SEMI standard G38-87 [108], with the thermal test dies calibrated to an accuracy of  $\pm 0.4^\circ\text{C}$ . Unlike for the populated board, diode voltage measurements were recorded directly using a digital multi-meter, having 5.5 digit precision.

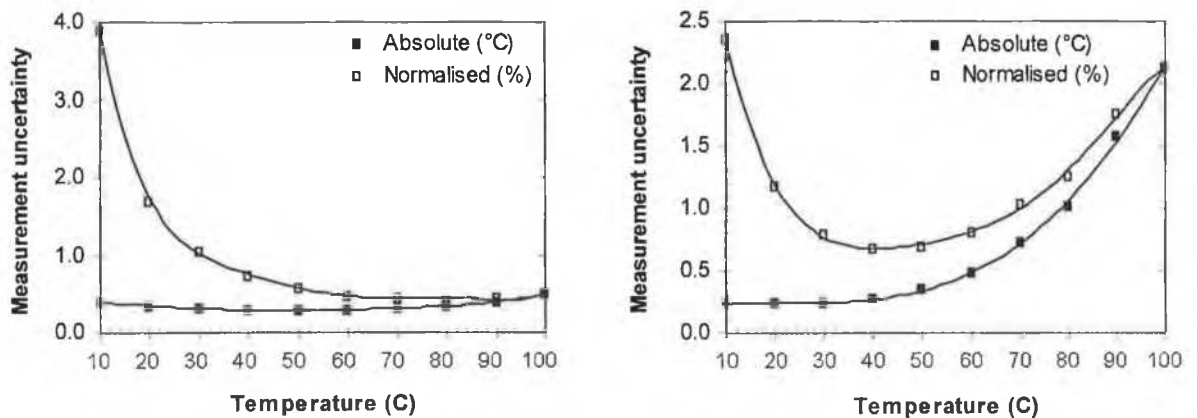
Corresponding component-board surface temperature measurements were recorded using infrared thermography only. These measurements were made using the same instrumentation and experimental set-up as employed for the populated board, Figure 3.10(b). Both the component and PCB surfaces were sprayed with the same matt black paint as applied to the surfaces of the packages on the populated board. The infrared measurements are presented in Lohan and Davies [106] and [77] for free convection, and a 2 m/s airflow respectively. Although not reported, corresponding measurements were also made at 4 m/s.

Component junction and surface temperature measurements were referenced to the quiescent ambient air temperature in free convection, or the free-stream air temperature measured upstream of the PCB in forced convection. The reference ambient air temperature was measured using a Type-T thermocouple accurate to within  $\pm 1^\circ\text{C}$ .

Component power dissipation was measured to an accuracy of  $\pm 0.2\%$ . Characterisation was performed for a component power dissipation of 3W for all tests.

### 3.3.3.2 Uncertainty in Experimental Measurements

**Populated Board.** The estimated uncertainties in measured component junction temperature, and component surface and ambient air temperature, both measured using thermistors, are given as a function of operating temperature in Figure 3.13. Lohan and Davies [106] only reported normalised uncertainties. For the purpose of comparing numerical predictions with measurements in this study, corresponding absolute uncertainties are estimated here for each test configuration. In addition, uncertainties in measured component-board infrared surface temperature are also given. These estimates are based on an Nth order, single-sample uncertainty analysis [204-208], details of which are given in Appendix B. The value of a given measured quantity is estimated to lie within  $\pm$  the estimated uncertainty interval of its recorded value with a confidence level of 95%.



(a) Diode junction temperature measurement

(b) Thermistor temperature measurement

**Note:** Normalised uncertainty (%) in (a) is the ratio of the absolute uncertainty ( $^\circ\text{C}$ ) to the measured junction temperature rise ( $^\circ\text{C}$ ) above ambient conditions. The normalised uncertainty (%) in (b) is the ratio of the absolute uncertainty ( $^\circ\text{C}$ ) to the measured thermistor temperature ( $^\circ\text{C}$ ).

**Figure 3.13** Cumulative uncertainties in component junction and surface temperature measurement for the populated board characterisation.

*Junction temperature measurement.* As shown in Figure 3.13(a), for the range of operating junction temperatures considered in this study,  $44^\circ\text{C}$ - $96^\circ\text{C}$ , the uncertainty in measured junction temperature ranges from  $\pm 0.4^\circ\text{C}$  (0.7%) in forced convection to  $\pm 0.6^\circ\text{C}$

(0.5%) in free convection. Worst-case absolute uncertainties occurred in free convection, due to high component operating temperature, while worst-case normalised uncertainties arose at the highest free-stream velocity (4 m/s) due to low operating temperature.

As detailed in Appendix B, the uncertainty in component junction temperature is solely due to that in thermistor measurement of ambient air temperature, which was  $\pm 0.3^\circ\text{C}$  over the range of ambient air temperatures considered, 13-20 $^\circ\text{C}$ , Figure 3.13(b), as uncertainty in voltage measurement was negligible due to high instrument precision, Table B.1. The uncertainty in ambient air temperature results from thermistor transducer accuracy, which was  $\pm 0.2^\circ\text{C}$  in the range of ambient air temperatures, [202], and a systematic error introduced by the data acquisition system.

*Component surface thermistor temperature measurement.* As shown in Figure 3.13(b), the cumulative uncertainty in thermistor temperature measurement ranged from  $\pm 0.3^\circ\text{C}$  (0.7%) to  $\pm 1.5^\circ\text{C}$  (1.7%) over the range of component operating surface temperatures considered, 40 $^\circ\text{C}$ -89 $^\circ\text{C}$ . This uncertainty was primarily attributed to the data acquisition system. Due to the negative temperature coefficient of the thermistor transducer, the thermistor output voltage decreased with temperature, thereby resulting in lower measurement resolution by the data acquisition system. Consequently, the uncertainty in component surface temperature increased with temperature, Figure 3.13(b). Worst-case uncertainties occurred for the simultaneously powered non-insulated Stage 3 PCB in free convection and the simultaneously powered insulated PCB in a 2 m/s airflow.

*Component-board surface infrared temperature measurement.* Uncertainty in this variable was not reported by Lohan and Davies [106]. The overall uncertainty in infrared surface temperature was estimated by combining the infrared system calibration error against a Type-T thermocouple measurement,  $\pm 1^\circ\text{C}$ , with the corresponding thermocouple resolution, by the root-sum-square method. Lohan and Davies conservatively quote thermocouple accuracy as  $\pm 1^\circ\text{C}$ , which represents the nominal error limit for this class of thermocouples [209]. Therefore, the estimated overall uncertainty in infrared surface temperature was  $\pm 1.4^\circ\text{C}$ .

Based on Figure 3.13(b), it can therefore be noted that for surface temperatures less than 88 $^\circ\text{C}$ , thermistor measurements can be considered as more accurate than the corresponding infrared data. Although thermistors only provide point measurements, the infrared thermographs presented in the next section show that the temperature variation over each heat slug surface above the die region, was less than 0.4 $^\circ\text{C}$ . Therefore, the thermistor data is considered as the primary metric for the measurement of package surface temperature.

*Component power dissipation.* The uncertainty in component power dissipation, associated with uncertainties in voltage and current measurement,  $\pm 10^{-5}$  V and  $\pm 5 \times 10^{-3}$  A

respectively, was  $\pm 5$  mW (0.2%), with the exception of the simultaneously powered Stage 3 cases. For these configurations, power dissipation was set with a worst-case 60 mW (2%) deviation across the component array. Therefore for these configurations, worst-case overall uncertainty in component power dissipation was 60 mW (2%).

*Free-stream air velocity.* The uncertainty in free-stream air velocity is primarily due to the measured variation of the wind tunnel working section velocity profile upstream of the PCB, 3%, as velocity measurement error was negligible due to high instrument precision.

**SEMI Standard PCB.** Unlike for the characterisation of the populated board, both diode calibration and ambient air temperature measurement were performed using Type-T thermocouples. Lohan and Davies [77] conservatively quote thermocouple accuracy as  $\pm 1^\circ\text{C}$ , as noted above. However, calibration of such thermocouples shows that they are typically accurate to within  $\pm 0.5^\circ\text{C}$  [35].

*Junction temperature measurement.* As for the populated board, the uncertainty in measured component junction temperature is solely due to that in the ambient air temperature. Based on a thermocouple measurement accuracy of  $\pm 0.5^\circ\text{C}$ , the uncertainty in junction temperature ranges from  $\pm 0.6^\circ\text{C}$  (2.0%) in forced convection to  $\pm 0.7^\circ\text{C}$  (1.2%) in free convection. This uncertainty would rise to  $\pm 1.2^\circ\text{C}$  (4.5%) in forced convection and  $\pm 1.5^\circ\text{C}$  (2.6%) in free convection if the Type-T thermocouple accuracy was taken as  $\pm 1^\circ\text{C}$ , but such estimates would be excessively conservative.

Uncertainties in measured component-board infrared surface temperature, component power dissipation and free-stream air velocity are the same as estimated above for the populated board.

The estimated uncertainties in all variables are given in Table 3.1 for both the populated and SEMI PCBs, with further details given in Table B.1.

**Table 3.1** Measured quantities and estimated uncertainties for characterisation of the PQFP 160 component on the populated board and SEMI PCB.

<i>Parameter and unit</i>	<i>Nominal value</i>		<i>Uncertainty</i>
$T_j$ ( $^\circ\text{C}$ )	Populated PCB	44 - 96	$\pm 0.4$ (0.7%) to $\pm 0.6$ (0.5%)
	SEMI PCB	47 - 84	$\pm 0.6$ (2.0%) to $\pm 0.7$ (1.2%)
$T_s$ ( $^\circ\text{C}$ )	Populated PCB	Thermistor: 40 - 89 Infrared: 13 - 90	$\pm 0.3$ (0.7%) - 1.5 (1.7%)
	SEMI PCB, infrared	10 - 80	$\pm 1.4$
$T_{\text{ref}}$ ( $^\circ\text{C}$ )	Populated PCB	13 - 20	$\pm 0.3$
	SEMI PCB	10 - 20	$\pm 0.5$
$Q_{\text{diss}}$ (W)	Populated PCB	3.0	Individually powered, $\pm 5 \times 10^{-3}$ (0.2%) Simultaneously powered, $\pm 6 \times 10^{-2}$ (2.0%)
	SEMI PCB	3.0	$\pm 5 \times 10^{-3}$ (0.2%)
$u$ (m/s)	Populated PCB	2 - 4	3%
	SEMI PCB	1 - 4	3%

Note: Uncertainty is given as both an absolute value, and normalised value (%) in parenthesis ( ).



From the data reported by Lohan and Davies [106], junction temperature measurements were overall repeatable to within  $\pm 0.5^\circ\text{C}$  and  $\pm 1^\circ\text{C}$  for the SEMI PCB and populated board respectively.

The repeatability of the component junction temperature measurements indicated that random errors had a negligible contribution on measurement uncertainty, the main contributor of which was attributed to a systematic error in the instrumentation.

The above analyses demonstrate the suitability of the measurement techniques employed for producing accurate experimental data.

### 3.3.3.3 Thermal Characterisation Data

This section presents the experimental data used to assess numerical predictive accuracy for the populated board and SEMI PCB test configurations, namely component junction and component-board surface temperature measurements.

#### 3.3.3.3.1 Populated Board

The free convection data for the populated board is for Stage 1 and the non-insulated Stage 3 PCBs. In forced convection at 2 and 4 m/s, characterisation data is presented for all three stages. The Stage 2 experimental data is confined to component H individually powered, with devices (A,F,K) acting as a source of upstream aerodynamic disturbance in forced convection.

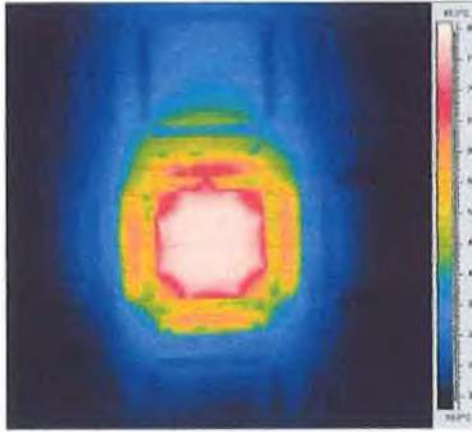
Infrared thermographic measurements are presented for Stage 1 in free convection, Stage 2 in forced convection, and the simultaneously powered Stage 3 cases.

**Free convection.** Measured component junction and surface temperature are presented in Table 3.2 for Stage 1, and Tables 3.3 and 3.4 for individually and simultaneously powered component configurations respectively on the non-insulated Stage 3 PCB. The corresponding junction-to-package top (case) temperature drop is also given. Infrared thermographs for the Stage 1 PCB are presented in Figure 3.14, with thermographs for the simultaneously powered non-insulated Stage 3 PCB shown in Figure 3.15.

**Table 3.2** Measured component junction and surface temperatures for a single-board mounted component at position H (Stage 1) in free convection.

$T_i$ ( $^\circ\text{C}$ )	$T_s$ ( $^\circ\text{C}$ )		$\Delta T_{jc}$ ( $^\circ\text{C}$ )	
	Thermistor	Infrared	Thermistor	Infrared
85.6	80.3	79.9	5.3	5.7

**Note:**  $\Delta T_{jc}$  refers to junction-to-package top (case) temperature drop. Measurement uncertainty for junction temperature,  $\pm 0.5^\circ\text{C}$ , and surface temperature,  $\pm 1.1^\circ\text{C}$  and  $\pm 1.4^\circ\text{C}$  for thermistor and infrared measurement respectively. Component power dissipation = 3W. Ambient air temperature,  $19.6^\circ\text{C}$ .



**Note:** Measurement uncertainty,  $\pm 1.4^{\circ}\text{C}$ . Component power dissipation = 3W. Ambient air temperature,  $19.6^{\circ}\text{C}$ .

**Figure 3.14** Surface temperature infrared thermographs for component H individually powered on the Stage 1 PCB in free convection.

**Table 3.3** Measured component junction and surface temperatures for individually powered component configurations on the non-insulated Stage 3 PCB in free convection.

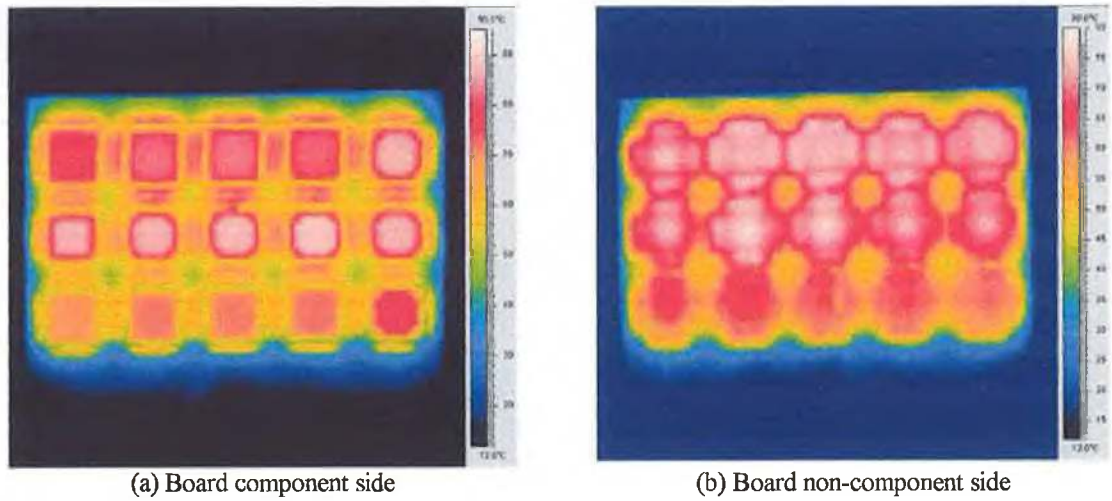
Component	$T_j (^{\circ}\text{C})$	$T_s (^{\circ}\text{C})$	$\Delta T_{jc} (^{\circ}\text{C})$
C	72.7	68.5	4.2
F	81.8	76.4	5.4
G	77.9	73.3	4.6
H	79.4	73.0	6.4
I	80.8	75.2	5.6
J	81.5	77.6	3.9
K	82.0	76.7	5.3
M	70.3	65.5	4.8

**Note:**  $\Delta T_{jc}$  refers to junction-to-package top (case) temperature drop. Measurement uncertainty for junction temperature,  $\pm 0.5^{\circ}\text{C}$  and surface temperature,  $\pm 1.0^{\circ}\text{C}$  recorded using thermistors. Component power dissipation = 3W. Ambient air temperature,  $15.8^{\circ}\text{C}$ .

**Table 3.4** Measured component junction and surface temperatures for the simultaneously powered non-insulated Stage 3 configuration in free convection.

Component	$T_j (^{\circ}\text{C})$	$T_s (^{\circ}\text{C})$		$\Delta T_{jc} (^{\circ}\text{C})$	
		Thermistor	Infrared	Thermistor	Infrared
A	94.9	88.5	87.8	6.4	7.1
B	87.4	82.3	82.2	5.1	5.2
C	87.9	82.9	83.6	5	4.3
D	87.3	81.7	82.8	5.6	4.5
E	85.3	81.0	80.2	4.3	5.1
F	93.0	87.0	87.7	6.0	5.3
G	96.1	88.5	90.0	7.6	6.1
H	95.1	88.0	88.8	7.1	6.3
I	92.9	85.6	87.5	7.3	5.4
J	92.4	87.0	87.2	5.4	5.2
K	85.9	79.9	80.2	6.0	5.7
L	78.3	73.6	73.1	4.7	5.2
M	76.7	72.3	72.1	4.4	4.6
N	77.1	72.3	72.4	4.8	4.7
O	76.7	71.8	70.4	4.9	6.3

**Note:**  $\Delta T_{jc}$  refers to junction-to-package top (case) temperature drop. Measurement uncertainty for junction temperature,  $\pm 0.6^{\circ}\text{C}$ , and surface temperature,  $\pm 1.5^{\circ}\text{C}$  and  $\pm 1.4^{\circ}\text{C}$  for thermistor and infrared measurement respectively. Component power dissipation = 3W. Ambient air temperature,  $13.2^{\circ}\text{C}$ .



**Note:** Measurement uncertainty,  $\pm 1.4^\circ\text{C}$ . Component power dissipation = 3W. Ambient air temperature,  $13.2^\circ\text{C}$ .

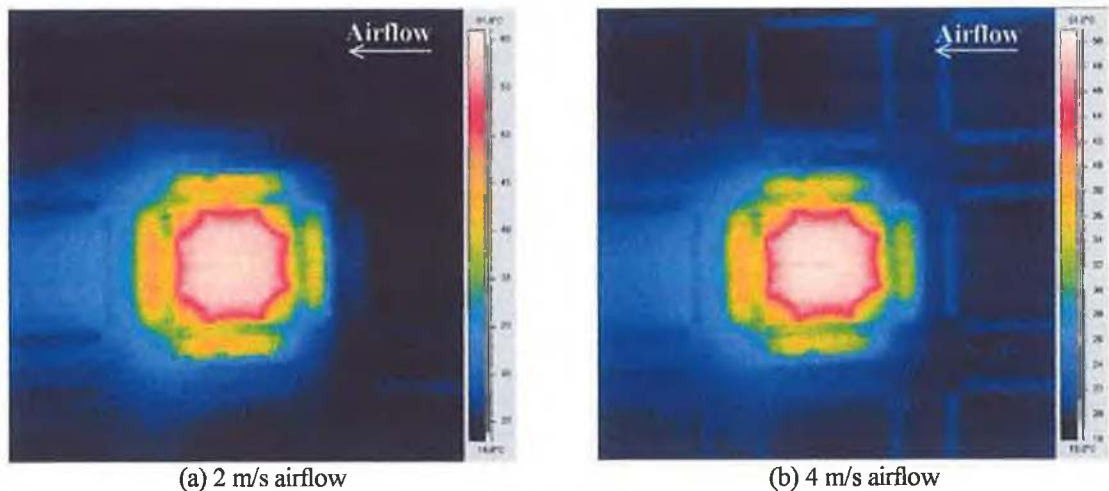
**Figure 3.15** Surface temperature infrared thermographs for the simultaneously powered non-insulated PCB Stage 3 configuration in free convection.

**Forced convection.** Measured component junction and surface temperature, with corresponding junction-to-case temperature drops for both 2 and 4 m/s airflow, are presented in Table 3.5 for Stages 1 and 2, and Tables 3.6 to 3.12 for Stage 3. Corresponding thermographs for component H individually powered on the Stage 2 PCB are presented in Figure 3.16 for both 2 and 4 m/s airflow. The thermographs for the simultaneously powered, non-insulated Stage 3 PCB are presented in Figure 3.17 for 4 m/s airflow. The thermographs for the simultaneously powered insulated Stage 3 PCB are shown in Figure 3.18 for both 2 and 4 m/s airflow.

**Table 3.5** Measured component junction and surface temperatures for component H individually powered on the Stage 1 and 2 PCBs in forced convection.

PCB topology	Airflow (m/s)	$T_j$ ( $^\circ\text{C}$ )	$T_s$ ( $^\circ\text{C}$ )		$\Delta T_{jc}$ ( $^\circ\text{C}$ )	
			Thermistor	Infrared	Thermistor	Infrared
Stage 1	2.0	65.6	---	---	---	---
	4.0	58.2	---	---	---	---
Stage 2	2.0	62.6	57.9	59.0	4.7	3.6
	4.0	54.2	48.4	50.1	5.8	4.1

**Note:**  $\Delta T_{jc}$  refers to junction-to-package top (case) temperature drop. Measurement uncertainty for junction temperature,  $\pm 0.4^\circ\text{C}$ , and surface temperature,  $\pm 0.5^\circ\text{C}$  and  $\pm 1.4^\circ\text{C}$  for thermistor and infrared measurement respectively. Component power dissipation = 3W. Ambient air temperature,  $19.6^\circ\text{C}$ .



**Note:** Measurement uncertainty,  $\pm 1.4^\circ\text{C}$ . Component power dissipation = 3W. Ambient air temperature,  $19.6^\circ\text{C}$ .

**Figure 3.16** Surface temperature infrared thermographs for component H individually powered on the Stage 2 PCB in forced convection.

**Table 3.6** Measured component junction and surface temperatures for individually powered component configurations on the non-insulated Stage 3 PCB in a 2 m/s airflow.

Component	$T_j$ ( $^\circ\text{C}$ )	$T_s$ ( $^\circ\text{C}$ )	$\Delta T_{jc}$ ( $^\circ\text{C}$ )
A	57.2	51.1	6.1
F	57.0	52.5	4.5
G	58.4	52.7	5.7
H	60.2	54.9	5.3
I	60.1	54.6	5.5
J	60.7	55.7	5.0
K	57.4	52.1	5.3

**Note:**  $\Delta T_{jc}$  refers to junction-to-package top (case) temperature drop. Measurement uncertainty for junction temperature,  $\pm 0.4^\circ\text{C}$ , and surface temperature,  $\pm 0.4^\circ\text{C}$  recorded using thermistors. Component power dissipation = 3W. Ambient air temperature,  $15.8^\circ\text{C}$ .

**Table 3.7** Measured component junction and surface temperatures for individually powered component configurations on the non-insulated Stage 3 PCB in a 4 m/s airflow.

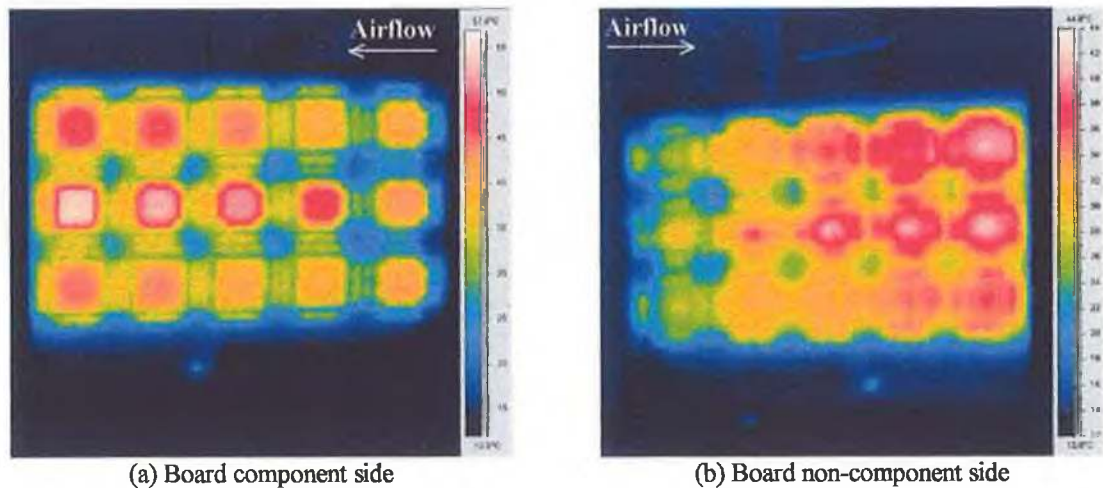
Component	$T_j$ ( $^\circ\text{C}$ )	$T_s$ ( $^\circ\text{C}$ )	$\Delta T_{jc}$ ( $^\circ\text{C}$ )
A	48.8	42.0	6.8
F	48.7	42.8	5.9
G	50.4	44.9	5.5
H	52.4	46.4	6.0
I	51.4	45.9	5.5
J	51.9	47.3	4.6
K	48.7	42.2	6.5

**Note:**  $\Delta T_{jc}$  refers to junction-to-package top (case) temperature drop. Measurement uncertainty for junction temperature,  $\pm 0.4^\circ\text{C}$ , and surface temperature,  $\pm 0.3^\circ\text{C}$  recorded using thermistors. Component power dissipation = 3W. Ambient air temperature,  $15.8^\circ\text{C}$ .

**Table 3.8** Measured component junction and surface temperatures for the simultaneously powered non-insulated Stage 3 configuration in a 4 m/s airflow.

Component	$T_j$ (°C)	$T_s$ (°C)		$\Delta T_{jc}$ (°C)	
		Thermistor	Infrared	Thermistor	Infrared
A	47.6	40.9	41.3	6.7	6.3
B	44.8	40.2	40.4	4.6	4.4
C	48.6	44.2	44.3	4.4	4.3
D	50.3	45.8	46.1	4.5	4.2
E	51.0	46.6	46.6	4.4	4.4
F	48.4	42.9	43.5	5.5	4.9
G	53.2	47.3	47.7	5.9	5.5
H	57.4	50.9	51.6	6.5	5.8
I	57.8	51.7	52.5	6.1	5.3
J	59.0	54.5	54.4	4.5	4.6
K	47.5	41.5	42.0	6.0	5.5
L	45.1	39.8	40.0	5.3	5.1
M	—	40.6	41.0	—	—
N	48.4	43.8	44.1	4.6	4.3
O	50.3	44.8	44.0	5.5	6.3

**Note:**  $\Delta T_{jc}$  refers to junction-to-package top (case) temperature drop. Measurement uncertainty for junction temperature,  $\pm 0.4^\circ\text{C}$ , and surface temperature,  $\pm 0.4^\circ\text{C}$  and  $\pm 1.4^\circ\text{C}$  for thermistor and infrared measurement respectively. Component power dissipation = 3W. Ambient air temperature,  $13.2^\circ\text{C}$ .



**Note:** Measurement uncertainty,  $\pm 1.4^\circ\text{C}$ . Component power dissipation = 3W. Ambient air temperature,  $13.2^\circ\text{C}$ .

**Figure 3.17** Surface temperature infrared thermographs for the simultaneously powered non-insulated Stage 3 configuration in a 4 m/s airflow.

**Table 3.9** Measured component junction and surface temperatures for individually powered component configurations on the insulated Stage 3 PCB in a 2 m/s airflow.

Component	$T_j$ (°C)	$T_s$ (°C)	$\Delta T_{jc}$ (°C)
A	71.1	63.5	7.6
F	72.2	66.1	6.1
G	70.3	64.0	6.3
H	72.7	66.1	6.6
I	73.6	67.0	6.6
J	72.8	67.9	4.9
K	70.4	63.9	6.5

**Note:**  $\Delta T_{jc}$  refers to junction-to-package top (case) temperature drop. Measurement uncertainty for junction temperature,  $\pm 0.5^\circ\text{C}$ , and surface temperature,  $\pm 0.7^\circ\text{C}$  recorded using thermistors. Component power dissipation = 3W. Ambient air temperature,  $17^\circ\text{C}$ .

**Table 3.10** Measured component junction and surface temperatures for individually powered component configurations on the insulated Stage 3 PCB in a 4 m/s airflow.

Component	$T_j$ (°C)	$T_s$ (°C)	$\Delta T_{jc}$ (°C)
A	59.3	52.2	7.1
F	58.8	52.3	6.5
G	60.0	53.8	6.2
H	61.6	55.0	6.6
I	62.4	55.6	6.8
J	61.6	56.2	5.4
K	59.3	52.9	6.4

Note:  $\Delta T_{jc}$  refers to junction-to-package top (case) temperature drop. Measurement uncertainty for junction temperature,  $\pm 0.4^\circ\text{C}$ , and surface temperature,  $\pm 0.4^\circ\text{C}$  recorded using thermistors. Component power dissipation = 3W. Ambient air temperature,  $17^\circ\text{C}$ .

**Table 3.11** Measured component junction and surface temperatures for the simultaneously powered insulated Stage 3 configuration in a 2 m/s airflow.

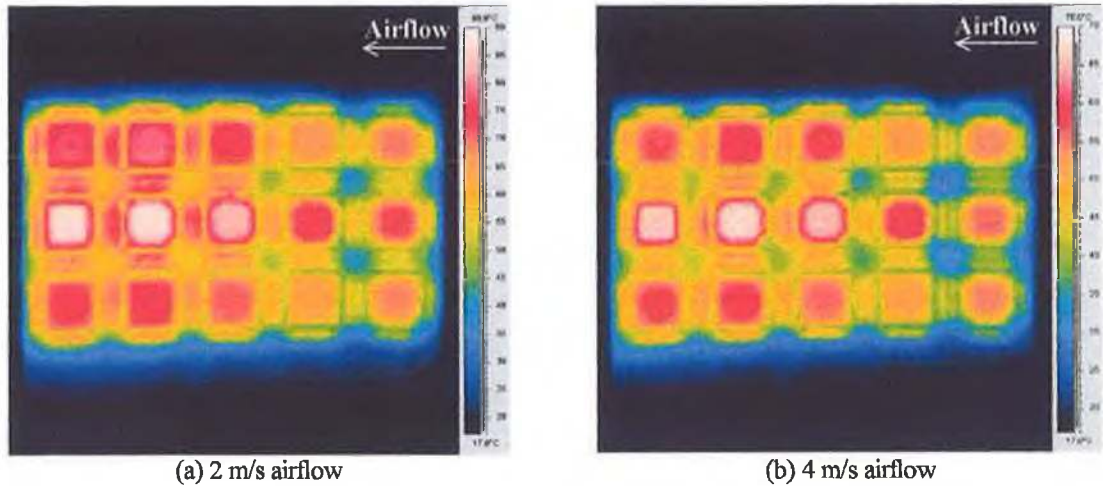
Component	$T_j$ (°C)	$T_s$ (°C)		$\Delta T_{jc}$ (°C)	
		Thermistor	Infrared	Thermistor	Infrared
A	77.5	70.6	69.6	6.9	7.9
B	72.5	67.2	66.9	5.3	5.6
C	79.5	73.7	74.9	5.8	4.6
D	83.9	77.7	79.1	6.2	4.8
E	82.5	77.7	77.8	4.8	4.7
F	79.3	73.3	73.6	6.0	5.7
G	82.1	76.1	75.6	6.0	6.5
H	90.2	82.6	83.9	7.6	6.3
I	93.8	86.3	87.4	7.5	6.4
J	93.0	86.7	87.4	6.3	5.6
K	75.1	69.0	68.9	6.1	6.2
L	70.8	65.5	65.5	5.3	5.3
M	---	71.0	71.6	---	---
N	80.3	74.6	75.6	5.7	4.7
O	80.6	75.3	74.6	5.3	6

Note:  $\Delta T_{jc}$  refers to junction-to-package top (case) temperature drop. Measurement uncertainty for junction temperature,  $\pm 0.6^\circ\text{C}$ , and surface temperature,  $\pm 1.4^\circ\text{C}$ , for both thermistor and infrared measurement. Component power dissipation = 3W. Ambient air temperature,  $18.1^\circ\text{C}$ .

**Table 3.12** Measured component junction and surface temperatures for the simultaneously powered insulated Stage 3 configuration in a 4 m/s airflow.

Component	$T_j$ (°C)	$T_s$ (°C)		$\Delta T_{jc}$ (°C)	
		Thermistor	Infrared	Thermistor	Infrared
A	61.8	54.5	54.6	7.3	7.2
B	58.1	52.9	52.8	5.2	5.3
C	62.2	56.9	56.0	5.3	6.2
D	63.9	59.1	59.3	4.8	4.6
E	62.0	57.1	57.1	4.9	4.9
F	62.3	55.8	56.4	6.5	5.9
G	66.1	60.0	60.3	6.1	5.8
H	71.7	64.8	66.2	6.9	5.5
I	73.9	67.2	67.9	6.7	6.0
J	72.2	66.5	66.5	5.7	5.7
K	61.1	54.7	55.0	6.4	6.1
L	57.7	52.8	52.4	4.9	5.3
M	---	55.6	56.4	---	---
N	63.4	58.4	58.5	5.0	4.9
O	64.1	58.1	57.8	6.0	6.3

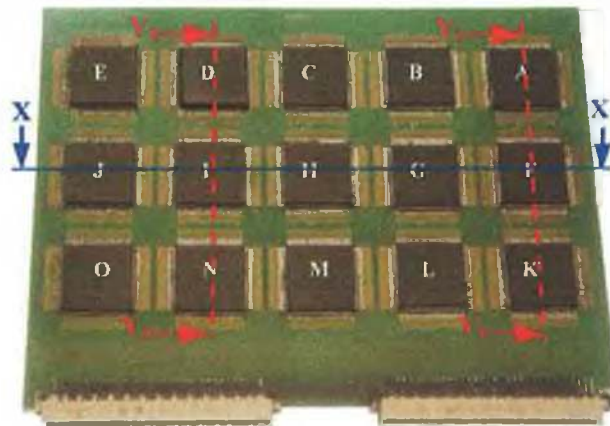
Note:  $\Delta T_{jc}$  refers to junction-to-package top (case) temperature drop. Measurement uncertainty for junction temperature,  $\pm 0.4^\circ\text{C}$ , and surface temperature,  $\pm 0.6^\circ\text{C}$  and  $\pm 1.4^\circ\text{C}$  for thermistor and infrared measurement respectively. Component power dissipation = 3W. Ambient air temperature,  $18.1^\circ\text{C}$ .



**Note:** Measurement uncertainty,  $\pm 1.4^{\circ}\text{C}$ . Component power dissipation = 3W. Ambient air temperature,  $18.1^{\circ}\text{C}$ .

**Figure 3.18** Surface temperature infrared thermographs for the simultaneously powered insulated Stage 3 PCB in forced convection, board component side.

To assess numerical predictive accuracy in this study, surface temperature profiles were extracted from the thermographs about the packages' centre in both the stream-wise and span-wise airflow directions. The analysis planes used are defined in Figure 3.19. Plane X-X represents the central span-wise and stream-axis axis in free and forced convection respectively. Planes Y<sub>1</sub>-Y<sub>1</sub> and Y<sub>2</sub>-Y<sub>2</sub> are used for free convection analysis.



**Note:** The position of each component on the PCB is identified by the lettering, A to O. A, F and K are leading edge components in forced convection. Axes X-X, Y<sub>1</sub>-Y<sub>1</sub> and Y<sub>2</sub>-Y<sub>2</sub> denote planes for surface temperature analysis.

**Figure 3.19** Definition of component-board infrared surface temperature profile analysis planes on the populated board, used to assess numerical predictive accuracy.

From the data presented, it can be noted that component surface temperature measurements performed using infrared thermography and thermistors are typically within  $\pm 0.7^\circ\text{C}$  of each other. Worst-case discrepancy was  $1.9^\circ\text{C}$  for component I on the simultaneously powered Stage 3 PCB in free convection, Table 3.4. These discrepancies are within the bounds of worst-case measurement uncertainty estimated by combining the uncertainties associated with both measurement methods by the root-sum-square method,  $\pm 2.1^\circ\text{C}$ .

### 3.3.3.3.2 SEMI Standard PCB

Measured component junction temperatures for both package designs II and III in free and forced convection are presented in Table 3.13. This data is supplemented by infrared component surface temperature measurements for package design II, from which corresponding junction-to-package top (case) temperature drops were calculated. Corresponding thermographs for package design II are presented in Figure 3.20 for the board component side.

**Table 3.13** Measured steady-state PQFP 160 component junction and surface temperatures for package designs II and III mounted on the SEMI PCB.

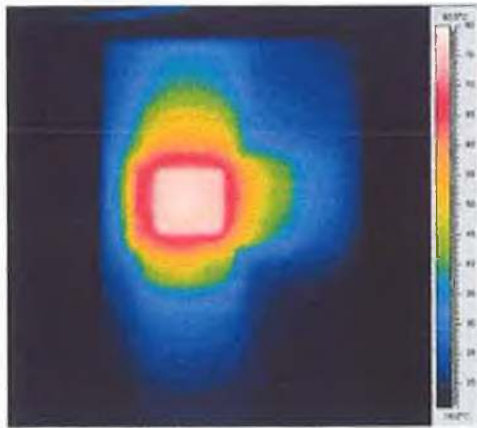
Airflow velocity (m/s)	Design II			Design III
	$T_j$ ( $^\circ\text{C}$ )	$T_s$ ( $^\circ\text{C}$ )	$\Delta T_{jc}$ ( $^\circ\text{C}$ )	$T_j$ ( $^\circ\text{C}$ )
0	80.6	79.1	1.5	74.4
1.0	67.3	---	---	---
2.0	58.8	58.9	-0.1	54.8
4.0	48.2	48.4	-0.2	44.0

**Note:**  $\Delta T_{jc}$  refers to junction-to-package top (case) temperature drop. Junction temperature measurement uncertainty,  $\pm 0.7^\circ\text{C}$  and  $\pm 0.6^\circ\text{C}$  for free and forced convection respectively, and surface temperature,  $\pm 1.4^\circ\text{C}$  recorded by infrared thermography. Component power dissipation = 3W. Ambient air temperature,  $17^\circ\text{C}$ .

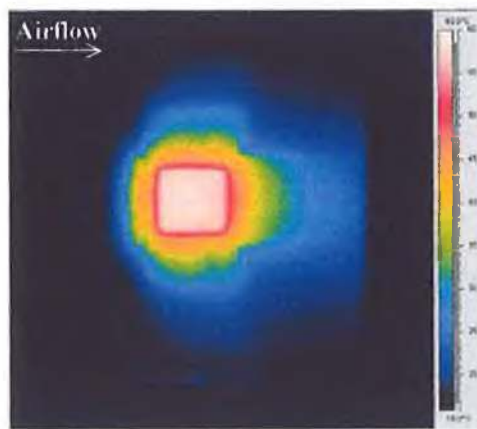
The measured negative junction-to-case temperature drops for package design II in 2 and 4 m/s airflows reflect infrared temperature measurement error. Although the infrared system was calibrated to  $\pm 1.4^\circ\text{C}$  over the temperature range 30 –  $100^\circ\text{C}$ , maximum error results at lower temperature.

As for the populated board, surface temperature profiles were extracted from the thermographs about the packages' centre in both the stream-wise and span-wise airflow directions to assess numerical predictive accuracy. The analysis planes used are defined in Figure 3.21. Plane Y represents the stream-axis and span-wise axis in free and forced convection respectively.

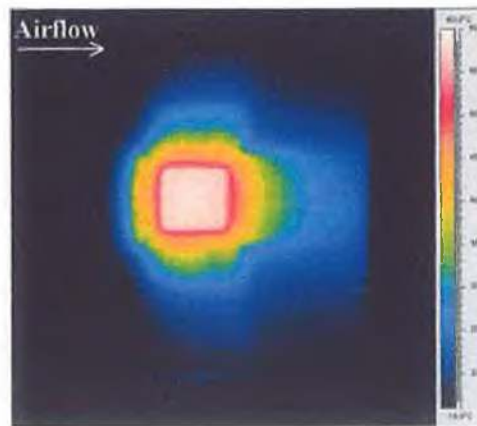




(a) Free convection



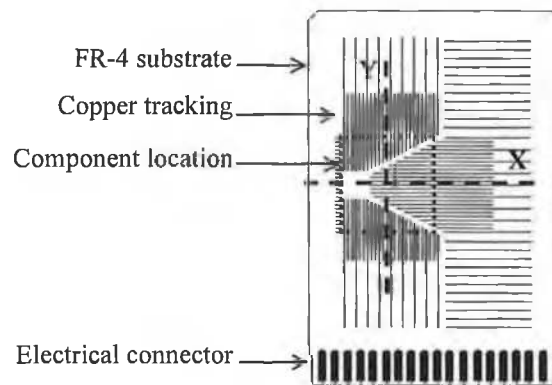
(b) 2 m/s airflow



(c) 4 m/s airflow

**Note:** Measurement uncertainty,  $\pm 1.4^\circ\text{C}$ . Component power dissipation = 3W. Ambient air temperature,  $17^\circ\text{C}$ .

**Figure 3.20** Surface temperature infrared thermographs for package design II on the SEMI standard PCB.



**Note:** The dashed lines identify the surface temperature profile analysis planes X and Y.

**Figure 3.21** Definition of component-board infrared surface temperature profile analysis planes on the SEMI standard PCB, used to assess numerical predictive accuracy

### 3.3.3.3.3 Assessment of the Experimental Data for Benchmark Purposes

The characterisation data presented for the populated and SEMI PCBs in the previous section has been previously analysed to provide a physical insight into component-board heat transfer [12,77,99,106,115]. The objective here is to assess the suitability of the measurements to serve as benchmark data, as no previous discussion has been given on this aspect.

The suitability of the characterisation environments and experimental methods to generate accurate data were demonstrated in Sections 3.3.3.1 and 3.3.3.2, with the measurements shown to be repeatable and reproducible. However, inherent variation in sample thermal resistance also needs to be considered, which could result from manufacturing tolerances, variation in material thermo-physical properties or the presence of packaging defects. If such factors were to significantly alter component thermal resistance, this could lead to erroneous conclusions on numerical predictive accuracy, as the models are based on nominal geometric dimensions and material properties.

The characterisation data for individually powered components on the non-insulated Stage 3 PCB provides an assessment of sample variation, which is analysed for each package design.

In free convection, Table 3.3, for package design I, measured differences in junction temperature between samples (G,H,I), which have a similar thermal footprint, are within worst case 2.9°C, which represents 4.9% variation in junction-to-ambient thermal resistance. F and K, which also share a similar footprint, operate within 0.2°C of each other. As previously noted, package designs I and II have a similar thermal resistance. This permits comparison of samples F and J's operating temperatures, which are within 0.3°C of each other. For package design III, the measured difference in operating

temperature between samples C and M is 2.4°C, which represents 4.8% variation in junction-to-ambient thermal resistance.

In forced convection, the leading edge components (A,F,K) operate within 0.6°C and 1°C of each others at 2 and 4 m/s respectively, Tables 3.6 and 3.7. Previous thermal characterisations studies [93] have shown for similar PCB topologies that the component Nusselt number becomes row-independent by the third component column, counted from the board leading edge. This trend holds here for samples (H,I,J), who operate within 0.4°C and 1°C of each others at 2 and 4 m/s respectively, Tables 3.6 and 3.7.

For the simultaneously powered Stage 3 configuration in forced convection, worst-case asymmetry in the span-wise direction about the PCB central stream-wise axis between the operating temperatures of devices (B to E) and (L to O), which all have the same heat slug design, does not exceed 1.9°C, Table 3.4.

On the SEMI PCB, measurements were undertaken for a single component sample for both package designs II and III, whose junction-to-ambient thermal resistances differed by on order 10%, Table 3.13. This difference is comparable to the mean difference in thermal resistance between samples (G,H,I) and (C,M) and on the Stage 3 PCB, 13%, Table 3.3.

Based on these observations, it can be concluded that sample variation for a given package design is not a significant factor in this study. However, the consistency of the data did not eliminate the possibility of packaging defects, which is now assessed from inspection of the measured component junction-to-case temperature drops for each package design.

On the populated board, the measured junction-to-case temperature drops for package designs I, II and III, are on average 6.1°C, 5.0°C and 4.9°C respectively, based on thermistor measurement of surface temperature. When account is made of measurement uncertainty, these values appear independent of convective environment, powering configuration, PCB topology and component location on the board. This suggests an insensitivity of the component internal heat transfer paths to operating conditions, an aspect analysed further in Chapter 5. However, the magnitude of the above temperature drops, when accounting for measurement uncertainty, clearly exceeds what would be expected in such a package construction. The junction-to-case thermal resistance of 160-lead PowerQuad2 packages is in the region of 0.4°C/W, independently of heat slug design [210]. Thus if all of the heat generated by the die was to be dissipated from the package top surface, considered as isothermal, the junction-to-case temperature drop would be 1.2°C.

In this regard, the measured junction-to-case temperature drop for package design II, is on order 1°C on the SEMI PCB, in contrast with sample J on the populated board, on order

5.0°C. This clearly indicates the presence of an in-built thermal resistance within the samples mounted on the populated board. The fact that the measured junction-to-case temperature drops for a given package design on the populated board are consistent suggests the presence of an interfacial resistance, such as typically caused by delamination. Corresponding comparison could not be made for package design III on the SEMI board, for which component surface temperature was not recorded. However, as previously observed, the difference in junction-to-ambient thermal resistance between package designs I and III on both the SEMI PCB and populated board were comparable. This suggests that the package design III sample mounted on the SEMI board was also defect-free.

The component structural analyses presented in the next section, revealed that delamination of the die attach layer occurred in the samples mounted on the populated board as a result of the component-board assembly process used, which differed from that applied to the SEMI PCB. As will be shown, the interfacial defects identified can be accurately accounted for in the component numerical models, thereby not undermining the benchmark data in any way.

### **3.3.4 Component Structural Analysis**

For benchmark purposes it is essential that the component numerical models be based on samples of known geometry. Inconsistencies between vendor supplied and actual component geometry are not uncommon for thermal test components, which essentially serve for research purposes and thus are less rigorously documented than commercial samples [211]. In addition, package structural integrity needs to be assessed for potential packaging defects that could arise during manufacturing, board assembly or operation. Such defects could increase the device internal conductive resistance. Otherwise, potentially erroneous conclusions on numerical predictive accuracy could be derived.

As inspection of the characterisation data presented in Section 3.3.3.3 revealed the presence of an additional thermal resistance within the PQFP 160 samples mounted on the populated board, component internal geometry and structural integrity were assessed using both destructive and non-destructive testing techniques. Non-destructive testing consisted of X-Ray imaging [212] and Scanning Acoustic Microscopy (SAM) [213]. Destructive testing was undertaken using precision grinding [214], coupled with high-power microscopy for imaging of exposed section planes. This combined approach serves to eliminate potential modelling uncertainties associated with possible deviation from nominal component design.

The principles and application of SAM and X-Ray imaging to component failure analysis are described by Pecht et al. [215]. As X-Ray absorption coefficient is related to atomic number, X-Ray images are a grey scale representation of the object's mass, whereby image colour contrast reflects the variance in shape, thickness and density of the object analysed. SAM is an inspection method for the detection of interfacial defects, such as cracks, voiding, porosity, coplanarity and delamination within electronic components. This technique uses the high sensitivity of ultrasonic waves to interface density variations to characterise interface homogeneity and detect discontinuities or irregularities.

Due to the prohibitive cost of such analyses for all components, a selective approach was employed to combine cross sectioning, SAM and X-Ray microscopy for the three package designs. The small deviation in both junction-to-ambient thermal resistance between samples of the same package design, and corresponding junction-to-package top temperature drops (Section 3.3.3.3.3), suggested that if present, potential packaging defects were likely to result from the same mechanism. On this basis, analysis was limited to a selection of samples for each package design, namely samples (A,G,H) for design I, and samples J and C for designs II and III respectively. Based on the findings obtained, it was not necessary to extend the analysis to other samples. While the samples characterised on the SEMI PCB were not available for testing, their measured junction-to-package top temperature drop suggested the absence of a packaging defect. As both these samples originated from the same production batch as corresponding devices on the populated board, package geometry was determined using the populated board samples.

***Internal Architecture.*** X-Ray imaging was performed to visualise the overall package geometry, viewed from the package top, using a X-TEK VTX-125K system having a resolution of 1  $\mu\text{m}$ . Cross sectioning and specimen preparation were performed in accordance with standard industry practices. Section planes were imaged using stereo and optical microscopes having a resolution of 1  $\mu\text{m}$ . Photograph magnification ranged from 4x to 4400x. The samples were vertically cross-sectioned about the package centre. Geometric parameters for the die, die attach layer, paddle, leadframe, heat slug and encapsulant body for each package design were extracted from cross sectioning. Additional geometric details for the heat slug were obtained from X-Ray imaging.

The measured architectures of the three package designs are presented in Figures 3.22 to 3.24. For package design I, the heat slug is composed of an exposed 16 mm square section extending internally into an octagonal shape, with triangular protrusions at its edges, Figure 3.22(b). This structure is commonly termed a “CAT” in the electronics packaging industry. Package design II contains an 18 mm square heat slug, Figure 3.23. Package design III has

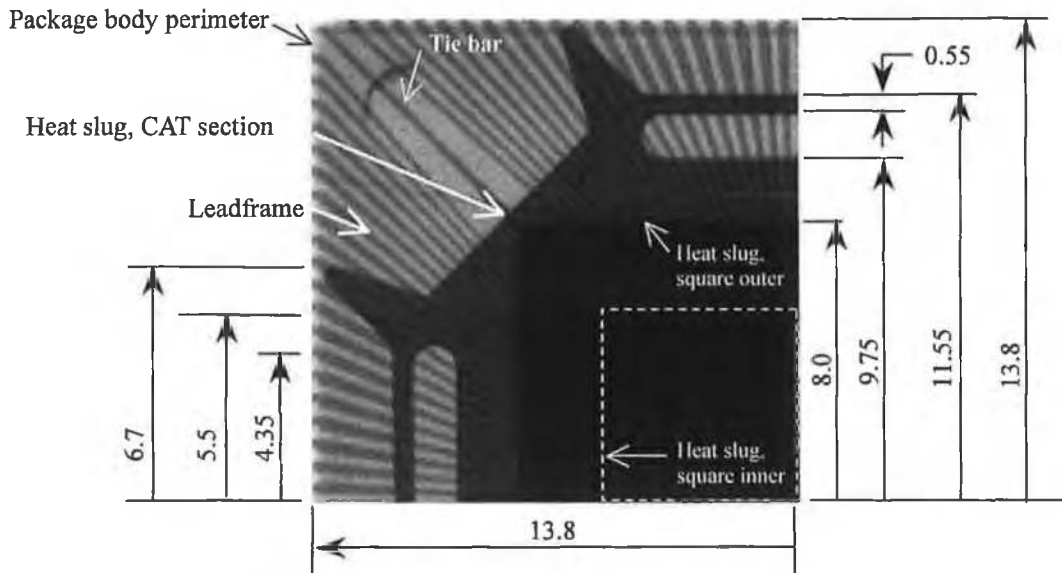
a heat slug composed of an exposed 20 mm circular section, extending internally into a square shape, Figure 3.24. While in package design I, the die is attached to a paddle, for both designs II and III it is directly bonded to the heat slug. In package design I, the heat slug is not mechanically or chemically bonded to the paddle. This design was an attempt to de-couple thermo-mechanical stress possibly induced by thermal contraction warpage of the heat slug on the die after moulding encapsulation process. The tendency of PQFP packages to residual warpage as a result of Coefficient of Thermal Expansion (CTE) mismatch of the constituent materials (die, leadframe and moulding compound) is well documented [216]. As shown in Figure 3.22(a,c,d), package design I contains tie bars, which protude diagonally from the paddle corners to the package corners, in the same plane as the paddle. Their purpose is to anchor the paddle within the package during moulding encapsulation.

**Structural Analysis.** Prior to cross sectioning, SAM was employed to qualitatively assess mechanical integrity at two critical interfaces for each package design, namely the die/encapsulant interface, and die/paddle or die/heat slug interface depending on package design. The scans were conducted using a Sonix HS 1000 machine, equipped with a 15 MHz transducer. The SAM images were taken in C-SAM mode to permit selective depth inspection, with the acoustic wave penetrating the sample from the package base. For ease of interpretation, the images are presented in C-scan format, which is a digital image of the surface acoustic signature. Interpretation of C-mode images is based on image contrast, with uniform monochrome pattern indicating structural integrity, and a grey scale pattern, the presence of discontinuities caused by structural defects. For ease of reference, areas of delamination are coloured red in the present images.

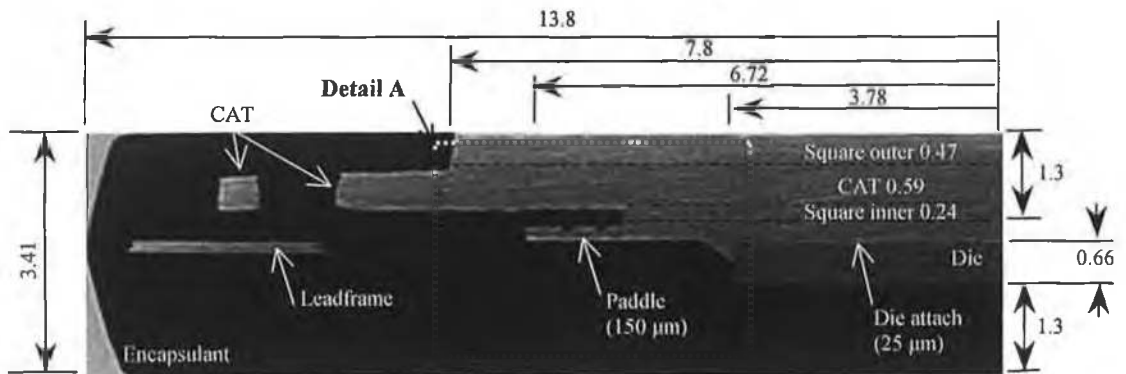
The images obtained for samples G and C, package designs I and III respectively, are presented in Figure 3.25. Additional scans are presented in Section A.3 for samples (A,G,H), package design I, which were obtained using a different equipment having lower resolution, but reveal the same trends.

**Die-encapsulant interface.** For both samples, the imaged die-encapsulant interfaces in Figures 3.25(a) are essentially monochrome, indicating structural integrity. The red- and yellow coloured region at the top right-hand side corner of sample C in Figure 3.25(a,ii), indicative of poor surface integrity, were found to result from a scratch on the package external top surface distorting the acoustic signal.

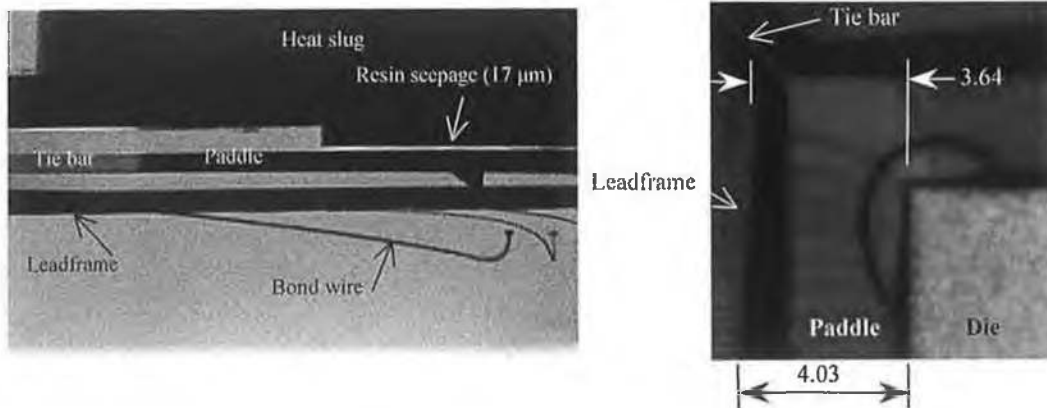
Although images are only presented for two samples, it is unlikely that delamination existed at this interface for the other samples, as resin delamination from the die surface would have been likely to cause breakage of wire bonds, hence loss of component functionality.



(a) X-Ray imaging, plan view, showing heat slug detail (quarter geometry).



(b) Cross section through package centre axis (half geometry)

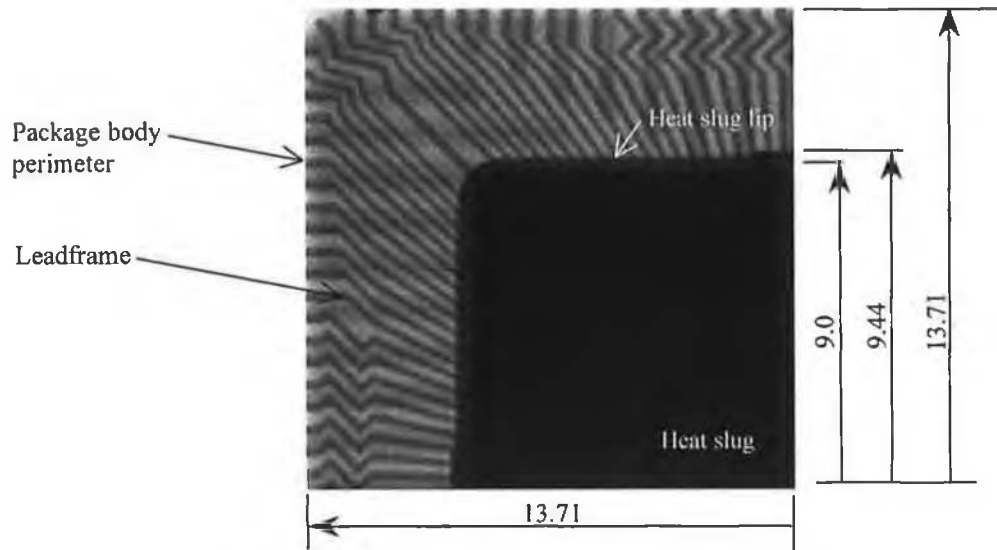


(c) Magnified view of Detail A in (b), derived from X-Ray imaging.

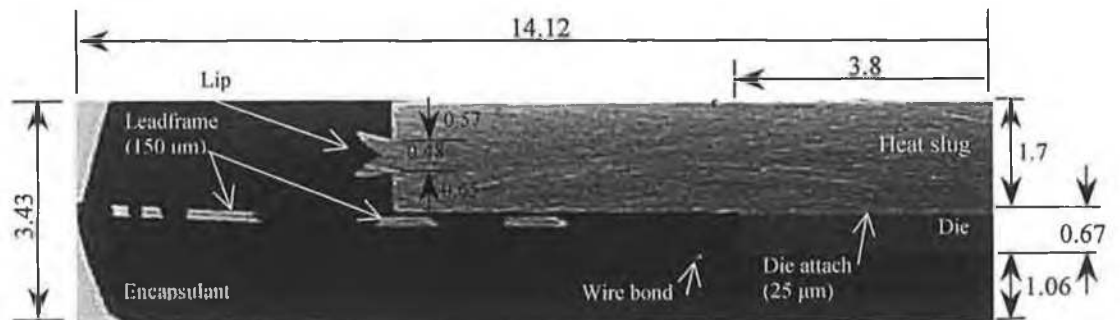
(d) Die to leadframe separation, derived from SAM imaging (quarter geometry).

Note: All dimensions are in millimetres (mm), unless otherwise specified.

Figure 3.22 160-lead PQFP component geometry, package design I.



(a) X-Ray imaging, plan view, showing heat slug detail(quarter geometry).

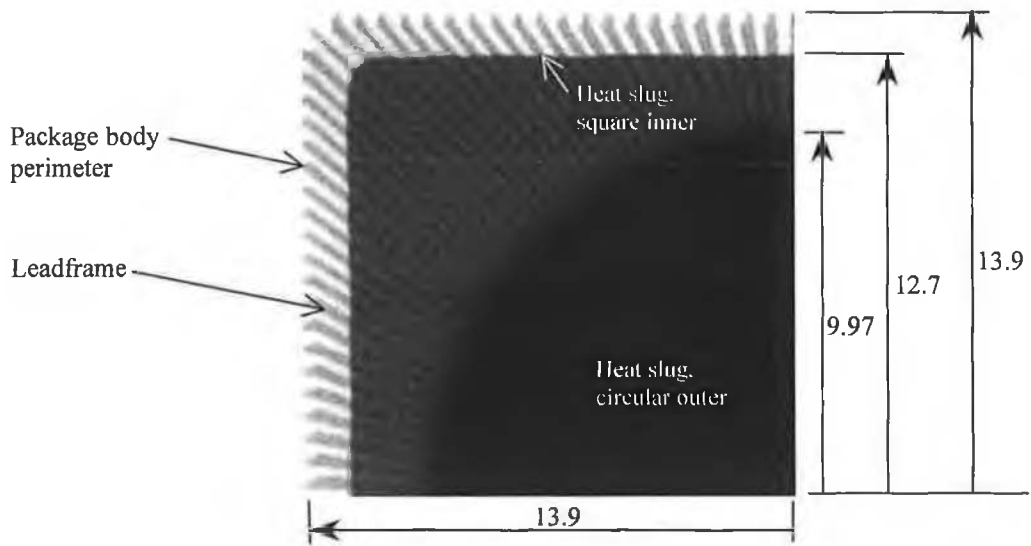


(b) Cross section through package centre axis (half geometry).

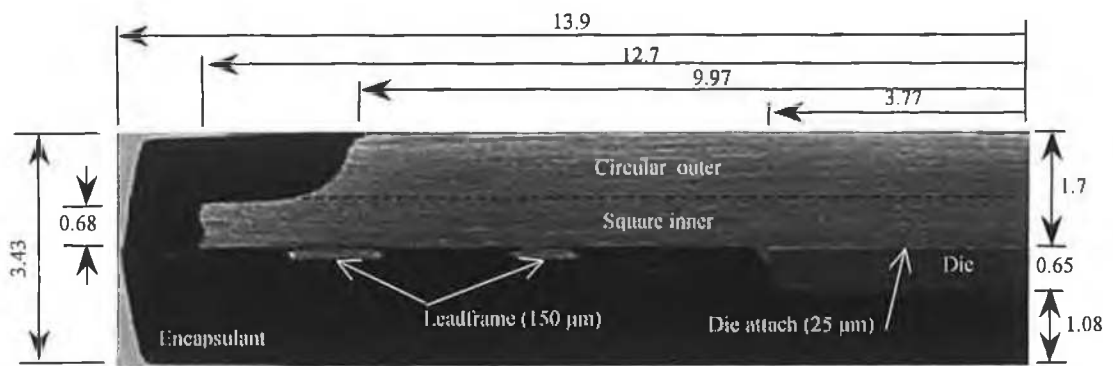
Note: All dimensions are in millimetres (mm), unless otherwise specified.

Figure 3.23 160-lead PQFP component geometry, package design II.

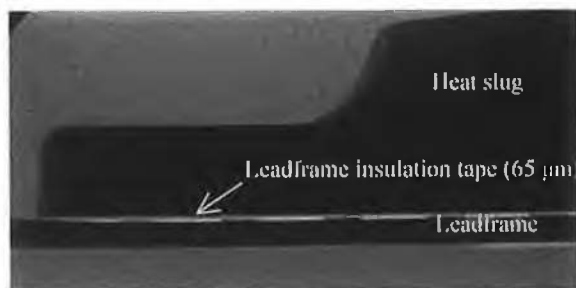




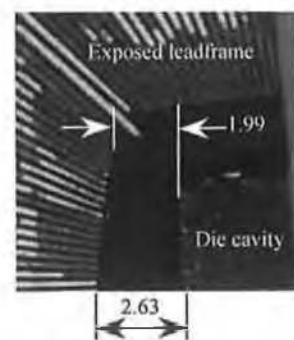
(a) X-Ray imaging, plan view, showing heat slug detail (quarter geometry).



(b) Cross section through package centre axis (half geometry).



(c) X-Ray imaging, showing magnified side view of the leadframe - heat slug interface.



(d) Die to leadframe separation, derived from cross sectioning.

Note: All dimensions are in millimetres (mm), unless otherwise specified.

Figure 3.24 160-lead PQFP component geometry, package design III.

*Die attach layer.* In Figure 3.25(b), colour contrast in the imaged die/paddle and die/heat slug interfaces for package design I and III respectively, reveals extensive delamination of the die attach layers. Although the loss of signal (red coloured regions) in sample G's imaged interface only appears pixelated underneath the die, Figure 3.25(b,i), the expert's interpretation was that the delamination affected the entire die surface area in both samples. Note that the dark coloured region at the top right-hand side corner of sample C's die region in Figure 3.25(b,ii), results from the same scratch on the package external surface, that distorted the SAM image of the die top surface in Figure 3.25(a,ii).

The SAM images obtained using a different equipment for package design I, samples (A,G,H) in Figure A.5, although of poorer resolution, also show delamination of the die attach layers over the full area of the dies. The delamination patterns at the die corners of sample G in Figure A.5(b) match those obtained for this sample in Figure 3.25(b,i).

Subsequent cross sectioning revealed that the delamination was located at the die attach/paddle and die attach/heat slug interface in package designs I and III respectively, along which a continuous air gap of on order 2 to 3  $\mu\text{m}$  thickness was measured, Figure 3.26.

Die attach delamination in the samples mounted on the populated board, is suspected to have occurred during component-to-board assembly. Whereas the components on the SEMI boards were assembled using a standard convective reflow process, a manual soldering process was used for the populated board. The latter process subjected the package parts to elevated temperatures (over 200°C) for a considerably longer period than in a standard reflow process.

Consequently, considerable thermo-mechanical stress would have been induced in the packages due to differential thermal expansion of the materials adjacent to the die-metal interface, whose CTEs are on order 3 ppm/°C, 17 ppm/°C and 22 ppm/°C for the die, paddle and heat slug materials respectively. Differential thermal expansion between mating materials is a well-documented source of interfacial delamination in IC packages, studied by for example [216]. CTE mismatch is amplified by thermal shock and cycling during soldering [217]. Matijasevic et al. [218] described the resulting mechanisms of thermal expansion induced stress within a typical die-die attach-paddle structure, which can overcome the adhesive bond between the die and paddle, thereby resulting in delamination.

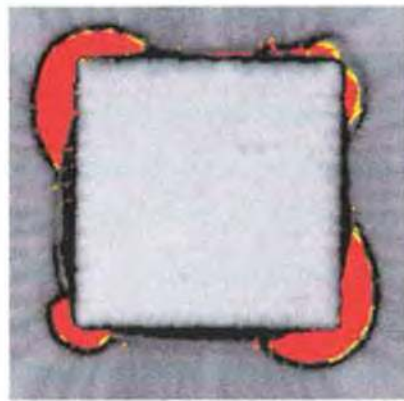
A contributing factor to the delamination could have been the possible presence of ingressed moisture, trapped at the die/paddle or die/heat slug interface. Epoxy, used in IC encapsulants and die attach adhesives, is hygroscopic and absorbs water when exposed to humidity [219]. During soldering, the absorbed water turns into steam which can build up considerable vapour pressure, driving the interface towards delamination. This mechanism is referred to as "pop-corning" [10,219,220]. The relative contributions of each

mechanism, namely differential thermal expansion and vapour expansion pressure, are however not known in this instance.

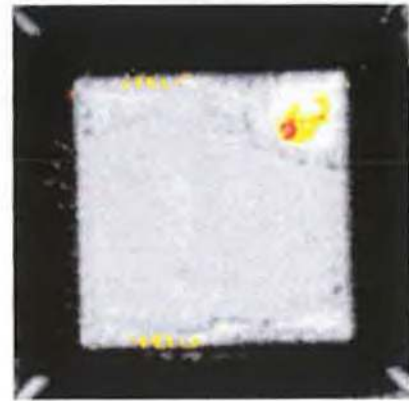
Chowdhury et al. [221] studied experimentally the impact of die attach delamination on the PowerQuad2's thermal performance for varying degrees of moisture ingress which resulted in different extents of delamination. For the same thermal test die and die attach material as used in the present components, Chowdhury et al. measured an air gap thickness of 2 to 3  $\mu\text{m}$  when the delamination extended over the entire die attach/heat slug interface, Figure 3.27(a). This agrees remarkably well with the delamination thickness measured in this study, Figure 3.26. The associated increase in component junction-to-ambient thermal resistance they measured,  $1.4^\circ\text{C}/\text{W}$ , was found to be independent of convective environment, Figure 3.27(b), as observed in Section 3.3.3.3. Not surprisingly therefore, this magnitude is in line with that observed from the characterisation data presented in Section 3.3.3.3.

From discussion with the component vendor, Analog Devices, die attach delamination was a defect extremely common if not generalised for the PowerQuad2 package in the early to mid 1990's, which was still an emerging packaging solution. The samples used in this study were PowerQuad2 prototypes for the packaging of ICs manufactured by Analog Devices in 1992. As this defect was generally not found to impact on device functionality, unless cracking of the resin or die surface delamination occurred, pulling off the bond wires, it was deemed acceptable at the time. Subsequent research identified the mechanisms causing die attach delamination, as summarised above. As a corrective action in regard to hygro-thermomechanical stress damage, a JEDEC standard was established in the early 1990's to control the moisture exposure of electronic assemblies. Subsequently, temperature cycle testing became one of the most important reliability tests for plastic encapsulated IC assemblies to screen for delamination defects. Die attach delamination defects in the PowerQuad2 package were subsequently reduced by the development of a delamination resistant moulding compound, exhibiting both improved moisture resistance and suitable elastic properties, as well as the use of dry-pack conditions prior to component assembly onto PCBs [222]. Such defects are no more tolerated in IC packages.

*Paddle-heat slug interface, package design I.* X-Ray imaging from the package side, Figure 3.22(c), highlights the presence of a continuous film of seeped resin at this interface. Its thickness was determined at on order 15 to 19  $\mu\text{m}$  across the interface. Resin seepage is not uncommon in PQFP packages containing a heat slug, as this part is not mechanically or chemically bonded to the paddle, but instead manually inserted into the mould cavity [211]. The moulding pressure can therefore cause the resin to seep between the paddle and heat slug during the IC encapsulation process.



(i) Package design I

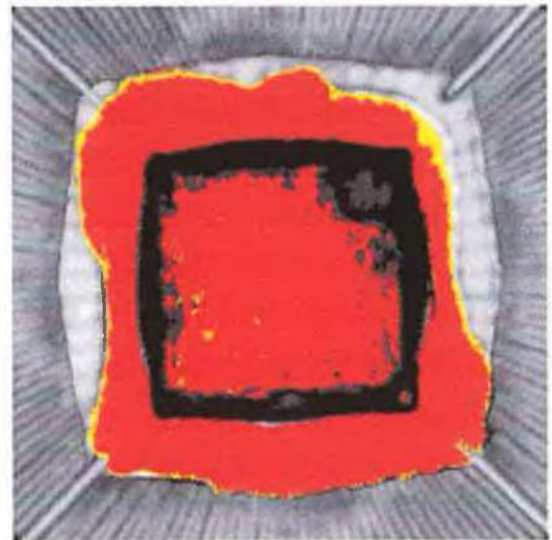


(ii) Package design III

(a) SAM imaging of the die top - moulding compound interface



(i) Package design I, die-paddle interface

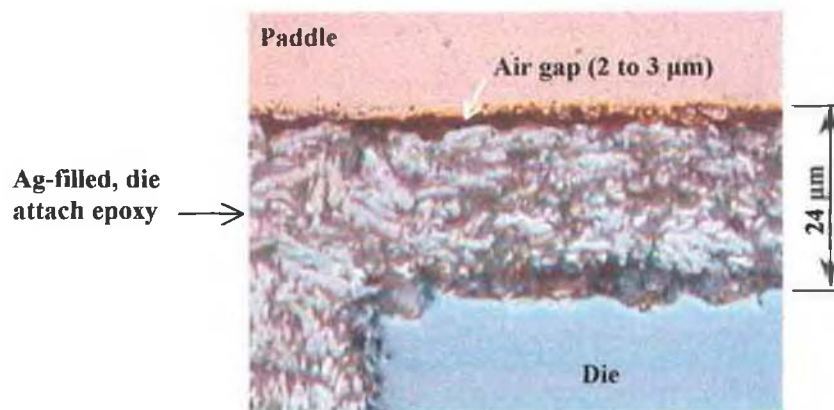


(ii) Package design III, die-heat slug interface

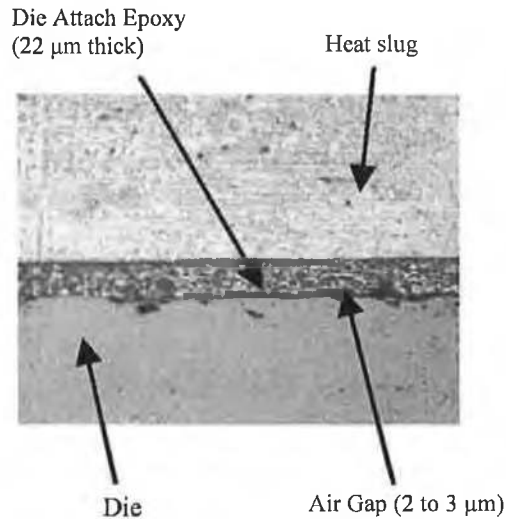
(b) SAM imaging of the die attach layer

**Note:** Images for package designs I and III were taken from components G and C respectively. Red coloured regions indicate delamination.

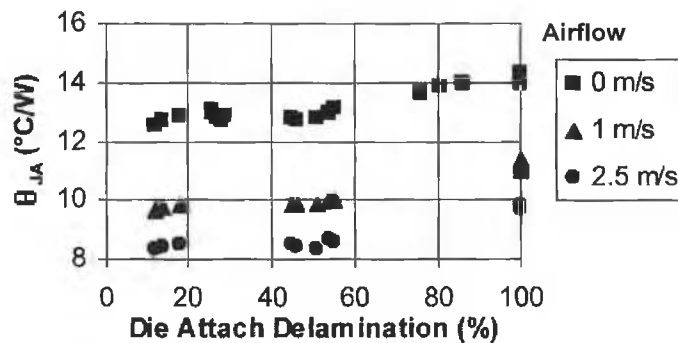
**Figure 3.25** Scanning Acoustic Microscopy (SAM) analysis for the 160-lead PQFP component geometry.



**Figure 3.26** Magnified view of the die - paddle interface for package design I, showing delamination.



(a) Typical micrograph of a cross sectioned sample, showing delamination at the die attach/heat slug interface



(b) Junction-to-ambient thermal resistance as a function of percentage of die attach delamination

**Figure 3.27** Impact of measured die attach delamination on component thermal resistance for a 208-lead PowerQuad2 package [221].

The above analyses provide accurate geometric detail for component numerical modelling. The source of increased thermal resistance in the packages mounted on the populated board was identified. The similarity of package designs II and III's junction-to-package top temperature drop, 5.0°C and 4.9°C respectively, reflects die attach delamination from the heat slug surface. For package design III, the presence of seeped resin between the paddle and heat slug contributes to an additional thermal resistance, resulting in a total junction-to-package top temperature drop of on order 6.1°C.

The component numerical models described in Chapter 4 are constructed based on the foregoing findings. As will be shown, the interfacial resistances identified do not undermine the benchmark data as they can be accurately accounted for in the numerical models.

### 3.3.5 Experimental Airflow Visualisation

The thermal characterisation data presented in Section 3.3.3.3 is augmented by experimental visualisations of the forced-air flows over the populated boards, performed in this study using two complimentary techniques, consisting of smoke-flow and a novel paint-film evaporation method. Airflow visualisations performed over the SEMI PCB using a paint-flow method by Lohan et al. [223], are also presented.

These analyses will serve to (i) demonstrate how two complimentary flow visualisation techniques can easily be applied to visualise forced airflows over PCBs; (ii) highlight the relationship between flow phenomena, PCB topology and convective heat transfer; and in doing so, (iii) propose that flow visualisation be considered as a valuable tool in the early design stage to both guide designers towards the selection of an appropriate flow modelling strategy, and enable cautious interpretation of the temperature predictions in PCB regions exposed to complex flows.

While it is recognised that detailed fluid flow and heat transfer measurements provide a more accurate assessment of the flow phenomena than qualitative methods, such measurements generally require access to expensive and specialised equipment more suited to the research environment, and their use may only act to prolong the design cycle. As will be demonstrated in Chapter 7, qualitative flow measurements were sufficient to link temperature prediction errors with corresponding flow field predictions in this study. While water flows offer better resolution of the primary flow features than air [59,68], the present flow visualisations were performed using airflows due to the availability of wind tunnels and the lower cost involved.

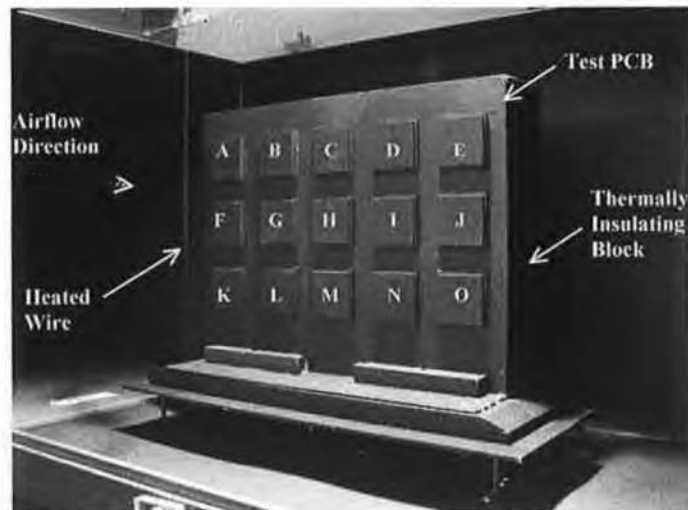
#### 3.3.5.1 Experimental Methods

The literature abounds in flow visualisation methods and their application to a very large range of situations, and Azar and Rodgers [59] summarise those most applicable for visualising airflows in electronic systems. Flow visualisation methods can be grouped into two categories; those suited to investigate the complexity of the streamlines just above a surface, or those suited to characterise the surface heat transfer properties. These analyses combined, can provide a detailed description of the flow phenomena and their effects on the heat transfer processes.

Flow visualisation was carried on the populated board, for Stages 1, 2 and 3. Nylon flatpacks were used to represent the functional components thermally characterised by Lohan and Davies [106] for flow visualisation purposes.

***Smoke-Flow Visualisation.*** The flow streamlines over the test PCBs were visualised using the smoke-wire technique [58,68,164]. Smoke was introduced into the flow using a

0.18 mm diameter, heated nichrome wire, placed upstream of the PCB's leading edge and flush with its surface, as illustrated in Figure 3.28. This wire had a resistance of 19 Ohm/m and a 10V power pulse was used to combust tiny oil droplets on the wire to give strands of bright white smoke that illuminated the downstream flow fields. The oil used was Dantec's Safex 'Standard' fog fluid [224]. As indicated in Figure 3.28, the PCB was placed centrally and vertically within a wind tunnel having a 300 x 300 mm test section, Figure 3.29, which generated uniform velocities up to 10 m/s. The visualised flows were recorded using a Sony Cybershot digital video camera for free-stream air velocities of 2 and 4 m/s. However, the smoke-flow visualisations performed for 4 m/s were of poor visual quality. This was attributed to the smoke streaks more rapidly diffusing by turbulent mixing at the higher velocity. In addition, the wire Reynolds number, based on wire diameter, was of the order of the critical value quoted by Garimella [68], 40, above which wakes from the smoke-wire can become unsteady. Global flow characteristics, such as boundary layer thickness, regions of flow re-attachment and re-circulation, were however observed. Therefore, all flow visualisations presented here are for 2 m/s.



**Note:** The lettering A to O identifies component location.

**Figure 3.28** Stage 3 PCB mounted vertically within the wind tunnel test section for smoke-flow visualisation.



**Figure 3.29** Wind tunnel used for paint-film evaporation and smoke-flow visualisation.

**Paint-Film Evaporation.** This method was used to highlight the impact of the flow features visualised using the smoke-wire technique, on the surface heat transfer. Heat transfer rates are indicated by monitoring the rate at which a thin, evenly applied layer or film of paint, initially wet, evaporates from the PCB surface in a forced airflow. The drying of the PCB surface is a mass transfer process. Based on the Reynolds analogy which can be used to relate mass transfer, shear stress and heat transfer for boundary layer flows, regions of high mass transfer would correspond to high heat transfer and shear stress. However multiple stagnation lines exist on populated PCBs resulting from flow separation or re-attachment, and in these regions the Reynolds analogy is not applicable as high heat transfer rates exist, yet shear stress is zero [62]. Therefore, on the assumption that the paint is evenly distributed over the entire PCB surface, the drying sequence should highlight regions of high mass transfer, analogous to high heat transfer rate, which may not necessarily coincide with regions of high shear stress.

The application of this technique is a refinement of that presented by Eveloy et al. [128]. The paint-film applied in this study consists of an ethanol - talc powder mixture, in the approximate ratio 30:1. The use of this mixture enabled a faster drying sequence than with the isopropanol – talc powder mixture used in [128]. Consequently, contrary to [128], the PCB was not pre-heated prior to applying the paint-film to accelerate the evaporation process. Pre-heating could result in non-uniformity of the board surface temperature during board cooling. Such a transient heat transfer process could adversely impact on the adiabatic drying, hence evaporation sequence. Although this factor was not found to be a significant issue in [128], it was eliminated here considering the greater complexity of the PCB topologies and associated flow fields.

As in [128], the PCB was horizontally orientated within the wind tunnel test section to facilitate the application of the paint mixture, but without airflow. Contained within a sealed bottle, the ethanol - talc powder liquid mixture is pressurised by a small hand pump and forced through a nozzle located approximately 250 mm above and downstream of the horizontal PCB surface. Access to the PCB is achieved by removing a window on the wind tunnel test section's top wall, Figure 3.28. As the jet of fine mist emerges it is directed towards the PCB at an angle of 30° and allowed to descend onto the PCB surface. The jet is removed once the entire PCB surface has been wetted. Note that this paint-film is so thin that it only acts to dampen the PCB surface and excess paint build-up or droplets in certain regions should be avoided. At this stage the test section is resealed, airflow applied and the visualisation results are obtained by recording the evaporation process for up to five minutes. The contrast between the dry regions, indicative of high heat transfer, and the wet regions, is enhanced through the use of the talc powder that leaves a grey finish when



dry. The transient evaporation process was recorded using a Sony Cybershot digital video camera. The accuracy of this qualitative method is dependent upon applying a thin, evenly distributed film of paint across the entire surface. As this condition is difficult to achieve, several evaporation sequences of the same PCB topology were visualised and while some variation existed, the images presented here reflect the dominant features always present.

### 3.3.5.2 Visualised Flows

Interpretations of the flow fields visualised about the PCBs are presented, which will be used as supporting qualitative data to provide an insight into instances of numerical component junction temperature prediction errors. The results obtained are presented in order of increasing flow complexity, from the single board mounted components to the insulated Stage 3 PCB. The airflow direction is from left-to-right in all flow visualisation images presented.

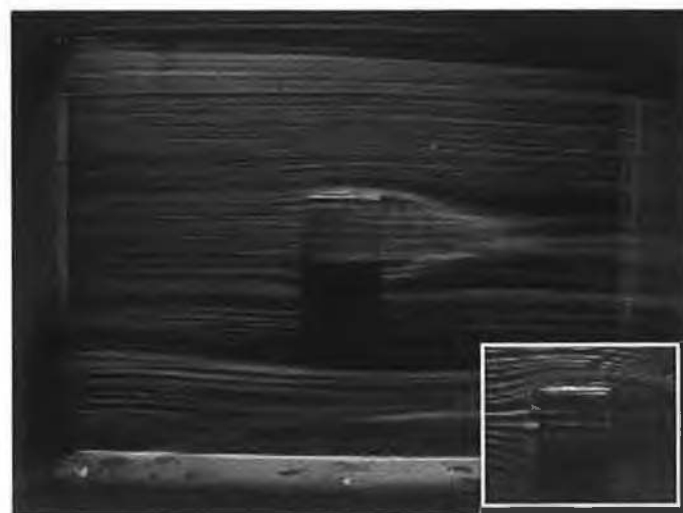
***Stage 1 PCB Topology.*** The smoke-flow and paint-film flow visualisations are presented in Figures 3.30 and 3.31 respectively.

***Smoke-Flow Visualisation.*** In this instance, the smoke was introduced 2 mm upstream of the PCB's leading edge and flush with its front surface. The streamlines in Figure 3.30 display characteristics of steady, laminar flow at all locations on the PCB, except in the vicinity of the component and its downstream wake region. The development of a classic horseshoe vortex, identified by Boyle and Asante [61] and Azar and Russell [84], upstream of the component, and its tails sweeping inwards immediately downstream of the component are identified in the Figure 3.30(a) inset. The impact of the reattaching flow after one component-length downstream of the component's trailing edge is also striking.

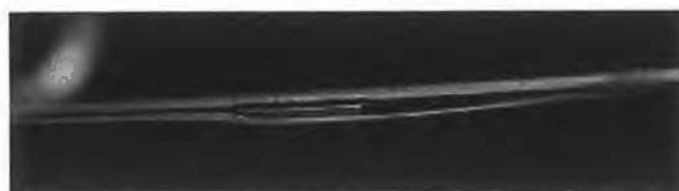
***Paint-Film Evaporation.*** Notable features in the paint-film evaporation sequence presented in Figure 3.31 indicate that, as expected, the highest heat transfer rates exist close to the PCB's leading edge and component top surface, Figure 3.31(a). These high heat transfer rates are revealed as the wet paint-film, represented by the black surface, slowly evaporates from these regions first, leaving a dry, grey surface. The impact of the weaker flows that reattach directly downstream of the component, are also apparent in Figure 3.31(a), but it is clearly shown in Figure 3.31(b) however that the highest heat transfer rates downstream of the component lie at the reattachment point. These observations are reinforced as time elapses in Figures 3.31(b) and 3.31(c), with the paint film completely evaporating after 220 s. The wake region immediately downstream of the component displayed the weakest heat transfer, drying after 210 s.

As highlighted in the description of this technique, the application of a thin, evenly distributed film of paint across the entire board surface is a condition difficult to achieve, which necessitated that several evaporation sequences of the same PCB topology were visualised to identify the dominant features always present. Evidence of a slightly uneven paint-film is shown in Figure 3.31, where the upper right corner of the PCB in Figures 3.31(b) and 3.31(c) remains wetter than the lower right corner. However, repetition of this test showed that both regions dry at the same rate, but in all cases the distinguishing features of the flow about and immediately downstream of the component were always present.

Comparison of the results obtained from both flow visualisation methods in Figures 3.30 and 3.31, highlights how these methods complement each other. Each method helps to identify important features of both the flow phenomena and the heat transfer, and when combined they can form a clear impression of the flow condition.



(a) PCB front view (inset also at 2 m/s)



(b) PCB plan view inclined at 4° to horizontal

**Note:** Smoke introduced 2 mm upstream and flush with the PCB surface.

**Figure 3.30** Smoke-flow visualisation over the Stage 1 PCB at 2 m/s.



(a) Degree of evaporation after 50 s



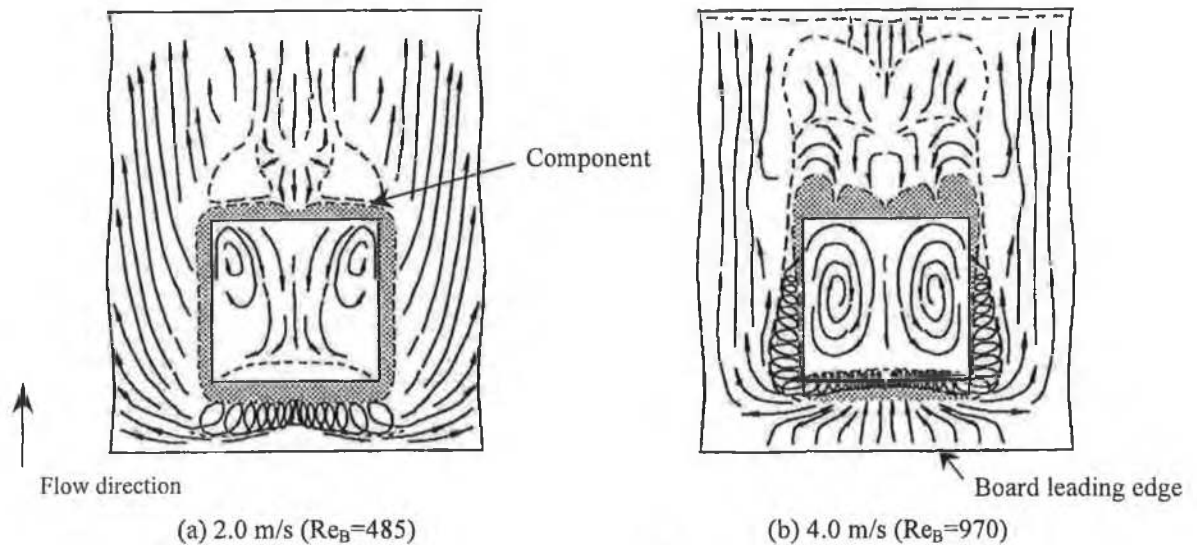
(b) Degree of evaporation after 105 s


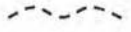


(c) Degree of evaporation after 220 s

**Figure 3.31** Paint-film evaporation sequence from the Stage 1 PCB at 2 m/s using an ethanol paint film.

**SEMI PCB.** Lohan et al. [223] present a series sketches, derived from dried oil-streak patterns created by forced airflows of velocity of 2 to 4 m/s over the single board-mounted component. These sketches, presented in Figure 3.32, outline the sensitivity of the flow phenomena to the free-stream velocity over the range of airflows considered. Despite the fact that the Reynolds number, based on the component height (B), does not exceed 970, significant flow disturbance was evident about the component as illustrated in Figure 3.32.



**Note:** Powder deposits,  . Local flow boundary,  .  
 $Re_B$  represents the Reynolds number, based on the component height, B.

**Figure 3.32** Interpretations of oil-streak patterns on the SEMI standard PCB, obtained in 2 and 4 m/s airflows [223].

**Stage 2 PCB Topology.** Discussion is confined to the smoke-flow visualisations, presented in Figure 3.33, to highlight the impact of aerodynamic disturbance generated by the leading edge components (A,F,K), upstream of component H.

*Smoke-Flow Visualisation.* Figure 3.33 shows that the complexity of the flow field increased significantly from that shown for the single-component PCB in Figure 3.30(a). In Figure 3.33(a), the flow field over the majority of the PCB is dominated by two features that emanate from each component on the leading edge: the reattachment of the flow over the component top surface and its interaction with the tails of the horseshoe vortex that flow around each component. Resulting from their closer proximity to the PCB's leading edge, shorter reattachment lengths are recorded for the leading edge components, in Figure 3.33(a) than for component H in Figure 3.30(a). This is clearly evident when Figure 3.33(b) is compared with Figure 3.30(b).



(a) Front view



(b) Plan view with smoke flow over component A

Note: Smoke introduced 4 mm upstream and flush with the PCB surface

**Figure 3.33** Smoke-flow visualisation over the non-insulated Stage 2 PCB at 2 m/s.

**Stage 3 PCB Topology.** The smoke-flow visualisations and paint-film evaporation results are presented in Figures 3.34-3.35 and 3.36 respectively.

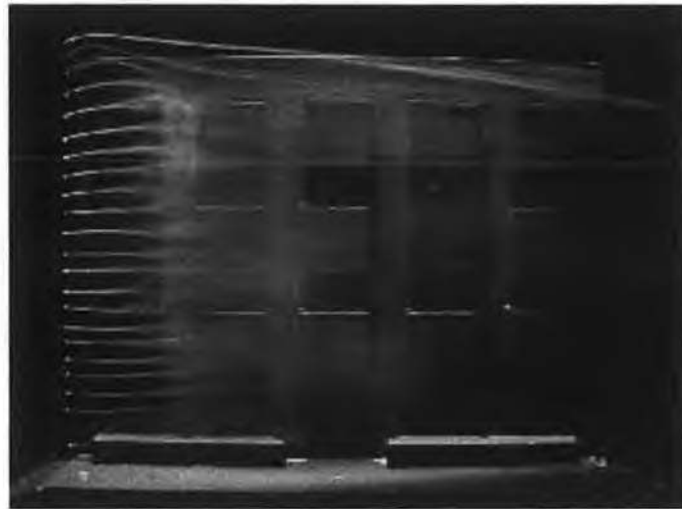
*Smoke-Flow Visualisation, non-insulated PCB.* In Figure 3.34, the smoke-flow patterns at the PCB leading edge reveal similar flow features to those for the Stage 2 configuration, Figure 3.33. The tightly packed streamlines tend to flow closely to the component-PCB surfaces near the leading edge. This is particularly evident both in the regions between the components, and for the streamlines that impact close to the front face corners of the leading edge components and sweep inwards over their top surface as they flow downstream.



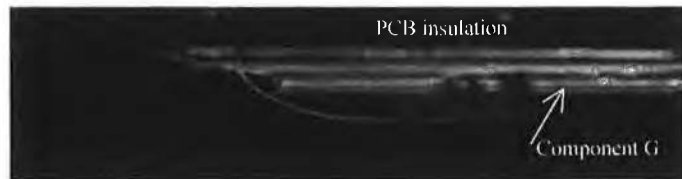
**Note:** Smoke introduced 4 mm upstream and flush with the PCB surface.

**Figure 3.34** Smoke-flow visualisation over the non-insulated Stage 3 PCB at 2 m/s.

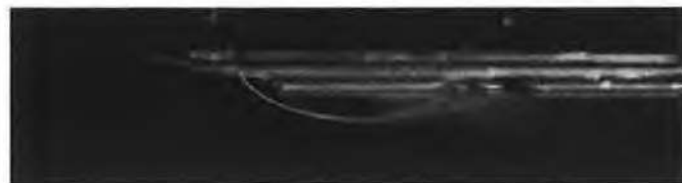
Insulated PCB. For the same wire position in the insulated case, Figure 3.35(a), the leading edge streamlines no longer follow the component-PCB contours. Instead, the flow field is now dominated by a strong reattaching flow that sweeps inwards from the PCBs left-hand-side leading edge corner, and the mainstream flow that reattaches in a region just downstream of the leading row components A,F,K. The magnitude of the separation zone beneath this reattaching mainstream flow is best viewed in plan view, with Figures 3.35(b) and 3.35(c) showing the flow over the central F component. This clearly shows a larger separation zone than that generated by the non-insulated PCB. The extent of this separation zone over component A was similar. Since the impact angle of the re-attaching flow is much greater for the insulated PCB in Figures 3.35(b) and 3.35(c) than in the non-insulated case, it is not surprising that the smoke streak lines break down much more in Figure 3.35(a) than in Figure 3.34, indicating a higher degree of flow mixing and turbulence downstream of the leading row. Inspection of a single streamline over the central F component in Figures 3.35(b) and 3.35(c) highlights the unsteady nature of this separating/reattaching flow. As both these images were taken from the same image sequence, but 230 ms apart, it is obvious that the location of the re-attachment point varies, indicating unsteady flow characteristics. Analysis of many such image sequences revealed that this flow phenomenon was non-periodic and fluctuated randomly at frequencies between 3 and 9 Hertz. It was concluded therefore that localised characteristics of the flow over the insulated PCB were unsteady, and that the strong re-attachment zone immediately downstream of the leading row components could pose problems for modelling heat transfer in this region.



(a) Front view



(b) Plan view – still 1

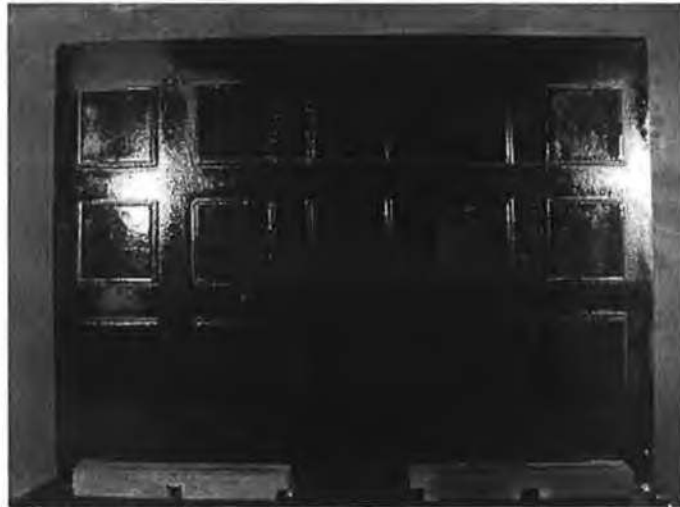


(c) Plan view – still 2

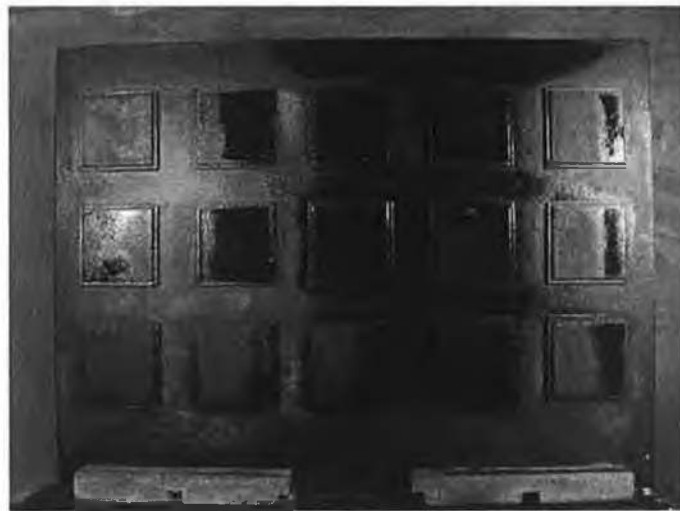
**Note:** Time lapse between stills 1 and 2 is approximately 230 ms. Smoke introduced 4 mm upstream and flush with the PCB surface, and in plan view, aligned with the central stream-wise axis of component F.

**Figure 3.35** Experimentally visualised flow field on the insulated Stage 3 PCB at 2 m/s.

*Paint-Film Evaporation.* To highlight the impact of the smoke-flow patterns presented for the insulated PCB in Figure 3.35, an impression of the heat transfer characteristics associated with this flow was obtained using the paint-film evaporation technique in Figure 3.36. The impact of the vortices that sweep inwards over the PCB from the leading edge, left corner is evident in Figure 3.36(a), as the paint-film begins to dry first at this point. Figure 3.36(b) highlights the impact of the separation and reattachment zones downstream of the leading edge. Note in Figure 3.36(b) that the heat transfer rate is less over the leading edge of component F, signifying the impact of the separation zone identified in Figure 3.36(b), and that the trailing edge of the first row components and the leading edge of the second row components begin to dry first, signifying the higher heat transfer associated with the reattaching flow in this region.



(a) Evaporation status after 15 seconds



(b) Evaporation status after 35 seconds



(c) Evaporation status after 60 seconds

**Note:** The bright regions in (a) represent reflections from the overhead lighting.

**Figure 3.36** Paint-film evaporation from the insulated Stage 3 PCB at 2 m/s using Ethanol.



From an inspection of the smoke-flow images in Figure 3.30 and 3.36, it is clear that there is a significant increase in the flow complexity as a result of the combined effects of including more components on the PCB and also by including system level effects, generated in this case using the insulating block on the PCB non-component side. It must also be concluded, however, that these system level effects generated the greatest level of flow disturbance and should therefore not be ignored when either experimental or numerical studies are undertaken.

The application of two complimentary flow visualisation techniques to help identify the complex flow phenomena that develop over forced air-cooled PCBs was demonstrated. Combined and individually, the flow visualisation methods enabled the location of aerodynamically sensitive regions on the boards to be identified. Characteristics of the visualised flows were highlighted that may pose significant challenge for the prediction of component heat transfer using CFD analysis. These analyses will also be used to help explain instances of numerical prediction errors in Chapter 7.

### **3.4 Transient Component Heat Transfer Configurations**

The test configurations are based on the PQFP 160's package design II, Figure 3.7, mounted on the SEMI standard PCB, Figure 3.9. The characterisation of this test vehicle for steady-state heat transfer was described in Section 3.3.3. Davies et al. [115] and Lohan and Davies [77] studied the test assembly's transient thermal response to power- and air temperature cycling conditions in airflows from 0 to 4 m/s, representative of component reliability screening test environments. In addition, the component transient thermal response to a standard convective reflow soldering temperature profile in a 4 m/s airflow, was also measured.

#### **3.4.1 Characterisation Methods**

The dynamic component junction temperature measurements are reported in Davies et al. [115] for free convection, and Lohan and Davies [77] for forced convection. The measured free convection component transient response considered in this study was not presented by Davies et al., who only report the corresponding steady-state thermal resistance.

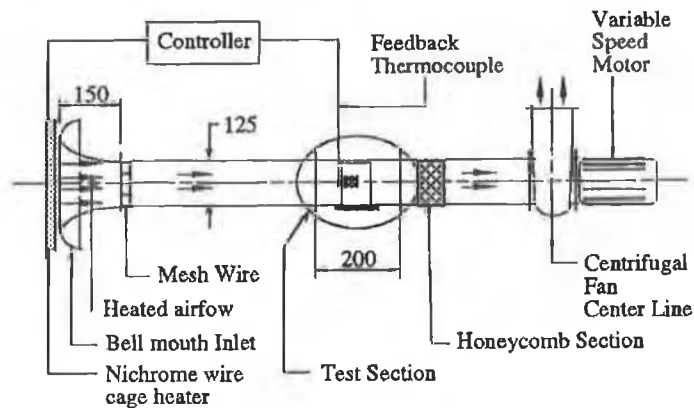
Free convection characterisation was performed in a still-air enclosure described in Section 3.3.3.1. Forced convection characterisation was performed in a variable speed heated wind tunnel capable of producing air temperature ramp rates of 60°C/min over the temperature range 20 to 170°C. As shown in Figure 3.37, the PCB assembly was vertically mounted at the centre of the wind tunnel test section, which had cross-sectional dimensions

of 125 x 125 mm and length 200 mm. The velocity profile measured upstream of the PCB's leading edge had a variation less than 3% over 80% of the profile for the velocity range under analysis, 1 to 4 m/s, independently of ambient air temperature. Corresponding air temperature profiles were uniform to within  $\pm 3\%$  for the temperature range under analysis, 20 to 200°C. Air temperature control to an accuracy of 2°C was achieved using a programmable controller and feedback thermocouple located beside the test assembly in the test section. Turbulence intensity measurements made by hot wire anemometry yielded an average value of 2% for the velocity range of interest.

Junction temperature, component power dissipation and airflow velocity measurements were made using the same instrumentation and to the same accuracy as for steady-state characterisation of the SEMI PCB (Section 3.3.3.1). The component transient thermal response was recorded using a standard high-speed data acquisition system.

For the reflow temperature profile, junction temperature could not be measured as a result of the solder joints reflowing at elevated temperatures. Consequently, component and board surface temperatures were only recorded using Type-T thin-film thermocouples, accurate to within  $\pm 1^\circ\text{C}$  and having 10 ms response time. Davies et al. [115] present two temperature measurements, taken on one component span-wise lead shoulder and on the board surface, centrally located beneath the encapsulant body.

The transient operating conditions used to simulate reliability screening environments are given in Tables 3.14 to 3.16. For Tests I and II, the component is operated with a continuous pulse of 3W power dissipation at a fixed ambient air temperature. Tests III to VIII correspond to passive component operation in dynamic ambient air temperature conditions. Tests IX and X combine 3W dynamic power dissipation and dynamic ambient air temperature conditions. The convective reflow soldering temperature profile is given in Table 3.17. The power- and air temperature cycling boundary conditions form well-defined Neumann- and Dirichlet type boundary conditions respectively for numerical modelling.



**Figure 3.37** Variable speed heated wind tunnel [77].

**Table 3.14** Component dynamic power dissipation in fixed ambient conditions.

<i>Test case</i>	<i>Convecting environment</i>	<i>Duration of power-on from start of test (s)</i>
I	Free	1000
II	Forced, 1 m/s	247.5

Note: Ambient air temperature = 20°C. Component power dissipation = 3W.

**Table 3.15** Passive component operation in dynamic ambient air temperature conditions.

<i>Test case</i>	<i>Free-stream air velocity (m/s)</i>	<i>Ramp rate (°C/min)</i>	<i>Dwell time (s)</i>
III	1.0	15	300
IV	1.0	25	300
V	2.25	5	60
VI	2.25	15	60
VII	2.25	25	60
VIII	4.0	15	120

Note: Ramp rate refers to rate of change of ambient air temperature from 30°C to 110°C. Dwell time refers to duration at maximum ambient air temperature.

**Table 3.16** Combined component dynamic power dissipation in varying ambient air temperature conditions.

<i>Test case</i>	<i>Free-stream air velocity (m/s)</i>	<i>Ramp rate (°C/min)</i>	<i>Dwell time (s)</i>	<i>Duration of power-on from start of test (s)</i>
IX	1.0	15	60	180
X	2.25	15	60	180

Note: Ramp rate refers to rate of change of ambient air temperature from 30°C to 110°C. Dwell time refers to duration at maximum ambient air temperature. Component power dissipation = 3W.

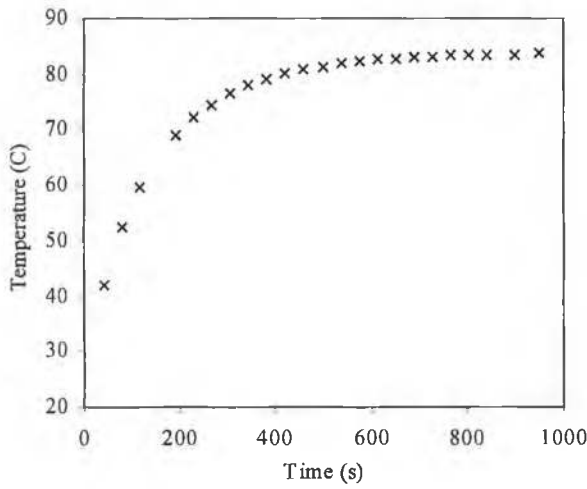
**Table 3.17** Typical convective solder reflow thermal profile in a 4 m/s airflow.

<i>Time (s)</i>	0 - 200	200 - 240	240 - 310	310 - 550	550 - 800
<i>Ramp Rate (°C/min)</i>	+40	0	+40	-40	0

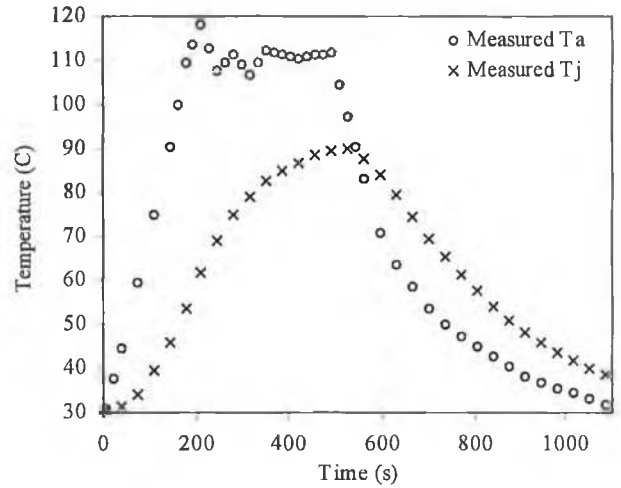
### 3.4.2 Characterisation Data

The component junction temperature measurements for component dynamic power dissipation in fixed ambient conditions, Tests I and II, are presented in Figures 3.38 and 3.39 respectively. Component junction and ambient air temperature measurements for passive component operation in dynamic ambient conditions, Tests III to VIII, are presented in Figures 3.40 to 3.45. Corresponding measurements for combined component dynamic power dissipation in varying ambient conditions, Tests IX and X, are given in Figures 3.46 and 3.47 respectively. The component transient response to the convective solder thermal profile is given in Figure 3.48.

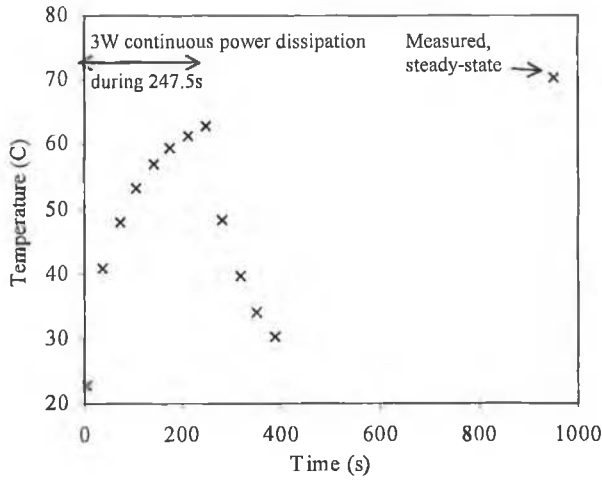
For tests involving air temperature cycling, the measured temperature difference between ambient air and component junction in Figures 3.40 to 3.45 is due to the thermal capacitance of the test assembly.



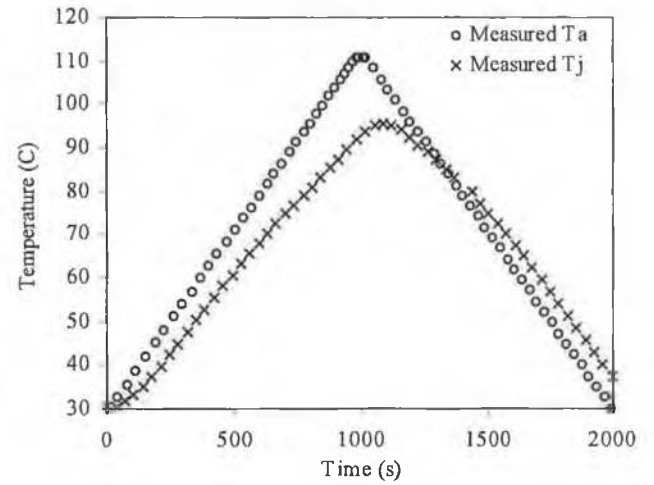
**Figure 3.38** Measured transient component junction temperature rise for a continuous power dissipation of 3W in a quiescent air at 20°C, Test I.



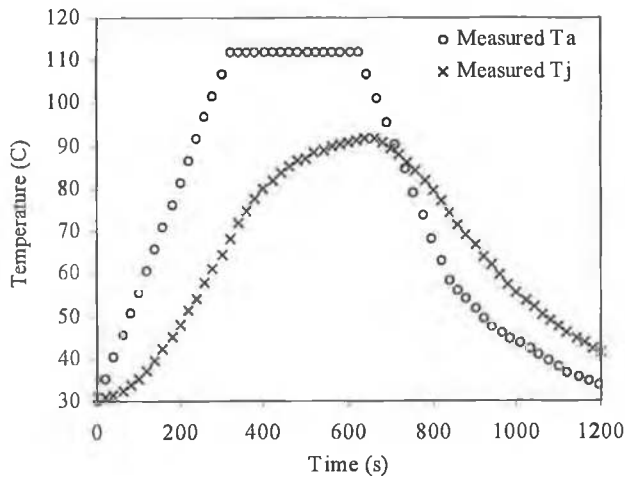
**Figure 3.41** Measured passive component junction temperature in dynamic ambient air temperature conditions (25°C/min ramp, 300s dwell time), in a 1 m/s airflow, Test IV.



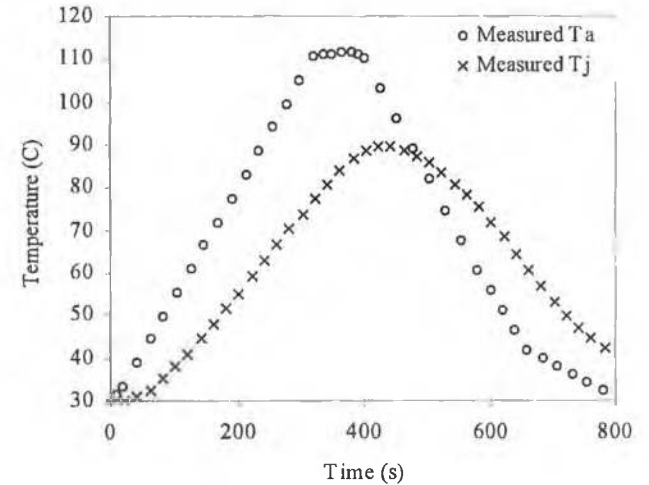
**Figure 3.39** Measured component junction temperature rise for both continuous and pulsed 3W component power dissipation in a 1 m/s airflow at 20°C, Test II.



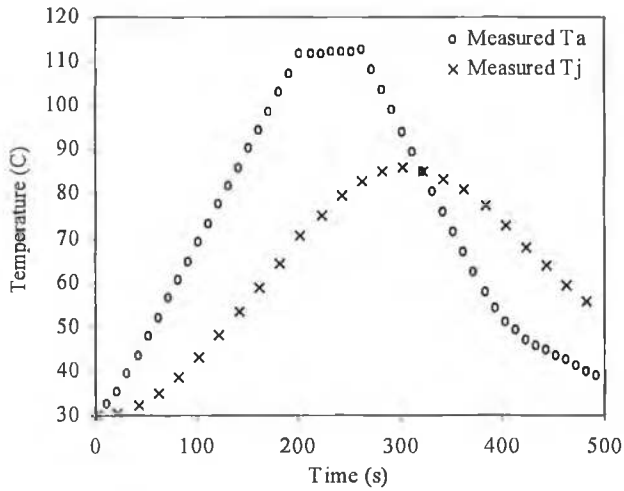
**Figure 3.42** Measured passive component junction temperature in dynamic ambient air temperature conditions (5°C/min ramp, 60s dwell time), in a 2.25 m/s airflow, Test V.



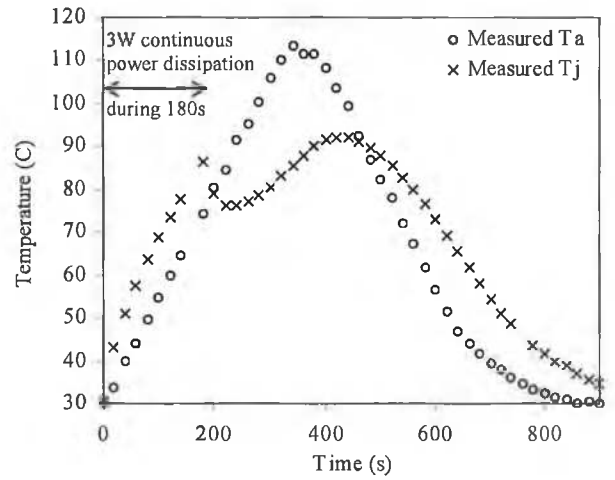
**Figure 3.40** Measured passive component junction temperature in dynamic ambient air temperature conditions (15°C/min ramp, 300s dwell time), in a 1 m/s airflow, Test III.



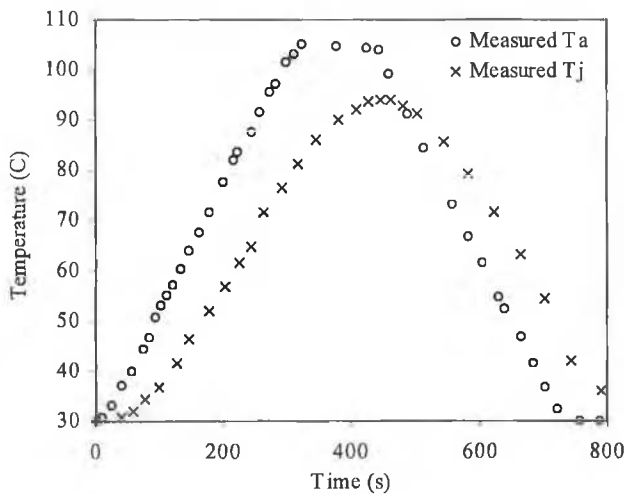
**Figure 3.43** Measured passive component junction temperature in dynamic ambient air temperature conditions (15°C/min ramp, 60s dwell time), in a 2.25 m/s airflow, Test VI.



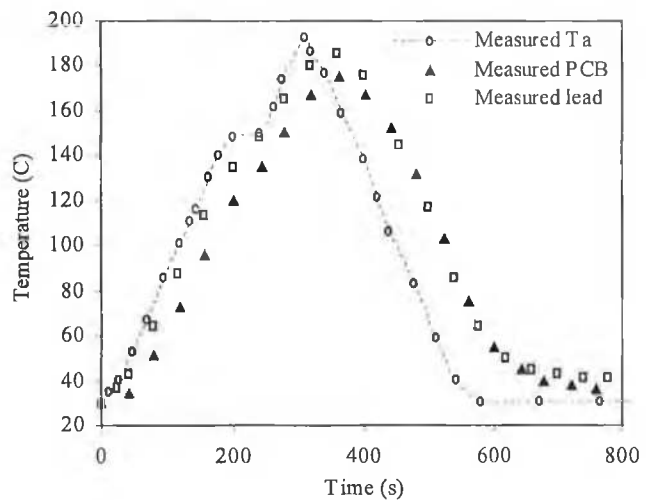
**Figure 3.44** Measured passive component junction temperature in dynamic air temperature conditions (25°C/min ramp, 60s dwell time), in a 2.25 m/s airflow, Test VII.



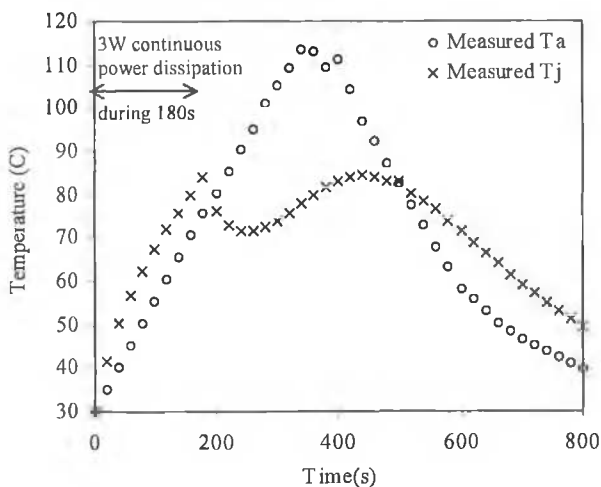
**Figure 3.47** Measured transient component junction temperature rise for a pulsed 3W component power dissipation in dynamic ambient air temperature conditions (15°C/min ramp, 60s dwell time), in a 2.25 m/s airflow, Test X.



**Figure 3.45** Measured passive component junction temperature in dynamic ambient air temperature conditions (15°C/min ramp, 120s dwell time), in a 4 m/s airflow, Test VIII.



**Figure 3.48** Measured passive component junction temperature in dynamic ambient air temperature conditions representative of those in a standard convective reflow soldering process.



**Figure 3.46** Measured transient component junction temperature rise for a pulsed 3W component power dissipation in dynamic ambient air temperature conditions (15°C/min ramp, 60s dwell time), in a 1 m/s airflow, Test IX.

### 3.5 Component Compact Thermal Modelling Test Configurations

This section details the test configurations and benchmark data used to assess the predictive performance of CTMs. The test configurations combine two different package types, 8-lead Small Outline (SO8) and thermally enhanced 208-lead Plastic Quad Flat Pack (PQFP 208), individually mounted on different PCB constructions, which were thermally characterised in a range of convective environments. Both the small package size of the SO8 and its dependence on lead conduction to the PCB combined, amplify the sensitivity of the component operating temperature to the PCB's heat spreading properties. These attributes make the SO8 a suitable choice to assess CTM prediction of component-board thermal interaction. The PQFP 208 serves to assess CTM capability to model the thermal behaviour of complex component architectures.

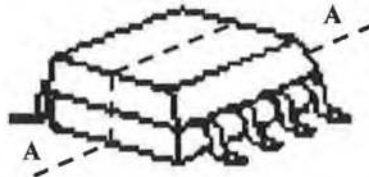
The SO8 and PQFP 208 test vehicles were thermally characterised by Lohan et al. [149,225] and Rodgers et al. [35] respectively, with only the relevant characterisation data presented here to form benchmarks for component compact thermal modelling. This data comprises of component junction temperature and component-board surface temperature measurements, performed using thermal tests dies and infrared thermography respectively.

#### 3.5.1 SO8 Component Configurations

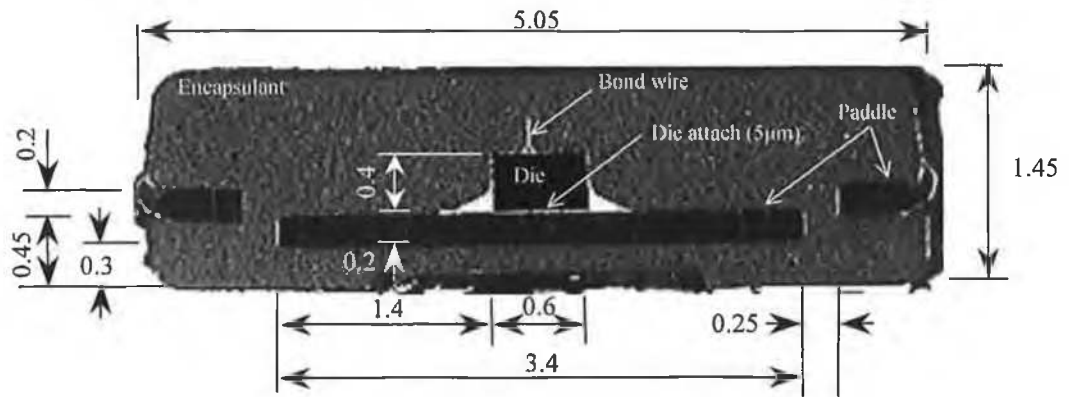
The vendor (Infineon) supplied test component external geometry details are given in Figure A.2. The package internal architecture, shown in Figure 3.49, corresponds to the standard design illustrated in Figure 3.3(a). Component internal geometry was verified using X-Ray imaging, and cross sectioning coupled with high power microscopy for imaging of exposed section planes [149]. All package geometry details were found to conform to vendor nominal data, with the exception of the die attach layer thickness. This parameter was determined at 5  $\mu\text{m}$ , in contrast to the nominal vendor value, 10  $\mu\text{m}$ . The embedded thermal test die layout is given in Figure A.4(b).

This component was mounted on two FR4-based test PCBs, an 1S/0P PCB conforming to JEDEC standard EIA/JESD51-3 [226] and a 2S/2P PCB to EIA/JESD 51-7 [227], as well as a non-standard 1S/1P copper-based IMS, Figure 3.50. These PCB constructions, referred to as FR4 #1, FR4 #2 and IMS respectively, are illustrated in Figure 3.50(b). All test boards had the same surface layout, Figure 3.50(a). For both FR4 #2 and IMS, internal planes were continuous, and had 100% copper coverage.

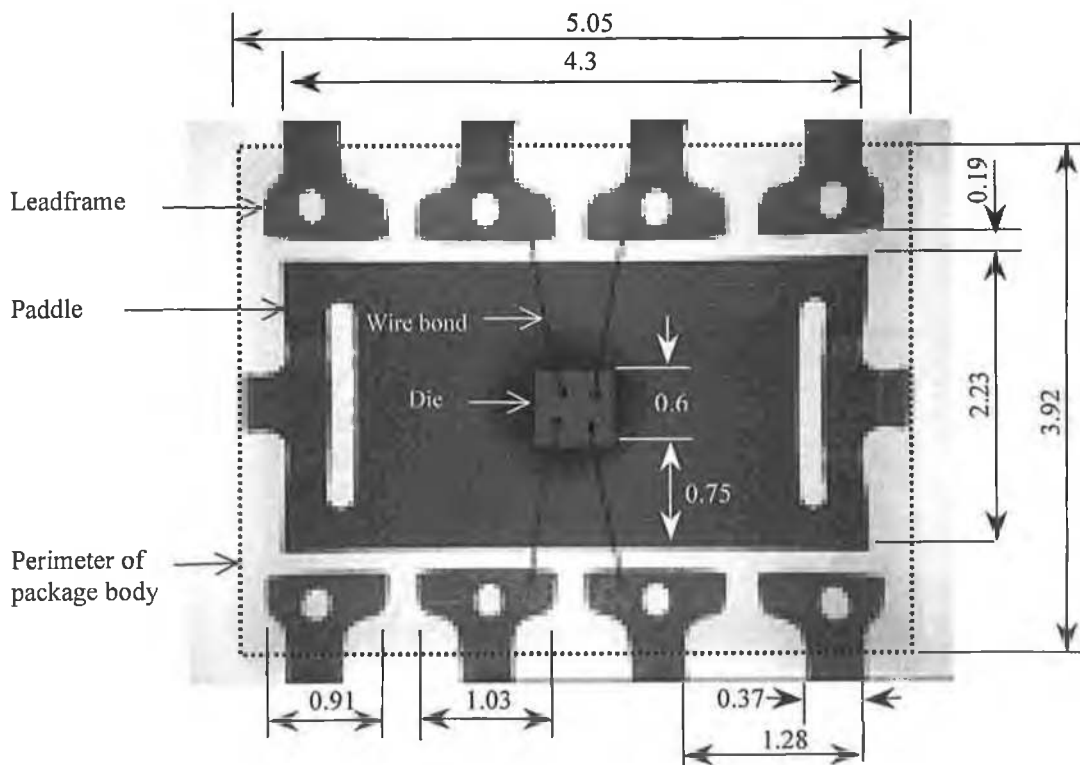
Free convection characterisation was performed in a still-air cubical enclosure of volume 0.02832  $\text{m}^3$ , conforming to JEDEC EIA/JESD51-2 [109]. Forced convection characterisation conformed to JEDEC EIA/JESD51-6 [110], and was undertaken in a wind tunnel having a test section of cross sectional dimensions 300 x 300 mm, for airflows of 1 to 5 m/s.



(a) Package external geometry (5 x 4 mm).



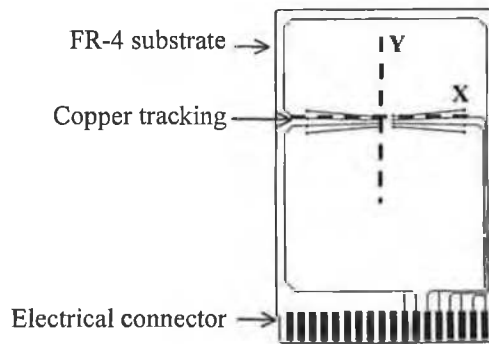
(b) Cross section view taken through package centre axis, Plane A-A, imaged using high-power microscopy.



(c) X-Ray imaging from top view.

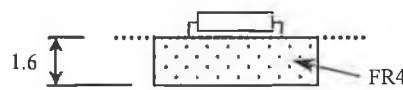
**Note:** All dimensions are in millimetres (mm), unless otherwise specified.

**Figure 3.49** Cross sectional analysis and X-Ray imaging of an SO8 package [149].

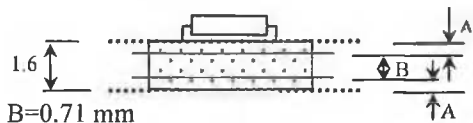


**Note:** X and Y refer to surface temperature profile analysis planes in the stream-wise and span-wise airflow directions respectively.

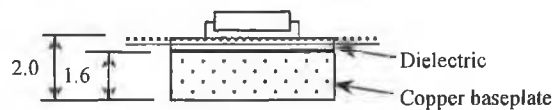
(a) Surface layout



**FR4 #1:** 1S/0P test PCB to EIA/JESD 51-3. Copper signal traces are 70  $\mu\text{m}$  thick.



**FR4 #2:** 2S/2P test PCB to EIA/JESD 51-7. Copper signal traces and internal power planes are 70  $\mu\text{m}$  and 35  $\mu\text{m}$  thick respectively. Power planes have 100% copper coverage.



**IMS:** non-standard 1S/1P test PCB. Copper signal traces and internal power plane are both 70  $\mu\text{m}$  thick. Power plane has 100% copper coverage.

**Note :** Signal-layer (S), ..... ; Power-layer (P), (—).

(b) Internal construction

**Note:** PCB size = 114.3 x 76.2 mm. All dimensions are in millimetres (mm), unless otherwise specified.

**Figure 3.50** SO8 test PCB constructions [149].

The velocity profile upstream of the PCB leading edge, measured using a hot wire anemometer, approximated well to a plug-profile, with less than 3% velocity variation over 80% of the profile. Free-stream turbulence intensity, measured using a hot wire anemometer, was less than 2%.

The thermal test dies used for component junction temperature measurement were calibrated to an accuracy of  $\pm 0.5^\circ\text{C}$  [225].

For infrared surface temperature measurements, the test vehicles were sprayed with a paint having a known emissivity of 0.92. An Agema Thermovision 550 infrared imaging system, operating in the 3.6 to 5  $\mu\text{m}$  spectral range, was used. For this short-wave system, measurement



resolution was approximately 0.45 mm, while spatial temperature resolution was estimated at 1.5 mm. As this lower resolution would result in temperature averaging in regions of localised high spatial temperature gradients, this factor will be taken in consideration when comparing predictions and measurements. The infrared imaging system was calibrated to an accuracy of  $\pm 0.5^\circ\text{C}$  [149]. The infrared measurements used in this study were taken for free convection.

The estimated uncertainties in measured component junction temperature, surface temperature, ambient air temperature, component power dissipation and free-stream air velocity are given in Table 3.18. These estimates are based on an Nth order, single sample uncertainty analysis as described in Appendix B.

Measured component junction temperatures in both free and forced convection are presented in Table 3.19. For free convection characterisation, component-board surface temperature profiles extracted from the corresponding infrared thermographs about the package centre in the direction of package width, are presented in Figure 3.51 as a function of PCB construction. Measured component-PCB surface temperature profiles about the package centre in the direction of package length on FR4#2 PCB are shown in Figure 3.52.

**Table 3.18** Measured quantities and estimated uncertainties for both free and forced convection thermal characterisation of the SO8 component.

<i>Parameter and unit</i>	<i>Nominal value</i>	<i>Uncertainty</i>
$T_i$ ( $^\circ\text{C}$ )	88 - 125	$\pm 0.5$ (1%) to $\pm 0.9$ (1%)
$T_s$ ( $^\circ\text{C}$ )	20 - 105	$\pm 0.5$
$T_{\text{ref}}$ ( $^\circ\text{C}$ )	20	$\pm 0.2$
$Q_{\text{diss}}$ (W)	0.5	$\pm 1 \times 10^{-4}$
$u$ (m/s)	1 - 5	3%

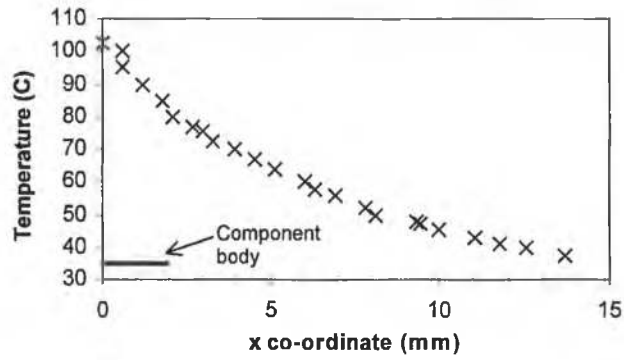
**Note:** Uncertainty in junction temperature is given as both an absolute value ( $^\circ\text{C}$ ), and normalised value (%) in parenthesis ( ). The normalised uncertainty is the ratio of the absolute uncertainty to the measured junction temperature rise above ambient conditions.

**Table 3.19** Measured steady-state component junction temperatures ( $^\circ\text{C}$ ) for a single board-mounted SO8 component in free and forced convection.

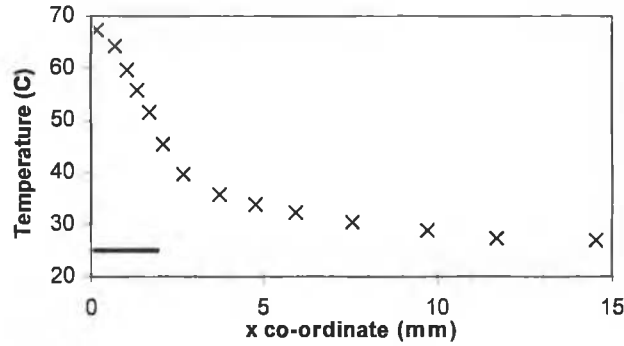
<i>Airflow velocity (m/s)</i>	<i>PCB construction</i>		
	<i>FR-4 #1</i>	<i>FR-4 #2</i>	<i>IMS</i>
0	124.3	84.9	71.5
2	100.2	77.2	67.2
5	88.6	74.3	66.0

**Note:** FR-4 #1, FR-4 #2 and IMS refer to PCB construction, Figure 3.50(b). Measurement uncertainty,  $\pm 1\%$ . Component power dissipation = 0.5 Watts. Ambient air temperature =  $20^\circ\text{C}$ . Percentage error in parenthesis ( ) is calculated based on measured component junction temperature rise above ambient air temperature.

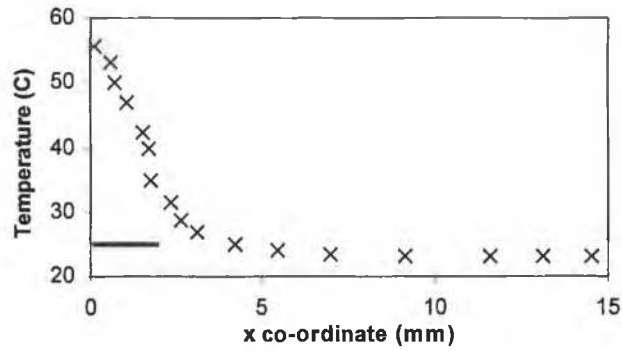
Component junction temperature measurements were found to be reproducible to within  $\pm 1^\circ\text{C}$ . The measurements were undertaken for two component samples for each test PCB. While this is not a sufficient statistical criterion to capture the true stochastic mean, measured differences in junction temperature about the mean between samples were typically within  $\pm 0.5^\circ\text{C}$  (0.7%).



(a) FR4 #1

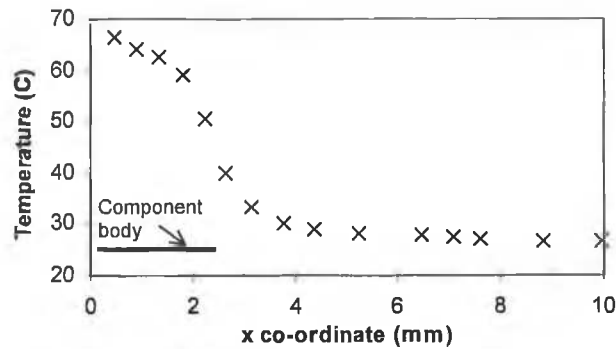


(b) FR4 #2



(c) IMS

Note: Measurement uncertainty,  $\pm 0.5^\circ\text{C}$ . Component power dissipation = 0.5 W. Ambient air temperature =  $20^\circ\text{C}$ . **Figure 3.51** Measured component-PCB surface temperature profiles in the direction of package width for a single SO8 component in natural convection, as a function of PCB construction, Figure 3.50(b).



Note: Measurement uncertainty,  $\pm 0.5^\circ\text{C}$ . Component power dissipation = 0.5 W. Ambient air temperature =  $20^\circ\text{C}$ . **Figure 3.52** Measured component-PCB surface temperature profiles in the direction of package length for a single SO8 component mounted on FR4#2 PCB in natural convection.

### 3.5.2 PQFP 208 Component Configurations

The vendor (ST Microelectronics) supplied package external geometry details for the PQFP 208 test component are given in Figure A.3. Component internal geometry was verified using X-Ray imaging, and cross sectioning coupled with high power microscopy for imaging of exposed section planes [211]. In addition, sample mechanical integrity was qualitatively investigated using SAM at critical interfaces within the package body. The package internal architecture, shown in Figure 3.53, corresponds to the thermally enhanced design in Figure 3.3(b), having an embedded heat slug exposed at the package base. The heat slug is composed of an octagonal section, extending internally into stacked CAT-shaped and square portions, Figure 3.53. The thermal test die layout is given in Figure A.4(c). The FR4 test PCB, conforming to JEDEC standard EIA/JESD51-3 [226], is shown in Figure 3.54.

Forced convection characterisation conformed to SEMI G38-0996 [108], and was undertaken in a wind tunnel having a test section of cross sectional dimensions 200 x 200 mm, for 2 m/s airflow. The quality of the working section airflow was the same as described for characterisation of the SO8.

The thermal test dies used for component junction temperature measurement were calibrated to an accuracy of  $\pm 0.2^\circ\text{C}$ .

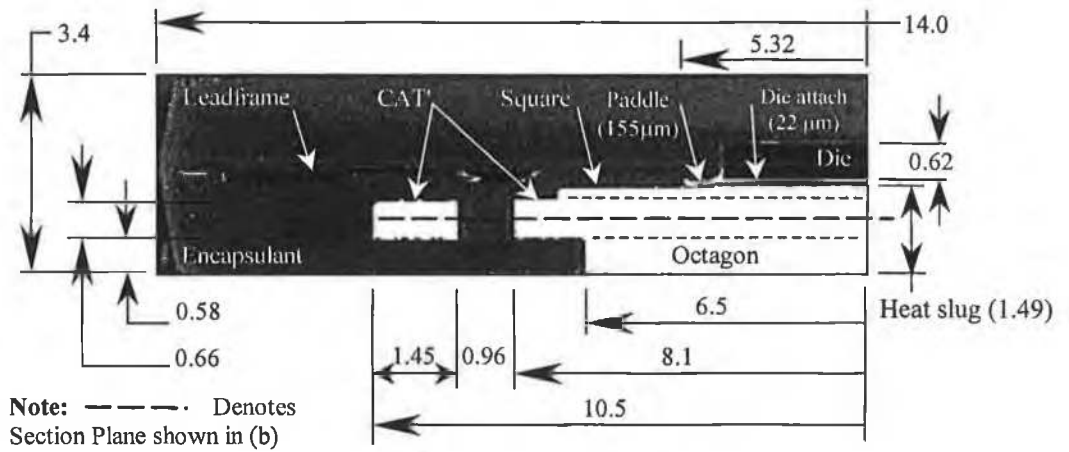
For infrared surface temperature measurements, the test vehicles were sprayed with a paint having a known emissivity of 0.92. The measurements were performed with an Inframetrics Model 760 infrared imaging system, operating in the 8 to 12  $\mu\text{m}$  spectral range. This equipment had a measurement resolution of 100  $\mu\text{m}$  and a spatial temperature resolution of approximately 0.35 mm. The infrared imaging system was calibrated to an accuracy of  $\pm 0.7^\circ\text{C}$ .

The estimated uncertainties in measured component junction temperature, surface temperature, ambient air temperature, component power dissipation and free-stream air velocity are given in Table 3.20. These estimates are based on an Nth order, single sample uncertainty analysis as described in Appendix B.

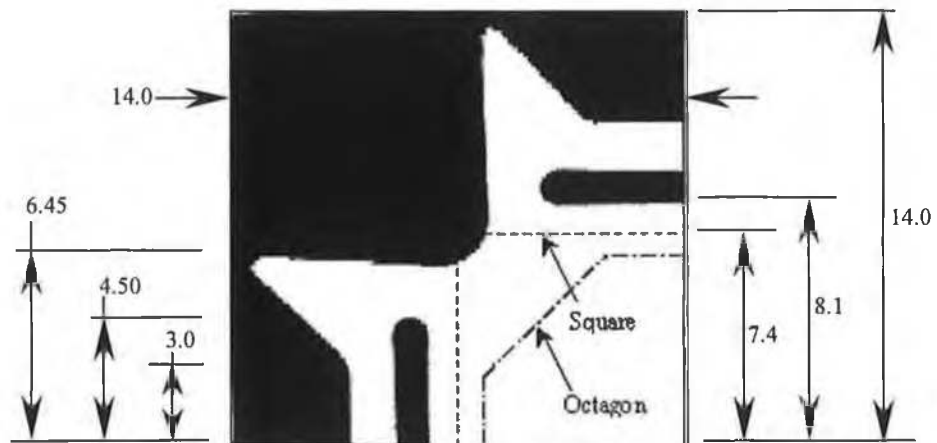
**Table 3.20** Measured quantities and estimated uncertainties for characterisation of the PQFP208 component.

<i>Parameter and unit</i>	<i>Nominal value</i>	<i>Uncertainty</i>
$T_j$ ( $^\circ\text{C}$ )	46-49	$\pm 0.2$ (1.0%)
$T_s$ ( $^\circ\text{C}$ )	46-50	$\pm 0.7$
$T_{ref}$ ( $^\circ\text{C}$ )	20	$\pm 0.2$
$Q_{diss}$ (W)	2	$\pm 1 \times 10^{-4}$
$u$ (m/s)	2	$\pm 0.063$ (3%)

**Note:** Uncertainty is given as both an absolute value, and normalised value (%) in parenthesis ( ). For junction temperature, the normalised uncertainty (%) is the ratio of the absolute uncertainty ( $^\circ\text{C}$ ) to the measured junction temperature rise above ambient conditions. For free-stream velocity, the normalised uncertainty (%) is the ratio of the absolute uncertainty (m/s) to the measured velocity.

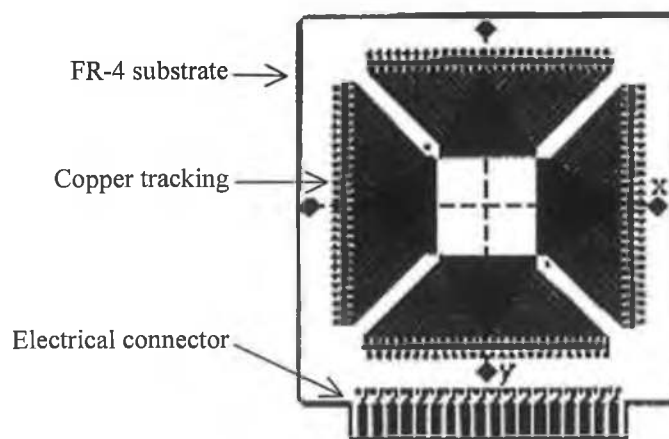


(a) Cross-section view through package centre axis (half geometry)



(b) Plan view of quarter package along section plane defined in (a), showing heat slug detail

Figure 3.53 PQFP 208 component internal architecture [211].



Note: PCB size = 114.3 x 101.6 x 1.6 mm. Copper signal traces are 70 μm thick. X and Y refer to surface temperature profile analysis planes in the stream-wise and span-wise airflow directions respectively.

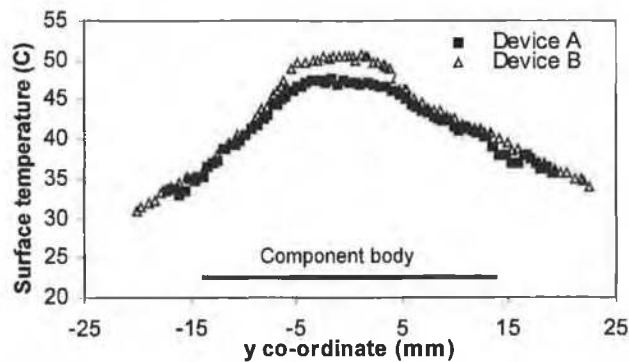
Figure 3.54 PQFP 208 test PCB [35].

Experimental characterisation was undertaken for two component samples. Measured component junction temperatures in a 2 m/s airflow are given in Table 3.21. Component-board surface temperature profiles, extracted from the corresponding infrared thermographs about the package centre in the stream-wise and span-wise airflow directions, are presented in Figure 3.55.

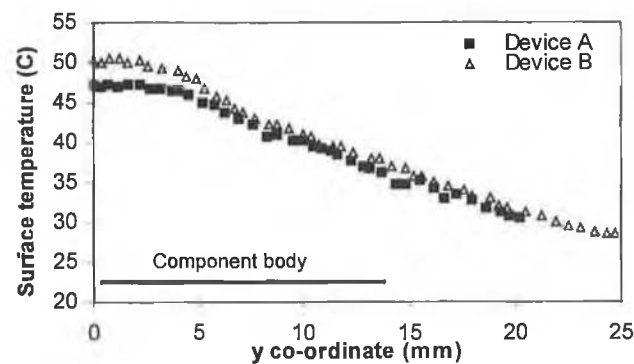
**Table 3.21** Measured component junction temperature for a single board-mounted PQFP 208 in a 2 m/s airflow.

<i>Sample</i>	<i>Measured (°C)</i>
Device A	46.4
Device B	48.4

**Note:** A and B refer to component sample characterised. Measurement uncertainty,  $\pm 0.2^\circ\text{C}$ . Component power dissipation = 2 W. Ambient air temperature =  $20^\circ\text{C}$ .



(a) Temperature profile in the stream-wise direction, Figure 3.54



(b) Temperature profile in the span-wise direction, Figure 3.54

**Note:** Device A and B refer to sample tested. Measurement uncertainty,  $\pm 0.7^\circ\text{C}$ . Component power dissipation = 2 W. Ambient air temperature =  $20^\circ\text{C}$ .

**Figure 3.55** Measured component-PCB surface temperature profiles for a single board-mounted PQFP208 component in a 2 m/s airflow.

The 2°C junction temperature discrepancy between the two PQFP samples tested, Table 3.21, reflected in the surface temperature profiles above the die region in Figure 3.55, was found to essentially result from the presence of a few-micron thick film of resin at the paddle/heat slug interface in Device B [211]. However outside the die region (10 x 10 mm), the magnitude and shape of the measured surface temperature profiles for both samples are in good agreement, indicating that the presence of seeped resin does not alter package internal heat spread and component-board thermal interaction. Resin seepage therefore acts as an interfacial contact thermal resistance. No defect was found at other interfaces. Device A was free of defect, and was therefore considered as a more realistic reference to assess predictive accuracy [35].

### **3.6 Summary**

A range of experimental benchmarks was compiled and presented to assess CFD predictive accuracy for component heat transfer in both application environments, and environments representative of reliability screening and assembly processes.

The suitability of the experimental data to be used as benchmark data was demonstrated.

Bearing in mind that CFD vendors are continually improving code performance, such benchmarks could be re-used to assess the predictive accuracy of future software upgrades, or other CFD codes.

## 4.0 Numerical Models

### 4.1 Introduction

In this chapter, the fluid flow modelling approaches employed in commercially-available Computational Fluid Dynamics (CFD) codes that are of relevance for the analysis of air-cooled electronic component-board heat transfer are briefly reviewed. Candidate turbulent flow models are selected to assess their capability to predict component heat transfer in this study.

Component and Printed Circuit Board (PCB) numerical modelling methodologies are developed for both steady-state and transient heat transfer, and applied to the benchmark test cases described in Chapter 3. While detailed component modelling serves to generate the *à priori* junction temperature predictions, component compact thermal models are also derived to investigate their capability to approximate multi-mode component heat transfer.

### 4.2 Fluid Flow Modelling

The governing conservation equations of fluid dynamics solved by CFD analysis are given in Appendix C. In this section, an overview of the fluid flow modelling strategies currently available in CFD codes dedicated to the thermal analysis of electronic equipment is given. Although in-depth analysis of code calculation strategies and turbulence modelling capabilities is beyond the scope of this thesis, their potential shortcomings for the analysis of component heat transfer are highlighted. Alternative flow modelling strategies available in general-purpose CFD codes are considered which could provide improve predictive accuracy.

As outlined in Chapter 1, the application of eddy viscosity turbulence models is likely to remain the most realistic approach for modelling turbulent heat transfer in electronic equipment for the foreseeable future. In this approach, turbulence is represented as enhanced fluid mixing, by inclusion of a turbulent viscosity in the viscosity terms in the momentum equations, and a turbulent conductivity in the conduction term in the temperature equation. The turbulent flow modelling capabilities of CFD codes dedicated to the analysis of electronics cooling are typically confined to zero-equation mixing length and standard two-equation high-Reynolds number  $k$ - $\epsilon$  differential flow models, used in conjunction with “law-of-the-wall” wall functions. These turbulence models are by far the most widely-used and validated [15], and are considered as computationally viable in a design environment.

In the mixing length model the turbulent viscosity is expressed as a simple algebraic formula, based on the product of a turbulent velocity scale and length scale. Such models

are applicable in flows where the turbulence properties develop in proportion to a mean flow length scale. The more sophisticated  $k$ - $\epsilon$  turbulence model allows for the effects of transport of turbulence properties by convection and diffusion, and for the production and destruction of turbulence. Two partial differential transport equations, for the turbulent kinetic energy ( $k$ ) and the rate of dissipation of turbulent kinetic energy ( $\epsilon$ ), are solved. Both the mixing length and high-Reynolds number  $k$ - $\epsilon$  models are primarily valid for turbulent core flows, and are not applicable in regions close to solid walls where viscous effects predominate over turbulent ones [65,66]. To solve for the turbulent exchange of heat and momentum between solid surfaces and the fluid in the near-wall region, "law-of-the-wall" wall functions are employed. These are based on empirical formulae for wall surface friction and heat transfer, whereby heat and momentum flux are proportionalised through the Reynolds analogy. In this approach, the viscosity-affected inner region, comprising of the viscous sub-layer and buffer layer, is not resolved. Instead, the region between the wall and the fully-turbulent region is bridged, with the wall functions generally requiring the near-wall fluid node to be located outside the viscous sub-layer. This approach eases the necessity for fine gridding in the near-wall region, which would otherwise be required to resolve it using an appropriate turbulence model.

If turbulent fluid flow exists within electronics enclosures, it is usually confined and constrained by many closely spaced solid objects, which thus have the dominant effect in determining flow patterns, pressure drops and temperature distributions. To capture such flow fields, the use of the  $k$ - $\epsilon$  model is generally required, but unfortunately for system level analysis its application is not feasible due to computationally excessive fine grid requirement, necessary to accurately represent the velocity gradients involved and hence estimate turbulent viscosity. Consequently, the mixing length models are typically employed for such analysis. However due to the dominant effect of near-wall turbulence on heat transfer, its representation may be more critical. In such instances the use of zero-equation models could provide reasonable estimates of turbulent viscosity, without introducing dramatic errors into heat transfer predictions, providing that the wall functions are applicable. This hypothesis forms the turbulence modelling strategy employed in dedicated CFD codes.

However, this strategy is not suited to detailed analysis of heat transfer in air-cooled populated PCBs, where fluid flow is usually classified as a low-Reynolds number flow. Turbulence may be generated locally by protruding components, and depending on the local Reynolds number, may decay locally or persist until the next downstream protrusion where it may be enhanced. As turbulence is confined within the shear layers in vicinity of the components, and the overall flow field remains essentially laminar, the standard  $k$ - $\epsilon$



turbulence model is not specific for this type of flow. In addition, for turbulent flow calculations the prediction of heat transfer is extremely sensitive to the wall boundary conditions, hence wall treatment [228]. “Law-of-the-wall” wall functions are justified for boundary layer type flows, but are inadequate for separating, reattaching or recirculating flow conditions where the Reynolds analogy does not hold [67]. Anderson [163] and Behnia et al. [228] have cautioned on this limitation specifically for the analysis of electronic component heat transfer. Furthermore, wall functions become less reliable in situations where low-Reynolds number or near-wall effects are pervasive in the flow domain, and the hypotheses underlying the wall functions cease to be valid [65]. Although more accurate wall treatment for separating or reattaching flow can be obtained using non-equilibrium wall functions [229], as with standard wall functions they are not intended for low-Reynolds number flows.

Despite the limitations of the standard  $k$ - $\epsilon$  turbulence model and wall function approach, vendors of CFD codes dedicated to the analysis of electronics cooling argue that the use of more sophisticated turbulence models is generally not justified for the majority of industrial analyses undertaken with their software. Ignoring computational constraints, advanced models may only offer a small improvement in predictive accuracy, providing that both the exact geometry of the problem and all boundary conditions are known to a high degree of accuracy. As such detailed information is generally not available during the design phase, approximations are required which only enable global flow field and temperature predictions to be obtained. By contrast, standard turbulence models can provide efficient analysis and solution stability on simple grids. However, this view is likely to become soon outdated with increased computational power, which should facilitate the application of more sophisticated turbulence models to electronic system thermal design.

Improved near-wall modelling can be achieved using turbulence models specific for low-Reynolds number, wall-bounded flows, which permit the governing equations to be integrated all the way to the wall. Such models typically make use of damping and correction functions to achieve proper behaviour near the wall [65]. An alternative solution is the two-layer zonal model [230], whereby a one-equation ( $k$ ) turbulence model is applied in the viscosity-affected near-wall region, and either a standard  $k$ - $\epsilon$  or more advanced Renormalization Group (RNG)  $k$ - $\epsilon$  or Realizable  $k$ - $\epsilon$  model is employed in the fully turbulent core region. In both approaches the integration to the wall requires a very fine near-wall grid resolution in the viscous sub-layer.

In contrast to turbulent flows, laminar steady flows can be accurately solved providing that the grid applied is sufficiently fine and that the solvers and discretization techniques are well chosen [22]. Using a laminar flow model, the calculation of the surface heat

transfer does not rely on wall functions as integration is performed all the way to the wall. The calculation of surface heat transfer is therefore not problematic at stagnation points. A no slip wall boundary condition is assumed at the near-wall grid cell, with surface heat transfer being by molecular diffusion. The wall temperature boundary condition is simply linked to the near-wall grid cell by the thermal conductivity of the fluid, such that:

$$q'' = \frac{k_{\text{fluid}}}{\Delta y} (T_w - T_{\text{nw}}) \quad (4.1)$$

where  $q''$  is the heat flux from the wall to the fluid grid cell,  $k_{\text{fluid}}$  is the fluid thermal conductivity,  $\Delta y$  is the distance from the wall to the cell centre,  $T_w$  is the wall temperature, and  $T_{\text{nw}}$  is the near-wall grid cell temperature.

However as discussed earlier, it is unlikely that the flow field over a populated electronic board remains fully laminar. Unfortunately due to the difficulty in defining a characteristic dimension, hence transition Reynolds number, that adequately describes the fluid flow regime in non-dimensional form over the board [177], no meaningful Reynolds number, based on either component length or board length, can be used for the *à priori* selection of a laminar or turbulence model. Consequently in this study, the fluid domain for all forced convection test cases was solved using both laminar and a range of turbulent flow models. This included both standard turbulence models for the thermal analysis of electronic equipment, namely mixing length and high-Reynolds number  $k$ - $\epsilon$  flow models, and three alternative candidate low-Reynolds number turbulence models, including a two-layer zonal model. Such an evaluation will permit perspective to be given on the capabilities of dedicated CFD codes for the prediction of electronic component heat transfer, and the potential for improved predictive accuracy. The specifics of each turbulence model are given in the following section, with their mathematical formulation presented in Appendix C.

### 4.3 Numerical Software

Numerical analysis was undertaken using Flotherm, Version 3.2 for standard flow modelling, and Fluent, Version 6.1 to assess alternative flow models. The selection of these software was outlined in Section 2.6.1. Both CFD codes use the finite volume method [231] to discretize the problem into a set of non-overlapping, contiguous finite volumes, over which the conservation are solved. Details of the computational methods are given in the respective user manuals [69,70]. This section focuses on the codes' turbulent flow modelling capabilities of relevance for this study, and their application to the analysis of component-PCB heat transfer.

### 4.3.1 Flotherm

The computational method is based on a structured, Cartesian staggered finite volume discretization [231]. A variant of the SIMPLEST algorithm [232] is used to couple the velocity and pressure fields, with first-order accurate upwinding as a convective term treatment, second-order accurate upwinding for the diffusive terms, and first-order accurate temporal discretization. The standard Gauss-Seidel algorithm is used as equation solver.

For turbulent flow analysis, Flotherm can solve fluid turbulent viscosity using either an algebraic mixing length model, referred to as LVEL [233], and the second-order, high-Reynolds number  $k$ - $\epsilon$  differential model [234]. Both models use wall functions as near-wall treatment.

Although the LVEL model was developed specifically for low-Reynolds number turbulent flows in electronic cooling applications, it is only intended for practical, coarse grid computations of global flow and temperature distributions, rather than detailed component-board level analyses. The LVEL model automatically calculates a length scale for each fluid cell by solving a Laplacian type differential equation to determine the distance of the cell from all apparent walls. This length scale, together with the locally computed velocity is used to compute a turbulent viscosity. This approach is an improvement of traditional mixing length models, whereby a fixed characteristic length scale is defined for the problem in question, and in some instances, a fixed velocity. Automatic calculation of both the local length- and velocity scales in the LVEL model, produces lower values of the turbulent viscosity in near-wall regions compared to other mixing length models, thereby making the model more applicable to low-Reynolds number wall-bounded flows.

Two wall function formulations are available for use in conjunction with the  $k$ - $\epsilon$  model in Flotherm, standard and revised. The performance of the standard model [235] is limited if the first grid cell is within the viscous sub-layer, as wall skin friction and heat transfer can be considerably overestimated as will be shown in this study. The revised formulation remedies this issue with proprietary corrections blending together turbulent viscosity in the near wall region and the bulk flow. This formulation requires at least one and typically up to six grid cells within the viscous sub-layer to obtain a grid independent solution [163,236]. Heat and momentum flux are proportionalised through the Reynolds analogy, of which a modified form, Taylor-Prandtl, is applied when the near-wall fluid node is located outside the viscous sub-layer. As at stagnation points the Reynolds analogy is not valid, to evaluate surface convective heat transfer the friction velocity is deduced from the near-wall cell value of kinetic energy calculated using the  $k$ - $\epsilon$  model [237]. The revised wall function formulation was employed for all computations performed using the  $k$ - $\epsilon$

model in this study, as the near-wall grid imposed by the board surface copper tracking (71  $\mu\text{m}$ ) resulted in  $y^+$  values considerably lower than 11.5.

In the LVEL model the wall function [238] employed is not  $y^+$  constrained. However, no correction is applied at stagnation points and hence no heat transfer is predicted.

For radiative heat transfer, Flotherm uses a surface-to-surface, gray-diffuse radiation model. The effects of surface size, separation distance and orientation on the energy exchange between two surfaces are accounted for by a geometric view factor function. The code's view factor calculation is based on the Monte Carlo method.

#### **4.3.2 Fluent**

The computational method is based on a cell-centred, unstructured finite volume discretization [239,240] and a SIMPLE-type segregated solution procedure [70]. All computations in this study were performed using second-order upwind scheme for the convective terms and central differencing for the diffusive terms.

A suite of eddy viscosity turbulent flow models suited to the analysis of low-Reynolds number, wall-bounded flows are available in Fluent, namely: the one-equation Spalart-Allmaras model [241], several low-Reynolds number variants of the  $k$ - $\epsilon$  model [131,132,242-244], two two-equation  $k$ - $\omega$  models [245,246], and a two-layer zonal model [247]. As it is generally accepted that low-Reynolds number  $k$ - $\epsilon$  models do not possess the degree of universality and robustness necessary for practical engineering analyses, such models were not evaluated in the current work. These models perform well according to the cases used by the authors to validate them, but fail to varying degrees when applied to other flow types and flows with different Reynolds number [65]. The Shear Stress Transport (SST)  $k$ - $\omega$  model [246] is a refinement of the Wilcox  $k$ - $\omega$  model [245] and is considered to be more robust in terms of stable convergence. Based on these considerations, the one-equation Spalart-Allmaras model, two-layer zonal model and SST  $k$ - $\omega$  model were selected for evaluation in this study.

The Spalart-Allmaras model is a one-equation model that solves a modelled transport equation for the eddy viscosity. Although this model was derived for aerospace applications involving wall-bounded flows, Madhavan and Joshi [248] recently reported its application to the analysis of heat transfer in data centres. This model was considered in this study due to both its suitability for wall-bounded flows, and lower computational expense relative to the following two-equations models.

The two-layer zonal model is an alternative to the wall function approach for modelling the near-wall region when using a high-Reynolds number  $k$ - $\epsilon$  model. The fluid domain is subdivided into a viscosity-affected region and a fully-turbulent region. The demarcation

of the two regions is determined by a wall-distance-based, turbulent Reynolds number,  $Re_y$ . In the fully turbulent region ( $Re_y > 200$ ), a  $k-\epsilon$  model is employed. In the viscosity-affected near-wall region ( $Re_y < 200$ ), the one-equation model of Wolfshtein [249] is applied. This model solves the same transport equation for momentum and the turbulent kinematic energy as for the standard high-Reynolds  $k-\epsilon$  model, but a different algebraic equation is used to calculate the turbulent viscosity. In this instance, the two-layer zonal model was employed in conjunction with either a standard high-Reynolds number  $k-\epsilon$  [235] or RNG  $k-\epsilon$  [250,251]. The RNG  $k-\epsilon$  model is derived using a more rigorous statistical technique as opposed to the standard  $k-\epsilon$  model, which results in improved predictions of near-wall flows, including separating and recirculating flow, detailed wake flow and vortex shedding behaviour. Its modelling is suitable for low-Reynolds number situations, where the flow is fully turbulent in regions of limited extent, and effectively laminar in the remaining region of the domain, or transitional flows.

The SST  $k-\omega$  model blends a standard  $k-\omega$  model in the inner region of the boundary layer, and a high-Reynolds number  $k-\epsilon$  model [235] in the outer part. The standard  $k-\omega$  model is based on modelled transport equations for the turbulence kinetic energy ( $k$ ) and the specific dissipation rate ( $\omega$ ), which represents the frequency of the vorticity fluctuations. The  $k-\omega$  model is essentially a direct translation of the low-Reynolds number  $k-\epsilon$  model, with the addition of transition specific closure coefficients [66]. In the SST  $k-\omega$  model, the definition of the turbulent viscosity is modified to account for the transport effects of the principal turbulent shear stress. It also incorporates a damped cross-diffusion term in the  $\omega$  equation.

In this study the constants used in the respective candidate turbulence models corresponded to their default values in the code. As the Spalart-Allmaras, two-layer zonal and  $k-\omega$  models are designed for near-wall modelling in conjunction with appropriate near-wall meshes, no wall functions were employed.

In this study the performance of the above candidate turbulence models could not be evaluated directly against that of the standard high-Reynolds number  $k-\epsilon$  model in Fluent, as the wall function formulations available, namely standard [235] and non-equilibrium [229], are both  $y^+$  constrained. Consequently, their performance will be compared against that of the same standard  $k-\epsilon$  model implemented in Flotherm, used in conjunction with the code's revised wall functions.

A suite of radiation models is available in Fluent, of which the Discrete Ordinates model [252] was employed in this study. The model solves radiative transfer in the form of a transport equation for radiation intensity, with the solution method identical to that used for the fluid flow and energy equations. The code's surface-to-surface radiation model could

not be employed as it is not applicable to problems involving symmetry boundary conditions. As outlined later in this Chapter, the use of such boundary conditions was necessary for some of the computational models, to ease computational constraints in Fluent.

As Fluent does not possess pre-processing capabilities, Icepak, Version 4.0.12 [253], was employed to construct the numerical models. Icepak is a software dedicated to the thermal analysis of electronic equipment, which uses the Fluent solver architecture for thermal and fluid flow calculations. However, access to Fluent's turbulence models is restricted to a mixing-length, standard two-equation high-Reynolds number  $k$ - $\epsilon$  and RNG  $k$ - $\epsilon$  flow models, all relying on standard wall functions. Consequently no turbulent flow analyses could be performed for benchmarking purposes using Icepak, which was only used to construct and mesh the numerical models. The computational models were imported in Fluent, where turbulence flow modelling, radiation modelling, and numerics were specified prior to solving.

It should be noted that  $y^+$  constraints associated with the use of standard wall functions are not a limitation for the majority of system-level heat transfer computations performed on electronic equipment, where computational constraints prohibit the PCB surface copper tracking layer to be explicitly modelled. Instead, the PCB substrate and copper tracking are modelled as a single solid block having effective thermo-physical properties [190,191]. In this approach therefore, the near-wall grid cell can be defined to encompass the turbulent buffer layer, thereby making standard wall functions applicable. Parametric studies, as performed by Agonafer and Moffatt [254], or automated mesh adaptation upon the  $y^+$  value, are typically required to ensure the appropriateness of the near-wall grid.

However, for detailed board-level analysis, the PCB substrate and copper tracking require to be modelled separately to correctly capture the local influence of the copper surface traces on PCB heat spread [149]. In addition, the near-wall fluid grid cell needs to be close enough to the board surface to fully resolve the effect of local flow conditions on convective heat transfer. Therefore, the availability of a revised wall function formulation in Flotherm reinforced the selection of this code for evaluating standard turbulent flow modelling in this study.

Unlike Flotherm, Icepak's mesher has non-conformal meshing capabilities. This feature can offer computational savings for the analysis of component-board heat transfer, by enabling superfluous grid detail in the far-field to be employed for the resolution of the PCB thermofluids. However, this did not compensate for the computational memory requirements incurred using unstructured meshing in this study, which were found to be three to four times those for a Cartesian structured grid system in Flotherm. It should be

noted that the computational constraints incurred in Fluent were not related to the turbulence model used, as verified by laminar flow analyses.

#### 4.4 Numerical Modelling Strategy

The numerical modelling strategy employed to analyse the benchmark test cases described in Chapter 3 is outlined.

The component and board numerical models were constructed in the same manner in both CFD codes. All component and PCB geometry dimensions and constituent material thermo-physical properties used for numerical modelling corresponded to nominal vendor specifications. Component internal architecture was verified using non-destructive and destructive testing for each package type in Chapter 3. For the PQFP 160 component, delamination of the die attach layer, and resin seepage between the paddle and heat slug in package design I, were both modelled as per structural analysis findings. In the approach employed therefore, no calibration is made to the numerical models in a possible attempt to improve predictive accuracy. This work therefore also permits the suitability of the pragmatic modelling strategy employed to be assessed for use in a design environment. While detailed component modelling is the *à priori* methodology for benchmark purposes, the predictive performance of component compact thermal models (CTMs) is also assessed.

When permissible, computational constraints for the respective test cases were eased by taking advantage of the symmetry of the heat transfer processes involved. In addition, the computational domains were confined to the fluid domain in the vicinity of the PCB, to permit the computational grid to be effectively used to focus on the resolution of the component-PCB thermofluids. Domain boundary conditions were prescribed at a sufficient distance from the PCB assembly so as not to introduce any unintentional elliptical effects.

The computational expenses associated with unstructured meshing prohibited sufficient grid resolution to be applied to full board geometry models in Fluent. The insulated Stage 3 PCB configurations could therefore not be modelled, as no symmetry of the heat transfer processes could be exploited to ease computational constraints. Consequently, the low-Reynolds number turbulent flow models were evaluated for the non-insulated PCB case. While the insulated case presented more challenging flow conditions for numerical analysis, the significant errors obtained using the standard k- $\epsilon$  flow model for the non-insulated PCB indicated that this configuration still provided a sufficient level of

complexity for assessing the predictive capability of more advanced turbulent flow models. These models were evaluated using the non-insulated Stage 1 and 3 PCB configurations in a 4 m/s airflow. Measurements for the non-insulated Stage 3 configuration existed for both individually and simultaneously powered components (Section 3.3), thereby permitting the prediction of both aerodynamic and thermal factors to be studied. By contrast, data for simultaneously powered components was not available in a 2 m/s airflow.

The fluid domain for all free convection analyses was solved as laminar using Flotherm. The forced airflows were solved using both laminar and a range of turbulent flow models.

Using standard turbulent flow modelling in Flotherm, the two-equation  $k$ - $\epsilon$  flow model predictions form the *à priori* turbulent flow predictions, with the LVEL model only evaluated due to its greater applicability for system level analysis. Flotherm's revised wall function formulation was employed for all computations performed using the  $k$ - $\epsilon$  model.

The accuracy obtained with the standard  $k$ - $\epsilon$  model in Flotherm will be considered as the base line accuracy, based on which the performance of alternative turbulence models, namely the Spalart-Allmaras, two-layer zonal and SST  $k$ - $\omega$ , can be quantified. It should be noted that the objective of this study is not to compare the performance of two CFD codes, but that of different turbulence models for detailed board level analysis. However, previous studies that have explicitly compared component heat transfer predictions for laminar flow analysis between the two codes have reported comparable accuracy [148,255]. This is in line with what was found for the Stage 1 PCB analyses in this study.

The computational grids applied in Flotherm were structured Cartesian, while unstructured non-conformal hexahedral meshes were employed in Fluent. Because of the problem geometry however, which almost exclusively contained rectilinear objects aligned with the Cartesian co-ordinate system axes, the construction of the latter mesh was similar to a Cartesian grid.

Fluid domain gridding for a given test configuration differed in free and forced convection so as to resolve the respective boundary layer flows. Non-uniform grids were applied having highest density both within the component bodies to resolve conductive heat spread, and in the near-wall regions, to resolve the high velocity and temperature gradients within the hydrodynamic and temperature boundary layers respectively and thus their near-wall effects on both surface friction and heat transfer.

For the forced convection configurations, the respective grids were refined until they captured the main flow features anticipated in bluff-body flows, namely: leading edge separation, downstream reattachment and flow recirculation, as these may impact on the



prediction of both near-wall fluid temperature and heat transfer coefficient. In addition, the near-wall transverse grid was refined with two objectives; firstly, if turbulent conditions exist it is important to correctly capture the velocity component normal to the wall as it could contribute significantly to the transfer of momentum and energy through the boundary layer; and secondly, to enable the correct application of the appropriate turbulent flow model at the highest free-stream velocity.

Minimal guidance was available in the literature for gridding the PCB near-wall fluid domain. When possible, analytical or semi-empirical analysis was used to estimate boundary layer thickness growth over the board to guide the construction of the near-wall transverse grids. These grids were then refined by parametric analysis.

The grid volumes employed for the single board-mounted component configurations exceeded the minimum density required to produce grid independent solutions. However, the computational penalty incurred was not an issue in this study, the objective of which was to benchmark predictive accuracy. The grid volumes employed for the Stage 2 and 3 populated boards analyses represented the maximum employable with the available computational resources, as constrained by computer memory. Computation was performed using a DELL Precision 420 workstation with dual 1 GHz Pentium III processor and 2 GB RAM, operating on Windows 2000 Professional. While the computational grid volumes employed for the populated board analyses would be considered impractical in a design environment, the solutions obtained for the multi-component board analyses were not truly grid independent. Prediction sensitivity to both lower grid volumes, and finer grid resolution applied to half geometry models derived from quasi symmetry boundary conditions, was assessed. However, with regard to conductive modelling, the grid densities applied within the component bodies on the multi-component PCBs were verified to be adequate when applied as a lower bound test for the single component-PCB models.

All computations were performed using double precision because of small cell sizes in the near-wall regions.

In Flotherm, solution convergence was defined when the residual error sum for each variable was reduced to the termination error level, which was set to the software default settings, namely: 0.5% of the overall mass flow for pressure, 0.5% of the sum of overall momentum flows for velocity, and 0.5% of the sum of heat sources for temperature. In addition, for the k- $\epsilon$  flow model, the termination error level for turbulent kinetic energy (k) was 0.5% of the product at inlet of turbulent kinetic energy and mass flow, and for the rate of dissipated turbulent energy ( $\epsilon$ ), 0.5% of the product at inlet of the dissipated turbulent energy and mass flow. When these criteria could not be met, solution convergence was

also assessed based on the stabilisation of monitored solution variables with outer iteration count at point locations within the fluid domain and component bodies. Convergence difficulties were found to arise due to instabilities in the buoyant plume emanating from the populated board in free convection, or the wake downstream of this board in forced airflows when solving the flow domain as laminar.

Solution convergence in Fluent was assessed based on the normalised residual errors for all variables being less than  $5 \times 10^{-5}$ . In addition, convergence was also assessed based on the stabilisation of monitored solution variables with outer iteration count at point locations within the fluid domain and component bodies.

Grid aspect ratios were maintained within satisfactory ranges to eliminate convergence difficulties.

## **4.5 Component and PCB Modelling**

In this section, numerical modelling methodology is developed and applied to model the test configurations described in Chapter 3. Numerical grid discretization details and verification of solution independence to both grid and computational domain size are also outlined.

### **4.5.1 Component Modelling**

Both detailed and compact component thermal modelling methodologies are presented. Using a detailed approach, both the mechanical architecture and thermo-physical properties of the component constituent elements are explicitly represented, with conduction solved within the component solid domain. By contrast, resistor network-based CTMs model steady-state component thermal behaviour using simplified few parameter-based representations of the package conductive domain [46,167].

The detailed component and PCB modelling methodologies are based on Rosten's et al. approach [103], with the following minor alterations: (i) air gap heat transfer beneath the component bodies is explicitly modelled, (ii) the PCB copper tracking thickness is explicitly represented, and (iii) the PCB surface copper tracking pattern geometry is modelled in finer detail. This methodology is extended to the modelling of transient component-PCB heat transfer in this study, which requires the representation of the thermal capacitance.

For component CTM derivation, the procedure presented by Aranyosi et al. [49] was adopted, which is a variant of the DELPHI approach [46,167].

The detailed and compact component thermal models are described in Sections 4.5.1.1 and 4.5.1.2 respectively, with the PCB models described in Section 4.5.2.

#### 4.5.1.1 Detailed Component Modelling

The PQFP 160 numerical models are presented in Figures 4.1 to 4.3 for package designs I to III respectively. The SO8 and PQFP 208 component numerical models are shown in Figures 4.4 and 4.5 respectively. Detailed component models for these packages were previously presented by Lohan et al. [149,225] and Rodgers et al. [35]. However, to both derive the CTMs from the detailed component models and accurately compare CTM versus detailed model predictive performance, both detailed models were re-constructed in this study.

Nominal dimensions for external package architecture are given in Figures A.1 to A.3 for the three component types. The measured internal architecture of the three PQFP 160 package designs was presented in Figures 3.22 to 3.24, with the SO8 and PQFP 208 internal geometries shown in Figures 3.48 and 3.52 respectively.

The component constituent material thermo-physical properties are listed in Tables 4.1 for the three package types. For the modelling of transient component heat transfer using the PQFP 160 component, specific heat capacity and density are also defined for the package constituent elements.

**Table 4.1** Vendor specified thermo-physical properties for component constituent elements.

<i>Package element</i>	<i>SO8</i>	<i>PQFP 208</i>	<i>PQFP 160</i>		
	<i>Thermal conductivity (W/m.K)</i>	<i>Thermal conductivity (W/m.K)</i>	<i>Thermal conductivity (W/m.K)</i>	<i>Density (kg/m<sup>3</sup>)</i>	<i>Specific heat capacity (J/kg.K)</i>
Encapsulant	0.62	0.63	0.63	1820	882
Silicon die	117.5 - 0.42 (T-100)			2330	712
Die attach	1.25	1.90	1.90	---	---
Leadframe / paddle	260	260	302	8900	385
Heat slug	N/A	260	398	8940	385
Leadframe insulation tape	---	---	0.2	---	---

Note: T = temperature in °C.

All package constituent elements were modelled with the exception of bond-wires due to the computational constraints associated with their small diameter, on order 30  $\mu\text{m}$ . In general neglecting wire conduction is not a limitation as bond-wires do not represent a significant thermal path due to their small cross sectional area [103]. In addition, for the PQFP devices, package heat spread is dominated by the heat slug.

All package features were represented by three-dimensional conducting solid blocks, with the exception of the die attach layer. Explicitly modelling its thickness, 5, 25 and 30  $\mu\text{m}$  for the SO8, PQFP 160 and PQFP 208 respectively, would introduce a layer of thin grid cells into the computational domain that could result in slow convergence of the iterative algorithm used to solve the equations for temperature. This layer was therefore modelled

using a conducting planar element, with conduction modelled only in the through-plane direction, thereby neglecting in-plane heat spread. This element type is imposed at a grid cell interface and has no thickness in the finite volume grid, but can be attributed a planar thermal resistance. This approximation was permissible as the die heat flux is uniformly distributed across the die attach layer. For certain package constructions, not explicitly modelling the die attach thickness can increase the thermal resistance of the die to package top, due to the increased encapsulant thickness between the die active area and package surface. This can be overcome by increasing the die thickness by an amount equalling the die attach thickness. Such a modification was only necessary for the SO8 package in this study. For the PQFP components, heat transfer was found to be insensitive to the modelled encapsulant thickness between the die and package surface, as on order 92% of die heat dissipation is directly to the heat slug.

Die heat dissipation was modelled as a Neumann-type boundary condition using a two-dimensional planar source element located on the die active surface. This element type is imposed at a grid cell interface and has no thickness in the finite volume grid. The use of a two-dimensional, rather than three-dimensional source, was justified in this instance as the die active area is confined to within 10  $\mu\text{m}$  of die thickness and the heat load generated by the thermal test die is uniformly distributed over its surface.

The tie bars in both the PQFP 160, package design I, and PQFP 208 were modelled in the same plane as the leadframe. To eliminate considerable computational expenses that would be incurred with modelling the tie bars diagonally orientated from the paddle corner to the package corner, as a result of their non-alignment with Flotherm's Cartesian co-ordinate system axes, the following approach was employed. The effect of tie bar on package heat spread was simulated using two tie bar elements aligned with the Cartesian co-ordinate system axes, extending from the paddle corner to the package sides. The tie bars elements were modelled at half the actual tie bar thickness. This is illustrated in Figure 4.5(b) for the PQFP 208 component. Although this approximation does not explicitly model tie bar heat spread, it is not a significant limitation in this instance, as the heat slug is the dominant heat spreader within the packages. Thus for the PQFP 160, numerical sensitivity analyses revealed that the tie bars had negligible effect on component thermal resistance. However for standard package constructions having no heat slug, the tie bars are an important heat transfer path which can lower junction-to-ambient thermal resistance by on order 2 to 3  $^{\circ}\text{C}/\text{W}$  [103].

To avoid potential computational constraints associated with explicitly modelling the leadframe and external leads geometries, both were modelled using a so-called 'compact' or 'smeared' approach [103,256]. This permits these geometries to be modelled as single

blocks having effective thermal conductivities based on the constituent materials volumetric ratios. In addition for the PQFP 160 component, effective density values are also defined, which are calculated based on the volumetric ratios of the constituent solid materials. The specific heat capacity values of the leadframe and external leads compact models equalled that of the metal. The calculated effective thermo-physical property values are given in Table 4.2 for the three package types. The thermal capacitances of both the die attach layer and PQFP 160 leadframe insulation tape are neglected due to their small thermal mass.

The robustness of this component modelling methodology has been demonstrated for steady-state heat transfer by Rosten's et al. [257], who obtained excellent agreement with component heat transfer predictions obtained by explicitly modelling the package leadframe and external lead geometry details in a Finite Element model. Repeating the validation procedure of Rosten et al. [257], Parry et al. [258] showed the methodology to be also applicable to the modelling of component transient heat transfer.

**Table 4.2** Effective thermo-physical properties values for the modelled leadframe and leads elements for the SO8, PQFP 208 and PQFP 160 packages.

Package element	Effective thermal conductivity, $k_{eff}$ (W/m.K)			Effective density, $\rho_{eff}$ (kg/m <sup>3</sup> )
	SO8	PQFP 208	PQFP 160	PQFP 160
Leadframe	Inner section: 208 (80% metal) Outer section: 96 (37% metal)	130 (50% metal)	151 (50% metal)	5360 (50% metal)
Leads	96 (37% metal)	106 (41% metal)	129 (43% metal)	3814 (43% metal)

Note:  $k_{eff} = \alpha k_1 + (1-\alpha) k_2$ , where  $\alpha$  is the metal volumetric ratio,  $k_1$  is the leadframe/lead thermal conductivity and  $k_2$  is the encapsulant/air thermal conductivity.  $\rho_{eff} = \alpha \rho_1 + (1-\alpha) \rho_2$ , where  $\alpha$  is the metal volumetric ratio,  $\rho_1$  is the leadframe/lead density and  $\rho_2$  is the encapsulant/air thermal density.

Both Flotherm and Icepak allow explicit modelling of the PQFP heat slugs' geometries, having angled surfaces relative to the Cartesian co-ordinate system axes. This was not possible with the Flotherm release previously employed by Rodgers et al. [35], Version 2.1 for modelling the PQFP 208 component. Instead Rodgers et al. modelled angled surfaces using a staggered staircase fashion, aligned with the Cartesian grid, which was then a standard approximation [259].

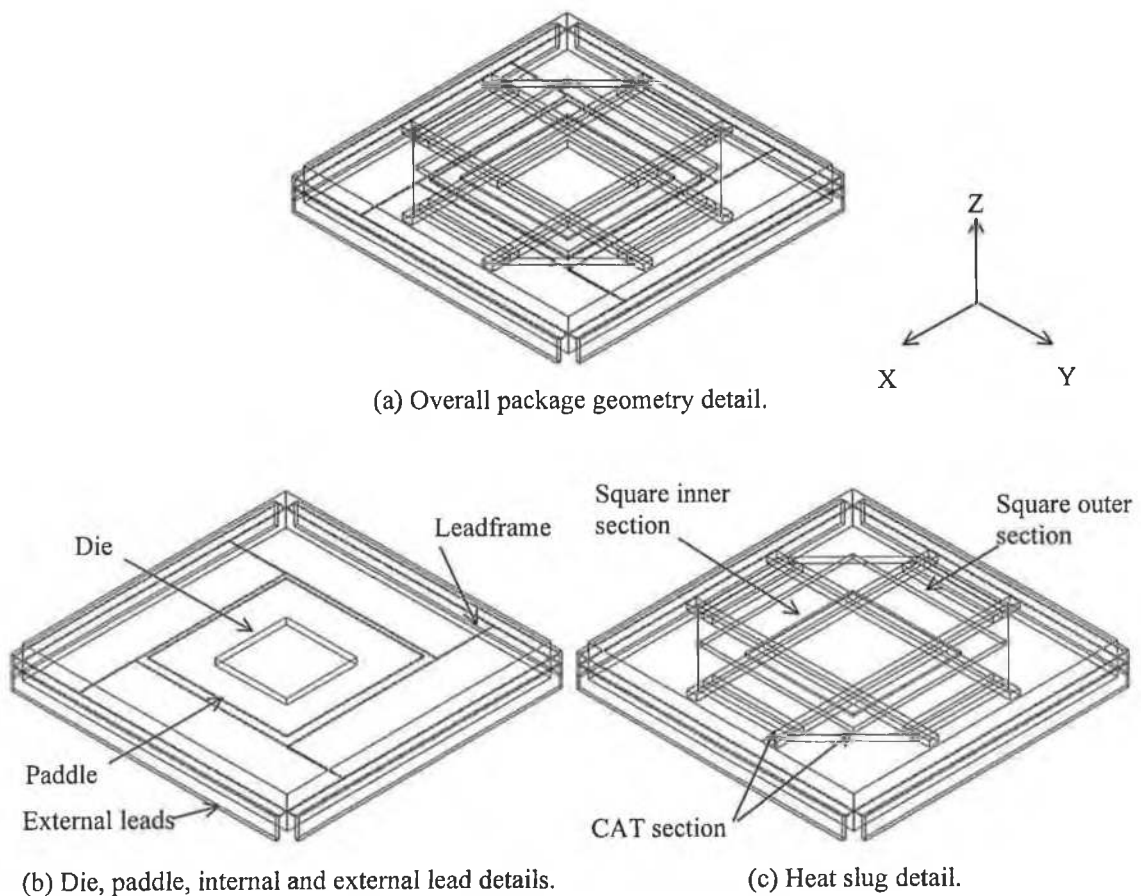
For the PQFP 160 components on the populated board, the delaminated die attach layer was modelled as a one-dimensional contact thermal resistance, with conduction modelled only in the through-plane direction. This approximation was appropriate as both the die heat flux is uniformly distributed across the die attach layer, and the delamination thickness is consistent throughout the interface (Section 3.3.4). Based on an average 2.5  $\mu\text{m}$  air gap thickness, the delamination thermal resistance was estimated at 1.48  $^{\circ}\text{C}/\text{W}$  using one-

dimensional conduction. This resistance was modelled in series with that of the die attach, using a single conducting planar element. Chowdury et al. [221] investigated the modelling of delamination at the die attach/heat slug interface of PowerQuad 2 packages in a similar way, and concluded that it could be accurately modelled as a constant air gap.

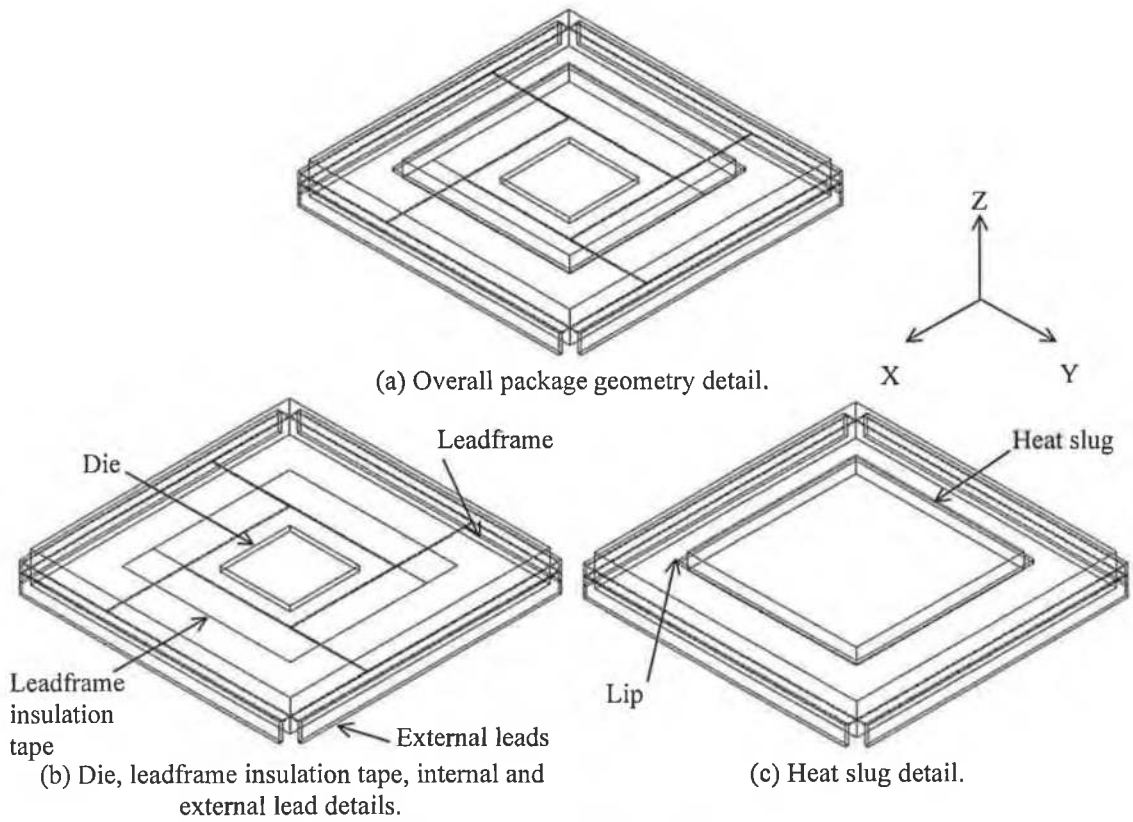
A similar approach was employed to model resin seepage between the paddle and heat slug in package design I. As the resin film thickness was consistent across the interface (Section 3.3.4), it was modelled as a contact thermal resistance of thickness of 17  $\mu\text{m}$ .

As will be shown in Chapter 5, the modelled interfacial contact thermal resistances accurately represent the additional thermal resistances induced within the package bodies, and do not alter in any way the package internal conductive heat transfer. This was verified by comparing the numerically predicted distributions of the component heat transfer paths for components modelled with and without the above interfacial thermal resistances. The predicted heat transfer paths were found to be insensitive to this modelling variable.

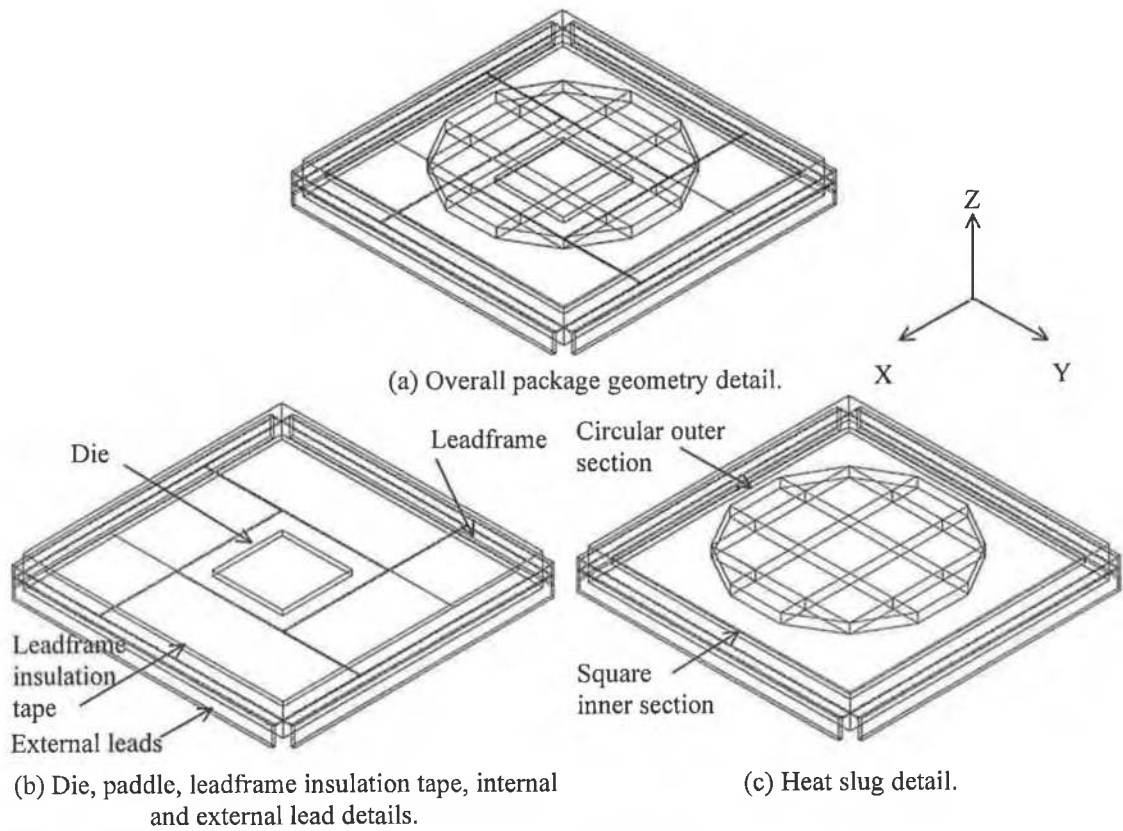
Numerical sensitivity studies to component modelling parameters are performed in Chapter 5 to assess the robustness of the models.



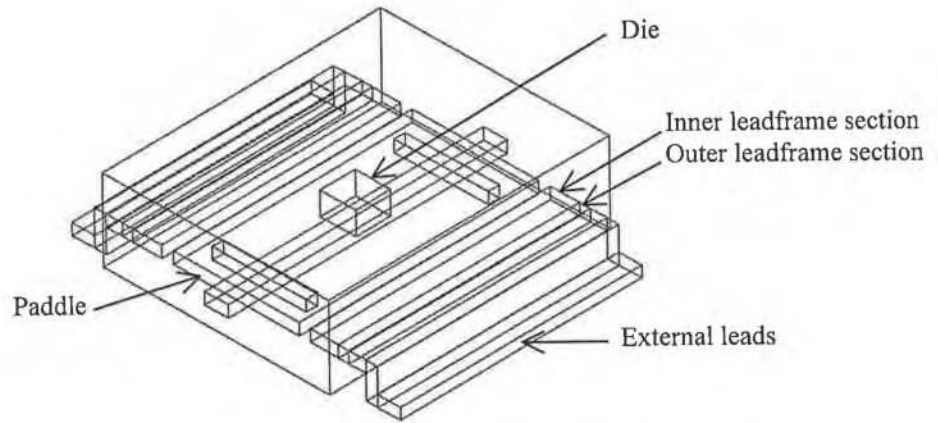
**Figure 4.1** PQFP 160 numerical model, package design I.



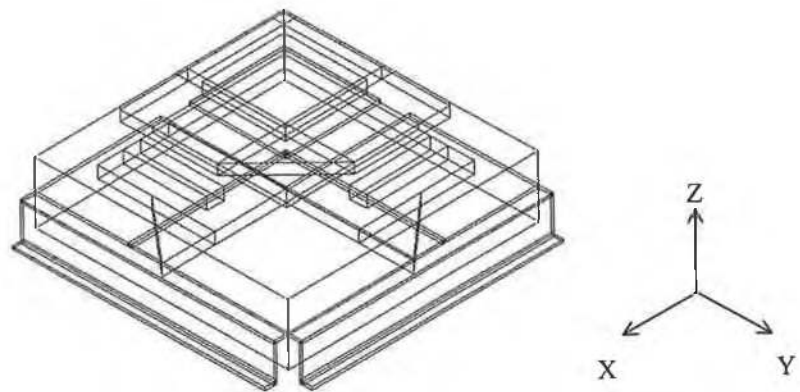
**Figure 4.2** PQFP 160 numerical model, package design II.



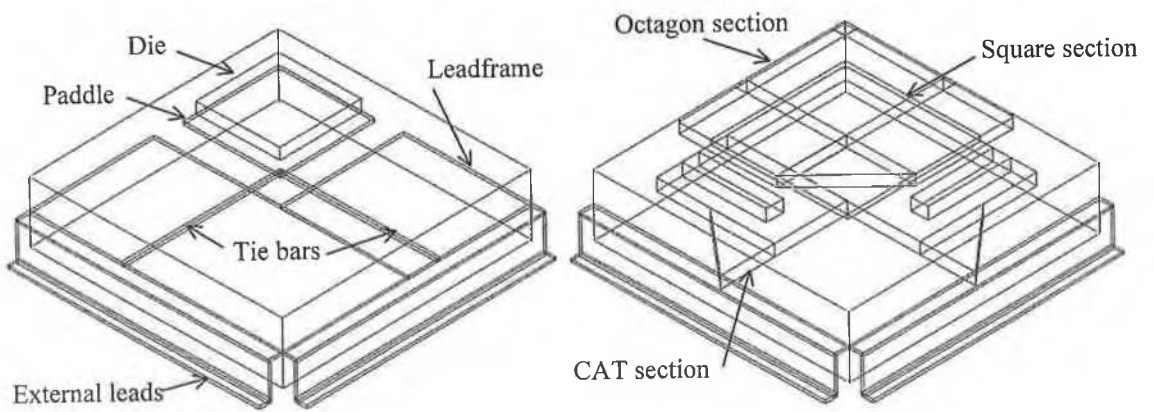
**Figure 4.3** PQFP 160 numerical model, package design III.



**Figure 4.4** Detailed SO8 numerical model.



(a) Overall package geometry detail.



(b) Die, paddle, tie bar, internal and external lead details.

(c) Heat slug detail.

**Figure 4.5** Detailed PQFP 208 numerical model (quarter geometry).



#### 4.5.1.2 Component Compact Thermal Modelling

This section details the derivation of the SO8 and PQFP 208 component CTMs and their implementation in Flotherm.

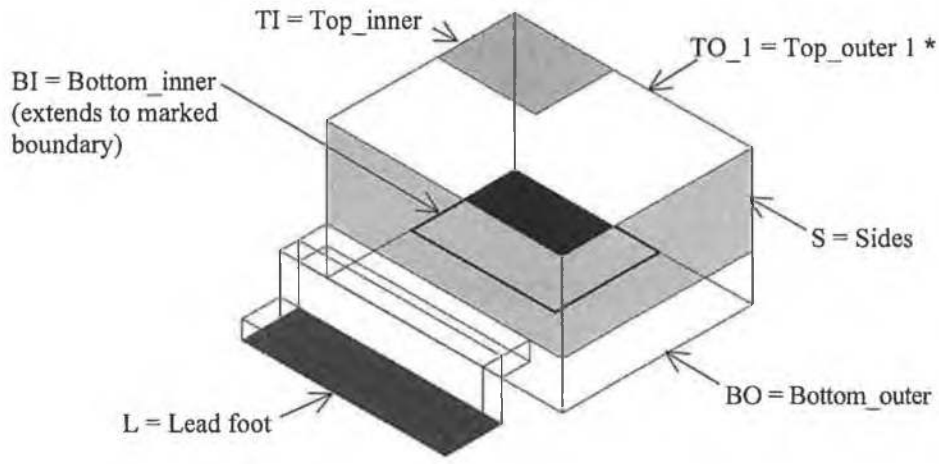
The CTMs were generated using a statistical parameter extraction-based method, outlined by Aranyosi et al. [49]. In this method, the CTM is derived from the thermal response of the detailed component model to non-redundant sets of Robin-type boundary conditions applied at the package prime lumped surfaces, consisting of uniform heat transfer coefficients with a fixed ambient temperature. These surfaces are defined in Figure 4.6 for both package types, with their areas given in Table 4.3. The detailed model thermal response data was generated using the same component model as used for CFD analysis. The eight sets of boundary conditions employed to generate the SO8 and PQFP 208 CTMs were chosen using a Design of Experiments approach [49] and cover the maximum and minimum possible heat transfer coefficients for each prime lumped surface. These sets are listed in Table 4.4. The CTM parameters were extracted using a non-linear optimisation technique which minimises the global errors in matching the junction temperature and heat flows through each prime surface, with constraints imposed on the maximum allowable errors for these variables. The cost function used in minimising global errors is given in [50].

Aranyosi et al.'s [49] methodology differs from the DELPHI approach [46,167] in the selection of the boundary conditions employed for CTM derivation. Whereas Aranyosi et al. [49] use a Design of Experiments approach, the DELPHI procedure uses a more extensive set of up to 99 boundary conditions [50], spanning the complete range of heat transfer coefficients encountered in electronics cooling applications. Ortega et al. [48] argue that such an exhaustive set is not required, as conceded by Lasance [260]. The Design of Experiments approach therefore permits to considerably reduce the computational expense incurred to compute the detailed model thermal response data. Aranyosi et al.'s [49] successfully applied their CTM generation methodology to thirteen electronic package families.

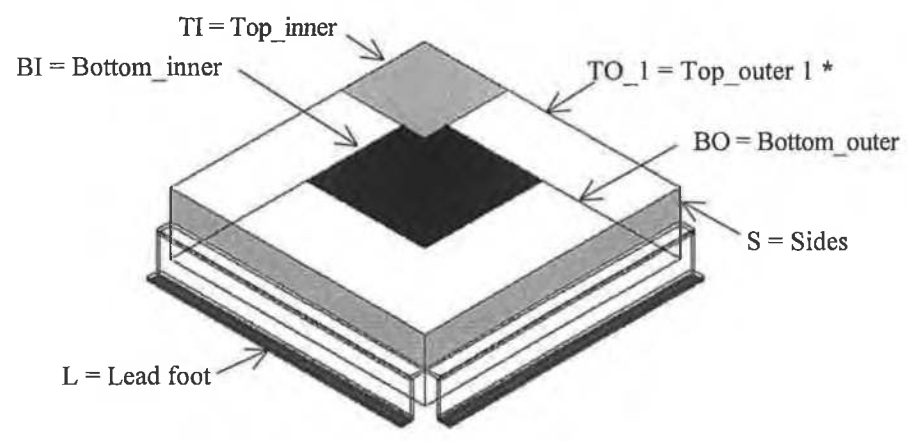
**Table 4.3** Prime lumped surface areas for the SO8 and PQFP 208 packages (quarter package geometry), Figure 4.6.

<i>Package prime lumped surface</i>	<i>Area (mm<sup>2</sup>)</i>	
	<i>SO8</i>	<i>PQFP 208</i>
<b>TI</b>	0.86625	21.16
<b>TO*</b>	8.40875	219.78
<b>BI</b>	1.70595	42.25
<b>BO</b>	3.29405	153.75
<b>L</b>	1.29	18.34

**Note:** \* Sides (S) lumped with Top\_outer 1 (TO\_1).



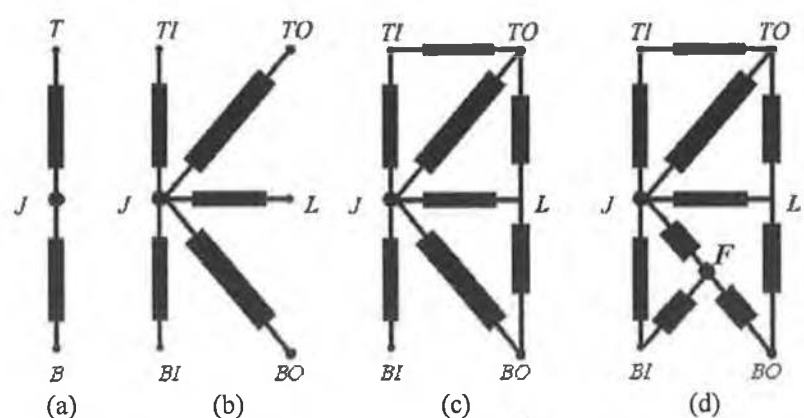
(a) SO8 package



(b) PQFP208 package

\* Note: TO surface area equals (TO\_1 + S) surface area, with side surface below area (S) treated as adiabatic.

Figure 4.6 Nomenclature for package prime lumped surfaces (quarter geometry).



Note: Nomenclature for package prime lumped surfaces given in Figure 4.6. F = floating node.

Figure 4.7 Illustrations of standard resistor network topologies for component compact thermal models. (a) two-node, (b) star-shaped, (c) shunted, and (d) shunted with floating node.

Examples of standard CTM resistor network topologies are shown in Figure 4.7. Considering the predictive limitations of two-resistor network topologies [172,173], only star-shaped and shunted topologies are evaluated in this study. Unlike star-shaped configurations, shunted topologies allow the redistribution of heat flows between the package external surfaces via shunt resistors [49,261], and consequently are considered to provide the *à priori* predictions in this study. In addition, to investigate if the prediction of the component-board thermal interaction could be improved, a shunted network having a floating node was also evaluated. This category of networks can provide additional flexibility in modelling the distribution of heat flows [49,262]. The shunted networks were optimised to predict component junction temperature and heat flows to within 5% and 10% of the detailed model respectively, while minimising the cost function used. The maximum allowable errors in junction temperature and heat flows were increased to 10% and 20% respectively for the star-shaped network.

To enable CTM implementation using Flotherm's Compact Component SmartPart feature, all network topologies were constrained to having no Side node. The SmartPart deals with this constraint by imposing the same temperature to the sides of the component body above the leads and the Top\_outer surface, as these surfaces represent the same node in the CTM network. In effect, the Compact Component Top\_outer surface extends down to the package sides above the leads, as shown in Figure 4.8. Consequently, as recommended by the CFD vendor [263], to generate the CTMs the same boundary condition was applied to the detailed model side surface above the package leads, and the Top\_outer surface, as illustrated in Figure 4.6. Both the Top\_inner / Top\_outer and Bottom\_inner / Bottom\_outer surface area ratios were defined based on the temperature and heat flux distributions predicted by the detailed numerical models.

The SO8 and PQFP 208 detailed models thermal response data to the boundary condition sets listed in Table 4.4, are given in Tables 4.5 and 4.6 respectively. One shunted network was generated for the SO8 component, while a star-shaped, shunted and shunted floating node network were derived for the PQFP 208. All network topologies contained 6 nodes, with the exception of the floating node network which had 7 nodes. The optimised values of resistors for the SO8 CTM are given in Table 4.7, with the network topology shown in Figure 4.10(a). The optimised values of resistors for the PQFP 208 CTM are given in Tables 4.8, 4.9 and 4.10 for the star-shaped, shunted and shunted floating node networks respectively. These topologies are illustrated in Figures 4.11(a) to 4.11(c). Network accuracy for each set of optimisation boundary conditions is detailed in Table 4.11 for the SO8 component, and Tables 4.12 to 4.14 for the PQFP 208.

**Table 4.4** Imposed set of thermal Boundary Conditions used to generate detailed component model thermal response data for five prime lumped surfaces, Figure 4.6.

BC no.	Applied heat transfer coefficient (W/m <sup>2</sup> .K)				
	TI	TO*	BI	BO	L
1	10	10	10	10	10
2	10	10	10	1000	1000
3	10	1000	1000	10	10
4	10	1000	1000	1000	1000
5	1000	10	1000	10	1000
6	1000	10	1000	1000	10
7	1000	1000	10	10	1000
8	1000	1000	10	1000	10

Note: \* Sides (S) lumped with Top\_outer 1 (TO\_1), Figure 4.6.

**Table 4.5** SO8 detailed model thermal response data to the Boundary Conditions defined in Table 4.4.

BC no.	Applied heat load (W)	Junction temperature (°C)	Heat flow (W)				
			TI	TO*	BI	BO	L
1	0.010	86.54	0.00056	0.00536	0.00112	0.00213	0.00083
2	0.145	90.10	0.00049	0.00373	0.00095	0.09771	0.04211
3	0.200	89.17	0.00036	0.13300	0.06485	0.00134	0.00045
4	0.240	85.07	0.00032	0.09657	0.05401	0.0648	0.02431
5	0.154	89.00	0.02837	0.00387	0.06914	0.00154	0.05109
6	0.195	90.14	0.02775	0.00364	0.06439	0.09872	0.00050
7	0.195	95.18	0.02283	0.13030	0.00102	0.00141	0.03944
8	0.215	89.35	0.02046	0.11133	0.00087	0.08200	0.00035

Note: \* Sides (S) lumped with Top\_outer 1 (TO\_1), Figure 4.6. Residual error sum for temperature less than 1% of the applied heat load. Thermal response data generated using quarter geometry model. Ambient temperature = 20°C.

**Table 4.6** PQFP 208 detailed model thermal response data to the Boundary Conditions defined in Table 4.4.

BC no.	Applied heat load (W)	Junction temperature (°C)	Heat flow (W)				
			TI	TO*	BI	BO	L
1	0.12	57.65	0.00573	0.05705	0.01161	0.04075	0.00484
2	1.40	55.56	0.00519	0.03428	0.00993	1.13648	0.21415
3	2.00	56.92	0.0049	0.99528	0.96875	0.02860	0.00245
4	2.80	56.71	0.00483	0.75132	0.91557	0.99158	0.13675
5	1.60	56.39	0.21737	0.04406	0.99747	0.03372	0.30735
6	2.40	56.12	0.21257	0.03822	0.94114	1.20512	0.00299
7	1.40	57.30	0.20197	0.95876	0.01114	0.02946	0.19870
8	2.10	56.40	0.19387	0.81795	0.01026	1.07602	0.00186

Note: \* Sides (S) lumped with Top\_outer 1 (TO\_1), Figure 4.6. Residual error sum for temperature less than 1% of the applied heat load. Thermal response data generated using quarter geometry model. Ambient temperature = 30°C.

**Table 4.7** Optimised values of resistors for SO8 CTM shunted network, Figure 4.10(a).

	Thermal resistance (°C/W)				
	J	TI	TO*	BI	BO
TI	131.11	---	---	---	---
TO*	---	12.49	---	---	---
BI	118.40	---	---	---	---
BO	154.48	---	---	---	---
L	---	60.05	---	138.20	44.47

Note: \* Sides (S) lumped with Top\_outer 1 (TO\_1), Figure 4.6.

**Table 4.8** Optimised values of resistors for PQFP 208 CTM star-shaped network, Figure 4.11(a).

	Thermal resistance (°C/W)				
	J	TI	TO*	BI	BO
TI	19.37	---	---	---	---
TO*	6.45	---	---	---	---
BI	0.87	---	---	---	---
BO	4.31	---	---	---	---
L	15.88	---	---	---	---

Note: \* Sides lumped with Top\_outer, Figure 4.6.

**Table 4.9** Optimised values of resistors for PQFP 208 CTM shunted network, Figure 4.11(b).

	Thermal resistance (°C/W)				
	J	TI	TO*	BI	BO
TI	---	---	---	---	---
TO*	---	---	---	---	---
BI	0.56	17.70	7.48	---	---
BO	5.06	---	---	46.42	---
L	---	---	5.82	27.84	6.69

Note: Sides (S) lumped with Top\_outer 1 (TO\_1), Figure 4.6.

**Table 4.10** Optimised values of resistors for PQFP 208 CTM shunted network having a floating node, Figure 4.11(c).

	Thermal resistance (°C/W)					
	F	J	TI	TO*	BI	BO
TI	3.67	---	---	---	---	---
TO*	---	4.59	---	---	---	---
BI	---	---	1.51	---	---	---
BO	33.52	---	0.57	---	---	---
L	42.57	1.36	---	---	---	---

Note: Sides (S) lumped with Top\_outer 1 (TO\_1), Figure 4.6.

*CTM network accuracy.* Considering the boundary conditions used for CTM generation in Table 4.4, the SO8 network accuracy in Table 4.11 is in all cases within 1.6% and 4.7% of the detailed model predictions for component junction temperature and heat flow respectively. Average errors for junction temperature and heat flow do not exceed 0.1% and 0.7% respectively.

For the same sets of imposed boundary conditions, average discrepancies in junction temperature and heat flow for the PQFP 208 network in Tables 4.12 to 4.14 do not exceed 0.5% and 1.7% respectively, with the shunted network displaying best accuracy.

Therefore for both package types, the accuracy of the networks generated meets the degree of boundary condition independence generally required for CTM parameters to be considered as applicable to any practical environment. This accuracy requirement is typically 5% to 10% for both junction temperature and heat flow [49,50,172].

In Chapter 5, it will be evaluated how network accuracy translates in actual PCB convective environments.

**Table 4.11** SO8 CTM resistor network accuracy versus detailed model for the imposed set of thermal Boundary Conditions defined in Table 4.4.

BC no.	Discrepancy (%)					
	Junction temperature	Heat flow (W)				
		TI	TO*	BI	BO	TI
1	-0.1	-0.1	0.1	0.0	0.0	0.0
2	-1.2	-0.1	0.0	0.0	-1.5	1.6
3	-0.2	-0.1	1.1	-1.0	0.0	0.0
4	0.4	-0.1	1.1	-0.9	0.3	-0.4
5	-0.9	4.7	-0.3	-3.0	0.0	-1.4
6	-0.5	3.1	-0.2	-0.7	-2.3	0.0
7	0.1	-1.8	0.1	0.0	0.0	1.7
8	1.5	-1.6	1.1	0.0	0.5	0.0
Max.	1.6	4.7	1.2	3.0	2.2	2.0
Mean	-0.1	0.5	0.4	-0.7	-0.4	0.2

Note: \* Sides (S) lumped with Top\_outer 1 (TO\_1), Figure 4.6.

**Table 4.12** PQFP208 CTM star-shaped resistor network accuracy versus detailed model for the imposed set of thermal Boundary Conditions defined in Table 4.4.

BC no.	Discrepancy (%)					
	Junction temperature	Heat flow (W)				
		TI	TO*	BI	BO	TI
1	-0.5	0.0	-0.2	-0.1	0.2	0.1
2	1.3	0.0	1.5	0.1	-2.2	0.6
3	1.7	0.0	-3.8	2.9	0.7	0.1
4	-6.1	0.0	0.5	-2.1	-0.5	2.1
5	3.1	0.5	0.9	2.4	0.5	-4.3
6	1.4	0.1	0.7	2.1	-3.0	0.1
7	-0.1	1.2	-4.3	0.0	0.8	2.3
8	-2.3	0.3	0.4	0.0	-0.9	0.1
Max.	6.1	1.2	4.3	2.9	3.0	4.3
Mean	-0.2	0.3	-0.5	0.7	-0.6	0.1

Note: \* Sides (S) lumped with Top\_outer 1 (TO\_1), Figure 4.6.

**Table 4.13** PQFP208 CTM shunted resistor network accuracy versus detailed model for the imposed set of thermal Boundary Conditions defined in Table 4.4.

BC no.	Discrepancy (%)					
	Junction temperature	Heat flow (W)				
		TI	TO*	BI	BO	TI
1	-0.3	0.0	0.1	-0.1	0.0	0.0
2	0.3	0.0	0.2	0.0	0.3	-0.5
3	-0.2	0.0	-0.3	0.2	0.2	0.0
4	-0.5	0.0	-0.8	1.0	1.0	-1.3
5	0.6	-1.1	0.0	0.1	0.1	1.0
6	0.0	-0.8	0.0	0.8	0.0	0.0
7	-0.5	0.5	-0.4	-0.1	0.1	-0.2
8	0.2	0.4	0.1	0.0	-0.5	0.0
Max.	0.6	1.1	0.8	1.0	1.0	1.3
Mean	0.0	-0.1	-0.1	0.2	0.2	-0.1

Note: \* Sides (S) lumped with Top\_outer 1 (TO\_1), Figure 4.6.

**Table 4.14** PQFP208 CTM shunted resistor network with floating node accuracy versus detailed model for the imposed set of thermal Boundary Conditions defined in Table 4.4.

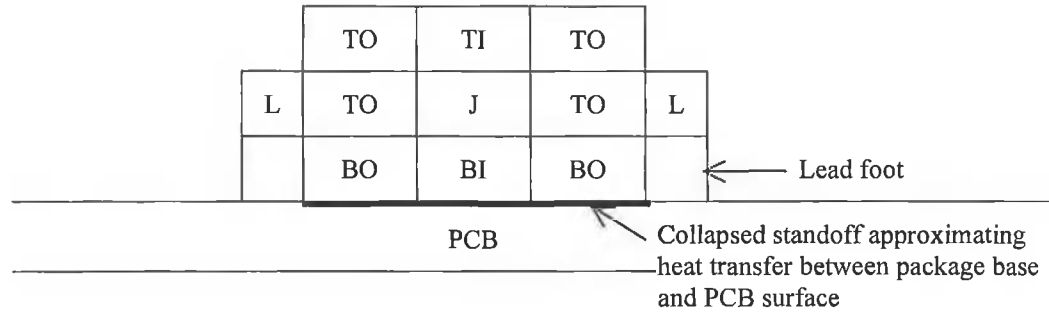
BC no.	Discrepancy (%)					
	Junction temperature	Heat flow (W)				
		TI	TO*	BI	BO	TI
1	-0.2	-0.1	0.2	0.0	0.0	0.0
2	0.7	-0.1	-0.1	3.2	0.1	-3.1
3	-2.0	-0.1	4.4	0.0	-4.2	0.0
4	0.1	-0.1	1.9	0.4	-0.1	-2.1
5	-1.4	8.4	-0.5	-0.4	-7.3	-0.2
6	1.6	4.5	-0.2	0.0	-0.9	-3.4
7	0.6	0.8	-0.5	-0.3	0.0	-0.1
8	5.0	0.0	2.0	0.0	0.1	-2.0
<b>Max.</b>	5.0	8.4	4.4	3.2	7.3	3.4
<b>Mean</b>	0.5	1.7	0.9	0.4	-1.5	-1.4

**Note:** \* Sides (S) lumped with Top\_outer 1 (TO\_1), Figure 4.6.

*CTM implementation in the CFD model.* CTM implementation in Flotherm using the Compact Component SmartPart, is illustrated in Figure 4.8 for a leaded package. Each SmartPart element represents a resistor node, whose external surface area equals that of the corresponding prime lumped surface defined for CTM derivation. In addition, each SmartPart element is isothermal, and thermally insulated from other elements unless interconnected by resistive links representing the CTM resistor network.

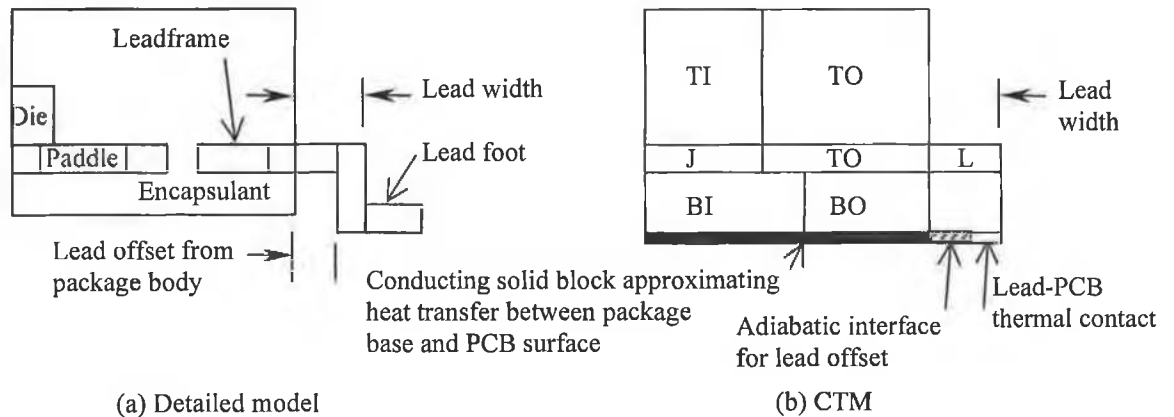
The SmartPart imposes two approximations to external component geometry modelling. Firstly, the heat transfer between the package base and PCB surface is not explicitly modelled. Instead, the air gap (standoff) is by default represented by a contact thermal resistance as shown in Figure 4.8. This is not a significant limitation as the heat transfer between the package base and PCB is primarily by gaseous conduction. Correspondingly, the CTM body height must be increased by an amount equalling the standoff to maintain the same aerodynamic disturbance as generated by the detailed component model. The second geometric constraint imposes that the CTM lead feet extend directly from the package body, Figure 4.8, with no offset between the leads and package sides as shown for the detailed model in Figure 4.9(a). In this study the CTM lead width was defined so as to generate the same aerodynamic disturbance as in the detailed component model. In addition, a contact thermal resistance was prescribed between the CTM lead foot base and the PCB surface, so as to better represent the location of the lead foot/PCB interface and thus the local PCB spreading resistance. As the CTM SmartPart overrides contacting planar thermal resistances, the above contact thermal resistance was modelled as a three-dimensional conducting block of thickness that of the standoff. Note that deactivating the lead foot extremity in the detailed component model had a negligible impact on component operating temperature. The modified CTM implementation is shown in Figure 4.9(b). The SO8 and PQFP 208 CTM representations in the CFD models are shown in Figures 4.10 and 4.11 respectively, with corresponding geometric details given in Table 4.15.

For package lead modelling, the Compact Component SmartPart supports the specification of either a single or two lead nodes, applicable to dual and quad packages respectively [263]. Both the single and two-lead node options were applied for the PQFP 208 test case, to assess CTM predictive sensitivity to lead node coupling and its impact on the prediction of the component-board thermal interaction.



**Note:** Nomenclature for the package prime lumped surfaces, corresponding to the resistor network nodes, are defined in Figure 4.6.

**Figure 4.8** Default geometry implementation of a resistor network-based CTM for a leaded package in Flotherm, using the code's Compact Component SmartPart.



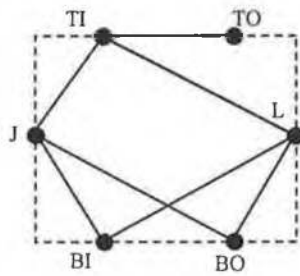
**Figure 4.9** Modified CTM implementation, shown for the SO8 component.

**Table 4.15** Geometric construction of CTM implementation in the CFD model.

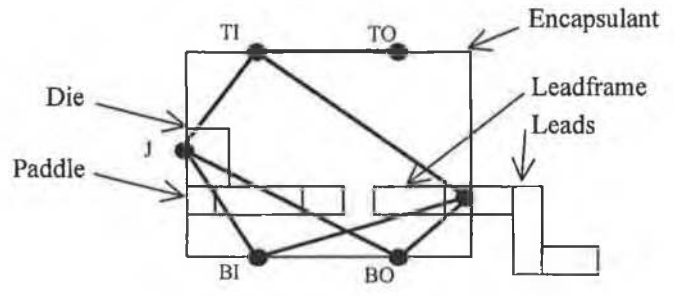
SmartPart element	Component model dimensions (mm)	
	SO8	PQFP 208
Overall body	5 x 4	28 x 28
Top_inner (TI)	2.1 x 1.65 x 0.95	9.2 x 9.2 x 1.605
Bottom_inner (BI)	3.06 x 2.23 x 0.429	13 x 13 x 1.095
Junction (J)	2.1 x 1.65 x 0.2	9.2 x 9.2 x 1.05
Standoff thickness	0.2	0.35
Lead width	0.5	0.8

**Note:** SO8 and PQFP 208 CTM implementations in CFD model shown in Figures 4.10 and 4.11 respectively. Element dimensions refer to length x width x height.

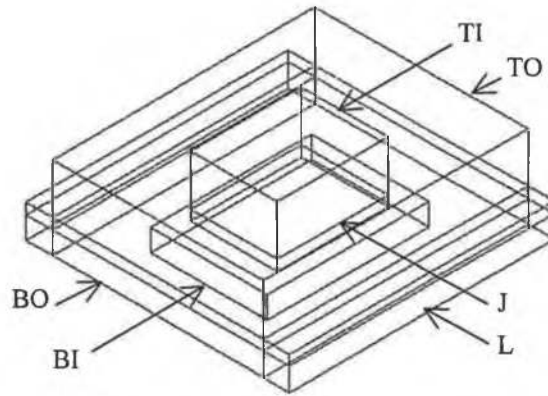




(a) Resistor network

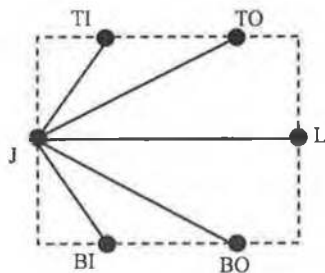


(b) Resistor network superimposed on detailed component model

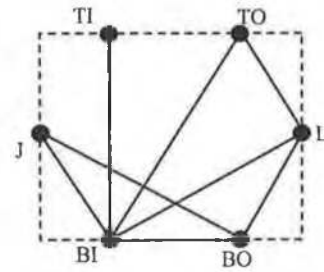


(c) Numerical model for network (a)

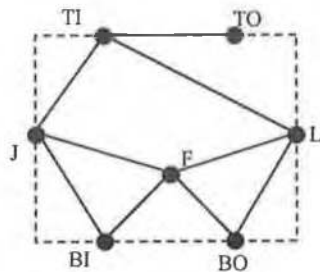
**Figure 4.10** SO8 component compact thermal model.



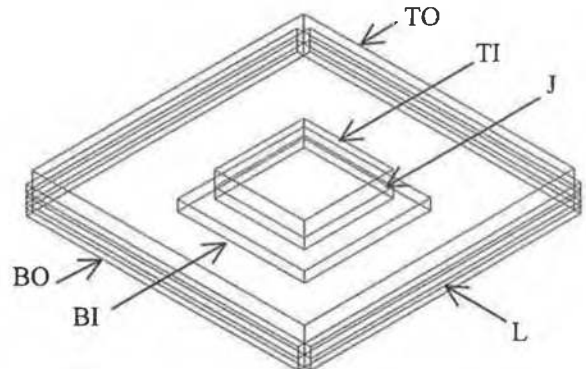
(a) Star-shaped resistor network



(b) Shunted resistor network



(c) Shunted resistor network with floating node



(b) Numerical model for networks (a), (b) and (c)

**Figure 4.11** PQFP 208 component compact thermal models.

#### 4.5.2 PCB Modelling

The numerical models for the single-component PCBs and populated board are shown in Figure 4.12 and Figure 4.13 respectively. Corresponding PCB layouts for the populated PCB, SEMI PCB, SO8 and PQFP 208 PCBs were given in Figures 3.8, 3.9, 3.49 and 3.53 respectively.

To correctly capture the local influence of the copper surface traces on PCB heat spread [149], the substrate and copper tracking were modelled separately using three-dimensional conducting blocks.

Discretely modelling the PCB surface copper tracking was not computationally feasible. To overcome computational constraints, a compact modelling approach similar to that employed for the component leadframe was used for modelling the PCB copper tracks and air interfills. As the surface copper tracks diverge significantly away from the component leads for the SO8 and PQFP 208 PCBs, Figures 3.49 and 3.53, they were modelled by a number of blocks spaced at regular intervals as shown in Figure 4.12. Their effective thermal conductivity values, based on the volumetric ratios of copper and air interfills, decreased as the tracks diverge further apart to reflect the increasing volumetric ratio of air. The same approach was used for the SEMI PCB, over which copper tracking density varied in different regions of the board, Figure 3.9. The embedded continuous copper planes in the multi-layer SO8 PCBs were each modelled individually as a single block. On the populated board's component side, the copper tracks surrounding each component were modelled as four individual blocks having the same effective thermal conductivity. On the board non-component side, where copper tracking density varied, the approach described for the SEMI PCB was employed.

The actual copper tracking thickness ( $71\ \mu\text{m}$ ) was modelled for both the SO8 and PQFP 208 PCBs. By contrast on both the SEMI PCB and populated board, copper tracking thickness was modelled at twice its actual value ( $35\ \mu\text{m}$ ) in Flotherm to avoid potential convergence difficulties, associated with the presence of thin grid cells. Accordingly therefore, the tracking effective thermal conductivity was halved. This modelling had a negligible aerodynamic impact as it only increased the board thickness by on order 4 %.

The constituent material thermo-physical properties for both the FR-4 based and IMS test boards are listed in Tables 4.16. The FR-4 substrate thermal conductivity was modelled as anisotropic using the values measured by Graebner and Azar [190], namely  $0.29\ \text{W/m.K}$  and  $0.81\ \text{W/m.K}$  in the substrate through-plane and in-plane directions respectively. These values reflect the material inherent anisotropy, highlighted in many experimental studies [146,264,265], whereas the vendor isotropic specification,  $0.3\ \text{W/m.K}$ , was only representative of the through-plane conductivity. All other material thermo-physical properties are board vendor specifications. The temperature dependency

of Styrofoam thermal conductivity was modelled for the elliptical insulating block attached to the Stage 3 PCB non-component side, Figure 3.6(b).

The effective thermal conductivity values applied to the tracking model blocks are given in Figure 4.12 and 4.13 for the single- and populated boards respectively. Thermal conductivity values of 385 W/m.K and 0.03 W/m.K were taken for copper and air respectively. For the modelling of transient component heat transfer, the copper tracking compact model blocks were also assigned effective density values based on the constituent material volumetric ratios. Their specific heat capacity value equalled that of copper.

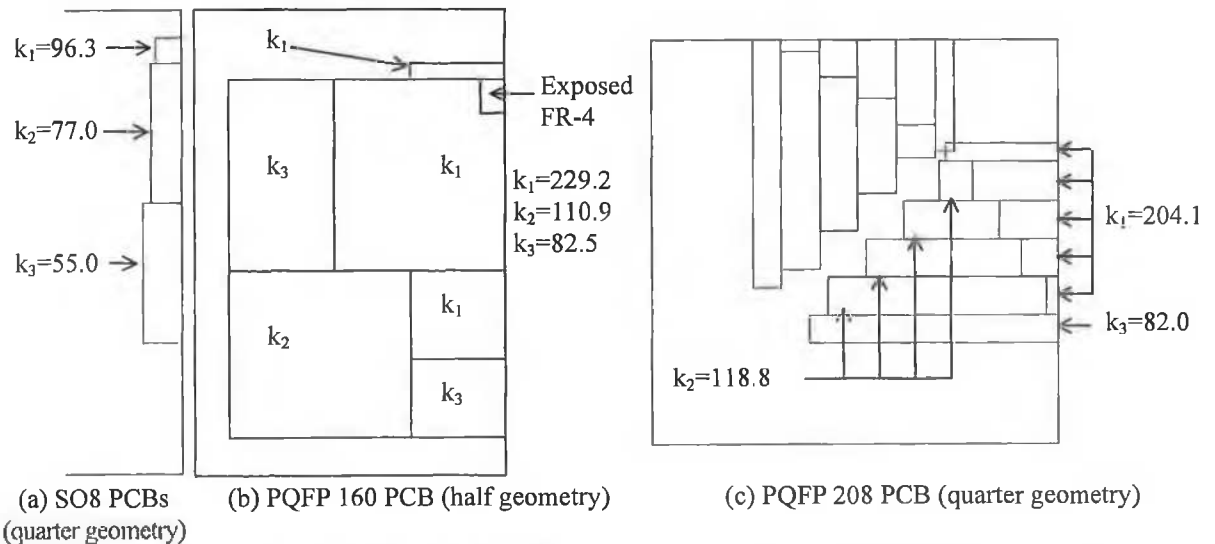
For the SO8 and PQFP 208 component compact thermal modelling configurations, the same PCB model was used for the compact and corresponding detailed model.

Based on infrared measurements of PCB surface temperature, which revealed negligible thermal interaction between the PCBs and their mechanical support, these fixtures were modelled as non-conducting.

**Table 4.16** Nominal material thermal property values for PCB constituent elements.

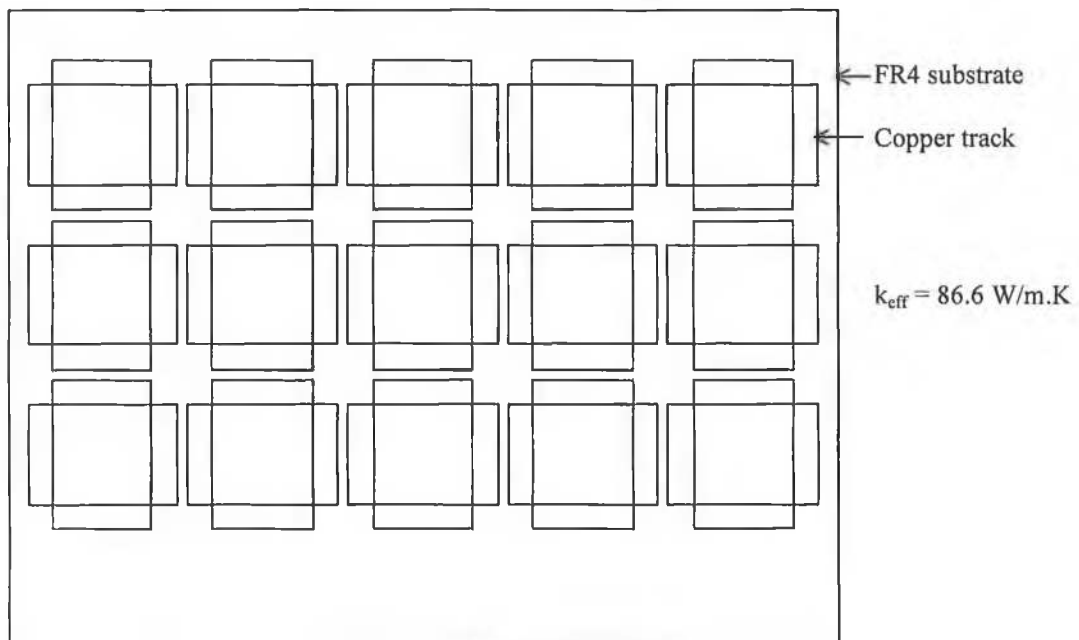
PCB design	Element	Thermal conductivity (W/m.K)	Density (kg/m <sup>3</sup> )	Specific heat capacity (J/kg.K)
FR-4 designs	FR-4 substrate	$k_{in} = 0.81, k_{tp} = 0.29$ *	1920	1300
	Copper tracking	385	8950	385
	Styrofoam, Stage 3 PCB	$0.026 + 1 \times 10^{-4} (T-10)$	45	1400
IMS design	Dielectric	2.2	---	---
	Copper base	400	8933	385

**Note:** \*  $k_{ip}$  and  $k_{tp}$  are in-plane and through-plane thermal conductivities values respectively [190]. T = temperature in °C.

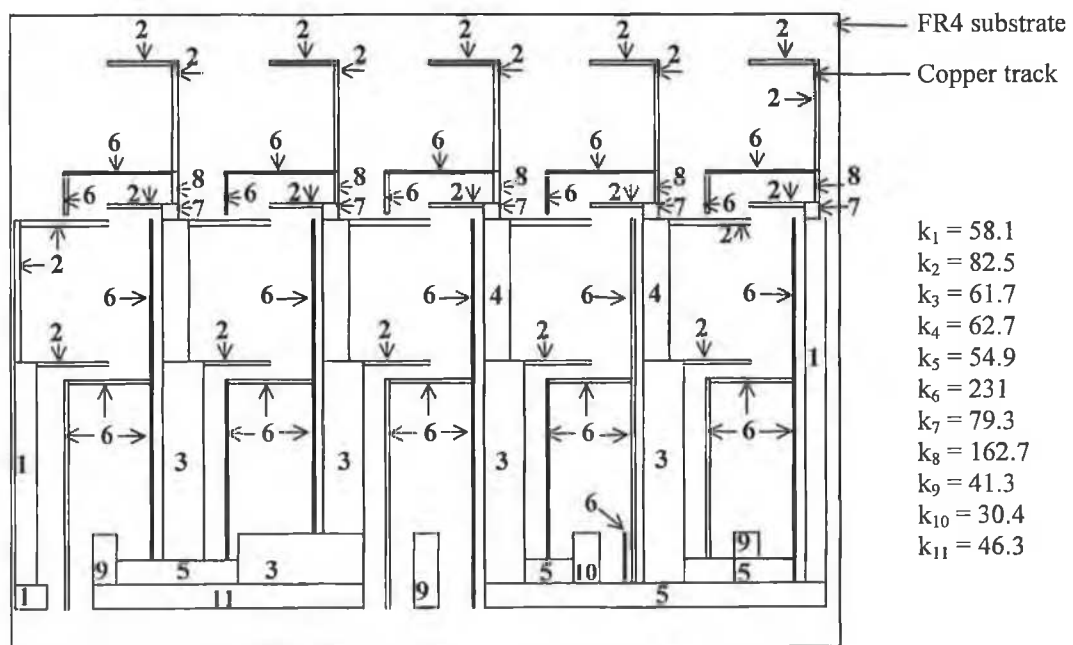


**Note:** Surface copper tracking thickness modelled as 71  $\mu\text{m}$ . Effective track thermal conductivity value calculated as  $k = \alpha k_{Cu} + (1-\alpha) k_{air}$ , where  $\alpha$  is the copper volumetric ratio,  $k_{Cu}$  and  $k_{air}$  are the thermal conductivities of copper (385 W/m.K) and air (0.03 W/m.K) respectively. For the PQFP 160 PCB, effective tracking conductivity halved as its thickness is modelled at twice actual value, 35  $\mu\text{m}$ .

**Figure 4.12** Numerical modelling of single-component PCBs copper tracking.



(a) Component side



(b) Non-component side

**Note:** Surface copper tracking thickness modelled as 71  $\mu\text{m}$ . Effective track thermal conductivity value calculated as  $k = \alpha k_{\text{Cu}} + (1-\alpha) k_{\text{air}}$ , where  $\alpha$  is the copper volumetric ratio,  $k_{\text{Cu}}$  and  $k_{\text{air}}$  are the thermal conductivities of copper (385 W/m.K) and air (0.03 W/m.K) respectively. Effective tracking conductivity halved as its thickness is modelled at twice actual value, 35  $\mu\text{m}$ .

**Figure 4.13** Numerical modelling of populated PCB copper tracking.

## 4.6 Numerical Models

### 4.6.1 Populated Board Test Configurations

This section describes the free and forced convection numerical models for the Stage 1, 2 and 3 populated board test configurations detailed in Section 3.3.

#### 4.6.1.1 Free Convection

The free convection analyses were undertaken using Flotherm, and the Stage 1 and non-insulated Stage 3 numerical models are shown in Figure 4.14.

The computational domains were confined to the fluid domain in the vicinity of the PCB to permit the computational grid to be effectively used to focus on the resolution of the component-PCB thermofluids. Free-air boundary conditions were applied at the computational domain boundaries, fixing the relative pressure to zero with any incoming air entering at the prescribed ambient temperature. These artificial boundaries were imposed at a sufficient distance from the PCB assembly so that no significant unintentional elliptical effects were introduced. Their locations relative to the PCB are defined in Table 4.17.

Due to computational constraints, different computational models were used for the analyses of the Stage 3 individually- and simultaneously powered component configurations.

*Simultaneously powered Stage 3 PCB.* For this configuration, the measured operating temperatures of components A and K were on order 10°C higher than those of E and O respectively, Table 3.4, due to different package designs. Consequently, the buoyancy-induced flow over the board was not symmetric in the span-wise direction about components C,H,M. The complete board geometry was therefore required to be modelled for this case, Figure 4.14(c).

To guide the gridding of the near-wall fluid domain for this model, as a starting point an estimate of the hydrodynamic boundary layer growth on the board non-component side was obtained by considering the PCB as an isothermal flat plate. Using the following analytical expression presented by Incropera and De Witt [266] for an isothermal vertical flat plate, the hydrodynamic / thermal boundary layer growth can be estimated as:

$$\delta_L \approx \frac{6L}{(Gr_L / 4)^{1/4}} \quad (4.2)$$

where  $\delta_L$  is the hydrodynamic or thermal boundary layer thickness, L is the PCB length in the stream-wise direction, and Gr is the PCB Grashof number. For air, the hydrodynamic

and thermal boundary layer thicknesses are comparable as the Prandtl number is of order unity.

Using an average PCB surface temperature obtained from the infrared thermographs presented in Figure 3.15(b), the board Grashof number, based on stream-wise length, was calculated to be  $1.8 \times 10^7$ . The board Raleigh number, thus less than  $1 \times 10^9$ , clearly indicated that a laminar velocity boundary layer existed on the PCB non-component side. Using Equation (4.2), the transverse hydrodynamic boundary layer thickness at the PCB trailing edge was calculated to be 19.5 mm. This near-wall distance was discretized using 21 grid cells spaced by a power-law grid distribution. On both the board component- and non-component sides, the first fluid grid node was set at 71  $\mu\text{m}$  distance from the PCB surface, coinciding with the copper tracking surface. The first fluid cell adjacent to the packages' top surface extended 100  $\mu\text{m}$  from the wall.

On the PCB component side, Equation (4.2) is not directly applicable to calculate the board boundary layer growth due to component interaction. Nevertheless, the fluid domain in the vicinity of the PCB surface was even more finely resolved by the transverse grid imposed by the respective component architectural features.

The remaining portions of the fluid domain both on the board non-component side and above the component surface were modelled using a power law grid spacing distribution in the transverse direction, with increasing cell size towards the domain boundaries.

This initial grid was then refined by parametric analysis. A computational grid volume of 3.75 million cells, details of which are given in Table 4.18 and visualised in Figure 4.15(c), was found to produce component junction temperature predictions that were within 0.1°C of those obtained using a denser grid constructed with 6 million cells.

*Individually powered Stage 3 PCB.* The above grid resolution of 3.75 million cells, was found to be insufficient for the analyses of the individually powered cases, for which component junction temperature predictions differed by up to 1°C relative to the 6 million grid. As the latter grid density would have been computationally prohibitive for the analyses of all individually powered cases, half board geometry models were used, Figure 4.14(b). These models had a symmetry boundary condition applied along the PCB central stream-wise axis, defined by the centre axis of components C,H,M. This modelling simplification was permissible as infrared imaging, showed that (i) for components C,H,M individually powered, the component-PCB surface temperature distributions were symmetric about the PCB central stream-wise axis, and (ii) for all other individually powered component configurations, board heat spread did not extend to the other half of the PCB. The symmetry plane was modelled as an adiabatic, frictionless and impermeable

surface. As both the board boundary layers were thinner and the thermal plumes were less buoyant than for the simultaneously powered cases, the computational domain size for the individually powered models was reduced in both the stream-wise (y) and transverse (z) airflow directions, to the dimensions given in Table 4.17. These modelling simplifications permitted a higher grid density to be employed for the resolution of component heat transfer, than would have been achieved using a complete board geometry model. For the half geometry models, a grid having 3.61 million cells, details of which are given in Table 4.18 and visualised in Figure 4.15(b), was found to produce component junction temperature predictions that were within 0.1°C of those obtained using an increased grid volume of 6 million cells.

The Stage 1 numerical model, Figure 4.14(a), was derived from the individually powered, Stage 3 model, Figure 4.14(b), by depopulating the PCB of the unnecessary components, without altering the computational grid.

**Table 4.17** Location of applied artificial boundary conditions relative to the PCB for the Stage 1 and non-insulated Stage 3 free convection numerical models, Figure 4.14.

<i>PCB topology and powering configuration</i>	<i>Top</i>	<i>Component side</i>	<i>Non-component side</i>	<i>Stream-wise edge</i>
Stage 1	180	37	29	35
Stage 3, individually powered	180	37	29	35
Stage 3, simultaneously powered	235	47	44	35

**Note:** All dimensions are in millimetres. Computational models constructed using Flotherm.

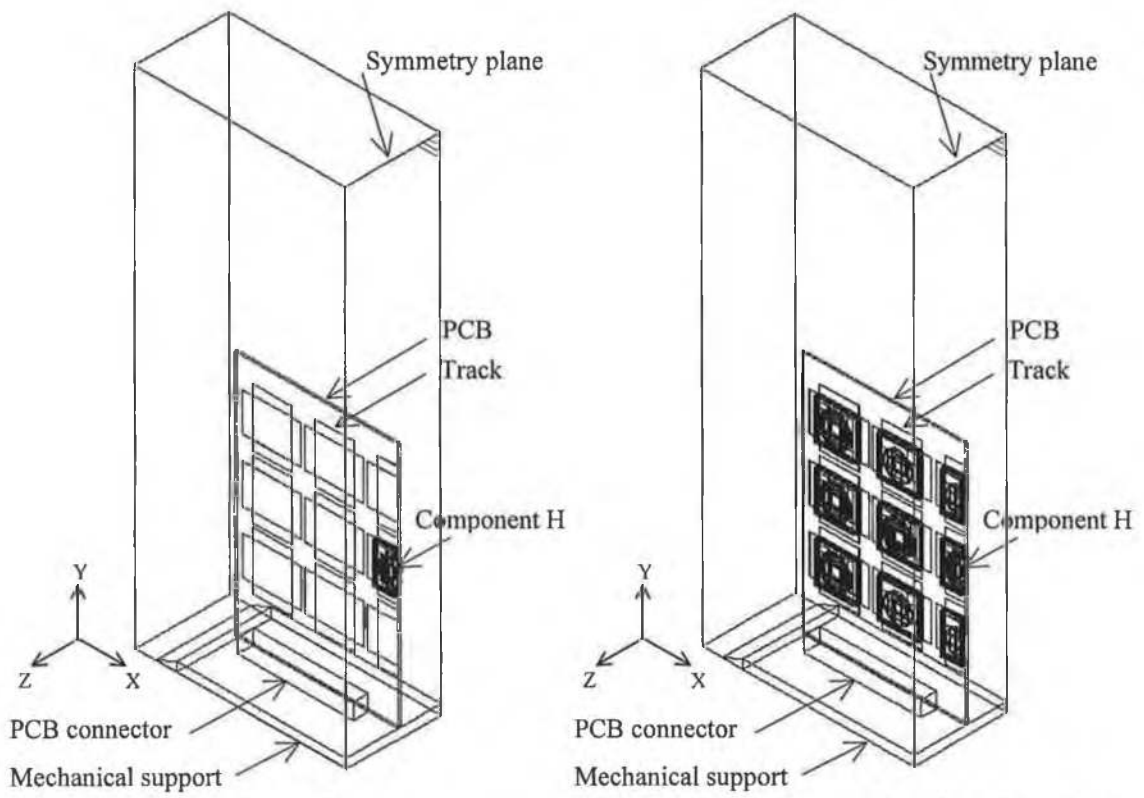
**Table 4.18** Computational domain size and grid discretization details for the Stage 1 and non-insulated Stage 3 free convection numerical models.

	<i>Stage 1, Stage 3, individually powered</i>				<i>Stage 3, simultaneously powered</i>			
	<i>x</i>	<i>y</i>	<i>z</i>	<i>Total, xyz</i>	<i>x</i>	<i>y</i>	<i>z</i>	<i>Total, xyz</i>
Domain size (mm)	151.5	365.0	67.6	---	303.0	420.0	92.6	---
Computational grid	171	243	87	3,615,111	237	172	92	3,750,288

**Note:** x, y and z co-ordinates refer to the span-wise, stream-wise and transverse flow directions respectively, Figure 4.14. Computational models constructed using Flotherm.

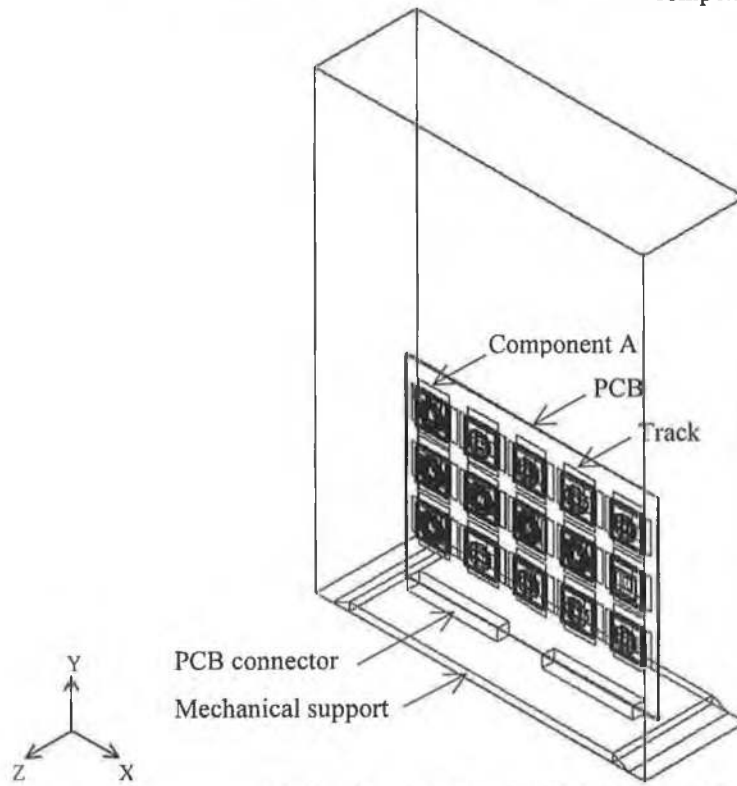
The fluid domain was solved as laminar and steady for all test configurations, with variable fluid property treatment applied. In addition, for the simultaneously powered Stage 3 case the flow field was also solved as unsteady.

Radiative heat transfer was modelled from the component top and bottom surfaces, PCB's FR-4 substrate and copper tracking surfaces. These surfaces were specified to radiate to a black body source external to the computational domain, whose temperature was prescribed at ambient surroundings. Radiating surfaces were finely subdivided to capture the influence of steep surface spatial temperature gradients.



(a) Stage 1 PCB

(b) Individually powered Stage 3 configurations, components (A-C, F-H, E-M)

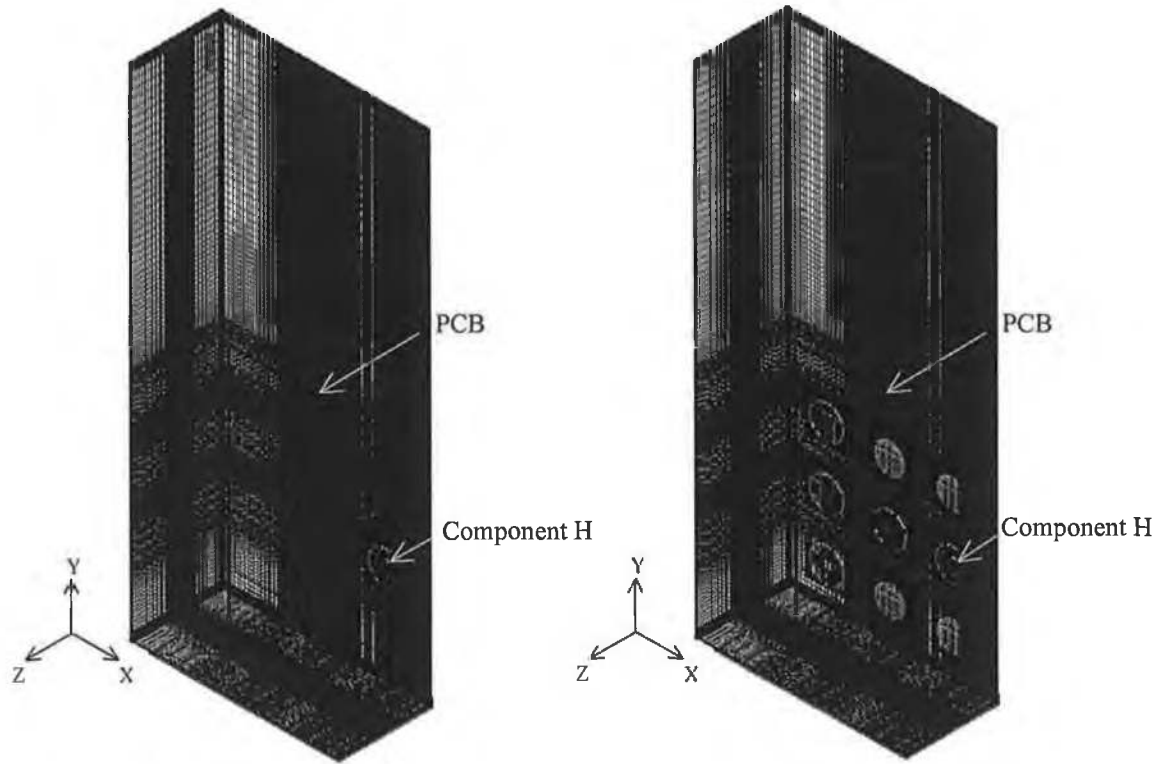


(c) Simultaneously powered Stage 3 configuration

Note: Unmarked computational domain boundaries are free-air boundaries. Gravity vector acts in (-y) direction. Computational models constructed using Flotherm.

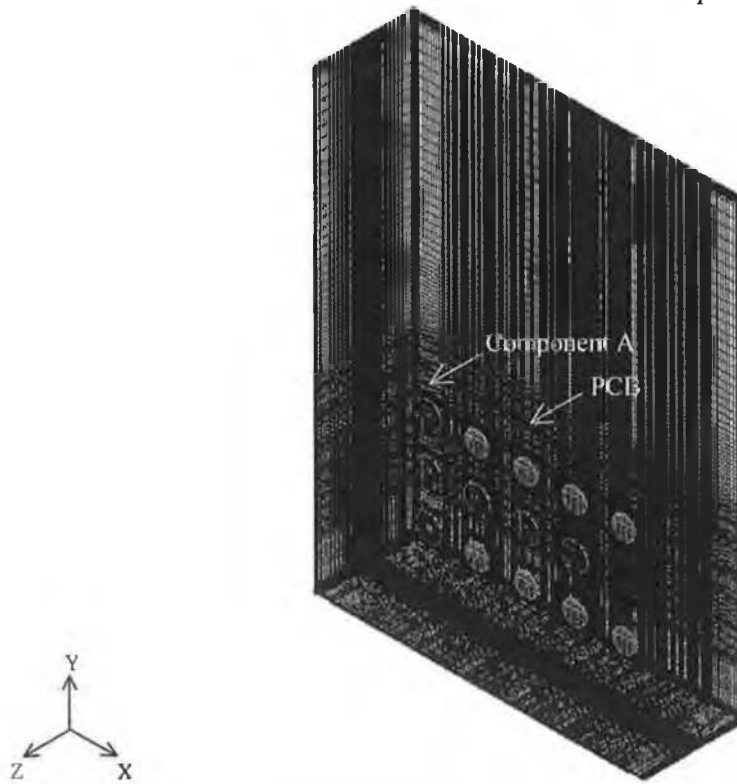
Figure 4.14 Non-insulated Stage 1 and 3 free convection numerical models.





(a) Stage 1

(b) Individually powered Stage 3 configurations, components (A-C, F-H, E-M)



(c) Simultaneously powered Stage 3 configuration

Note: Computational grid discretization details given in Table 4.18. Models constructed using Flotherm.

**Figure 4.15** Computational domain discretization grid applied for the free convection, non-insulated Stage 1 and 3 numerical models shown in Figure 4.14.

For the individually powered component configurations all solutions obtained were fully converged. However for the simultaneously powered case, the residual error sums for the respective variables could only be reduced to within 10% of their termination error levels when solving the flow as steady. The residual errors for all variables were found to be located within the thermal plume above the board. Note that grid aspect ratios were maintained within satisfactory ranges to minimise convergence difficulties. Convergence difficulties were therefore suspected to be caused by an instability in the thermal plume. This was supported by the calculated local Grashof number in the plume, on order  $10^8$ , which indicated that this flow was transitional [267,268]. Consequently, convergence for component junction temperature was assessed by monitoring this variable with outer iteration count. Component junction temperatures were found to remain invariant with iteration after stabilising, indicating that the predicted downstream instability did not adversely impact on PCB heat transfer. This was verified by solving the flow as unsteady, which led to improved convergence of the plume, but yielded the same junction temperature predictions as the steady-state model. The unsteady model predicted the plume to oscillate in the transverse flow direction at a very low frequency, approximately 0.03 Hz. However, the flow field over the board was predicted to be steady, which is in line with Drabbels [156], who encountered a similar modelling situation. Solving the flow as turbulent was also investigated, though not justified on the basis of either the board Grashof number, or that of the plume. The code's two-equation k- $\epsilon$  turbulence model, with revised wall function formulation, was employed. The predicted component junction temperatures were found to be on average 5°C lower than those obtained using the laminar flow model. Additionally, the k- $\epsilon$  flow model predicted the board boundary layers to turbulently expand, instead of merging into a single plume downstream of the PCB trailing edge, as experimentally visualised by smoke flow visualisation [201]. The use of the k- $\epsilon$  model was therefore not appropriate in this instance.

#### **4.6.1.2 Forced Convection**

In this section the computational models constructed using Flotherm for the Stage 1, 2 and 3 test configurations, and built in Icepak for the 4 m/s non-insulated Stage 1 and 3 configurations are described.

##### Flotherm Computational Models, Stages 1 to 3

The forced convection numerical models are shown in Figure 4.17 for Stages 1 and 2, and in Figure 4.18 for Stage 3. The computational domains were confined to the fluid domain in the vicinity of the PCB, to permit the computational grid to be effectively used

to focus on the resolution of the component-PCB thermofluids. The following artificial boundaries were imposed at a sufficient distance from the PCB assembly so that no significant unintentional elliptical effects were introduced. A uniform free-stream inlet velocity boundary condition was applied upstream of the PCB leading edge, and a pressure outlet boundary was positioned downstream of the PCB trailing edge. Free-stream boundaries were applied parallel to the PCB component- and non-component sides, and its stream-wise edge. These boundaries fixed the relative pressure to zero with any incoming air entering at both the prescribed ambient temperature and inlet free-stream velocity. Their location relative to the PCB are defined in Table 4.19 for both the non-insulated and insulated models. For turbulent flow analysis turbulence intensity was specified at 2% at the domain inlet boundaries, with the prescription of this boundary condition detailed in Appendix C for the k- $\epsilon$  flow model.

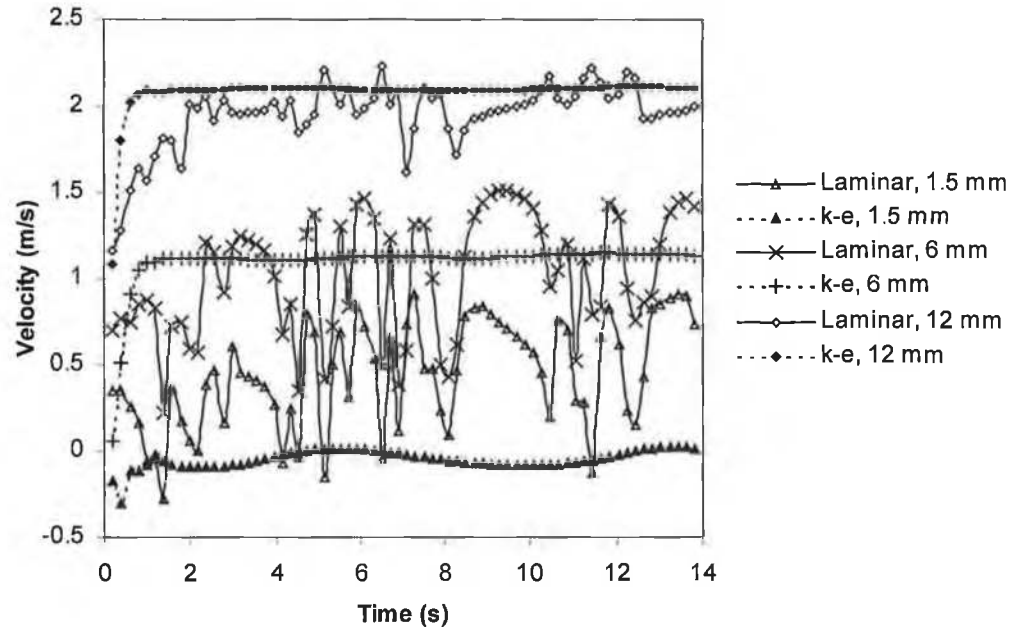
The fluid domain was solved using both laminar and turbulent flow models. For turbulent flow analysis, both the LVEL model, and the high-Reynolds number k- $\epsilon$  model with revised wall functions, were employed.

Based on experimental flow visualisation, the flow field was solved as steady for all analyses, with the exception of the insulated Stage 3 case at 2 m/s. This flow field was modelled as unsteady. It is acknowledged that the k- $\epsilon$  model is not suited to the analysis of the unsteady flow over the insulated PCB at 2 m/s. This is reflected in the time-invariant flow field predictions above component G at 2 m/s, plotted in Figure 4.16. However, as evident in the same figure, the laminar model does predict flow unsteadiness. The time invariance of the k- $\epsilon$  predictions possibly results from an overprediction of the turbulent viscosity damping out any transient flow features. This hypothesis is in line with the fact that the k- $\epsilon$  model yielded component junction temperature predictions that were within 2°C of those obtained when the flow field was solved as steady. However, the k- $\epsilon$  model was assessed for this case to reflect normal design scenarios, where there is no *à priori* knowledge of the flow regime, and whether it is steady or unsteady.

Variable fluid property treatment was applied for all analyses.

Radiation heat transfer was modelled in the same manner as for the free convection analyses, though its contribution was considerably lower in this instance.

For each test configuration a generic grid was employed to permit the application of both laminar and turbulent flow models. To resolve these flow features, the grid was constructed to meet the k- $\epsilon$  flow model gridding requirements at 4 m/s, which necessitated the finest detail.



**Note:** Distance given is the transverse location of the flow field monitor point above the centre of the package top surface.

**Figure 4.16** Numerically predicted flow unsteadiness in the stream-wise direction above component G on the insulated Stage 3 PCB in a 2 m/s airflow.

For the non-insulated PCB, the following approach was employed to guide the gridding of the near-wall fluid domain. The board non-component side can be considered as a flat plate over which the boundary layer can be characterised as a classical unheated starting length problem. Thus, the PCB hydrodynamic boundary layer would develop at the PCB leading edge, with the thermal boundary layer developing further downstream, depending on component topology and powering configuration. This is due to PCB heat spread being confined to the vicinity of the component, as shown by the infrared thermographs in Figure 3.17. The near-wall grid applied must resolve both boundary layers, with the thermal boundary layer being the thinner. As a starting point the board Reynolds number based on stream-wise length was calculated to be  $5.9 \times 10^4$  at 4 m/s. This value is less than  $1 \times 10^5$ , indicating that a laminar velocity boundary layer exists on the PCB non-component side. The corresponding hydrodynamic boundary layer growth can be estimated using the following analytical expression presented by Incropera and De Witt [269]:

$$\delta_L = \frac{5L}{\sqrt{Re_L}} \quad (4.3)$$

where  $\delta_L$  is the hydrodynamic boundary layer thickness,  $L$  is the PCB length in the stream-wise direction, and  $Re_L$  is the PCB Reynolds number.

Using Equation (4.3), the transverse hydrodynamic boundary layer thickness at the PCB trailing edge was calculated to be 4.8 mm at 4 m/s. The near-wall distance from the PCB non-component side corresponding to the thinner boundary layer thickness of 4.8 mm, was discretized using 13 grid cells spaced by a power-law grid distribution. The first fluid grid node was set at 71  $\mu\text{m}$  distance from the PCB surface, coinciding with the copper tracking surface.

On the PCB component side, Equation (4.3) is not directly applicable to calculate the board boundary layer growth due to component interaction. Nevertheless, the fluid domain in vicinity of the PCB surface was more finely resolved by the transverse grid imposed by the component architecture. To resolve the flow detail above the component surface, gridding of the near wall region followed the guidelines outlined by Burgos et al. [236] and Anderson [163]. Anderson found that the non-dimensional wall co-ordinate,  $y^+$ , needed to be less than 2, whereas Burgos et al. proposed that the distance from the wall equivalent to  $y^+ \approx 11.5$ , which defines the demarcation between the application of the linear and logarithmic laws-of-the-wall, be discretized by six cells uniformly spaced. The latter analysis is more easily applicable as in contrast to Anderson [163], the wall shear stress value is not required to be calculated for estimating  $y^+$ . Instead, Burgos et al. [236] propose the following empirical correlation to estimate the thickness of the viscous sub-layer:

$$\frac{y_s}{L} = 0.3966 - 0.0996 \log_{10}(\text{Re}_L) \quad (4.4)$$

where  $y_s$  is the distance from the wall equivalent to  $y^+ \approx 11.5$ ,  $L$  is the component length in the stream-wise direction, and  $\text{Re}_L$  is the Reynolds number based on component length.

Thus, for 4 m/s airflow velocity, Equation (4.4) yields that the first six fluid grid cells should be uniformly distributed within 0.373 mm from the component surface respectively, with near wall grid cells of 62  $\mu\text{m}$  thickness. It should be noted that both Burgos et al. and Anderson's recommendations were developed for large component bodies, such as the PQFP 160, where package top surface was the dominant heat dissipating path. In these studies therefore, high heat dissipation sensitised the modelling of convective heat transfer from the package top surface, thereby leading to fine gridding requirement in the near-wall region. This approach may however result in excessive gridding when applied to the present models, as only one third of the component heat loss was dissipated from the package top surface, Table 7.12. Therefore, the grid detail calculated using Burgos et al. criterion was modified by placing only four transverse grid cells within the distance defined by Equation (4.4) using a power law grid distribution, with the first fluid grid cell extending 71  $\mu\text{m}$  from the package surface.

The remaining portions of the fluid domain both on the board non-component side and above the component surface were modelled using a power law grid spacing distribution in the transverse direction, with increasing cell size towards the domain boundaries. The Stage 1 and 2 numerical models were derived from that of the non-insulated Stage 3 by depopulating the PCB of the unnecessary components, without altering the computational grid.

For the insulated Stage 3 PCB configuration, the gridding detail on the board component side was maintained as for the non-insulated case above. However, the grid on the board non-component side was redistributed to account for the elliptical insulation block.

The computational grid volumes used were of order 4 million grid cells, details of which are given in Table 4.20. Prediction sensitivity to finer grid resolution was investigated using half geometry models, with a symmetry boundary condition applied along the PCB central stream-wise axis (Plane X-X, Figure 3.6(a)). This approximation was made as worst-case asymmetry in measured component junction temperature in the span-wise direction about the PCB central stream-wise axis did not exceed 3.5°C on the insulated Stage 3 PCB. While the use of half geometry model would therefore be inappropriate to report predictive accuracy, it did permit grid sensitivity to be evaluated by doubling the overall grid volumes given in Table 4.20. Using these finer grids, junction temperature predictions varied by less than 1.5°C and 3°C for the non-insulated and insulated cases respectively, relative to the standard grid details applied to half board geometry. As will be shown, the magnitude of prediction errors reported typically exceeded these variations. Furthermore, net accuracy did not necessarily improve with the combined effects of the symmetry modelling and grid refinement. All models were verified to produce solutions that were independent to computational domain size, for either flow model applied and free-stream air velocity.

**Table 4.19** Location of applied artificial boundary conditions relative to the PCB for the forced convection Stages 1, 2 and 3 numerical models, Figures 4.17 and 4.18.

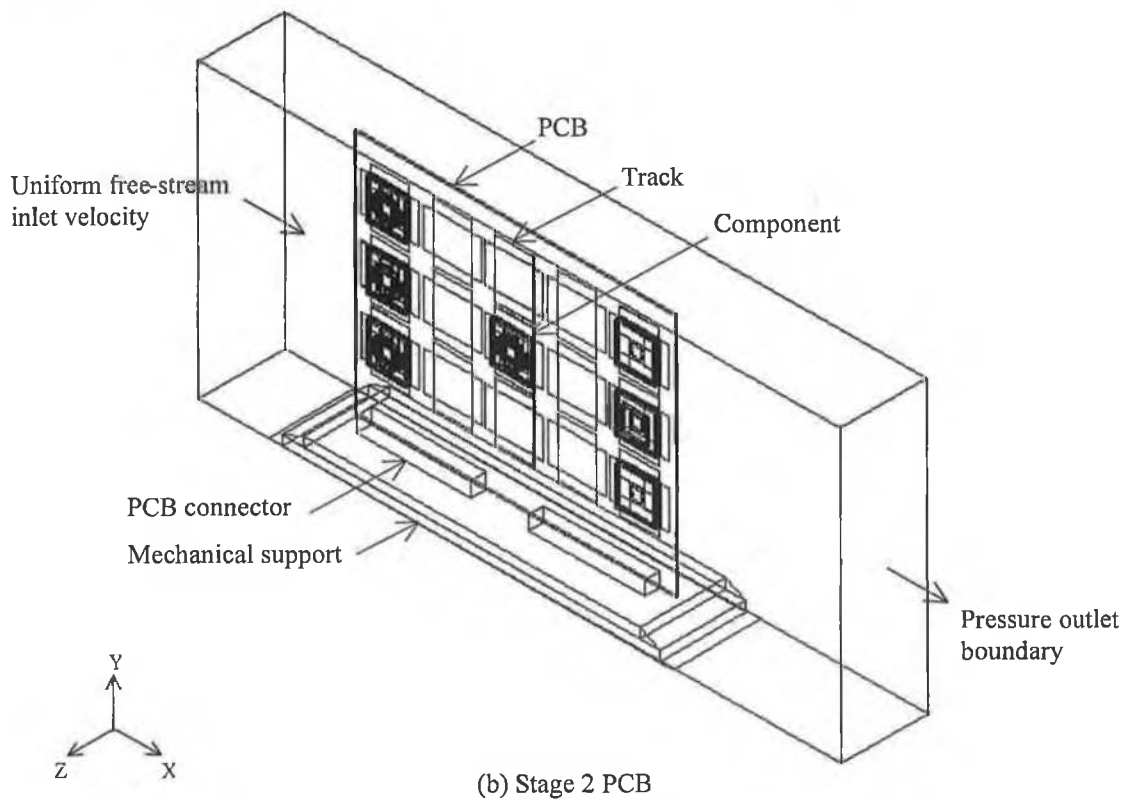
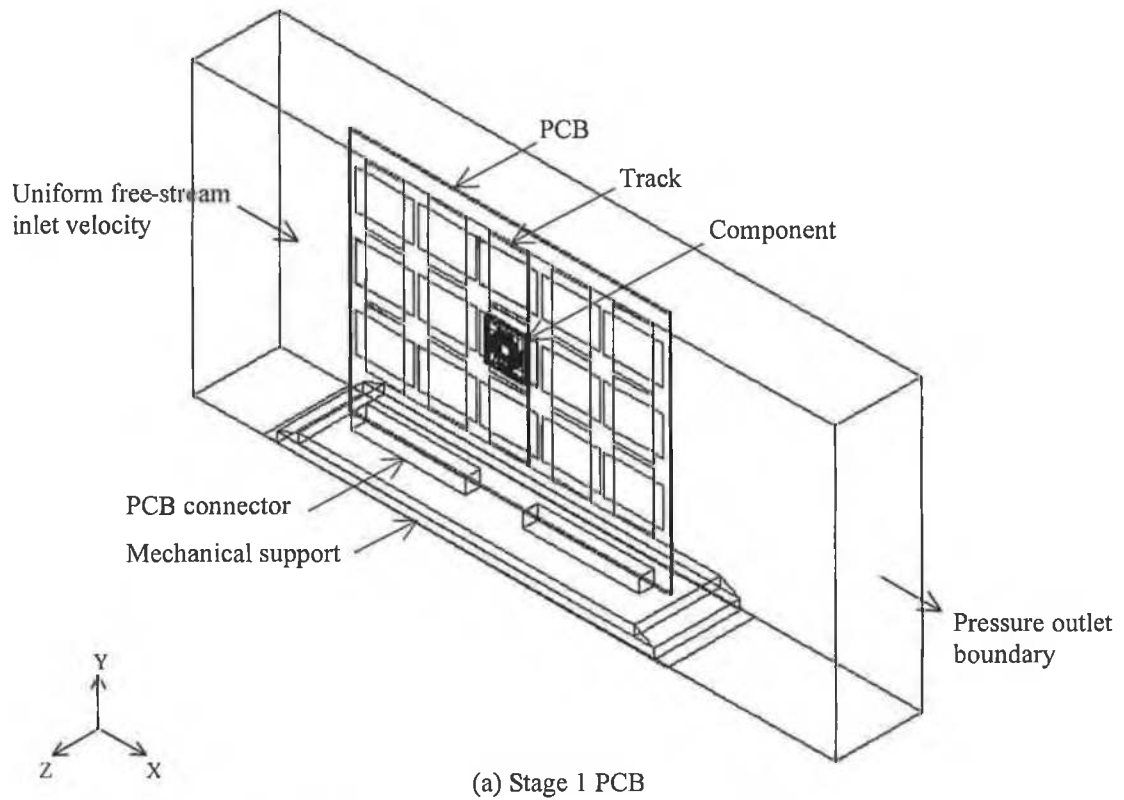
PCB model	Inlet	Outlet	Free-stream boundaries		
			Component side	Non-component/ insulation side	Stream-wise edge
Non-insulated	80	150	32	29	20
Insulated	100	150	65	50	37

Note: All dimensions are in millimetres. Computational models constructed using Flotherm.

**Table 4.20** Computational domain size and grid discretization details for the forced convection Stages 1, 2 and 3 numerical models.

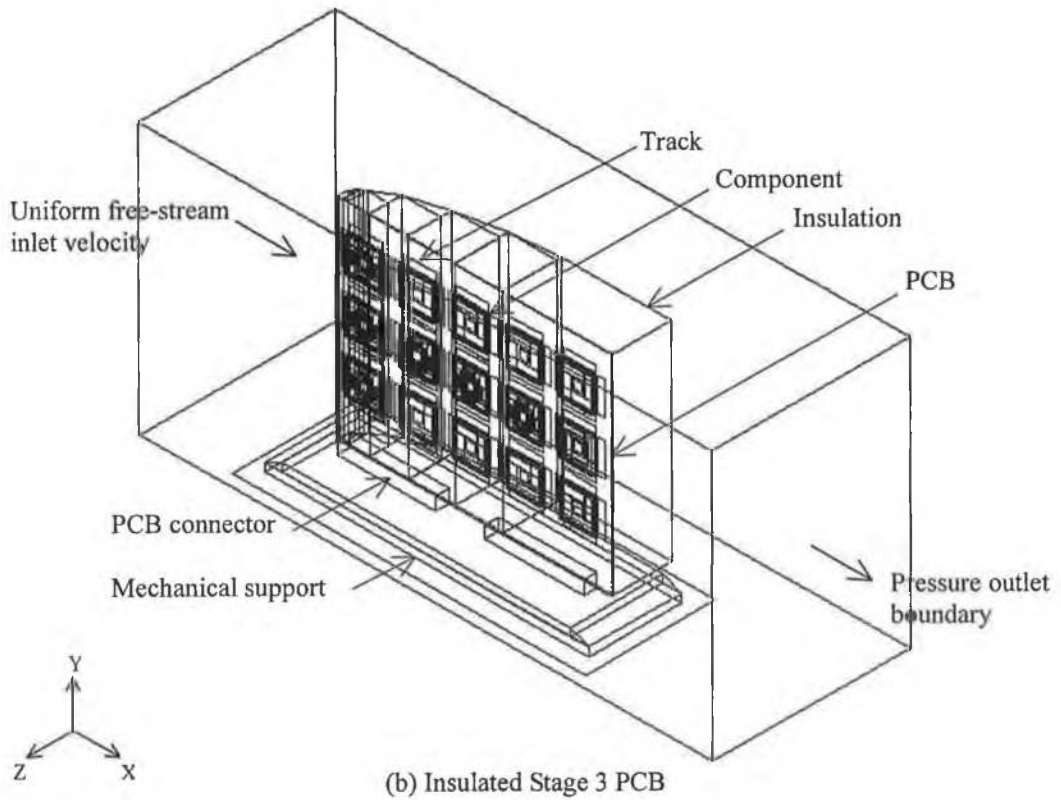
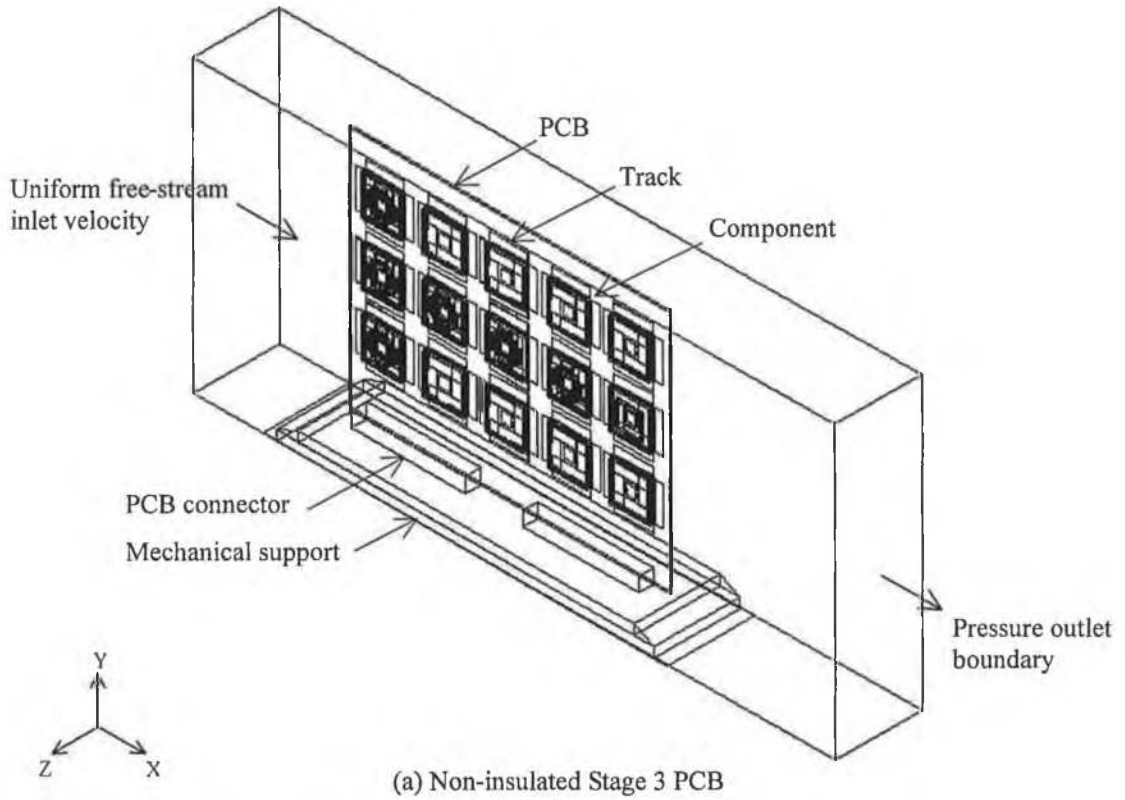
	Non-insulated PCB				Insulated PCB			
				Total, xyz				Total, xyz
Domain size (mm)	463	212	63	---	483	229	166	---
Computational grid cells	298	165	79	3,884,430	276	147	101	4,097,772

Note: x, y and z co-ordinates refer to the stream-wise, span-wise and transverse directions respectively, Figures 4.17 and 4.18. Computational models constructed using Flotherm.



**Note:** Unmarked computational domain boundaries are free-stream boundaries. Gravity vector acts in (-y) direction. Computational models constructed using Flotherm.

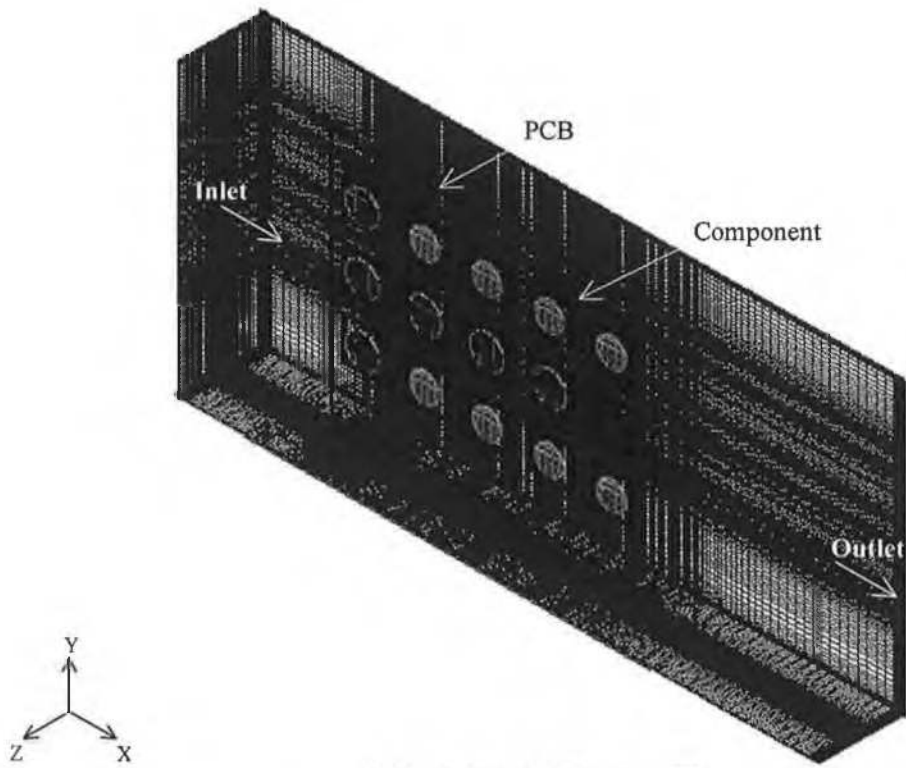
**Figure 4.17** Stages 1 and 2 forced convection numerical models.



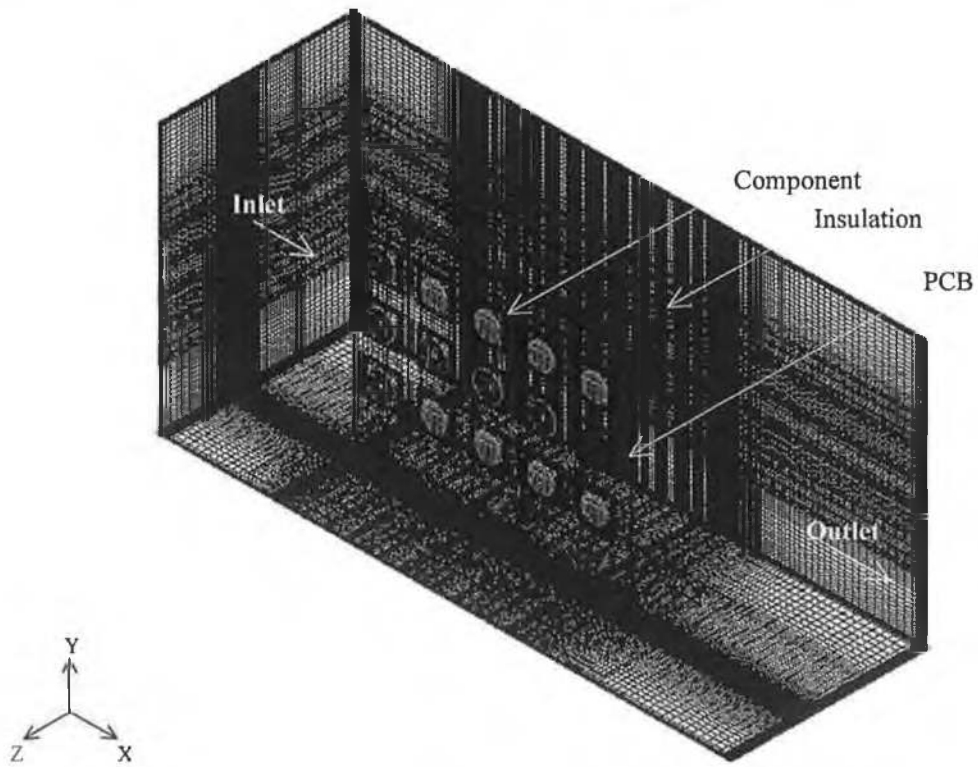
**Note:** Unmarked computational domain boundaries are free-stream boundaries. Gravity vector acts in (-y) direction. Computational models constructed using Flotherm.

**Figure 4.18** Stage 3 forced convection numerical models.





(a) Non-insulated Stage 3 PCB.



(b) Insulated Stage 3 PCB

**Note:** Computational grid discretization details given in Table 4.20. Models constructed using Flotherm.  
**Figure 4.19** Computational domain discretization grids applied to the Stage 3 forced convection numerical models shown in Figure 4.18.

While all turbulent flow solutions were fully converged, default convergence could not be obtained for laminar computations for the Stage 2 and 3 PCB configurations. For the insulated PCB cases, the residual error sums for pressure and x-velocity could only be reduced to within 6 % and 2% respectively of their termination error levels. The field errors for pressure were found to be located in the wake flow downstream of the board. As grid aspect ratios were maintained within satisfactory ranges to minimise convergence difficulties, it was suspected that the downstream domain outlet was not positioned at a sufficient distance from the PCB trailing edge to fully resolve the transient wake region. However, increasing the stream-wise length of the domain was computationally unfeasible as the grid volume already exceeded 4 million cells. Instead, to assess if convergence could be improved, a simplified PCB model was used, whereby both the component internal architecture and PCB copper tracking details were not modelled. As the software uses a structured grid, this permitted the superfluous grid detail that would otherwise be required to maintain low grid aspect ratios to be redeployed, thereby enabling the domain stream-wise length to be extended by 200 mm. However, convergence for pressure did not improve, while temperature predictions for the simplified components only changed by on average  $\pm 0.3^{\circ}\text{C}$  relative to those for the smaller domain. On this basis, it was concluded that the wake flow was sufficiently resolved so as not to adversely impact on component junction temperature prediction accuracy.

#### Fluent Computational Models, Stage 1 and Non-Insulated Stage 3

The numerical models for the Stage 1 and non-insulated Stage 3 test configurations, analysed in a 4 m/s airflow, are shown in Figures 4.20 and 4.21 respectively. As computational expenses associated with the unstructured mesh prohibited sufficient grid resolution to be applied to full board geometry models, computational constraints were eased by taking advantage of the symmetry of the heat transfer processes for each test configuration.

For the Stage 1 PCB, the numerical model was confined half board geometry, with a symmetry boundary condition applied along the PCB's central stream-wise axis. This symmetry plane was modelled as an adiabatic, frictionless and impermeable surface.

For the non-insulated Stage 3 PCB, worst-case asymmetry in measured component junction temperature in the span-wise direction about the PCB's central stream-wise axis (Plane X-X, Figure 3.6(a)), was  $\pm 1^{\circ}\text{C}$  about component I for the simultaneously powered configuration, Table 3.8. Taking advantage of this symmetry, the modelling of half board geometry was firstly evaluated, but computational constraints did not permit sufficient grid resolution to be applied to resolve the PCB thermofluids. Consequently, the suitability of

confining the model to the central stream-wise component row (components F - J), with symmetry planes applied at half component spacing between adjacent stream-wise component rows, Figure 4.21(a), was investigated. This was assessed using Flotherm, in which the complete board geometry could be modelled, Figure 4.18(a). For the high-Reynolds number  $k$ - $\epsilon$  model, component junction temperature predictions were only found to vary by a worst-case  $+0.9^{\circ}\text{C}$  and  $+0.7^{\circ}\text{C}$  for the individually and simultaneously powered component configurations respectively, relative to the predictions obtained by modelling the complete board geometry, using the same grid construction. This modelling approach was therefore appropriate, given the computational constraints. The symmetry boundary conditions were defined in the same way as for the Stage 1 numerical model.

The Stages 1 and 3 computational domains were constructed in a similar manner as the corresponding forced convection numerical models in Flotherm. A uniform 4 m/s free-stream velocity inlet boundary condition was applied upstream of the PCB leading edge, and a pressure outlet boundary was positioned downstream of the PCB trailing edge. Free-stream boundaries were applied parallel to the PCB component- and non-component sides. In addition for Stage 1, a free-stream boundary was also applied parallel to the PCB stream-wise edge. The location of these boundaries are defined in Table 4.21 for both models. Turbulence intensity was specified at 2% at the domain inlet boundaries, with the prescription of this boundary condition detailed in Appendix C for the respective turbulent flow models.

The fluid domain was solved as turbulent using the Spalart-Allmaras, two-layer zonal and SST  $k$ - $\omega$  models. The two-layer zonal model was employed in conjunction with both the standard high-Reynolds number  $k$ - $\epsilon$  and RNG  $k$ - $\epsilon$  flow models. Based on experimental flow visualisation the flow field was solved as steady, with variable fluid property treatment applied.

Radiative heat transfer was modelled from the component top and bottom surfaces, PCB's FR-4 substrate and copper tracking surfaces using the Discrete Ordinates model. In this instance, the gray radiation assumption was used, and the fluid treated as a non-participating medium.

The application of low-Reynolds number turbulence models necessitated a finer near-wall transverse grid resolution than required for the standard high-Reynolds number  $k$ - $\epsilon$  model. The non-insulated Stage 3 numerical model was discretized using an unstructured non-conformal hexahedral mesh, whereas a conformal mesh was employed for Stage 1. The non-conformal mesh permitted the superfluous grid cell volume in the far field upstream and downstream of the board, generated by the fine transverse grid in the vicinity of the PCB, to be redeployed to focus on the resolution of the PCB thermofluids. The first

fluid grid cell was set 35  $\mu\text{m}$  from the component- and board surfaces, which resulted in  $y^+$  values being on the order of unity.

The meshes obtained contained approximately 0.9 M and 1.5 M cells for Stages 1 and 3 respectively, with corresponding grid details given in Table 4.22. These grids are visualised in Figures 4.20(b) and 4.21(b) for Stages 1 and 3 respectively.

For the Stage 3 numerical model, the sub-domain defined by the inner mesh region was discretized using on order twice the grid resolution employed for the standard high-Reynolds  $k-\epsilon$  model in the same rectilinear volume. Using this mesh, the SST  $k-\omega$  model junction temperature predictions obtained using second-order accurate upwind scheme were found to differ by worst-case  $0.6^\circ\text{C}$  from those obtained using the first-order scheme, with negligible difference against the QUICK scheme. Mesh dependency of the solutions was also assessed using local adaptive solution features of the code to ensure an accurate resolution of the fluid temperature and velocity gradients. Mesh adaptation was found to have minimal impact on component junction temperature predictions in this instance. For Stage 1, increasing the grid volume to 1.5 M cells had negligible impact on junction temperature. Consequently, the mesh constructions given in Table 4.22 were considered as adequate for each model.

The solutions obtained were fully converged, with the normalised residuals for continuity, momentum, and the turbulent variables being less than  $5 \times 10^{-5}$ , and for energy and radiation intensity, less than  $10^{-9}$  and  $10^{-7}$  respectively.

**Table 4.21** Location of applied artificial boundary conditions relative to the PCB for the Stages 1 and 3 forced convection numerical models, Figures 4.20 and 4.21.

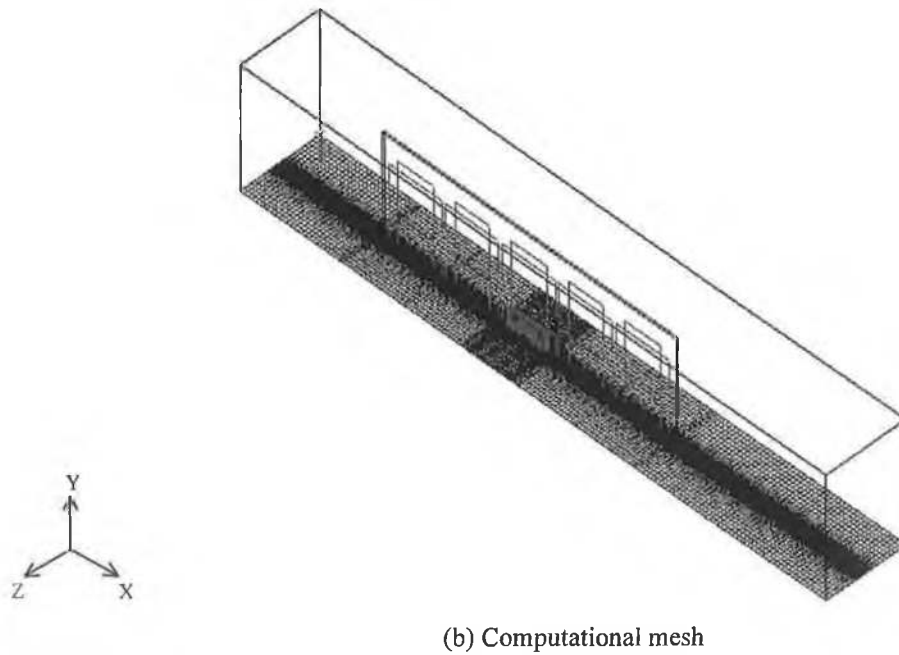
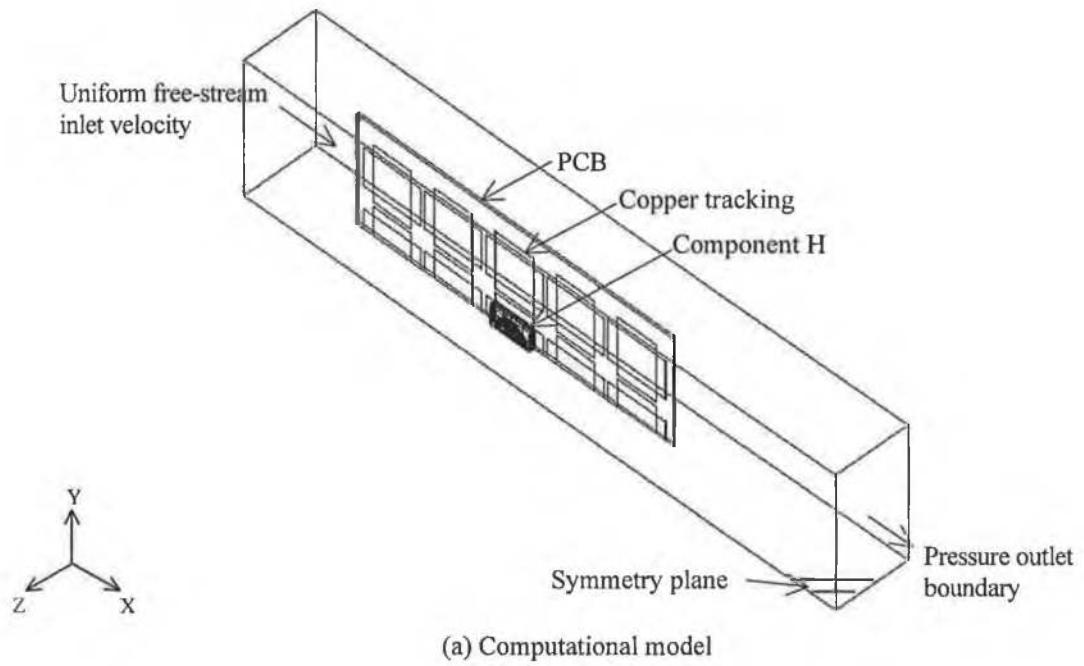
PCB model	Inlet	Outlet	Free-stream boundaries		
			Component side	Non-component/insulation side	Stream-wise edge
Stage 1 (half geometry)	80	150	32	29	20
Non-insulated Stage 3 (F - J)	55	150	30	27	---

**Note:** All dimensions are in millimetres. Computational models constructed using Icepak/Fluent.

**Table 4.22** Computational domain size and grid discretization details for the Stages 1 and 3 forced convection numerical models.

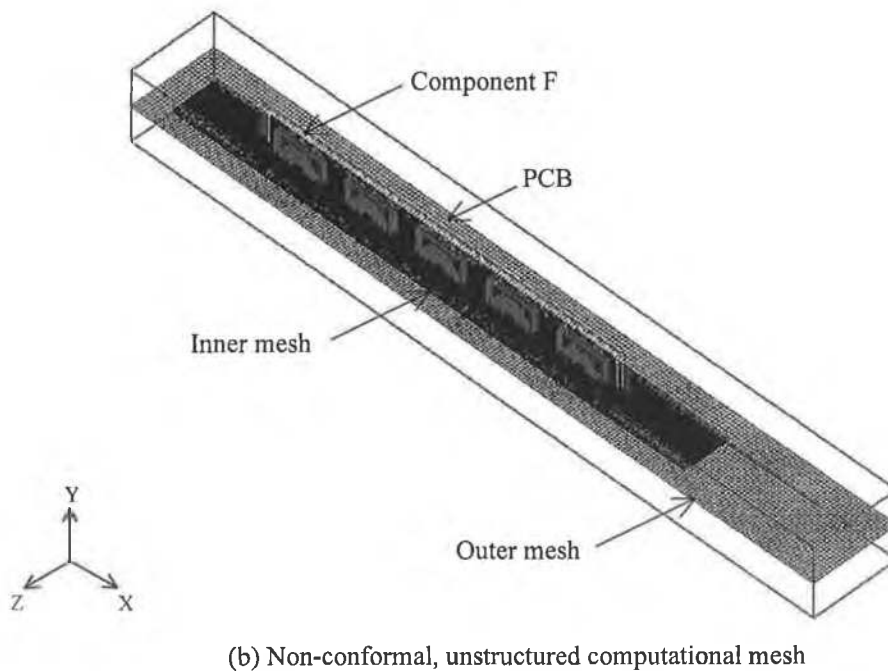
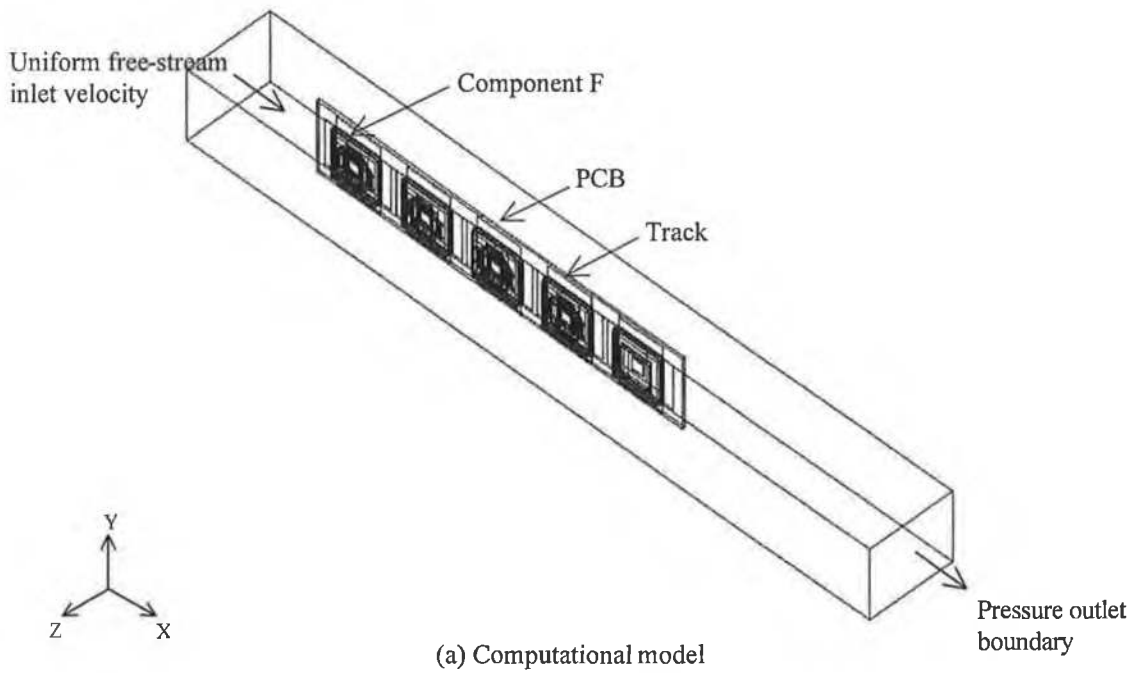
	Domain region	Stage 1 (half geometry)				Non-insulated Stage 3 (F - J)*			
		x	y	z	Total, xyz	x	y	z	Total, xyz
Domain size (mm)	Overall	463	100	63	---	438	45	58.6	---
	Inner	---	---	---	---	326	45	29.4	---
Computational grid cells	Overall	204	81	55	908,820	---			1,549,975
	Inner	---	---	---	---	---			1,463,200

**Note:** x, y and z co-ordinates refer to the stream-wise, span-wise and transverse directions respectively, Figures 4.20 and 4.21. \*Unstructured, non-conformal mesh, with Overall referring to the global computational domain, and Inner to the sub-domain discretized by the inner mesh. Computational models constructed using Icepak/Fluent.



**Note:** Unmarked computational domain boundaries in (a) are free-stream boundaries. Gravity vector acts in (-y) direction. Computational grid discretization details given in Table 4.22. Computational model constructed using Icepak/Fluent.

**Figure 4.20** Stage 1 forced convection numerical model (half geometry).



**Note:** Computational domain boundaries: z- and y-planes are defined as free-stream and symmetry boundary conditions respectively. Gravity vector acts in (-y) direction. Computational grid discretization details given in Table 4.22. Computational model constructed using Icepak/Fluent.

**Figure 4.21** Non-insulated Stage 3 forced convection numerical model (Central stream-wise component row, F - J).

#### 4.6.2 SEMI PCB Test Configurations

The numerical models for the single board-mounted PQFP 160 test configurations, presented in Sections 3.3 and 3.4 for steady-state and transient heat transfer respectively, are described here. Numerical analysis was undertaken using Flotherm, and the computational models are shown in Figures 4.22 and 4.23 for free and forced convection respectively.

*Free convection.* It was not necessary to extend the computational model to the enclosure walls as the enclosure roof did not adversely impact on the buoyant thermal plume emanating from the PCB assembly, and as there was negligible thermal stratification in the vicinity of the PCB assembly. Instead free-air boundary conditions were applied at the computational domain boundaries, positioned at a sufficient distance from the PCB assembly so that no significant unintentional elliptical effects were introduced. These free-air boundaries fixed the relative pressure to zero with any incoming air entering at the prescribed ambient temperature. Their location was approximately 62 mm from the PCB component- and non-component sides, 100 mm from both PCB vertical edges, flush with the bottom edge of the PCB, and 84 mm above the PCB top edge.

The board Grashof number, calculated from the thermographic measurements for steady-state heat transfer, was on order  $10^6$ . Consequently, the fluid domain was solved as laminar.

Radiative heat transfer was modelled from the component top and bottom surfaces, PCB FR-4 substrate and copper tracking surfaces. As outlined by Rosten et al. [103], it is not necessary to explicitly model the radiative exchange between the component-PCB surfaces and the enclosure walls, as the enclosure wall emissivity has negligible effect on the net radiative heat loss from the component-PCB. This is explained by the component-PCB radiation heat transfer being analogous to a small object radiating within a large cavity, for which gray-diffuse radiation heat transfer is analytically described by the following expression [270]:

$$q = \frac{\sigma A_1 (T_1^4 - T_2^4)}{\frac{1}{\varepsilon_1} + \left( \frac{A_1}{A_2} \right) \left( \frac{1}{\varepsilon_2} - 1 \right)} \quad (4.5)$$

where  $\sigma$  is the Stefan-Boltzmann constant,  $A_1$  and  $A_2$  are the small convex object and enclosure surface areas respectively, with  $T_1$  and  $T_2$  being the corresponding surface temperatures, and  $\varepsilon_1$  and  $\varepsilon_2$  the corresponding surface emissivities.

Thus from Equation (4.5), as the enclosure surface area is considerably larger than the

effective radiating area, the enclosure does not impact on the PCB net radiative heat loss. Therefore Rosten et al.'s [103] modelling approach can also be employed, whereby component-PCB surfaces are specified to radiate to a black body source at 20°C external to the computational domain. This method was applied to model radiation heat transfer from the component top and PCB surfaces.

*Forced convection.* For the forced convection models, a uniform free-stream velocity inlet boundary condition was applied 57.5 mm upstream of the PCB leading edge, and an outlet pressure boundary was positioned 100 mm downstream of the PCB trailing edge. The domain was extended to the wind tunnel test section walls in both the span-wise and transverse directions. The test section surfaces were modelled using the code's default friction setting for smooth surfaces. As discrepancies existed between the programmed and measured test section free-stream air temperature cycles, resulting from the thermal inertia of the heater, the experimentally recorded time-temperature profiles were modelled using a numerical heater located at the modelled test section inlet, Figure 4.23(a).

The calculated board Reynolds number for steady-state heat transfer at 4 m/s was on order  $2 \times 10^5$ , suggesting that the flow was possibly transitional [271]. Consequently, the fluid domain was solved as laminar for both free convection, and 1 m/s and 2.25 m/s airflows, and as both laminar and turbulent at 4 m/s. For turbulent flow analysis the standard high-Reynolds number k- $\epsilon$  flow model was employed. Variable fluid property treatment was applied.

Radiation was modelled as for the corresponding free convection analyses.

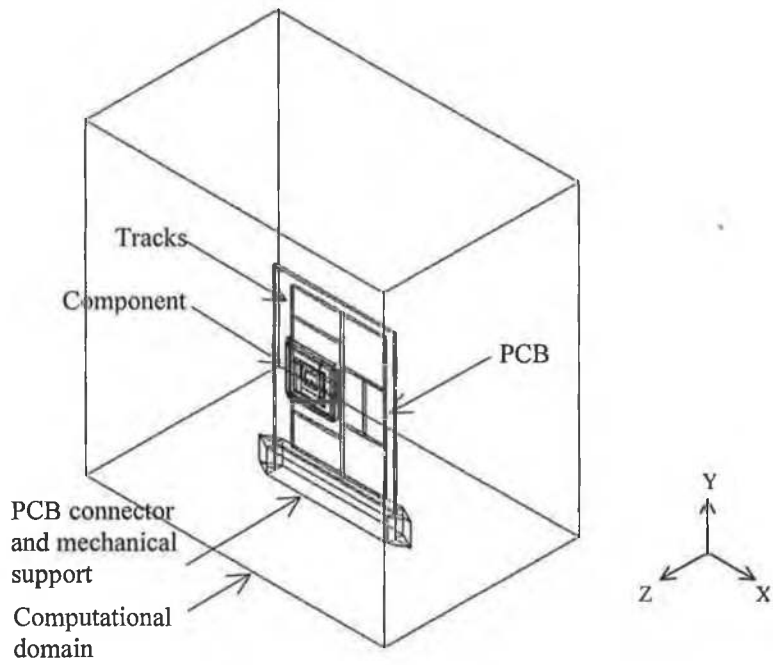
The spatial grid discretization details for both the free and forced convection numerical models are provided in Table 4.23, with the grids visualised in Figures 4.22(b) and 4.23(b). The grid construction followed similar guidelines as given for the populated board numerical models in Section 4.6.1.2. The solutions were verified to be grid-independent, with less than 0.5°C difference in junction temperature predictions obtained by halving the grid volumes given in Table 4.23.

**Table 4.23** Computational domain size and grid discretization details for the SEMI PCB free and forced convection numerical models, Figures 4.22 and 4.23.

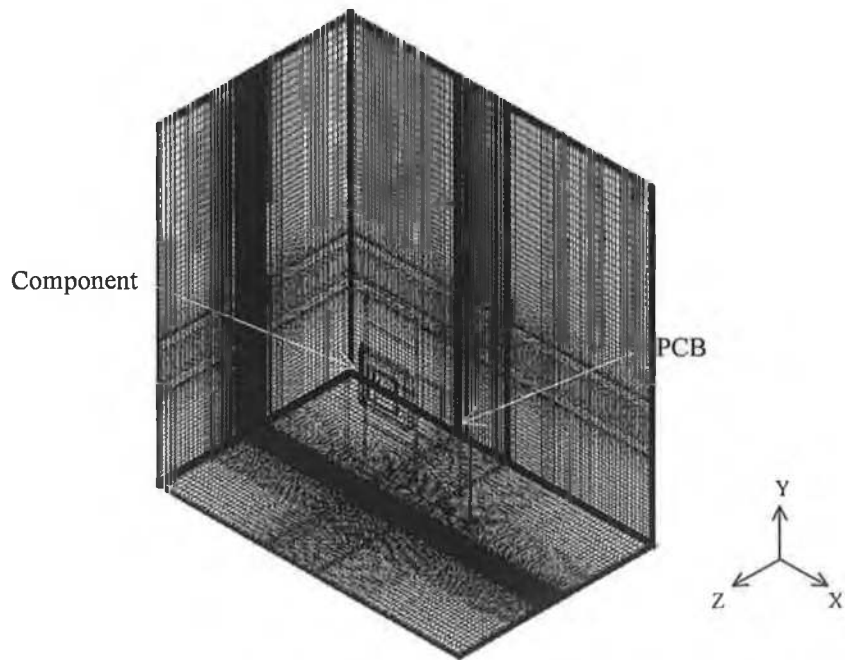
	<i>Free convection</i>				<i>Forced convection</i>			
	<i>x</i>	<i>y</i>	<i>z</i>	<i>Total, xyz</i>	<i>x</i>	<i>y</i>	<i>z</i>	<i>Total, xyz</i>
Domain size (mm)	193	200	125	---	235.5	128.0	125.0	---
Computational grid cells	124	93	114	1,314,648	132	79	114	1,188,792

**Note:** x, y and z co-ordinates refer to the direction of package width, length and height/the stream-wise, span-wise and transverse directions respectively.





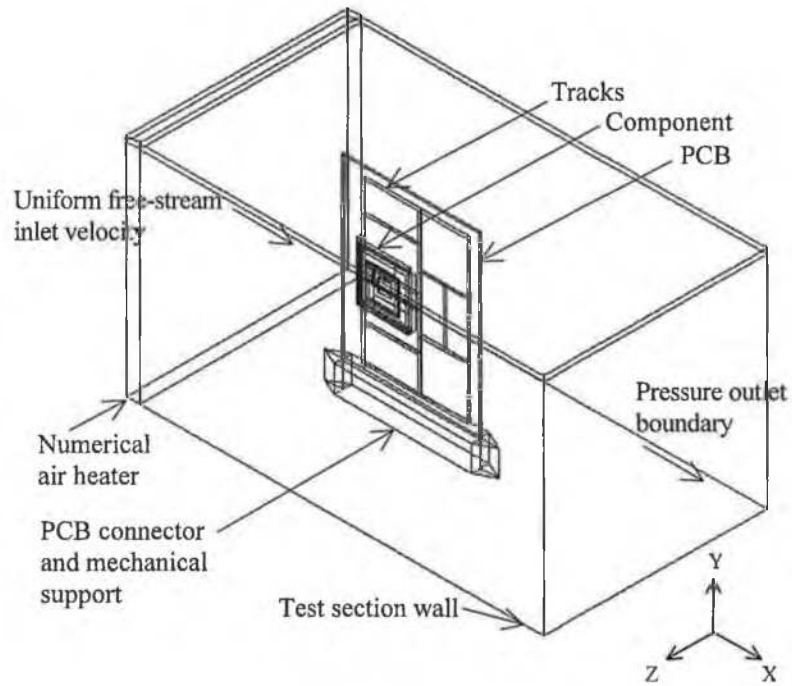
(a) Computational model



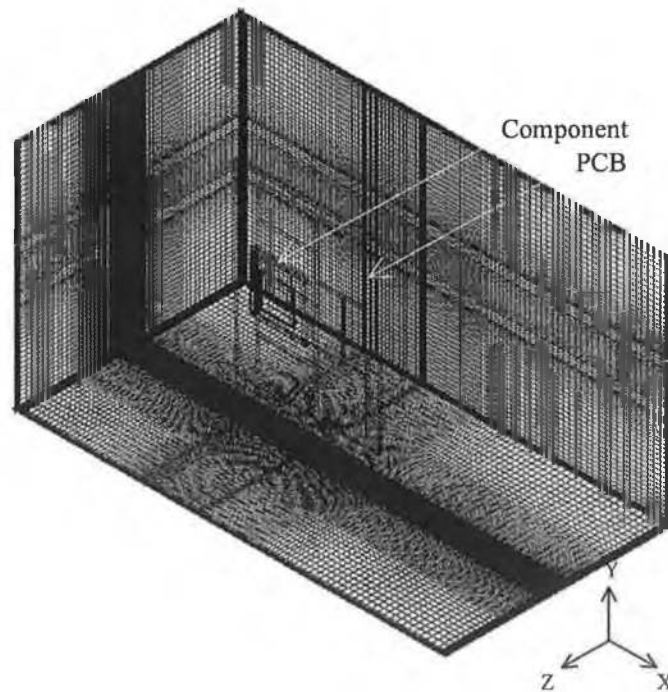
(b) Computational grid

**Note:** Computational domain boundaries are free-air boundaries, with the exception of the y-low plane, which is modelled as a wall boundary. Gravity vector acts in (-y) direction. Computational grid discretization details given in Table 4.23. Computational model constructed using Flotherm.

**Figure 4.22** Free convection numerical model for the single board-mounted PQFP 160 component.



(a) Computational model



(b) Computational grid

**Note:** Unmarked computational domain boundaries are wall boundaries. Gravity vector acts in (-y) direction. Computational grid discretization details given in Table 4.23. Computational model constructed using Flotherm.

**Figure 4.23** Forced convection numerical model for the single board-mounted PQFP 160 component.

For the analyses of the transient test configurations, both heat transfer and fluid flow were solved as unsteady. Non-uniform temporal grids were applied having highest density in the time intervals where high rates of temperature change were experimentally recorded on the test assembly. These grids were constructed using time steps ranging from 3 ms to 5 s. The solutions obtained were verified to be temporal grid independent.

All solutions were fully converged to the code's default settings.

#### **4.6.3 Compact Component Thermal Modelling Test Configurations**

Numerical models for the SO8 and PQFP 208 test configurations were previously presented by Lohan et al. [149,225] and Rodgers et al. [35] respectively, incorporating detailed component models. Lohan et al. analysed component heat transfer in both free convection [149] and 1 m/s airflow [225], and these analyses are extended here to both 2 and 5 m/s airflows. All analyses are undertaken using Flotherm.

The SO8 free and forced convection numerical models are shown in Figures 4.24 and 4.26 respectively, with the PQFP 208 forced convection model shown in Figure 4.28. The construction of the computational domains for free and forced convection heat transfer follows the approach taken for the single board-mounted PQFP 160 configurations in Section 4.6.2.

The computational domains used to incorporate the detailed component models represented quarter and half component-board geometry for free and forced convection respectively. These symmetry boundary conditions were permissible as infrared imaging showed that the component-PCB surface temperature profiles were symmetrical about the package centre in the directions of package length and width in free convection, and in the span-wise direction in forced convection, reflecting the symmetry of the heat transfer processes. Symmetry planes were modelled as adiabatic, frictionless and impermeable surfaces.

As Flotherm's Compact Component SmartPart does not support the use of a symmetry boundary condition, the complete component-board geometries required to be modelled to incorporate the CTMs.

For all models, the computational domains were confined to the fluid domain in the vicinity of the PCB to permit the computational grid to be effectively used to focus on the resolution of the component-PCB thermofluids.

For the SO8 free convection case, free-air boundary conditions were applied at the computational domain boundaries, fixing the relative pressure to zero with any incoming air entering at the prescribed ambient temperature. Their location relative to the PCB are defined in Table 4.24.

**Table 4.24** Location of applied artificial boundary conditions relative to the PCB for the SO8 free convection numerical models, Figure 4.24.

<i>Free-stream boundaries</i>		
<i>Component side</i>	<i>Non-component side</i>	<i>Edge</i>
50.0	25.0	11.9

Note: All dimensions are in millimetres.

**Table 4.25** Computational domain size and grid discretization details for the SO8 free convection numerical models.

	<i>Detailed component model (quarter geometry)</i>				<i>CTM (complete geometry)</i>			
	<i>x</i>	<i>y</i>	<i>z</i>	<i>Total, xyz</i>	<i>x</i>	<i>y</i>	<i>z</i>	<i>Total, xyz</i>
Domain size (mm)	50.0	50.0	76.6	---	100.0	100.0	76.6	---
Computational grid cells	68	64	116	507,832	136	129	116	2,035,104
Computational grid cells in [149]	44	51	47	105,468	---	---	---	---

Note: x, y and z co-ordinates refer to the direction of package width (leaded), length and height respectively, Figure 4.24.

For the forced convection cases, the computational domains were not extended to the walls of the wind tunnel test section as there was no flow interaction between the PCB in-plane surfaces and opposing parallel walls. Instead, free-stream boundaries were applied at a sufficient distance from the test assembly so that no significant unintentional elliptical effects were introduced. A uniform free-stream velocity inlet boundary condition was applied upstream of the PCB leading edge, and an outlet pressure boundary was positioned downstream of the PCB trailing edge. The location of the applied artificial boundary conditions relative to the PCB are given in Tables 4.26 and 4.28 for the SO8 and PQFP 208 models respectively.

**Table 4.26** Location of applied artificial boundary conditions relative to the PCB for the SO8 forced convection numerical models, Figure 4.26.

<i>Inlet</i>	<i>Outlet</i>	<i>Free-stream boundaries</i>		
		<i>Component side</i>	<i>Non-component side</i>	<i>Stream-wise edge</i>
30.0	43.8	25.4	25.0	11.9

Note: All dimensions are in millimetres.

**Table 4.27** Computational domain size and grid discretization details for the SO8 forced convection numerical models.

	<i>Detailed component model (half geometry)</i>				<i>CTM (complete geometry)</i>			
	<i>x</i>	<i>y</i>	<i>z</i>	<i>Total, xyz</i>	<i>x</i>	<i>y</i>	<i>z</i>	<i>Total, xyz</i>
Domain size (mm)	150	50	52	---	150	100	52	---
Computational grid cells	187	64	102	1,220,736	187	129	102	2,460,546

Note: x, y and z co-ordinates refer to the direction of package width, length and height/the stream-wise, span-wise and transverse directions respectively, Figure 4.26.

**Table 4.28** Location of applied artificial boundary conditions relative to the PCB for the PQFP 208 forced convection numerical model, Figure 4.28.

Inlet	Outlet	Free-stream boundaries		
		Component side	Non-component side	Stream-wise edge
30.0	44.0	38.4	25.0	12.0

Note: All dimensions are in millimetres.

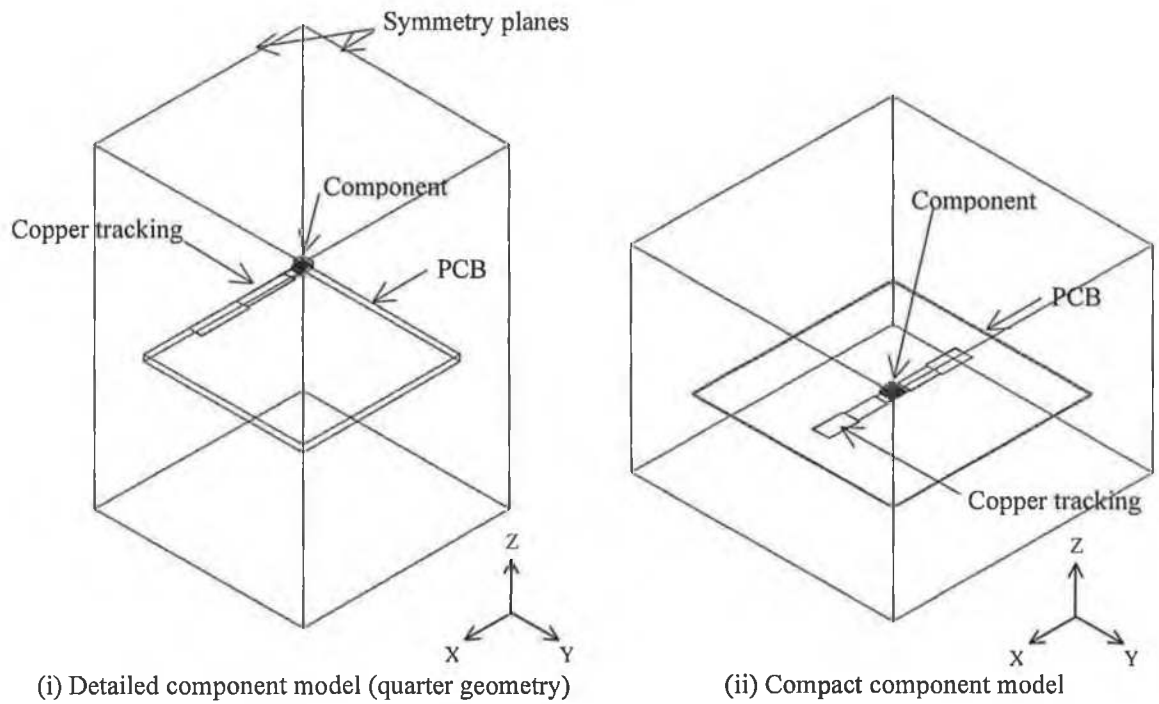
**Table 4.29** Computational domain size and grid discretization details for the PQFP 208 forced convection numerical models.

	Detailed component model (half geometry)				CTM (complete geometry)			
	x	y	z	Total, xyz	x	y	z	Total, xyz
Domain size (mm)	175.6	62.8	65.0	---	175.6	125.6	65.0	---
Computational grid cells	189	79	110	1,642,410	189	158	110	3,284,820
Computational grid cells in [35]	147	63	82	759,402	---	---	---	---

Note: x, y and z co-ordinates refer to the direction of package width, length and height/the stream-wise, span-wise and transverse directions respectively, Figure 4.28.

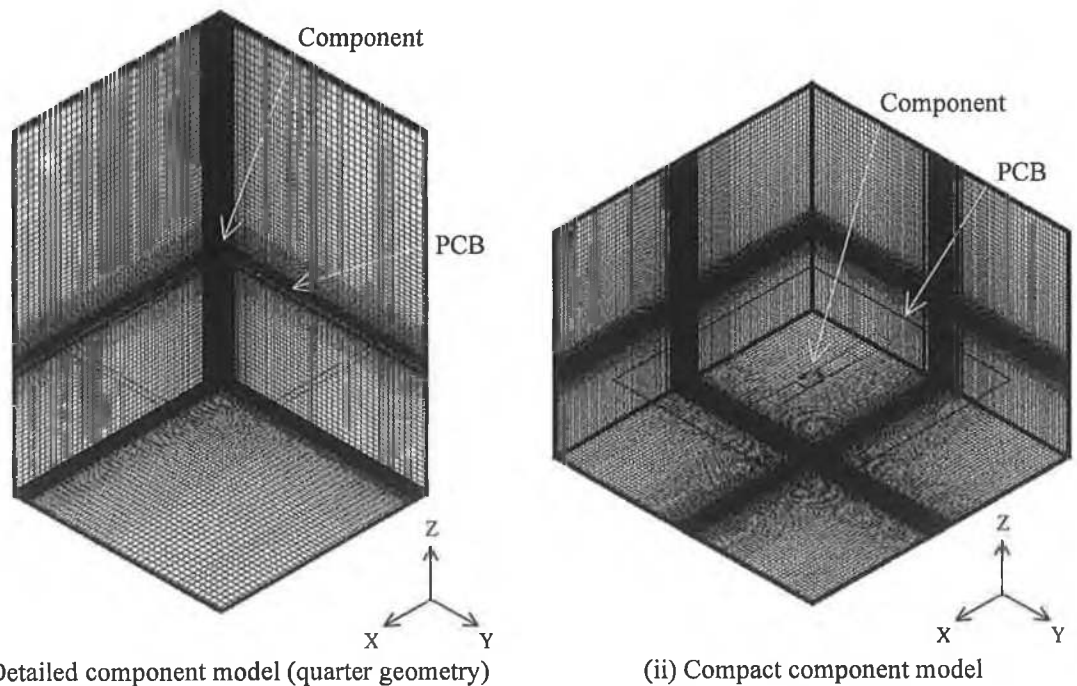
The fluid domain was solved as laminar for all test configurations, with the exception of the 5 m/s SO<sub>8</sub> case, which was solved using the standard high Reynolds k- $\epsilon$  flow model. However, predictive accuracy only decayed by 1°C using the laminar model for this case, indicating a low level of turbulent viscosity in the flow. Variable fluid property treatment was applied for all models. Radiative heat transfer was modelled from the PCB substrate and copper tracking surfaces, the component top and bottom surfaces for the detailed model, and the package top surface only for the compact model.

For each test case, the same computational domain grid construction was applied for compact and detailed component modelling. The grid details are given in Tables 4.25 and Table 4.27 for the SO<sub>8</sub> free and forced convection numerical models respectively, and in Table 4.29 for the PQFP 208 numerical models. These grids are visualised in Figures 4.25, 4.27 and 4.29 respectively, and were verified to produce grid independent solutions. The computational grid volumes employed for the complete SO<sub>8</sub> component-board geometry models were on order 2.0 and 2.5 million cells in free and forced convection respectively. For the PQFP 208 2 m/s case, a computational grid volume of approximately 2.3 M cells was employed for the complete geometry model. The grid employed for the SO<sub>8</sub> free convection model, was five times denser than that previously reported by Lohan et al. [149]. Lohan et al. [225] does not report the grid details for the corresponding forced convection analysis. For the PQFP 208 test configuration, the grid employed was twice as dense as that reported by Rodgers et al. [35].



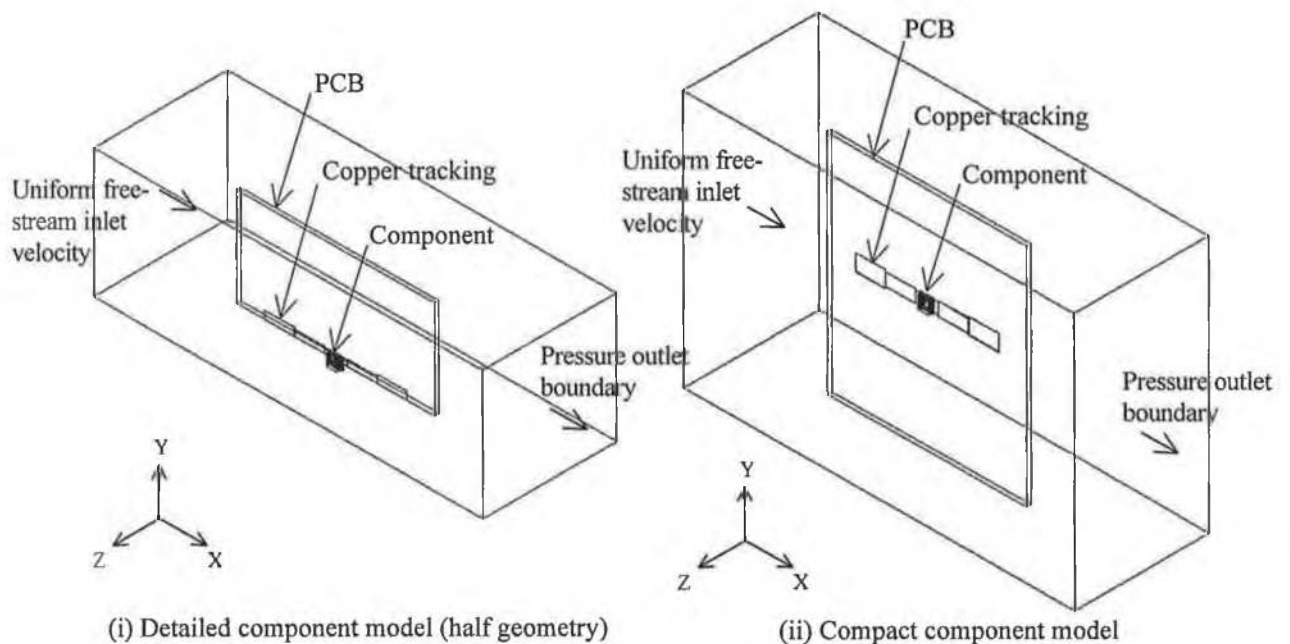
**Note:** Unmarked computational domain boundaries are free-air boundaries. Gravity vector acts in (-z) direction. Computational models constructed using Flotherm.

**Figure 4.24** Free convection numerical models for the single board-mounted SO8 component.



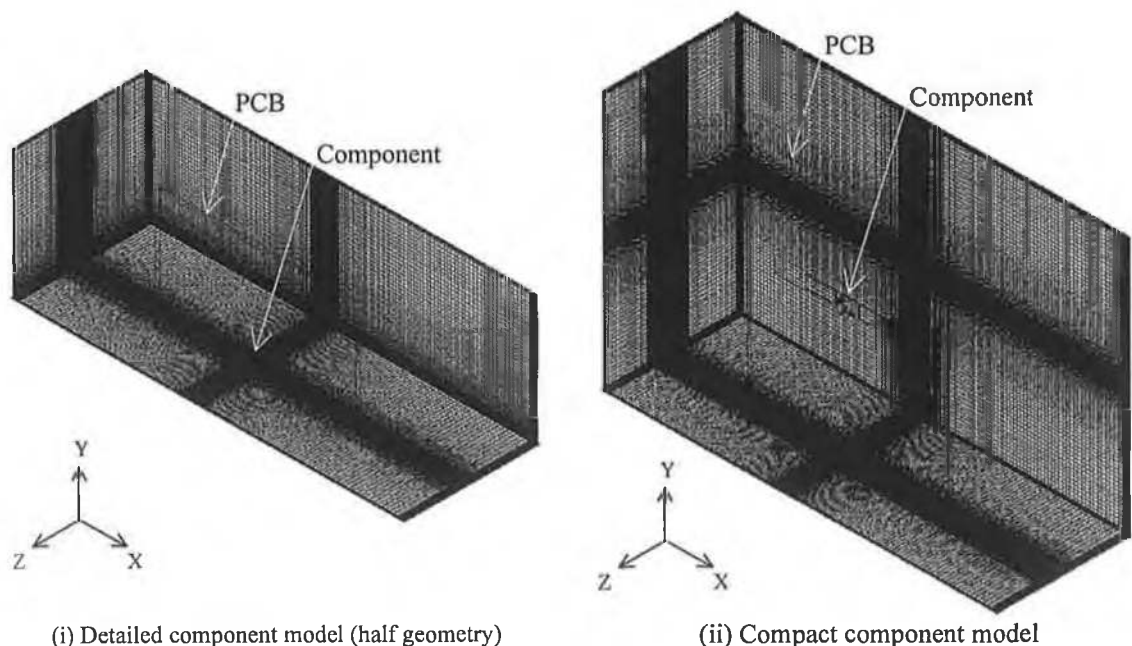
**Note:** Unmarked computational domain boundaries are free-air boundaries. Gravity vector acts in (-z) direction. Computational grid discretization details given in Table 4.25. Computational models constructed using Flotherm.

**Figure 4.25** Computational domain discretization grids applied to the free convection single board-mounted SO8 component numerical models shown in Figure 4.24.



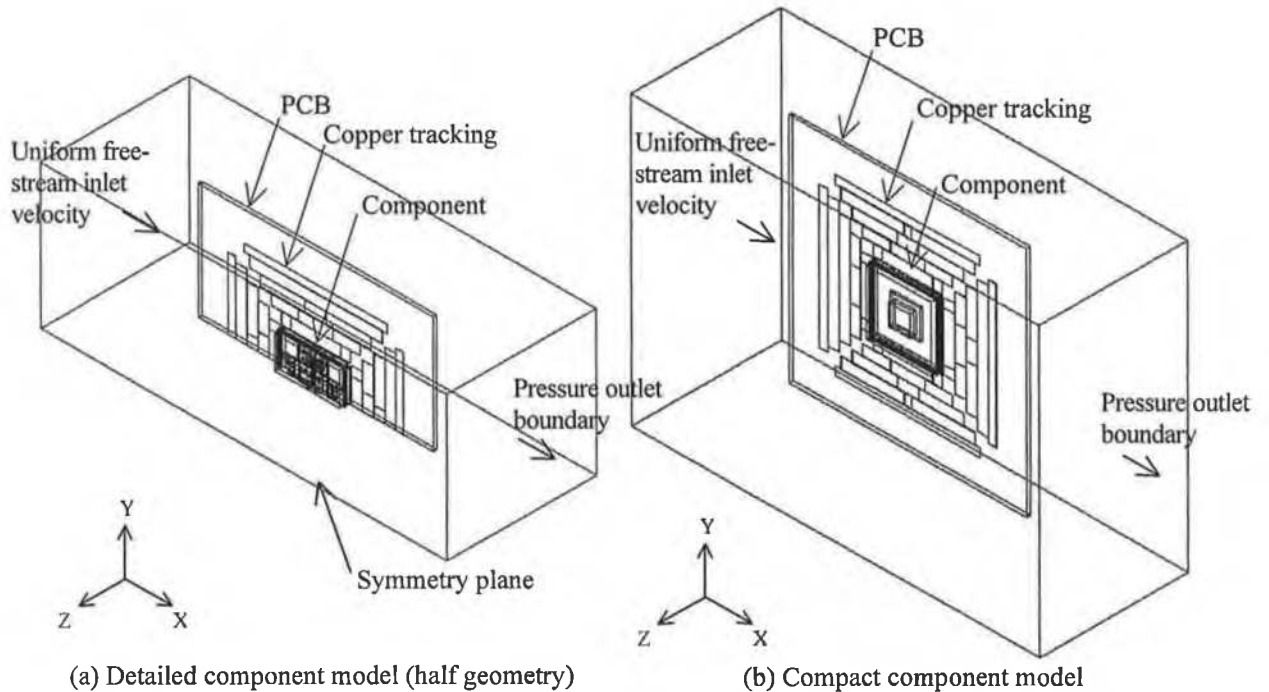
**Note:** Unmarked computational domain boundaries are free-stream boundaries. Gravity vector acts in (-y) direction. Computational models constructed using Flotherm.

**Figure 4.26** Forced convection numerical models for the single board-mounted SO8 component.



**Note:** Unmarked computational domain boundaries are free-stream boundaries. Gravity vector acts in (-y) direction. Computational grid discretization details given in Table 4.27. Computational models constructed using Flotherm.

**Figure 4.27** Computational domain discretization grids applied to the forced convection single board-mounted SO8 component numerical models shown in Figure 4.26.

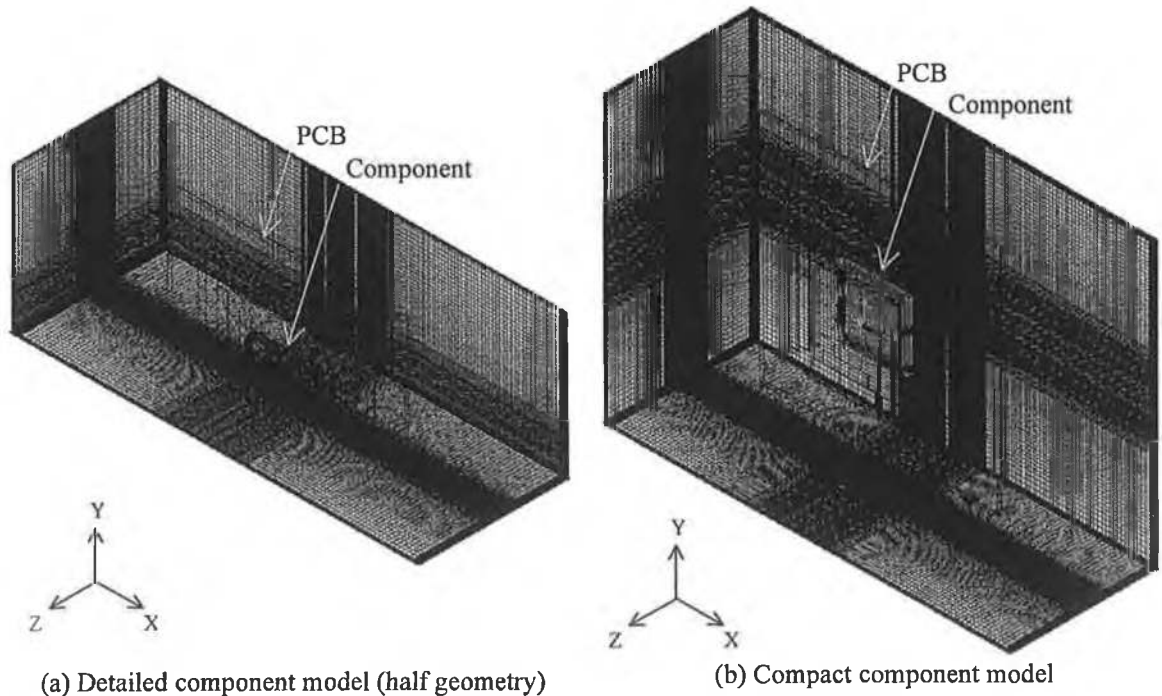


(a) Detailed component model (half geometry)

(b) Compact component model

**Note:** Unmarked computational domain boundaries are free-stream boundaries. Gravity vector acts in (-y) direction. Computational models constructed using Flotherm.

**Figure 4.28** Forced convection numerical models for the single board-mounted PQFP 208 component.



(a) Detailed component model (half geometry)

(b) Compact component model

**Note:** Unmarked computational domain boundaries are free-stream boundaries. Gravity vector acts in (-y) direction. Computational grid discretization details given in Table 4.29. Computational models constructed using Flotherm.

**Figure 4.29** Computational domain discretization grids applied to the forced convection single board-mounted PQFP 208 component numerical models shown in Figure 4.28.



It is acknowledged that such grid volumes are excessive for obtaining grid independent solutions. In addition, as the same gridding was applied to the compact and detailed component cases, these analyses do not permit the potential computational savings offered by component compact modelling to be highlighted. Such savings would be of value for system-level analyses, particularly using Cartesian grid systems, in which the component and board architectures generate grid bleeding into the fluid domain. Such aspects are outside the scope of the present study, which focuses on CTM predictive accuracy.

All solutions were fully converged to the software default settings.

#### **4.7 Summary**

CFD fluid flow modelling strategies for the analysis of electronic component heat transfer were reviewed. Methodologies for component and printed circuit board numerical modelling, and computational domain construction were outlined. The component numerical models were based on nominal package dimensions and material thermal properties.

Component junction temperature predictions for all models were computational domain independent and prediction sensitivity to grid resolution was quantified.

The numerical models defined for the single- and multi-component test configurations will be used in Chapters 5 to 7 to assess CFD predictive accuracy for component heat transfer using standard and alternative fluid flow modelling strategies.

## **5.0 Numerical Predictive Accuracy: Single Component Board Heat Transfer**

### **5.1 Introduction**

In this chapter, the detailed component-Printed Circuit Board (PCB) numerical modelling methodologies are assessed for both steady-state and transient heat transfer using the single-board mounted component configurations described in Sections 3.3 to 3.5.

Predictive accuracy is firstly assessed for steady-state component heat transfer, whereby the variable of thermal capacitance is eliminated. The validated component-PCB models will then be used in Chapters 6 and 7 to assess the capability of Computational Fluid Dynamics (CFD) analysis to predict multi-component board heat transfer.

Analysis of the transient component heat transfer configurations in this chapter will provide an insight into the potential of CFD to predict dynamic component thermal behaviour in thermal environments representative of those encountered in reliability testing and convective solder reflow assembly processes. The predictive performance of component compact thermal models (CTMs) implemented in a CFD environment is also evaluated for component steady-state heat transfer.

These analyses are undertaken using Flotherm. Acknowledging the difficulties in defining a dominant characteristic dimension, hence transition Reynolds number, that adequately describes the fluid flow regime in non-dimensional form over the PCB (Section 2.2), the fluid domain for the forced convection cases was solved using both laminar and turbulent flow models. The  $k$ - $\epsilon$  flow model predictions are the *à priori* predictions for turbulent flow analysis, with the LEVEL model only evaluated to provide a base-line accuracy for corresponding analyses of the populated boards in Chapter 7.

### **5.2 Validation of the PQFP 160 Component-PCB Numerical Models**

The numerical models for the three PQFP 160 package designs were described in Section 4.6.2. The free and forced convection numerical models for package design I mounted on the Stage 1 PCB are shown in Figures 4.14(a) and 4.17(a) respectively. Corresponding numerical models for package designs II and III on the SEMI standard PCB are presented in Figures 4.22 and 4.23 for free and forced convection respectively.

Numerical predictions for component steady-state junction temperature are presented in tabulated format, with component-PCBs surface temperature profiles shown in graphical format. These predictions are compared with corresponding experimental measurements. In addition to assessing the accuracy of *à priori* predictions, obtained using nominal component/board geometry and material properties, numerical model sensitivity to both

component and PCB modelling parameters is also investigated to determine if improved predictive accuracy could be obtained for subsequent studies. Finally, numerical energy balance analyses of component heat transfer are also presented which provide a better understanding of the heat transfer mechanisms associated with package heat loss.

### 5.2.1 Junction Temperature Predictions

Prediction discrepancy in free and forced convection is presented both as an absolute temperature error ( $^{\circ}\text{C}$ ), and percentage value in Table 5.1 for package design I mounted on the Stage 1 PCB, and in Table 5.2 for package designs II and III on the SEMI standard PCB.

The results show that in both free and forced convection, prediction accuracy is within  $\pm 3^{\circ}\text{C}$  of measurement for all package types, when account is taken of measurement uncertainty. Prediction sensitivity to PCB topology and flow model is discussed.

**Table 5.1** Comparison of measured and predicted component steady-state junction temperatures for the PQFP 160 package design I, characterised on the Stage 1 PCB.

Airflow (m/s)	Measured ( $^{\circ}\text{C}$ )	Prediction discrepancy ( $^{\circ}\text{C}$ )		
		Laminar	k- $\epsilon$	LVEL
0	86.0	+1.9 (2.9%)	---	---
2.0	66.0	+0.7 (1.5%)	+1.5 (3.3%)	-1.5 (3.3%)
4.0	58.6	+1.0 (2.6%)	+0.8 (2.1%)	-1.7 (4.4%)

**Note:** Measurement uncertainty,  $\pm 0.5^{\circ}\text{C}$  and  $\pm 0.4^{\circ}\text{C}$  for free and forced convection respectively. Percentage prediction error in parenthesis ( ) is calculated based on the measured component junction temperature rise above ambient air temperature. Component power dissipation = 3W. Ambient air temperature =  $20^{\circ}\text{C}$ .

**Table 5.2.** Comparison of measured and predicted component steady-state junction temperatures for the PQFP 160 package designs II and III, characterised on the SEMI standard PCB.

Airflow (m/s)	Package design II			Package design III		
	Meas. ( $^{\circ}\text{C}$ )	Prediction discrepancy ( $^{\circ}\text{C}$ )		Meas. ( $^{\circ}\text{C}$ )	Prediction discrepancy ( $^{\circ}\text{C}$ )	
		Laminar	k- $\epsilon$		Laminar	k- $\epsilon$
0	83.6	-2.3 (3.6%)	---	77.4	-1.9 (3.3%)	---
1.0	70.3	-2.1 (4.2%)	---	---	---	---
2.0	61.8	-1.7 (4.0%)	-2.7 (6.5%)	57.8	-2.0 (5.3%)	-2.9 (7.7%)
4.0	51.2	+2.0 (6.4%)	+0.9 (2.9%)	47.0	+2.1 (7.8%)	+0.9 (3.3%)

**Note:** Measurement uncertainty,  $\pm 0.7^{\circ}\text{C}$  and  $\pm 0.6^{\circ}\text{C}$  for free and forced convection respectively. Percentage prediction error in parenthesis ( ) is calculated based on the measured component junction temperature rise above ambient air temperature. Ambient air temperature =  $20^{\circ}\text{C}$ . Component power dissipation = 3W.

On the Stage 1 PCB, component junction temperature is consistently overpredicted using the laminar and k- $\epsilon$  flow models. By contrast on the SEMI standard PCB, component operating temperature is underpredicted, with the exception of the 4 m/s airflow. This variation in accuracy with PCB topology may reflect the impact of

component location relative to the board's leading edge. This factor results in different flow conditions about the component, to which the flow models display different sensitivity. On the SEMI PCB, junction temperature prediction sensitivity to free-stream airflow velocity may also possibly reflect changes in the flow conditions, experimentally visualised in Figure 3.32.

In forced convection, the laminar and  $k$ - $\epsilon$  flow model predictions are within  $1.1^{\circ}\text{C}$  of each other for both PCBs, indicating that the  $k$ - $\epsilon$  model predicts a low level of turbulent viscosity in the flow. This may not be surprising considering the laminar nature of the flows over the boards, as visualised in Figures 3.30 and 3.32. Despite its limitations, the LEVEL model predictions are on order within 6% of those for the  $k$ - $\epsilon$  model, Table 5.1.

Numerical sensitivity studies were performed to investigate junction temperature prediction sensitivity to potential modelling uncertainties.

The impact of potential uncertainties in nominal component and board constituent material thermo-physical properties was assessed by the following parametric analyses, performed in free convection.

For component modelling, the variables assessed were the thermal conductivity of the encapsulant, heat slug, die attach and die materials, and the volumetric copper content of the leadframe.

Although Fitzgerald and Davies [272] reported good agreement between thermal conductivity measurements of the epoxy encapsulant used in the present PQFP 160 package, Sumitomo EME-6300H, and the component vendor data, prediction sensitivity to this modelling variable was assessed. Varying encapsulant thermal conductivity by 20% was found to only impact on junction temperature predictions by  $1^{\circ}\text{C}$  (1.5%) for package design I, and  $0.5^{\circ}\text{C}$  (0.8%) for package design II. Prediction sensitivity to this parameter was negligible for package design III. The small prediction sensitivity to this parameter is due to the embedded heat slugs dominating heat spread within the package bodies. In contrast to the present results, component thermal resistance can be highly sensitive to encapsulant conductivity for standard PQFP constructions [103], which do not contain a heat slug, Figure 3.3(a). Regarding possible temperature dependency of the encapsulant conductivity, Fitzgerald and Davies [272] reported that its value only increased by 10% over a typical range of component operating temperatures. Based on the above sensitivity analyses, there was therefore no need to model this temperature dependency.

Although the heat slug thermal conductivity is well-documented [273], prediction sensitivity to this property was assessed by reducing its nominal value by 20%. This resulted in on order only  $0.6^{\circ}\text{C}$  rise in junction temperature for the three package designs. However, such a conductivity variation is extreme.

As the thermal resistance of the die attach layer is on order only 0.2°C/W, varying the die attach thermal conductivity by 20% had a negligible impact on junction temperature.

The local copper content of the leadframe varies about the average value modelled, 50%, due to the leadframe fingers slightly diverging away from the die towards the package side, thereby resulting in higher copper content in the vicinity of the die. Therefore, the copper content of the compact leadframe model was increased from 50% to 60%. This resulted in on order 0.6°C (0.9%) reduction in junction temperature. However, the extreme copper content assessed would not be representative of the overall leadframe design.

While the modelled temperature dependency of the die silicon thermal conductivity given in Table 4.1 is a recognised industry measurement [274], prediction sensitivity to this variable was found to be minimal. This results from the low die thermal resistance, due to both its relatively high conductivity and thinness.

For PCB modelling, junction temperature prediction sensitivity to the thermal conductivity of the FR-4 substrate was assessed. Graebner and Azar [190] reported measurement uncertainties of ±5% and ±10% for the in-plane and through-plane thermal conductivity values respectively. On this basis, the FR-4 in-plane thermal conductivity was varied by 10%, relative to its nominal value. This variation resulted in component junction temperature varying by 0.6°C (0.9%) and 0.4°C (0.6%) on the Stage 1 and SEMI standard PCB respectively. The small prediction sensitivity to this parameter is due to copper content dominating board heat spread.

Corresponding analyses in forced convection showed that junction temperature predictions were even less sensitive to these changes to the models than in natural convection. Based on the above numerical sensitivity studies, there was no justification to alter the component-board models described in Section 4.5.

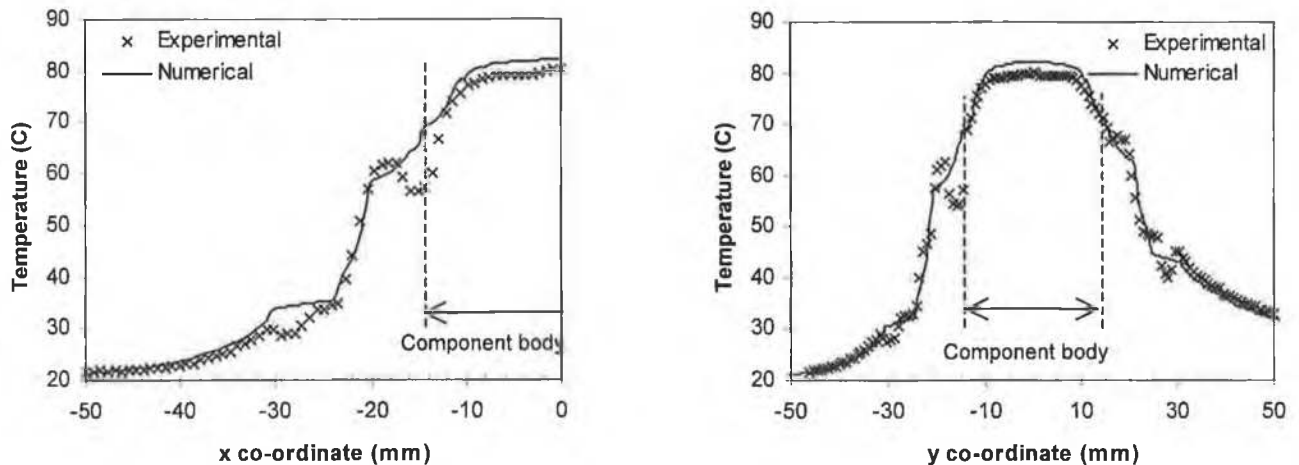
### **5.2.2 Component-Board Surface Temperature Profiles**

To further assess the modelling methodology, measured and predicted component-board surface temperature profiles were compared in Figure 5.1 for package design I on the Stage 1 PCB in free convection, and in Figure 5.2 for package design II on the SEMI PCB, both in natural and forced convection. These analyses are presented for both the stream-wise and span-wise airflow directions about the package centre, as defined by the reference planes in Figures 3.19 and 3.21 for the Stage 1 and SEMI PCBs respectively.

**Stage 1 PCB.** Overall, both the magnitude and shape of the predicted surface temperature profiles are in good agreement with measurements, both in the span-wise and stream-wise airflow directions. This indicates that the PCB model captures well the heat

spreading properties associated with both the surface traces, and the FR-4 substrate. The discrepancies between predictions and measurements over both the component leads, and PCB copper tracks at x- and y co-ordinate distances of 30 mm, are primarily attributed to experimental error. The former discrepancies are essentially due to (i) inaccurate camera emissivity setting for measuring lead temperature, as their surface was not sprayed (Section 3.3.3.1), and (ii) the limited spatial temperature resolution of the AGEMA infrared Thermovision 880 system, which would result in temperature averaging over the package leads and adjacent component top and PCB surfaces. The discrepancies over the copper tracks primarily result from inaccurate camera emissivity setting for measuring the temperature of the tracking plated portions. Package leads and tracking plated surfaces would have a surface emissivity considerably lower than 0.92.

Over the component surface, the shape of the predicted and measured surface temperature profiles in the directions of package width and length are in good agreement, indicating that the model correctly captures internal conductive heat spread. The discrepancy between measured and predicted surface temperature is in line with the overprediction of junction temperature in Table 5.1.



(a) Temperature profile in the span-wise direction

(b) Temperature profile in the stream-wise direction

**Note:** Analysis planes are defined in Figure 3.19, with the origin of x- and y- axes corresponding to the package centre. Uncertainty in temperature measurement =  $\pm 1.4^{\circ}\text{C}$ .

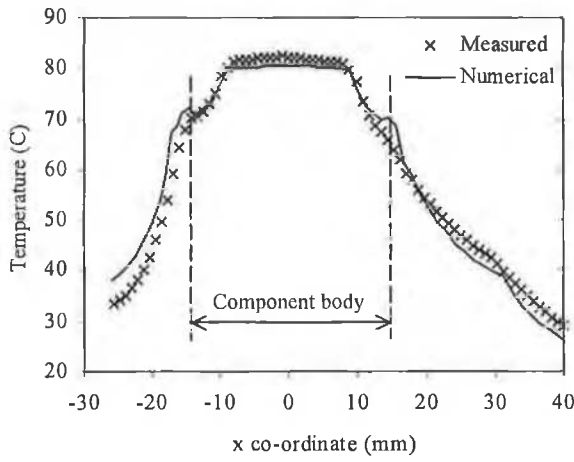
**Figure 5.1** Comparison of measured and predicted component-PCB surface temperature profiles on the Stage 1 PCB for a single board-mounted PQFP 160 component, package design I, at position H in free convection.

**SEMI PCB.** Unlike for the Stage 1 PCB, the complete component-board assembly was sprayed for uniform emissivity (Section 3.3.3.1). In both free and forced convection, the magnitude and shape of the measured and predicted component-PCB surface temperature

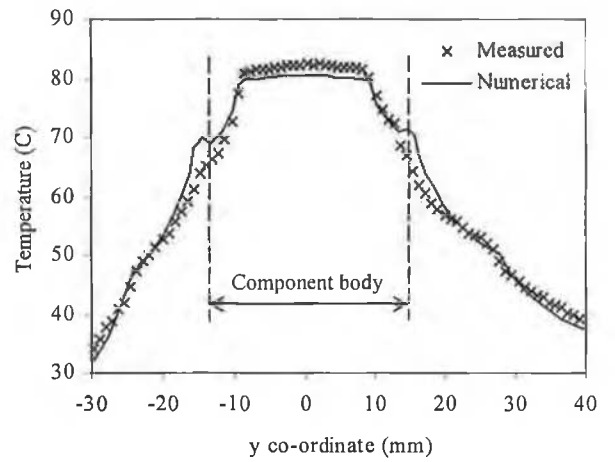
profiles are in good agreement in both the span-wise and stream-wise directions, Figure 5.2. This shows that (i) PCB heat spread, hence component-PCB thermal interaction is well captured by the model, (ii) component internal conductive heat spread for package design II is correctly modelled. The discrepancies between predictions and measurements over the component leads are primarily attributed to experimental error, associated in this instance with the limited spatial temperature resolution of the infrared measurement system. This factor may also explain the discrepancy between measured and predicted PCB temperatures in the vicinity of the component in the span-wise direction in free convection, Figure 5.2(a,i), on the profile left-hand side. In free convection, large temperature gradients exist in this region of the board as the copper tracks only extend by 5 mm from the component body, Figure 5.2(a,i).

In forced convection, discrepancies between predicted and measured board surface temperature are also noted downstream of the component, Figures 5.2(b,ii) and 5.2(c,ii). These contrast with the agreement obtained in both the span-wise direction, and upstream of the component in the stream-wise direction, where the same PCB modelling methodology was employed. These discrepancies therefore suggests that the flow phenomena downstream of the component are not fully captured. This could impact on the prediction of i) the board local convective heat transfer coefficient, ii) the advected air temperature adjacent to the wall. Both quantities impact on the prediction of the board surface temperature distribution. While for turbulent flow analysis, the surface heat transfer coefficient is calculated using wall functions (Section 4.2), interestingly the laminar and turbulent k- $\epsilon$  flow models are found to predict similar board surface temperature. This therefore indicates that inaccurate prediction of the board surface temperature is more likely to be attributable to inaccurate prediction of the air temperature adjacent to the board downstream of the component. Such discrepancies were also highlighted by Rodgers et al. [35] downstream of single board-mounted devices, in forced airflows, and will be further highlighted for the PQFP 208 component in Section 5.2.1. The impact of such discrepancies on predictive accuracy in multi-component PCB applications having a high degree of component thermal interaction will be discussed for the populated board configurations in Chapter 7. In line with corresponding junction temperature predictions, the board surface temperature downstream of the component is underpredicted at 2 m/s, and overpredicted at 4 m/s.

While no surface temperature measurements were available for package design III, the accuracy in junction temperature predictions for this package design, and in component-board surface temperature predictions for designs I and II, modelled with the same methodology, provides confidence in the model. This will be confirmed by the analysis of the populated board in free convection conditions, Chapter 6.

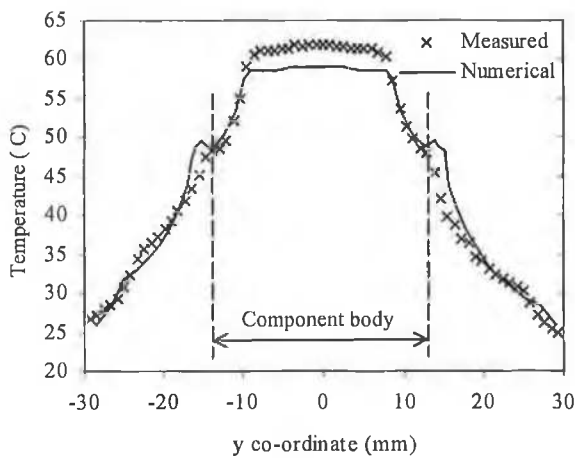


(i) Temperature profile in the span-wise direction

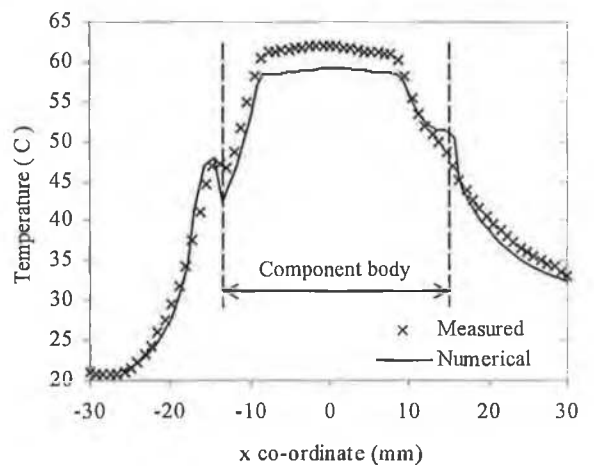


(ii) Temperature profile in the stream-wise direction

(a) Free convection

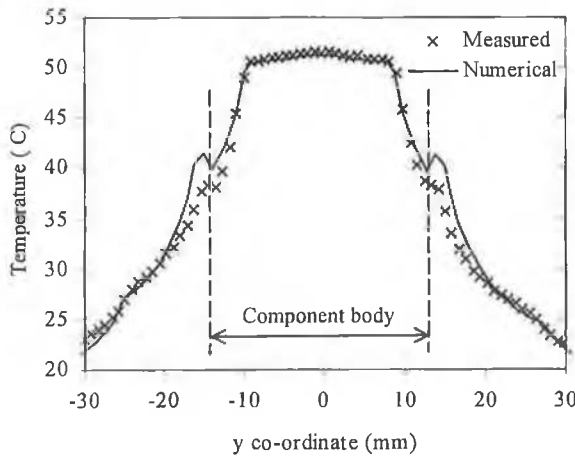


(i) Temperature profile in the span-wise direction

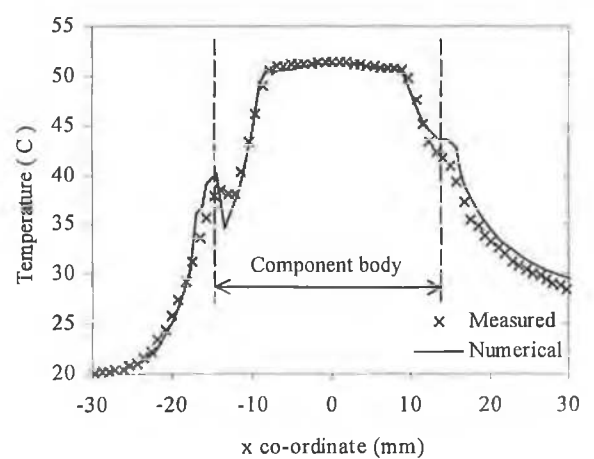


(ii) Temperature profile in the stream-wise direction

(b) 2 m/s airflow



(i) Temperature profile in the span-wise direction



(ii) Temperature profile in the stream-wise direction

(c) 4 m/s airflow

**Note:** Analysis planes are defined in Figure 3.14, with the origin of x- and y- axes corresponding to the package centre. Uncertainty in temperature measurement =  $\pm 1.4^\circ\text{C}$ . Predictions are based on laminar flow analysis for both free convection and 2 m/s airflow, and obtained using the k-e flow model for 4 m/s.

**Figure 5.2** Comparison of measured and predicted component-PCB surface temperature profiles on the SEMI PCB for a single board-mounted PQFP 160 component, package design II, in free and forced convection.



Overall, the component junction temperature and component-board surface temperature profile analyses show that the numerical models correctly capture both component internal conductive heat spread and component-PCB thermal interaction, thereby demonstrating the robustness of the modelling methodologies employed. The level of accuracy obtained is in line with that previously reported for other single-board mounted components, modelled with the same methodology [35]. However in forced convection, a weakness of the CFD code to fully capture downstream flow phenomena was highlighted.

Based on the foregoing analyses, any significant decay in predictive accuracy for the populated board configurations could be attributed to a weakness of the CFD code to predict the more complex flows and their impact on component-PCB heat transfer. Similarly, a decay in predictive accuracy for dynamic operating conditions would be associated with the modelling of the component-PCB assembly thermal capacitance.

### **5.2.3 Energy Balance Analyses of Component Heat Transfer**

Prediction accuracy for the three PQFP 160 package designs gives confidence in undertaking energy balance analyses of component heat transfer. The predicted energy balances are presented in Table 5.3 for the three package designs on the SEMI PCB, and in Table 5.4 for package type I on the Stage 1 PCB. Although no experimental characterisation data was available for package design I on the SEMI PCB, the predicted heat transfer paths for this component will permit the influence of heat slug design on component heat transfer to be assessed for the three package designs. The net heat flux through each heat transfer path is presented as a percentage of the total dissipated power. Energy balance analyses in forced convection were found to be flow model independent, with less than 1% difference between flow model predictions.

Considering first the SEMI PCB configurations, the energy balance analyses in Table 5.3 reveal that the dominant heat transfer path is by lead conduction, both in free and forced convection. Heat dissipation to the PCB is approximately 76% and 68% in natural and forced convection respectively, with the PCB therefore still acting as a cooling fin. As shown by Lohan et al. [149], this results in component junction temperature being highly sensitive to board construction, hence its modelling.

For a given convective environment, the distributions of the heat transfer paths for package designs I and II are within 1% of each other. Package design III's energy balance distribution is within 5% of that for designs I and II, displaying a higher dependence on lead conduction. This can be attributed to design III's larger heat slug promoting better heat spread within the package body, hence more efficiently distributing the heat to the

leadframe. This characteristic results in lower operating temperatures than for designs II and III, Table 5.2.

A redistribution of the heat transfer paths occurs between free and forced convection, where heat loss to the board diminishes by on order 8%. This reduction is driven by similar increases in heat loss from the package top and side surfaces.

Comparison of package design I's energy balance on the Stage 1 and SEMI PCBs in Tables 5.3 and 5.4 respectively highlights in this instance a weak sensitivity of the component heat transfer paths to PCB construction and aerodynamic conditions. Their impact is characterised by less than 3% variation between the respective energy balance distributions.

**Table 5.3** Numerical component energy balance (%) for the PQFP 160 component on the SEMI PCB.

Airflow velocity (m/s)	Package design I						Package design II						Package design III					
	Top		Base		Leads	Sides	Top		Base		Leads	Sides	Top		Base		Leads	Sides
	Conv.	Rad.	Conv.	Rad.	Cond.	Conv.	Conv.	Rad.	Conv.	Rad.	Cond.	Conv.	Conv.	Rad.	Conv.	Rad.	Cond.	Conv.
0	12	11	16	2	57	2	12	10	16	2	58	2	10	10	13	2	62	3
2	24	3	14	1	53	5	24	3	14	1	53	5	22	2	12	1	58	5
4	27	2	14	1	51	5	26	2	14	1	52	5	23	2	12	1	56	6

Note: Component power dissipation = 3W. Cond. = conduction, Conv. = convection, Rad. = radiation. Energy balance independent of flow model for forced convection.

**Table 5.4** Numerical component energy balance (%) for the PQFP 160, package design I, on the Stage 1 PCB.

Airflow velocity (m/s)	Top		Base		Leads	Sides
	Conv.	Rad.	Conv.	Rad.	Cond.	Conv.
0	12	11	13	2	60	2
2	25	6	12	1	52	4
4	28	5	12	1	50	4

Note: Component power dissipation = 3W. Cond. = conduction, Conv. = convection, Rad. = radiation. Energy balance independent of flow model for forced convection.

### 5.3 Transient Component Heat Transfer

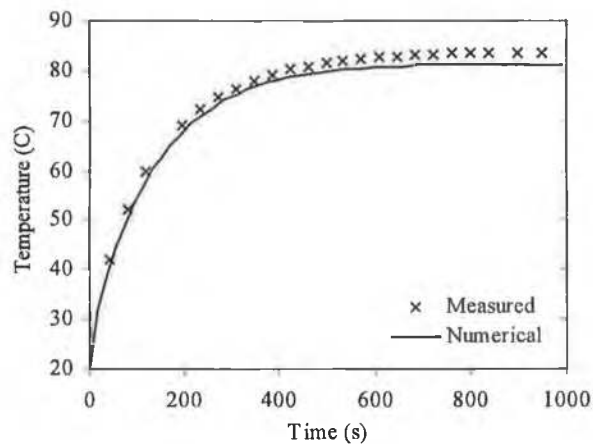
The PQFP 160 package design II, characterised on the SEMI PCB, is used to investigate the prediction of dynamic component thermal behaviour. The test configurations are described in Section 3.4. The free and forced convection numerical models are shown in Figures 4.22 and 4.23 respectively, and were validated for steady-state heat transfer in Section 5.1.

Before assessing the prediction of component thermal behaviour in thermal environments representative of those encountered in reliability testing and reflow soldering assembly processes, the numerical model is firstly assessed for component dynamic power dissipation in fixed ambient conditions. Any significant decay in predictive accuracy for such operating conditions relative to steady-state operation, would be associated with the modelling of the component-PCB assembly thermal capacitance.

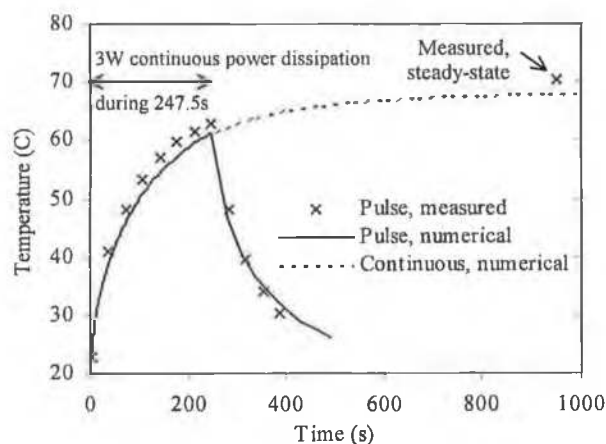
### 5.3.1 Numerical Model Validation

The modelling of the thermal capacitance is assessed based on the component thermal response to a pulse of 3 W power dissipation in fixed ambient conditions. This corresponds to Tests I and II, Table 3.14, characterising thermal behaviour in natural convection and 1 m/s airflow.

The measured and predicted component transient thermal responses are compared in Figures 5.3 and 5.4 for free convection and 1 m/s airflow respectively. For both convecting environments, predicted component junction temperatures are on order within  $-2^{\circ}\text{C}$  of measurement. In Figure 5.4, the cooling rate of the test assembly is also correctly predicted, indicating that the component-PCB junction-to-ambient thermal impedance is correctly modelled.



**Figure 5.3** Comparison of measured and predicted transient component junction temperature rise for a continuous power dissipation of 3W in a quiescent air at  $20^{\circ}\text{C}$ , Test I.



**Figure 5.4** Comparison of measured and predicted transient component junction temperature rise for both continuous and pulsed 3W component power dissipation in a 1 m/s airflow at  $20^{\circ}\text{C}$ , Test II.

As the component and board models are based on nominal material thermo-physical properties, the following numerical sensitivity analyses were undertaken to assess prediction sensitivity to critical parameters. The impact of reducing both the specific heat capacity and density values of the encapsulant and FR-4 materials by 10%, which would effectively increase their thermal capacitance by 20%, was assessed. Because the thermal mass of the silicon die is small relative to that of the overall assembly, and the properties of silicon are well documented [274], there was no need to evaluate the impact of these properties. For Test II, reducing the FR-4 substrate thermal capacitance only resulted in a reduction of the test assembly's thermal time constant of on order 6% relative to the nominal predicted response. When the capacitance of both the encapsulant and FR-4 were altered, the assembly's thermal time constant decreased by on order 14% relative to the nominal response. This only slightly improved the prediction of the assembly's thermal response, showing that potential uncertainties in material thermo-physical properties do not significantly impact on predictive accuracy in this instance. Consequently, the component-board models described in Section 4.5 were not altered.

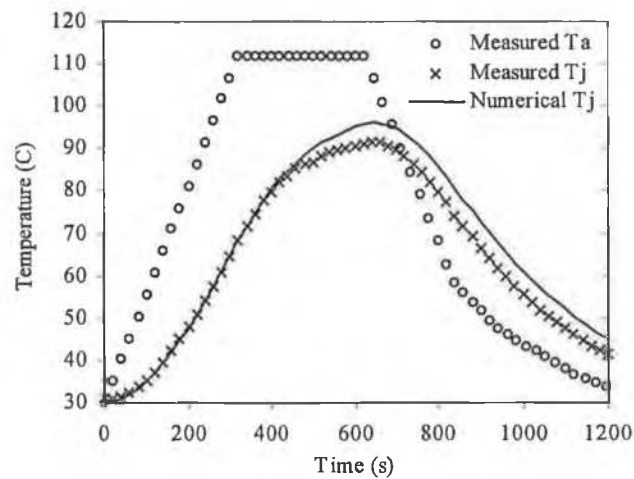
### 5.3.2 Reliability Testing

The component thermal response to air temperature cycling, Table 3.15, and combined air- and power cycling, Table 3.16, are analysed.

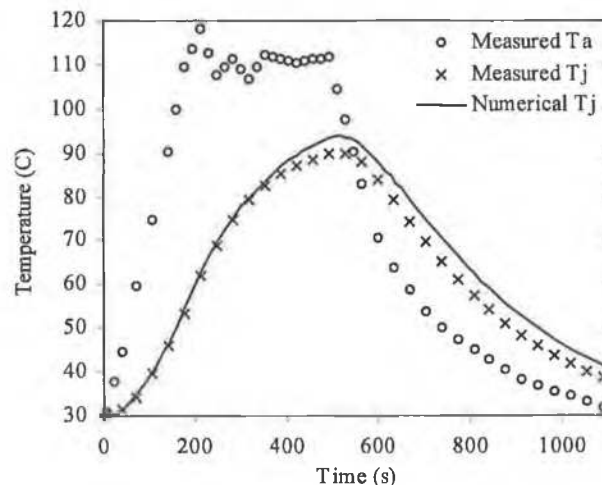
Passive component operation in dynamic ambient air temperature conditions. The measured and predicted component transient thermal responses are compared in Figure 5.5, 5.6 and 5.7 for 1 m/s, 2.25 m/s, and 4 m/s airflows respectively. For the 4 m/s analyses, in line with the predictions for steady-state heat transfer in Table 5.2, the predicted dynamic component thermal responses for laminar and turbulent flow analysis were found to be essentially similar, with the latter being slightly more accurate. For clarity therefore, only the k-ε flow model predictions are presented for this case.

*1 m/s air temperature cycles, Tests III and IV.* During the heating phase of the test assembly up to approximately 400 s, measured and predicted component junction temperatures are in excellent agreement for the two ramp rates applied, indicating that the system thermal impedance is correctly modelled. However, measurements and predictions begin to diverge beyond this point till the end of the imposed dwell, where the discrepancy stabilises at a maximum value of 4.6°C and 3.9°C for tests III and IV respectively. Despite this error, the shape of the predicted transient response during the cooling phase is in excellent agreement with measurement, as found during the heating phase up to 400 s. This trend confirms that the system thermal capacitance is correctly modelled, with the discrepancy observed during the dwell period being therefore related to the prediction of

the steady-state thermal resistance. Such a discrepancy was not found for the component powered-on cases, Tests I and II, and is primarily attributed to experimental error. Although air density variation was numerically accounted for, Lohan and Davies [77] measured a 6% increase in airflow velocity within the test section for the temperature range under analysis. This occurred as the wind tunnel motor operated at a fixed speed, with airflow velocity consequently increasing due to lower pressure drop. This velocity variation, which could not be modelled, would therefore result in the slight overprediction of the component-PCB thermal resistance during the dwell period.



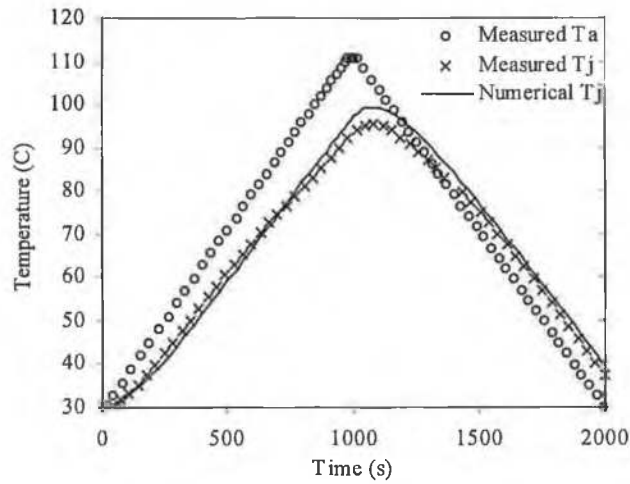
(a) 15°C/min ramp, 300s dwell time, Test III.



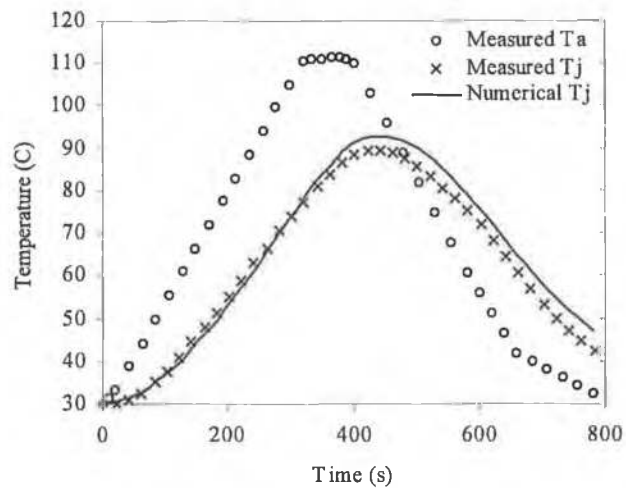
(b) 25°C/min ramp, 300s dwell time, Test IV.

**Figure 5.5** Comparison of measured and predicted passive component junction temperature in dynamic ambient air temperature conditions, in a 1 m/s airflow.

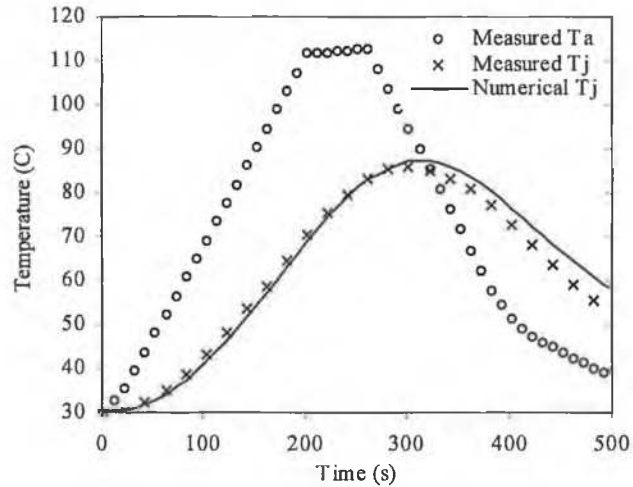
2.25 and 4 m/s air temperature cycles, Tests V to VIII. The same trends are observed at both 2.25 m/s and 4 m/s, in Figures 5.6 and 5.7 respectively, as for the 1 m/s analyses. However, minor discrepancies can be detected between measurements and predictions during the heating phase of the test assembly, which were not observed at 1 m/s. For a given ramp rate, increasing the airflow velocity reduces the thermal time constant of the component-PCB assembly, thereby resulting in a higher heating rate. While this could suggest a possible source of predictive discrepancies at high velocities, this seems unlikely in this instance, considering that (i) component steady-state heat transfer is accurately predicted at 2 and 4 m/s, Table 5.2, and (ii) the component thermal impedance was correctly predicted for 25°C/min ramp rate at 1 m/s, which imposed a faster heating rate than for 5°C/min and 15°C/min ramps at 2.25 m/s. Although the source of the discrepancies noted therefore remains unknown, their magnitude is not significant.



(a) 5°C/min ramp, 60s dwell time, Test V.

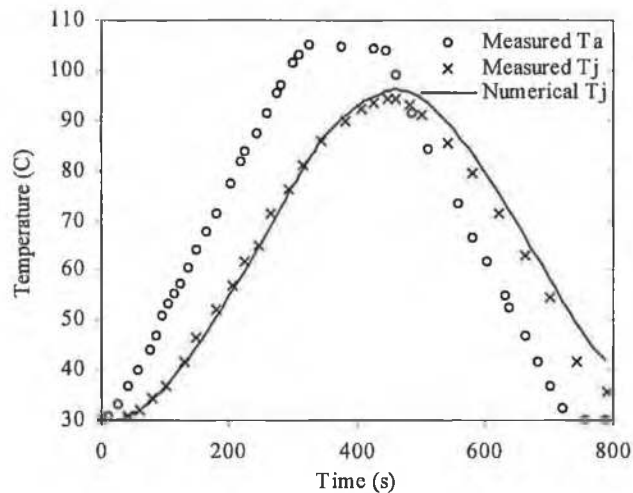


(b) 15°C/min ramp, 60s dwell time, Test VI.



(c) 25°C/min ramp, 60s dwell time, Test VII.

**Figure 5.6** Comparison of measured and predicted passive component junction temperature in dynamic ambient air temperature conditions, in a 2.25 m/s airflow.



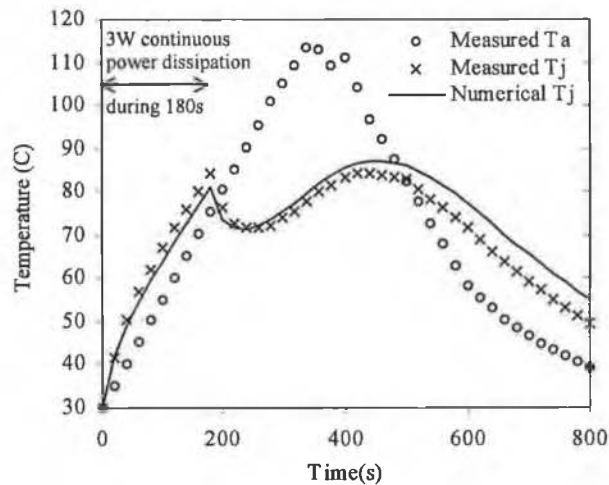
**Figure 5.7** Comparison of measured and predicted passive component junction temperature in dynamic ambient air temperature conditions (15°C/min ramp, 120s dwell time), in a 4 m/s airflow, Test VIII.

Combined component dynamic power dissipation in varying ambient air temperature conditions. Measured and predicted component junction temperatures are compared in Figures 5.8 for both 1 m/s and 2.25 free-stream air velocities, Tests IX and X respectively. Overall, the shape of the predicted component transient thermal response is in good agreement with measurement, both during the powered-on heating phase, and cooling phase beyond the imposed dwell period. Good accuracy is also obtained between the end of the power dissipation pulse and the end of the dwell period, during which a complex redistribution of the heat transfer paths occurs. Overall, prediction discrepancies reflect

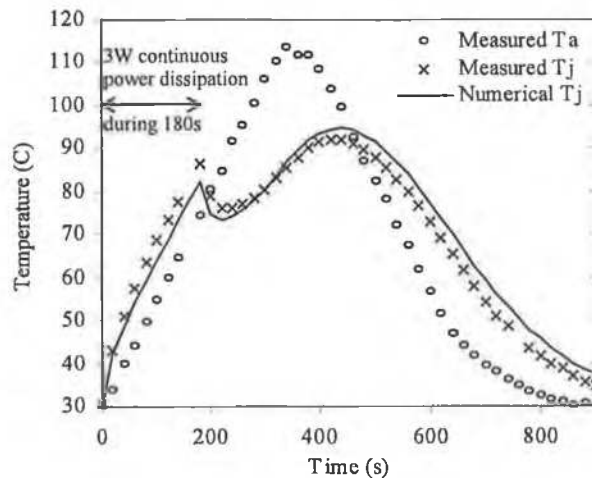
those observed for the active and passive component operation test cases previously analysed, that is:

(i) The junction-to-ambient thermal impedance is underestimated during component dynamic operation, as for Test II.

(ii) The junction-to-ambient thermal impedance is overestimated from the end of the imposed dwell period onwards, as for Tests III – VIII, which was primarily attributed to experimental error.



(a) 15°C/min ramp, 60s dwell time, in a 1 m/s airflow, Test IX.



(b) 15°C/min ramp, 60s dwell time, in a 2.25 m/s airflow, Test X.

**Figure 5.8** Comparison of measured and predicted transient component junction temperature rise for a pulsed 3W component power dissipation in dynamic ambient air temperature conditions.



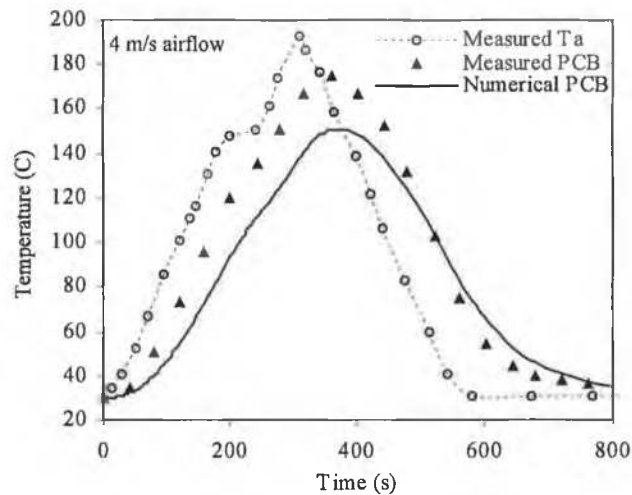
### 5.3.3 Convective Solder Reflow

The component transient thermal response to a standard convective reflow soldering temperature profile, the characteristics of which were given in Table 3.17, is analysed in Figure 5.9.

Contrary to the previous test configurations, poor agreement exists between measurement and prediction. Although predictions are only presented for the thermal response at the board surface beneath the component, considerable discrepancies also existed between the measured and predicted temperature profiles recorded at the component lead shoulder. As the component-board thermal impedance was found to be correctly modelled in previous tests, I-X, the higher ramp rate imposed for air temperature heating in the current test is unlikely to be a significant source of prediction error. Also, it would be anticipated that any physical free-stream velocity variation in the test section at elevated temperature would have contributed to overprediction of the thermal impedance, as previously observed, as opposed to the significant underprediction in Figure 5.9. As predictions and measurements diverge from the start of the imposed air temperature profile, in a temperature range comparable to that applied in previous tests, potential uncertainties in nominal material thermo-physical properties, associated with possible temperature dependency, are unlikely to be the primary source of the discrepancies in Figure 5.9. Furthermore, the magnitude of these discrepancies exceeds the prediction sensitivities found in Sections 5.2.1 and 5.3.1 for the steady-state thermal resistance and transient thermal impedance respectively. It should be noted that for a given airflow velocity and time, the difference between the ambient air and component junction temperatures increases with the ramp rate, as evident from the air temperature cycle tests in Figure 5.6. However, this trend does not hold when comparing the measured assembly thermal response for Test VIII (15°C/min), Figure 5.7, with that for the convective solder reflow (40°C/min), both for 4 m/s airflow. The temperature gradient between the PCB surface and junction is not a factor here, as the numerical model predicts a gradient of less than 4°C, indicating that the assembly is essentially isothermal.

Based on these considerations, the discrepancies between measurement and prediction for the solder reflow profile are essentially attributed to experimental error. This is likely to be associated with the use of thermocouples, whereas all other benchmarks were based on measured component junction temperature. It is suspected that in this instance, parasitic conduction from the ambient air to the measurement point via the thermocouple wires resulted in overestimation of the local board surface temperature. T-type thermocouples were used having one leg made of copper, which makes them prone to such errors [275,276]. In addition, the thermocouples wires were not insulated. As previously

highlighted (Section 1.2.2), accurate experimental characterisation of reflow thermal profiles using thermocouples can be difficult to achieve [79]. This highlights the potential value of using validated CFD models to aid optimise convective solder reflow thermal profiles.



**Figure 5.9** Comparison of measured and predicted passive component junction temperature in dynamic ambient air temperature conditions representative of those in a standard convective reflow soldering process.

#### 5.3.4 Summary of Results

The results of these analyses combined show that based on both nominal component/PCB geometry dimensions and material thermo-physical properties, single component-PCB transient heat transfer can be predicted with good accuracy, in both free and forced convection. In this instance therefore, confidence could be gained in applying CFD analysis to generate temperature boundary conditions for use in product electrical and thermo-mechanical performance analyses. This approach would permit the generation of more realistic temperature boundary conditions, as opposed to those obtained using prescribed convective heat transfer boundary conditions derived from semi-empirical analysis (Section 2.2). The passive component operation cases in varying ambient conditions indicate that CFD analysis could also be used to optimise assembly processes, where the aim is to minimise thermal gradients, hence stresses. CFD analysis could also serve to determine HALT (Highly Accelerated Life Testing) parameters. Such variables may be difficult, if not impossible to measure experimentally.

The results also suggest that the component modelling methodology employed would be sufficiently robust to be used for the derivation of dynamic component CTMs [55,277,278]. This study can therefore be seen as a contribution to this area. The

assessment of detailed modelling methodologies for transient component conductive heat transfer has been investigated by Schweitzer and Pape [114,279], but the findings cannot be extrapolated to convective board-level environments.

#### 5.4 Component Compact Thermal Modelling

The SO8 and PQFP 208 test configurations described in Section 3.5 are used to investigate the predictive performance of component CTMs for board-mounted component heat transfer. The SO8 natural and forced convection numerical models are shown in Figure 4.24 and 4.26 respectively, with the PQFP 208 forced convection model shown in Figure 4.28.

Before assessing CTM predictive accuracy, the detailed component-PCB numerical models are validated against experimental measurements. Any significant decay in CTM predictive accuracy relative to those models would be associated with potential limitations of the component compact models used, either in their resistor network or implementation into the CFD model, or a combination of both.

##### 5.4.1 Detailed Component Modelling

Component junction temperature prediction accuracy is presented both as an absolute temperature error ( $^{\circ}\text{C}$ ), and percentage value in Tables 5.5 and 5.6 and for the SO8 and PQFP 208 test configurations respectively. Corresponding component-board surface temperature profiles are presented in Figures 5.10-5.11 for the SO8 component, and Figure 5.12 for the PQFP 208.

The fluid domain was solved as laminar for all test cases, with the exception of the 5 m/s SO8 case, which was solved using the high-Reynolds number  $k$ - $\epsilon$  flow model. However, for this configuration predictive accuracy only decayed by  $1^{\circ}\text{C}$  using the laminar model, indicating a low level of turbulent viscosity in the flow. This is in line with the results for the SEMI test board, Table 5.2.

**SO8 component.** The SO8 model junction temperature predictions in Table 5.5 are overall within  $\pm 6^{\circ}\text{C}$  or 8% of measurements for the three convective environments considered, when account is made of experimental error. The natural convection predictions differ slightly from those reported by Lohan et al. [149], who used the same CFD code and component modelling methodology. These discrepancies are attributed to the coarser computational domain grid discretization applied in their study, which represents a fifth of the present grid volume, and a coarser subdivision of radiating surfaces. For natural convection therefore, the present predictions are considered as the *a priori* results.

**Table 5.5** Comparison of measured and predicted component junction temperatures for a single board-mounted SO8 component.

Airflow velocity (m/s)	Prediction discrepancy (°C)								
	FR-4 #1			FR-4 #2			IMS		
	Meas. (°C)	Detailed model	Lohan et al. [149]	Meas. (°C)	Detailed model	Lohan et al. [149]	Meas. (°C)	Detailed model	Lohan et al. [149]
0	124.3	-6.7 (6.4%)	-3.1 (3.0%)	84.9	+5.5 (8.5%)	+6.8 (10%)	71.5	+4.1 (8.0%)	+5.0 (9.7%)
2	100.2	-5.0 (6.2%)	---	77.2	+6.2 (11%)	---	67.2	+1.3 (2.8%)	---
5	88.6	-3.6 (5.2%)	---	74.3	+1.6 (2.9%)	---	66.0	+0.3 (0.7%)	---

**Note:** FR-4 #1, FR-4 #2 and IMS refer to PCB construction, Figure 3.50(b). Measurement uncertainty,  $\pm 1\%$ . Component power dissipation = 0.5 Watts. Ambient air temperature = 20°C. Percentage error in parenthesis ( ) is calculated based on measured component junction temperature rise above ambient air temperature.

Measured and predicted surface temperature profiles for natural convection are presented in Figures 5.10 and 5.11 for the package width and length directions respectively. The shape of the predicted surface temperature profiles over the package and board compare favourably with measurement, indicating that both package internal heat spread and component-PCB thermal interaction are overall correctly captured. Discrepancies exist between predictions and measurements over the package, and the board in the vicinity of the component, which are partly attributable to experimental error resulting from the limited spatial temperature resolution of the Agema Thermovision 550 infrared imaging system (Section 3.5.1). This limitation resulted in temperature averaging in regions of high spatial temperature gradients, thereby acting to amplify predictive discrepancies. However, the discrepancies in board surface temperature in the vicinity of the component in Figures 5.10(b) and 5.11 suggest that the board model for FR4 #2 overestimates heat spread in the direction of package width, resulting in an underprediction of heat spread in the direction of package length.

**PQFP 208 component.** The PQFP 208 junction temperature prediction in Table 5.6 is within  $-1^{\circ}\text{C}$  (4%) of measurement. Corresponding surface temperature profiles are presented in Figure 5.12. Both the magnitude and shape of the predicted surface temperature profiles over the package compare well with measurement, indicating that internal package heat spread is correctly modelled. The measured and predicted board surface temperature profiles are in excellent agreement in the span-wise direction, Figure 5.12(b), and upstream of the component in the stream-wise direction, Figure 5.12(a), indicating that PCB heat spread is well captured by the copper tracking model. While the same modelling methodology was employed downstream, the copper tracking surface temperature is underpredicted by on average  $2.5^{\circ}\text{C}$ . This discrepancy again suggests that the flow phenomena downstream of the component are not fully captured. This trend was previously highlighted for the single-board mounted PQFP 160 devices (Section 5.1.2).

**Table 5.6** Comparison of measured and predicted component junction temperatures for a single board-mounted PQFP 208 in a 2 m/s airflow.

<i>Measured</i> (°C)	<i>Prediction discrepancy</i> (°C)
46.4	-1.0 (3.8%)

**Note:** Measurement uncertainty,  $\pm 0.2^\circ\text{C}$ . Component power dissipation = 2 W. Ambient air temperature =  $20^\circ\text{C}$ . Percentage error in parenthesis ( ) is calculated based on measured component junction temperature rise above ambient air temperature.

The better accuracy obtained for the PQFP 208 component, relative to the SO8, is attributed to its lower dependence on the modelling of the board heat spreading resistance. This behaviour results from both the PQFP's larger package size and higher board copper content.

Overall, the level of predictive accuracy obtained for the SO8 and PQFP 208 configurations again demonstrates the robustness of the detailed component and board modelling methodology, and therefore provides confidence in assessing CTM performance for these test cases.

#### 5.4.2 Compact Thermal Model Predictive Accuracy

The accuracy of the networks generated for the SO8 and PQFP 208 detailed models was found to meet the degree of boundary condition independence generally required for CTM parameters to be considered as applicable to any practical environment (Section 4.5.1.2). Any significant decay in CTM accuracy relative to the detailed models would be associated with potential limitations of the compact models used, either in their resistor network or implementation into the CFD model, or a combination of both.

Component junction temperature prediction accuracy is presented both as an absolute temperature error ( $^\circ\text{C}$ ), and percentage value in Tables 5.7 - 5.8 for the SO8 configurations, and Tables 5.11 - 5.12 for the PQFP 208. Measured and predicted component-PCB surface temperature profiles are compared in Figures 5.10 and 5.11 for the SO8 component, and Figures 5.12 and 5.13 for the PQFP 208. The prediction of the PQFP208-PCB thermal interaction is further assessed as a function of component modelling in Figure 5.14. These results are complemented by numerical energy balance analyses of component heat transfer, presented in Tables 5.9 and 5.10 for the SO 8 natural convection and 2 m/s test cases respectively, and in Table 5.13 for the PQFP 208.

##### 5.4.2.1 SO8 Component

Comparison of measured and CTM junction temperature predictions in Table 5.7, highlights in some instances a significant decay in predictive accuracy relative to the detailed component model. However, a direct comparison between CTM and detailed

model predictions in Table 5.8 reveals that CTM predictive accuracy versus measurement are net values. For all convective environments, CTM discrepancies increase with PCB in-plane conductivity, from on average 8% for FR4 #1 to 18% for the IMS PCB. These discrepancies clearly exceed those obtained for any of the boundary condition sets applied for CTM generation in Table 4.11. This pronounced predictive sensitivity to PCB conductivity was not observed for the detailed component model in Table 5.5, and therefore must be related to the compact modelling used.

**Table 5.7** Comparison of measured and predicted component junction temperatures for a single board-mounted SO8 component.

Airflow velocity (m/s)	Prediction discrepancy (°C)								
	FR-4 #1			FR-4 #2			IMS		
	Meas. (°C)	Detailed model	CTM	Meas. (°C)	Detailed model	CTM	Meas. (°C)	Detailed model	CTM
0	124.3	-6.7 (6.4%)	-14.5 (14%)	84.9	+5.5 (8.5%)	-4.0 (6.2%)	71.5	+4.1 (8.0%)	-7.5 (15%)
2	100.2	-5.0 (6.2%)	-10.8 (13%)	77.2	+6.2 (11%)	-3.3 (5.8%)	67.2	+1.3 (2.8%)	-7.3 (15%)
5	88.6	-3.6 (5.2%)	-9.0 (13%)	74.3	+1.6 (2.9%)	-3.9 (7.2%)	66.0	+0.3 (0.7%)	-7.3 (16%)

**Note:** FR-4 #1, FR-4 #2 and IMS refer to PCB construction, Figure 3.50(b). Measurement uncertainty,  $\pm 1\%$ . Component power dissipation = 0.5 W. Ambient air temperature = 20°C. Percentage error in parenthesis ( ) is calculated based on measured component junction temperature rise above ambient air temperature.

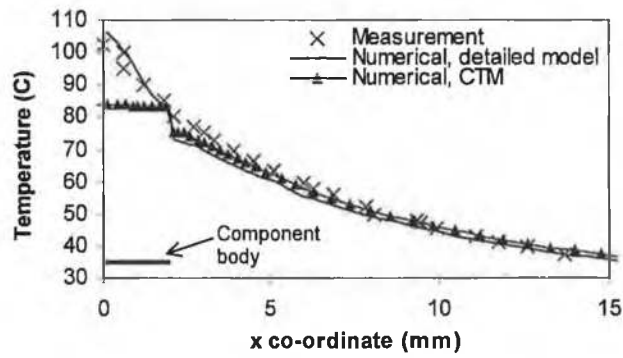
**Table 5.8** Compact versus detailed model junction temperature predictions for a single board-mounted SO8 component.

Airflow velocity (m/s)	Prediction discrepancy (°C)		
	FR-4 #1	FR-4 #2	IMS
0	-7.8 (8.0%)	-9.5 (13%)	-11.6 (21%)
2	-5.8 (7.7%)	-9.5 (15%)	-8.6 (18%)
5	-5.4 (8.3%)	-5.5 (9.8%)	-7.6 (16%)

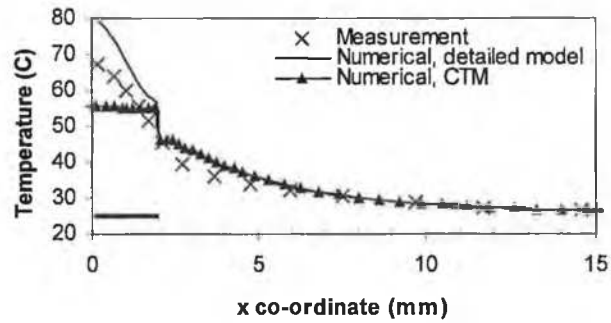
**Note:** FR-4 #1, FR-4 #2 and IMS refer to PCB construction, Figure 3.50(b). Component power dissipation = 0.5 W. Ambient air temperature = 20°C. Percentage error in parenthesis ( ) is calculated based on detailed component model junction temperature rise above ambient air temperature.

However, considering the natural convection cases, it is worth noting that CTM predictions of component heat loss to the board are within 3% of the detailed model predictions, Table 5.7, for the three PCB constructions. This is reflected in the agreement between the CTM and detailed model predictions of the board surface temperature in Figure 5.10. Considerable discrepancies exist, though, between the corresponding package surface temperature predictions, which result from imposed isothermal surfaces in the CTM. For the forced convection cases, CTM predictions of component heat loss to the board are within 6% of the detailed model predictions, Table 5.8, for the three PCB constructions.

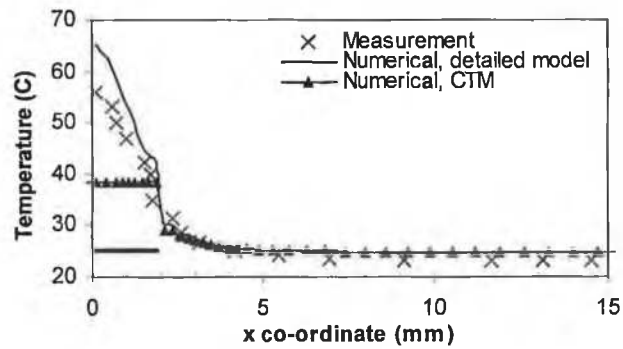
Possible sources of junction temperature discrepancy between the CTM and detailed model should be assessed in future work. However, the following PQFP208 analysis clearly highlights some compact modelling issues.



(a) FR4 #1

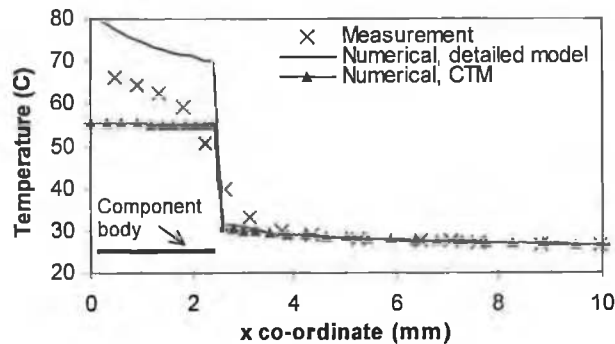


(b) FR4 #2



(c) IMS

**Figure 5.10** Comparison of measured and predicted component-PCB surface temperature profiles in the direction of package width for a single SO8 component in natural convection, as a function of PCB construction, Figure 3.50(b). Measurement uncertainty,  $\pm 0.5^\circ\text{C}$ .



**Figure 5.11** Comparison of measured and predicted component-PCB surface temperature profiles in the direction of package length for a single SO8 component mounted on FR4#2 PCB in natural convection. Measurement uncertainty,  $\pm 0.5^\circ\text{C}$ .

**Table 5.9** Comparison of compact and detailed model predictions of component heat transfer energy balance (%) for a single board-mounted SO8 component in natural convection.

PCB construction	Component model	Heat path (%)			
		Top	Sides	Bottom	Leads
FR-4 #1	Detailed	6.0	5.4	14.1	74.5
	CTM	---	---	91.3*	
FR-4 #2	Detailed	3.9	4.5	16.5	75.1
	CTM	---	---	94.6*	
IMS	Detailed	2.7	3.2	13.7	80.4
	CTM	---	---	97.4*	

Note: \* Flotherm Compact Component SmartPart output for conductive heat loss to board. Component power dissipation = 0.5 W. Ambient air temperature = 20°C.

**Table 5.10** Comparison of compact and detailed model predictions of component energy balance (%) for a single board-mounted SO8 component in a 2 m/s airflow.

PCB construction	Component model	Heat path (%)			
		Top	Sides	Bottom	Leads
FR-4 #1	Detailed	16.0	9.6	12.1	62.3
	CTM	---	---	76.4*	
FR-4 #2	Detailed	11.6	7.4	14.5	66.5
	CTM	---	---	84.3*	
IMS	Detailed	8.3	5.1	12.3	74.3
	CTM	---	---	92.2*	

Note: \* Flotherm Compact Component SmartPart output for conductive heat loss to board. Component power dissipation = 0.5 W. Ambient air temperature = 20°C.

#### 5.4.2.2 PQFP 208 Component

CTM performance is first analysed based on the use of a single lead node in Flotherm's Compact Component SmartPart (Section 4.5.1.2), thereby imposing that the four external lead quadrants be at the same temperature. CTM junction temperature predictions in Table 5.12 are within -0.9°C, -4°C and -5.4°C of the detailed model predictions the star-shaped, shunted and shunted floating node networks respectively. These predictions are ultimately within -1.9°C, -5.0°C and -6.4°C respectively of measurement, Table 5.11. Based on the metric of component junction temperature, it could therefore be concluded that the star-shaped network is the most applicable for this test case. However, both the energy balance analyses of component heat transfer in Table 5.13, and component-PCB surface temperature analyses in Figure 5.12, reveal actual CTM performance.

The total heat loss to the board via the package leads and base is underestimated by approximately 23%, 15% and 12% for the star-shaped, shunted and shunted floating node networks respectively relative to the detailed model predictions. These discrepancies clearly exceed those obtained in the derivation of the CTMs, Tables 4.15 to 4.17. This results in an underestimation of the board surface temperature, more pronounced for the star-shaped network, Figure 5.12. However, this network predicts a higher junction-to-



lead temperature difference, 13.4°C, than for the shunted network, 8.3°C. This higher junction-to-board thermal resistance therefore artificially contributes to better junction temperature prediction accuracy. Note that the junction-to-lead temperature difference for the detailed model is on average 10°C.

**Table 5.11** Comparison of measured and predicted component junction temperatures for a single board-mounted PQFP 208 in a 2 m/s airflow.

<i>Measured</i> (°C)	<i>Prediction discrepancy (°C)</i>						
	<i>Detailed model</i>	<i>CTM, star</i>		<i>CTM, shunted</i>		<i>CTM, shunted, floating node</i>	
		1 Lead node	1 Lead node	2 Lead nodes	1 Lead node	2 Lead nodes	
46.4	-1.0 (3.8%)	-1.9 (7.2%)	-5.0 (19%)	-3.3 (13%)	-6.4 (24%)	-4.5 (17%)	

**Note:** Measurement uncertainty,  $\pm 0.2^\circ\text{C}$ . Component power dissipation = 2 W. Ambient air temperature = 20°C. Percentage error in parenthesis ( ) is calculated based on measured component junction temperature rise above ambient air temperature. “1 Lead node” and “2 Lead nodes” refer to the number of lead nodes coupling the CTM to the board.

**Table 5.12** Compact versus detailed model component junction temperature predictions for a single board-mounted PQFP208 in a 2 m/s airflow.

<i>Prediction discrepancy (°C)</i>				
<i>Star-shaped</i>	<i>Shunted</i>		<i>Shunted, floating node</i>	
1 Lead node	1 Lead node	2 Lead nodes	1 Lead node	2 Lead nodes
-0.9 (3.5%)	-4.0 (16%)	-2.3 (9.1%)	-5.4 (21%)	-3.5 (14%)

**Note:** Detailed component model junction temperature prediction = 45.4°C. Component power dissipation = 2 W. Ambient air temperature = 20°C. Percentage error in parenthesis ( ) is calculated based on detailed model junction temperature rise above ambient air temperature. “1 Lead node” and “2 Lead nodes” refer to the number of lead nodes coupling the CTM to the board.

**Table 5.13** Comparison of compact and detailed model predictions of component energy balance (%) for a single board-mounted PQFP208 in a 2 m/s airflow.

<i>Component model</i>	<i>Heat path (%)</i>			
	<i>Top</i>	<i>Sides</i>	<i>Bottom</i>	<i>Leads</i>
<b>Detailed</b>	9.2	5.4	14.7	70.7
<b>CTM, star-shaped, 1 Lead node</b>	---	---	62.6*	
<b>CTM, shunted</b>	1 Lead node	---	---	70.6*
	2 Lead nodes	---	---	68.0*
<b>CTM, floating</b>	1 Lead node	---	---	73.4*
	2 Lead nodes	---	---	70.3*

**Note:** \* Flotherm Compact Component SmartPart output for conductive heat loss to board. Component power dissipation = 2 W. Ambient air temperature = 20°C.

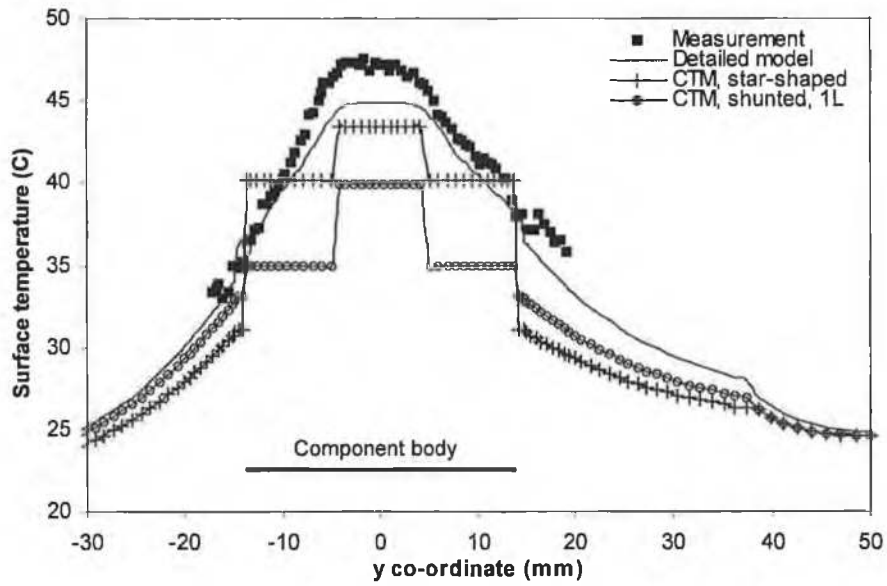
As the code’s Compact Component SmartPart does not explicitly break down total heat loss to the board via the individual heat transfer paths, i.e. package leads, Bottom\_inner and Bottom\_outer, an alternative approach, mean flow regions [69], was used to estimate these paths. It was found that while total heat loss to the board only differed by 8% between the star-shaped and shunted CTM, the star-shaped network predicted that 41% of total component power dissipation was via lead conduction, as compared to 59% for the

shunted network. For the detailed model, this heat transfer path accounted for 71% of the total power dissipation. This indicates that the CTMs used do not only inaccurately predict total heat loss to the board, but also the distribution of the associated heat transfer paths. As the star-shaped network dissipates 10% more heat to the board via the package base relative to the shunted network, the board temperature beneath the package is higher, Figure 5.14.

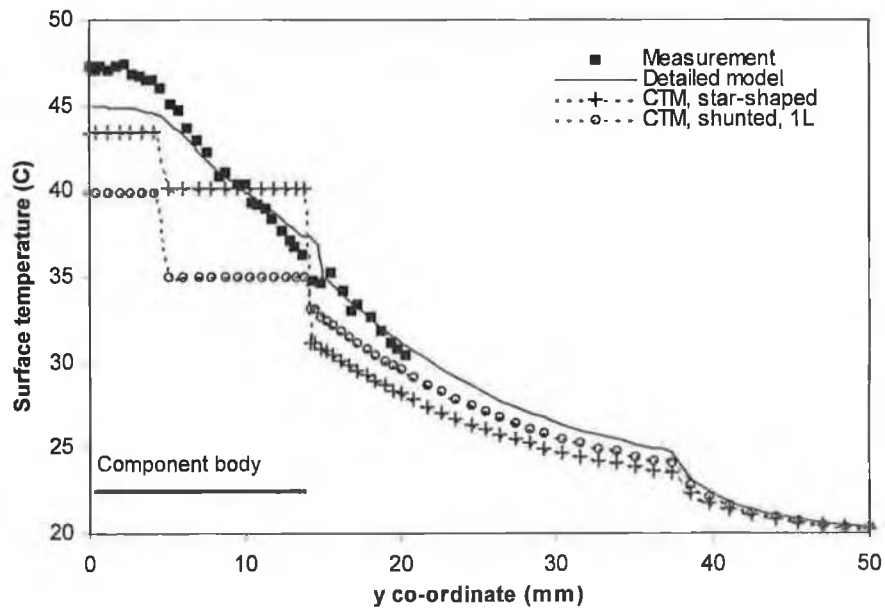
The use of a floating node network improves the prediction of total heat loss to the board, but results in a greater underprediction of junction temperature.

The predictive discrepancies in heat flow highlighted for the PQFP test case contrast with the agreement obtained for the SO8 cases. Although further work is required to study further sources of error, the coupling of the PQFP 208 Compact Component leads to the board was found to impact on the prediction of the board temperature distribution for this case. This variable was considered as the detailed numerical model predicts a temperature difference of 2.5°C between the upstream- and downstream lead feet, with the span-wise lead foot being at an intermediate temperature. CTM predictive sensitivity to this modelling parameter was investigated using two lead nodes, representing the stream-wise and span-wise lead groupings at different temperatures. For both shunted networks, CTM predictive accuracy improved using two lead nodes, both for junction temperature, Table 5.9, and component-PCB thermal interaction in the stream-wise direction, Figures 5.13(a) and 5.14. However, the discrepancy between the measured and predicted board surface temperatures in the span-wise direction increased, Figure 5.13(b). Therefore, neither one- or two-lead node modelling is satisfactory, but this modelling variable served to highlight prediction sensitivity to CTM lead node coupling to the board. While the current code's Compact Component SmartPart is a non-decomposable object, the sensitivity highlighted suggests that decomposition of the SmartPart into, for example, four quarter package CTMs, each representative of quarter geometry detailed model, could improve overall accuracy. This analysis may therefore be of value for future improvement of CTM implementation in the CFD code.

Considering that the CTM predicts twice the combined heat loss from the package top/sides relative to the detailed model, another potential source of error could be the omission of a Side node in the network topology. This may suggest a second area for improvement of CTM implementation in the CFD code.



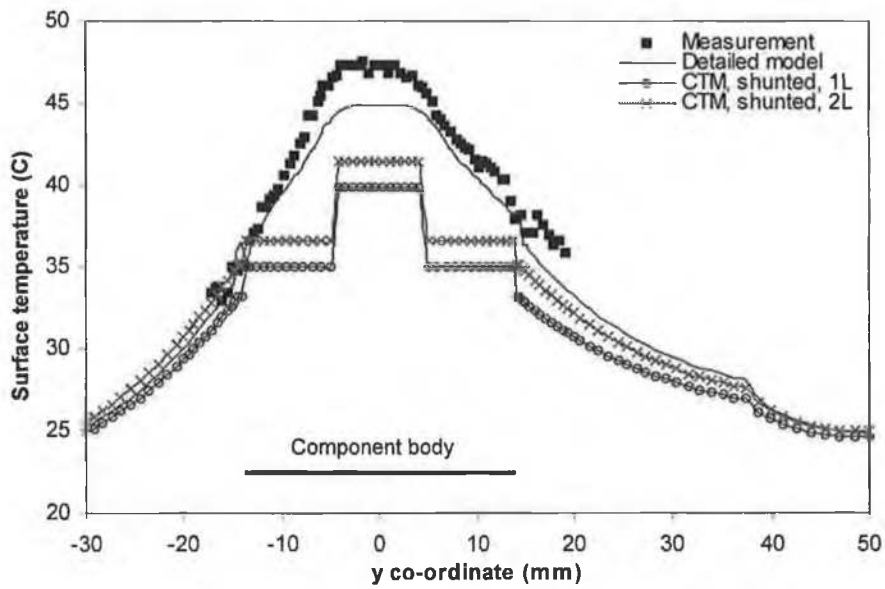
(a) Temperature profile in the stream-wise direction, Figure 3.54



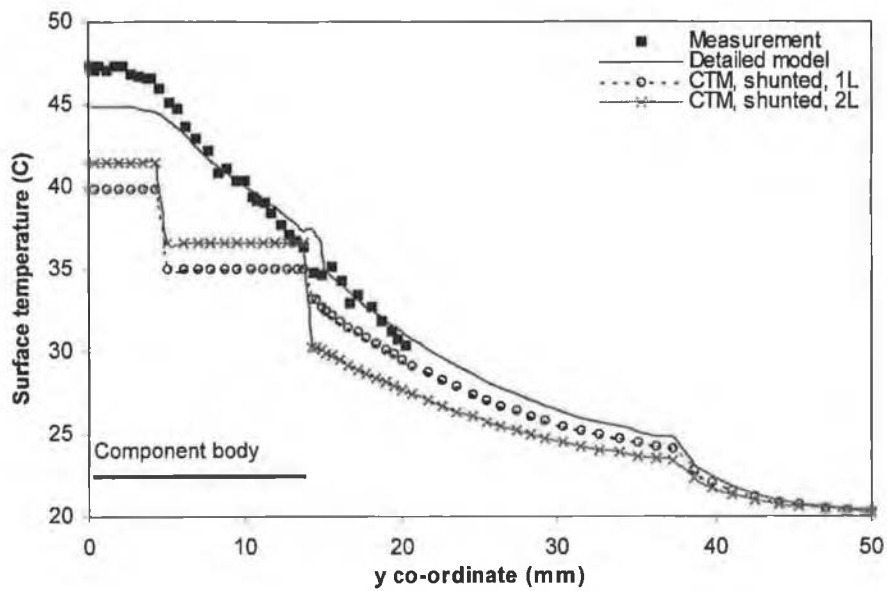
(b) Temperature profile in the span-wise direction, Figure 3.54

Note: CTM coupled to the board using a single lead node. Measurement uncertainty,  $\pm 0.7^\circ\text{C}$ .

**Figure 5.12** Comparison of measured and predicted component-PCB surface temperature profiles for a single board-mounted PQFP208 component in a 2 m/s airflow.



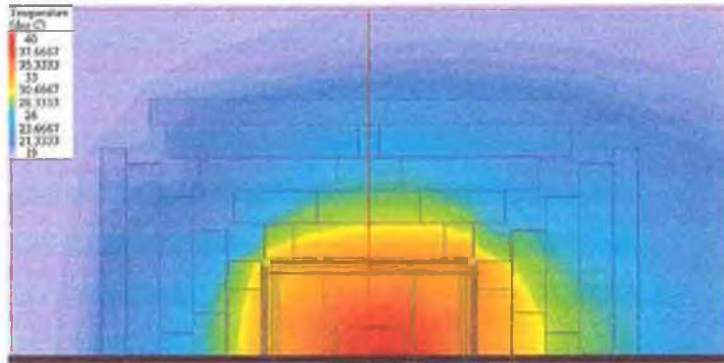
(a) Temperature profile in the stream-wise direction, Figure 3.54



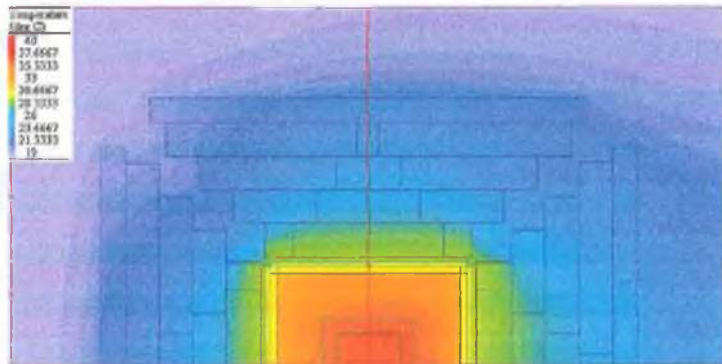
(b) Temperature profile in the span-wise direction, Figure 3.54

**Note:** “1L” and “2L” refer to the number of lead nodes coupling the CTM to the board. Measurement uncertainty,  $\pm 0.7^\circ\text{C}$ .

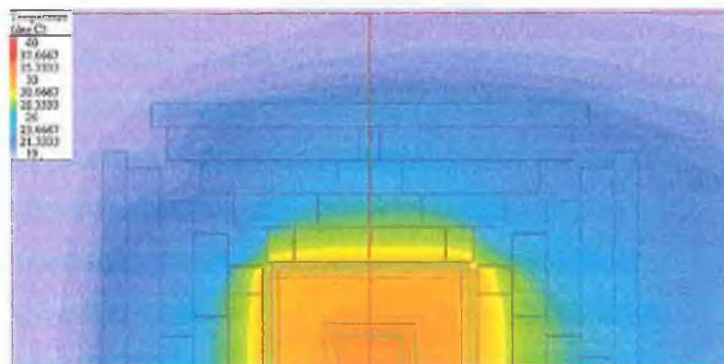
**Figure 5.13** Comparison of measured and predicted component-PCB surface temperature profiles for a single board-mounted PQFP208 component in a 2 m/s airflow as a function of CTM lead node modelling.



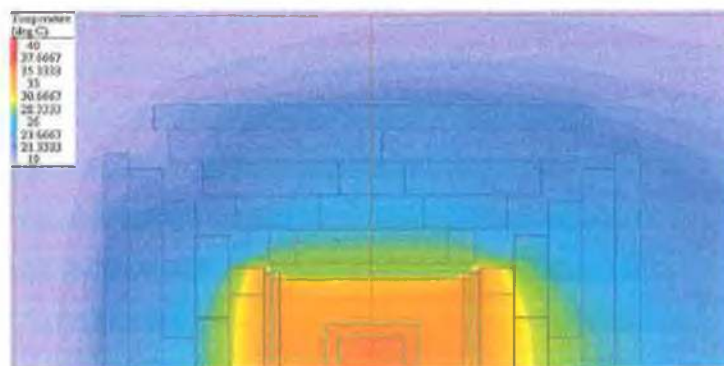
(a) Detailed model



(b) CTM, star-shaped network



(c) CTM, shunted network, 1 Lead node



(d) CTM, shunted network, 2 Lead nodes

Note: "1 Lead node" and "2 Lead nodes" refer to the number of lead nodes coupling the CTM to the board.

**Figure 5.14** Numerically predicted temperature distribution in the plane of PCB surface copper tracking for a single board-mounted PQFP 208 component in a 2 m/s airflow.

### 5.4.3 Summary of Results

Using a detailed component modelling approach, component junction temperature predictive accuracy was within  $-1^{\circ}\text{C}$  (4%) and  $\pm 6^{\circ}\text{C}$  or 8% of measurement for the PQFP 208 and SO8 test configurations respectively, demonstrating the robustness of the detailed component and board modelling methodologies.

Using star-shaped and shunted resistor network-based component compact thermal models, predictive accuracy was found to decay by 7% to 20% relative to the detailed component models. The metrics of measured component junction and component-PCB surface temperature, supported by numerical energy balances of component heat transfer, were used to provide an insight into potential sources of CTM predictive discrepancies. The coupling of the compact component leads to the board was shown to impact on predictive accuracy, and suggestions were made to improve CTM implementation in the CFD code.

### 5.5 Summary of Chapter 5

Using on a range of electronic component types, thermally characterised on different PCB constructions and convective environments, the robustness of the detailed modelling methodologies employed in this study was demonstrated for both steady-state and transient component heat transfer.

The use of component junction and surface temperature measurements has been shown to be effective for assessing the prediction of component-board thermal interaction. For all models, the accuracy of *à priori* predictions could not be improved as there was no justification in deviating from the modelling strategy employed.

The validated PQFP 160 component-PCB models will be used in Chapters 6 and 7 to assess the capability of CFD analysis to predict multi-component board heat transfer.

Using both nominal component/PCB geometry dimensions and material thermo-physical properties, conjugate transient heat transfer for a single-board mounted component was found to be accurately predicted for component dynamic power dissipation, in both fixed and varying ambient air temperature conditions. The results suggest that CFD analysis could play an important role in designing component reliability screening tests involving power- and air temperature cycling, and convective solder reflow thermal profiles.

The predictive performance of resistor network-based component compact thermal models was found to decay by 7% to 20% relative to the corresponding detailed component models. Overall, CTM accuracy would only be sufficient for the early design

phase. The nature of the predictive discrepancies highlight issues that would need to be resolved before CTMs could be routinely adopted for the prediction of electronic component operational temperature using CFD analysis.

## **6.0 Numerical Predictive Accuracy: Multi-Component Board Heat Transfer in Free Convection**

### **6.1 Introduction**

Despite ever-rising die heat fluxes, passive air-cooling is still employed for the thermal management of many electronic applications, either as a primary cooling mode, or back-up in the event of fan failure in a forced convection cooled system [81,280,281]. This cooling approach is simple, quiet, cost-effective, maintenance-free and reliable.

In this chapter, the prediction of multi-component board heat transfer is investigated in laminar free convection. The ability of the Computational Fluid Dynamics (CFD) code to predict component thermal interaction is assessed in two controlled steps, from individually powered component configurations on the Stage 3 Printed Circuit Board (PCB), to a fully powered configuration, where all components are simultaneously powered. The test configurations were described in Section 3.3 and the component-Printed Circuit Board (PCB) numerical modelling methodology was validated in Chapter 5.

These analyses are undertaken using Flotherm. Experimental and numerical results are compared for both steady-state component junction temperature and component-board surface temperature profiles. Numerical energy balance analyses of component heat transfer are also presented to investigate the sensitivity of component heat transfer to operating conditions.

Very little of the data presented here can be compared, or discussed in the context of past publications because there is little or nothing of relevance.

### **6.1 Individually Powered Component Configurations**

The numerical model for the Stage 3 PCB individually powered component configurations is shown in Figure 4.14(b). Component junction temperature prediction accuracy is presented both as an absolute temperature error ( $^{\circ}\text{C}$ ), and percentage value in Table 6.1.

Junction temperature predictions for the individually powered components on the multi-component PCB are overall within  $+3^{\circ}\text{C}$  (5%) of measurement when account is made of experimental error. This trend holds independently of package type and component location. The only exception to this is component G, for which prediction accuracy is slightly outside this band. Overall, junction temperature prediction accuracy is comparable to that obtained for the single board-mounted component configurations, Tables 5.1 and 5.2, where component-board thermal interaction was shown to be correctly captured. Therefore, the component and PCB modelling methodology translates to the Stage 3 PCB.



On this basis, any significant decay in predictive accuracy for the simultaneously powered configuration would probably be attributed to a potential weakness of the code to predict more complex flows and their impact on component-PCB heat transfer.

**Table 6.1** Comparison of measured and predicted junction temperatures for individually powered components on the non-insulated Stage 3 PCB in free convection.

<i>Component location</i>	<i>Measured (°C)</i>	<i>Prediction discrepancy (°C)</i>
A	---	---
B	---	---
C	76.9	+1.9 (3.3%)
D	---	---
E	---	---
F	86.0	+1.9 (2.9%)
G	82.1	+4.1 (6.6%)
H	83.6	+2.9 (4.6%)
I	85.0	+1.6 (2.5%)
J	85.7	+0.1 (0.2%)
K	86.2	+1.5 (2.3%)
L	---	---
M	74.5	+1.5 (2.8%)
N	---	---
O	---	---

**Note:** Component location is defined in Figure 3.6(a). Measurement uncertainty,  $\pm 0.5^\circ\text{C}$ . Percentage prediction error in parenthesis ( ) is calculated based on the measured component junction temperature rise above ambient air temperature. Component power dissipation = 3W. Ambient air temperature normalised to  $20^\circ\text{C}$ .

## 6.2 Simultaneously Powered Component Configuration

Component junction temperature prediction accuracy on the simultaneously powered Stage 3 PCB is presented in Table 6.2, with corresponding component-PCB surface temperature profiles shown in Figures 6.1 and 6.2.

In Table 6.2, junction temperature prediction accuracy is overall within to  $+5^\circ\text{C}$  or 7%, with the exception of component I, which is slightly outside this band. This represents a decay relative to the accuracy for the individually powered configurations, indicating that component thermal interaction is not fully captured.

Overall, the component powered-off temperature rise between the individually- and simultaneously powered configurations, that is its temperature rise due solely to component thermal interaction, is overpredicted by on average  $+3^\circ\text{C}$ , Table 6.3, with the notable exception of device I. Its temperature rise is overpredicted by on order 40%, thereby resulting in a worst-case junction temperature error in Table 6.2. The magnitude of this error is surprising when contrasted with the accuracy obtained for the other components in the same span-wise row. While components K and M, which are located in

the bottom span-wise component row, have the lowest measured temperature rise, this rise is overpredicted by on order 40%, Table 6.3. This clearly exceeds measurement uncertainty. It is suspected that the present discrepancies could be related to inaccurate prediction of the local flow conditions, whereby the components could be exposed to buoyancy-induced forced convection conditions [282,283]. Such conditions would result from the coupling between the self-induced buoyant flow for each component, and the considerably stronger, collective board flow. This hypothesis is supported by smoke-flow visualisations undertaken by Cole [201], who observed a complex coupling between the component self-induced flow and the global board flow on this PCB.

**Table 6.2** Comparison of measured and predicted component junction temperatures on simultaneously powered, non-insulated Stage 3 PCB in free convection.

<i>Component location</i>	<i>Measured (°C)</i>	<i>Prediction discrepancy (°C)</i>
A	101.7	+4.8 (5.9%)
B	94.2	+5.4 (7.3%)
C	94.7	+5.3 (7.1%)
D	94.1	+5.6 (7.6%)
E	92.1	+5.3 (7.4%)
F	99.8	+4.7 (5.9%)
G	102.9	+4.1 (4.9%)
H	101.9	+5.2 (6.3%)
I	99.7	+7.4 (9.3%)
J	99.2	+2.1 (2.7%)
K	92.7	+3.9 (5.4%)
L	85.1	+3.4 (5.2%)
M	83.5	+5.5 (8.7%)
N	83.9	+4.9 (7.7%)
O	83.5	+3.4 (5.4%)

**Note:** Component location is defined in Figure 3.6(a). Measurement uncertainty,  $\pm 0.6^{\circ}\text{C}$ . Percentage prediction error in parenthesis ( ) is calculated based on the measured component junction temperature rise above ambient air temperature. Component power dissipation = 3W. Ambient air temperature normalised to  $20^{\circ}\text{C}$ .

**Table 6.3** Comparison of measured and predicted component junction temperature rise between the individually and simultaneously powered component configurations on the non-insulated Stage 3 PCB in free convection.

<i>Component location</i>	<i>Measured (°C)</i>	<i>Prediction discrepancy (°C)</i>
C	17.8	+3.4
F	13.8	+2.8
G	20.8	0
H	18.3	+2.3
I	14.7	+5.8
J	13.5	+2.0
K	6.5	+2.4
M	9.0	+4.0

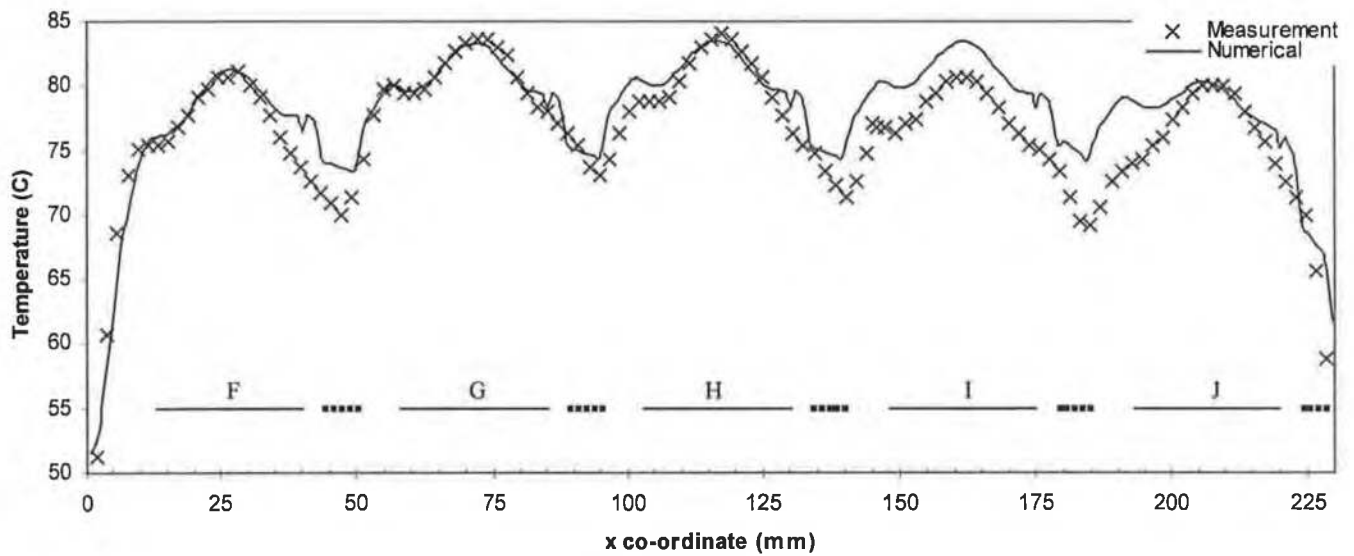
**Note:** Component location is defined in Figure 3.6(a). Measurement uncertainty in powered-off component temperature rise,  $\pm 0.8^{\circ}\text{C}$ . Component power dissipation = 3W. Ambient air temperature normalised to  $20^{\circ}\text{C}$ .

To further investigate the nature of junction temperature prediction discrepancies, measured and predicted component-PCB surface temperature distributions were compared on both the board component- and non-component sides. A representative sample of these analyses is presented in Figures 6.1 and 6.2, with the analysis planes used defined in Figure 3.19.

Considering first the board non-component side, Figure 6.1, measurements and predictions agree remarkably well, both qualitatively and quantitatively in the stream-wise and span-wise airflow directions, with the exception of localised discrepancies. As discussed for the single-board mounted component case, Stage 1 PCB, in Section 5.2.2, differences between predictions and measurements over the copper tracking regions in Plane X-X, Figure 6.1(a), are essentially attributable to experimental error. In line with the component junction temperature predictions in Table 6.2, the greatest discrepancy in surface temperature ( $2.7^{\circ}\text{C}$ ) is in the region of component I, Figures 6.1(a) and 6.1(c). Overall, however, the agreement between measured and predicted surface temperature distributions indicates that the numerical model accurately predicts heat loss from the board non-component side, which is predicted to account for 48% of total power dissipation. Considering the importance of this heat transfer path, the agreement between predictions and measurement indicates that component-board thermal interaction is accurately captured.

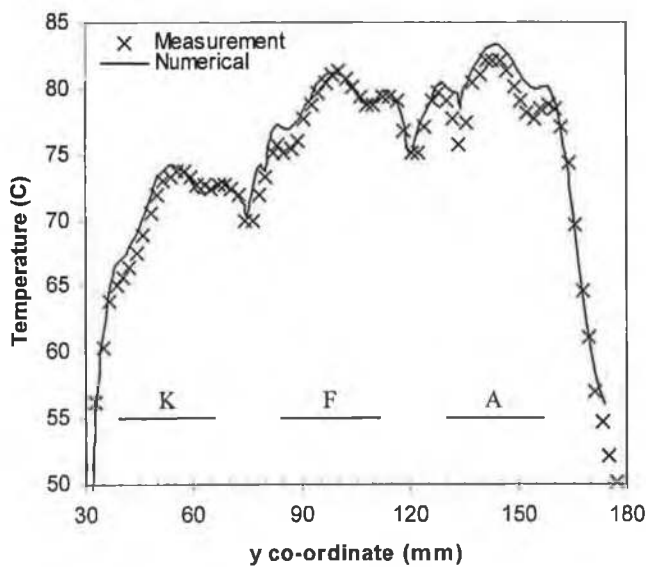
On the board component side, Figure 6.2, the shape of the predicted surface temperature distribution over the component bodies agree well with measurement, with the magnitude of discrepancies reflecting those of corresponding junction temperature prediction errors in Table 6.2. As for the Stage 1 PCB (Section 5.2.2), prediction discrepancies over the packages' leads and board surface copper tracking are primarily attributed to measurement error. However, measured and predicted temperature profiles are in good agreement in regions where the FR4 substrate is exposed, again indicating that component-board thermal interaction is overall well captured.

Overall for the simultaneously powered PCB, predictive accuracy for component junction temperature would qualify for the intermediate phase of the design process.

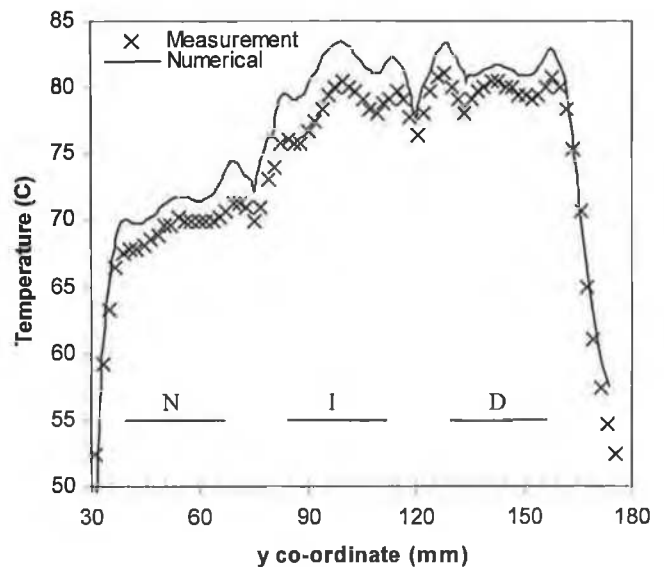


Note: (....) Copper tracking location on the board non-component side.

(a) Component locations F to J, Plane X-X



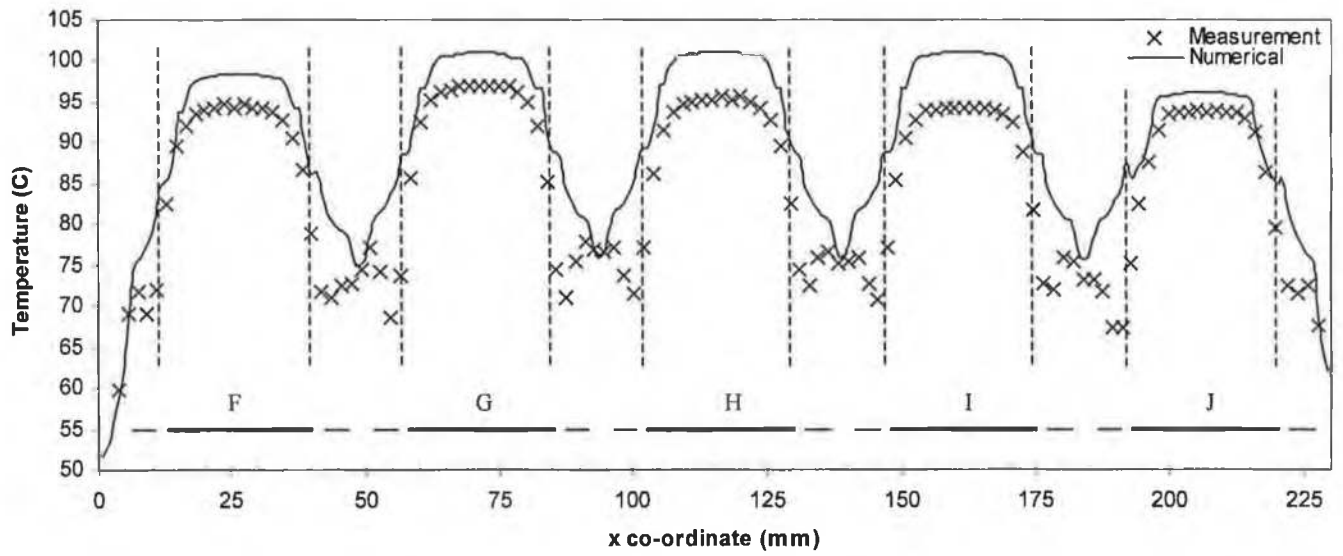
(b) Component locations A-F-K, Plane  $Y_1$ - $Y_1$



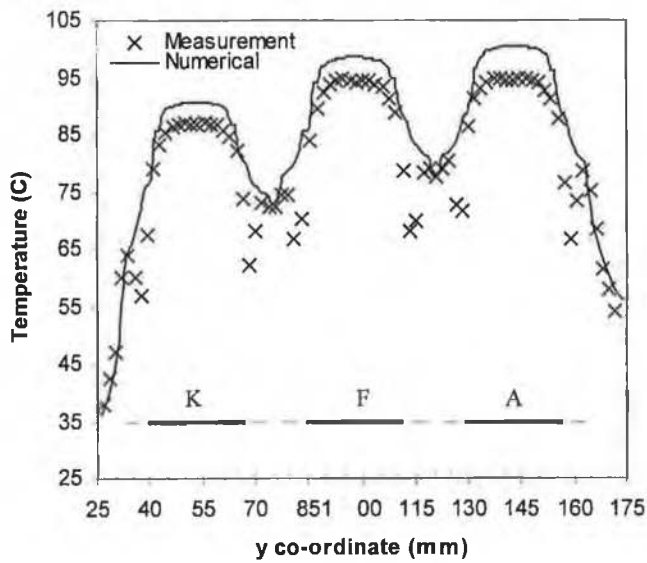
(c) Component locations D-I-N, Plane  $Y_2$ - $Y_2$

Note: (—) denotes component body location on the board component-side. Analysis planes defined in Figure 3.19. Uncertainty in temperature measurement =  $\pm 1.4^\circ\text{C}$ .

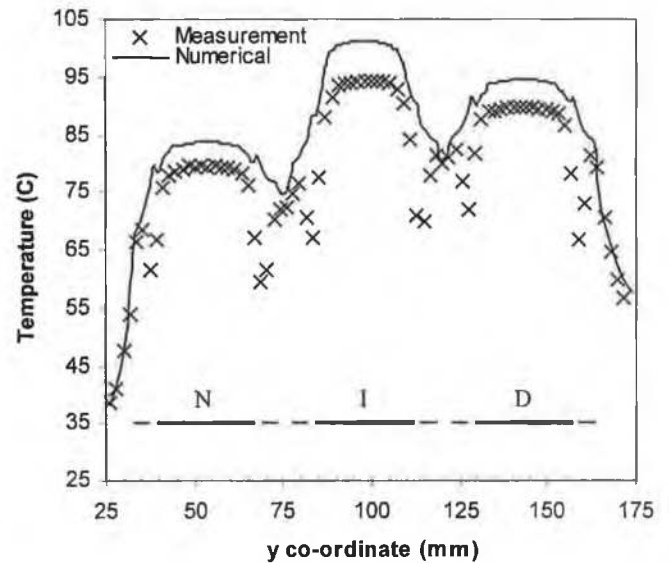
**Figure 6.1** Comparison of measured and predicted component-PCB surface temperature profiles on the board non-component side, for the simultaneously powered PCB in free convection.



(a) Component locations F to J, Plane X-X



(b) Component locations A-F-K, Plane  $Y_1$ - $Y_1$



(c) Component locations D-I-N, Plane  $Y_2$ - $Y_2$

Note: (—) denotes component body location, and (—) denotes copper tracking location on the board component side. Analysis planes defined in Figure 3.19. Uncertainty in temperature measurement =  $\pm 1.4^\circ\text{C}$ .

**Figure 6.2** Comparison of measured and predicted component-PCB surface temperature profiles on the board component side, for the simultaneously powered PCB in free convection.

### 6.3 Energy Balance Analyses of Component Heat Transfer

The numerical models are used to investigate the sensitivity of component heat transfer to component operating conditions. The predicted energy balance analyses of component heat transfer are presented for both the individually- and simultaneously powered Stage 3 component configurations in Table 6.4. The net heat flux through each heat transfer path is presented as a percentage of the total dissipated power.

Table 6.4 shows that lead conduction is the dominant heat transfer path, with package design III displaying this most strongly.

Considering first the individually powered configurations, component heat loss to the board, via the package leads and base, is on order 75%. Components having the same package design, located within the same span-wise component row, (B-E, F-I, L-O) were found to have the same energy balance. For package design III, devices located in the bottom span-wise row (L-O) dissipate 3% more heat to the board via lead conduction than those in the top span-wise row (B-E), possibly reflecting the influence of higher copper tracking density on the board non-component side. The same observation can be made for components A and K, which belong to the same stream-wise component row. The energy balance of component J individually powered is similar to that for the package design I devices in the same span-wise row (F-J), reflecting the similarity of their operating temperatures.

**Table 6.4.** Numerical component energy balances for individually and simultaneously powered components on the non-insulated Stage 3 PCB in free convection.

Component location	Heat path (%)											
	Individually powered						Simultaneously powered					
	Top		Base		Leads	Sides	Top		Base		Leads	Sides
	Conv.	Rad.	Conv.	Rad.	Cond.	Conv.	Conv.	Rad.	Conv.	Rad.	Cond.	Conv.
A	13	11	13	2	59	2	14	15	14	2	53	2
B - E	11	10	11	2	63	3	13	13	13	2	56	3
F - I	12	10	13	2	61	2	15	13	15	2	52	3
J	12	10	13	2	61	2	14	13	14	2	54	3
K	12	10	13	2	61	2	14	11	14	2	56	3
L - O	11	8	11	2	66	2	14	10	13	2	58	3

Note: Component power dissipation = 3W. Cond. = conduction, Conv.= convection, Rad. = radiation.

For the simultaneously powered component configurations, heat loss to the board reduced by on order 6% relative to the corresponding individually powered cases. This is due to conductive thermal interaction from adjacent devices reducing the component thermal footprint.

It is notable that all components display very similar behaviour, regardless of package type and location. This highlights the insensitivity of component heat transfer paths to component internal construction, due to the dominance of lead conduction to the PCB.

The above analyses illustrate how different component types thermally interact with the PCB, and their varying degree of sensitivity to thermal and aerodynamic conditions. This approach could be used in more complex applications to assess thermal design options for lowering component operating temperature. The alternative is expensive prototyping.

#### **6.4 Summary**

Numerical predictive accuracy for multi-component board heat transfer was experimentally assessed in free convection, using a CFD code dedicated to the thermal analysis of electronic systems. A systematic approach was employed to permit both the modelling methodology and solver capability to be carefully evaluated, whereby test case complexity was increased in controlled steps from single-board mounted components to the highly conjugate multi-component PCB.

Using nominal component dimensions and material thermo-physical properties, component junction temperature predictions were found to be overall within +5°C (7%) of measurement, independently of component location on the board. Such an accuracy would qualify for the intermediate thermal design phase, but would not be sufficient for temperature predictions to be used as boundary conditions for subsequent reliability and electrical performance analyses. In all instances, junction temperature was overpredicted, and would therefore lead to a conservative thermal design. The full complexity of component thermal interaction, as characterised by the component powered-off temperature rise, was shown not to be fully captured by the code.

## 7.0 Numerical Predictive Accuracy: Multi-Component Board Heat Transfer in Forced Convection

### 7.1 Introduction

In this chapter, Computational Fluid Dynamics (CFD) predictive accuracy is assessed for populated board heat transfer in forced convection. This is achieved using the Stage 2 and 3 Printed Circuit Board (PCB) test configurations described in Section 3.3, generating different airflow phenomena and varying degrees of component thermal interaction. To permit sources of numerical error to be isolated, predictive accuracy is assessed in controlled steps, from component H individually powered on the Stage 2 PCB, to the simultaneously powered, insulated Stage 3 configuration. The complexity of the thermofluids and thus the challenge posed for numerical prediction was highlighted in Section 3.3.3.3.

Experimental and numerical results are compared for both steady-state component junction temperature and surface temperature profiles. In addition, supporting airflow visualisations presented in Section 3.3.5 are used to help assess predictive accuracy. The component-board numerical modelling methodology was previously validated using the Stage 1 PCB (Section 5.2).

In the absence of a dominant length scale, hence transition Reynolds number, that adequately describes the heat transfer characteristic over the PCB, the fluid domain was solved using both laminar and a range of turbulent flow models as outlined in Section 4.2. Using Flotherm, predictive accuracy is evaluated for standard flow modelling approaches, which are typically employed for the thermal design of electronics. To investigate if improvements in predictive accuracy could be obtained using alternative flow modelling strategies, several candidate turbulent flow models are evaluated in Fluent. Such an evaluation will permit perspective to be given on both the capabilities of dedicated CFD codes for the prediction of electronic component heat transfer, and the potential for improved predictive accuracy.

As in Chapter 6, very little of the data presented here can be compared, or discussed in the context of past publications because there is little or nothing of relevance.

### 7.2 Standard Flow Modelling

Using Flotherm, predictive accuracy is evaluated for the standard high-Reynolds number  $k-\epsilon$  flow model, which forms the *à priori* prediction for turbulent flow, and the zero-equation LEVEL model, due to its greater applicability for system level analysis (Section 4.3.1).



Predictive accuracy is assessed for the Stage 2 and 3 PCBs, characterised in 2 and 4 m/s airflows. Stage 2 is firstly analysed with component H individually powered, and the leading edge devices (A,F,K) acting as a source of upstream flow disturbance. Both individually and simultaneously powered components on the non-insulated and insulated Stage 3 PCBs are then considered. The individually powered component configurations are used to isolate the impact of aerodynamic conditions on predictive accuracy. The simultaneously powered cases serve to assess the prediction of component thermal interaction. As the k-ε predictions form the *a priori* predictions for turbulent flow analysis, discussion focuses on the laminar and k-ε model results.

For the single board-mounted component H (Stage 1), component junction temperature predictive accuracy in both 2 and 4 m/s airflows was found to be within  $\pm 2^{\circ}\text{C}$  (4%) of measurement for all flow models, Table 5.1. Therefore, any significant decay in predictive accuracy for the populated PCBs could be attributed to a weakness of the CFD code to predict the more complex flows and their impact on component-PCB heat transfer.

### 7.2.1 Stage 2, Component H Individually Powered

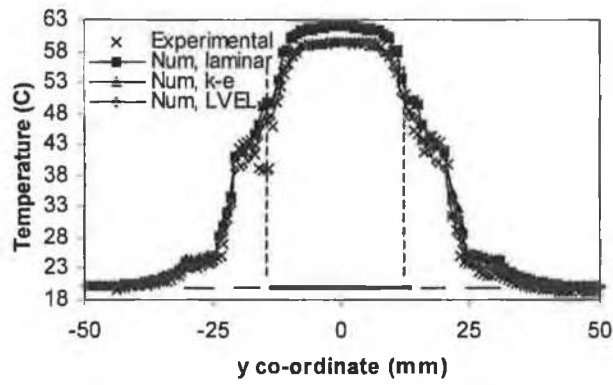
In Table 7.1, component H's junction temperature prediction accuracy decays relative to Stage 1, Table 5.1, to on average  $+5^{\circ}\text{C}$  (13%) of measurement for both the laminar and k-ε flow models. Both flow model predictions are within  $0.5^{\circ}\text{C}$  of each other, indicating that the k-ε model predicts a low level of turbulent viscosity in the flow. While H's measured operating temperature decreases by approximately  $4^{\circ}\text{C}$  from Stage 1 to 2, Tables 5.1 and 7.1, corresponding predictions remain similar. This invariance indicates that the flow models fail to capture the enhanced heat transfer resulting from upstream aerodynamic disturbance generated by the passive leading row devices (A,F,K), experimentally visualised in Figure 3.33.

**Table 7.1** Comparison of measured and predicted component junction temperatures for component H individually powered on the Stage 2 PCB in forced convection.

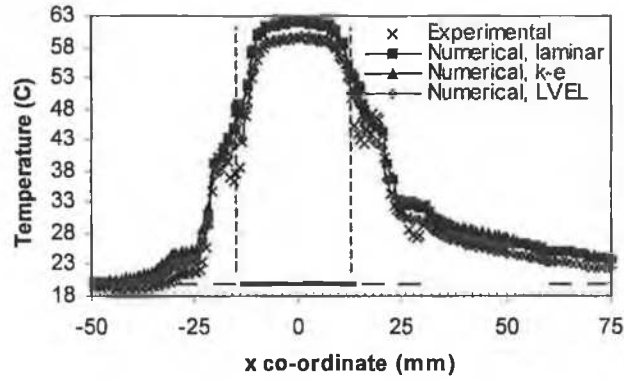
Airflow (m/s)	Measured ( $^{\circ}\text{C}$ )	Prediction discrepancy ( $^{\circ}\text{C}$ )		
		Laminar	k-ε	LVEL
2.0	63.0	+5.1 (12%)	+4.9 (11%)	+2.2 (5.1%)
4.0	54.6	+4.9 (14%)	+5.3 (15%)	+3.1 (9.0%)

**Note:** Measurement uncertainty,  $\pm 0.4^{\circ}\text{C}$ . Percentage prediction error in parenthesis ( ) is calculated based on the measured component junction temperature rise above ambient air temperature. Component power dissipation = 3W. Ambient air temperature =  $20^{\circ}\text{C}$ .

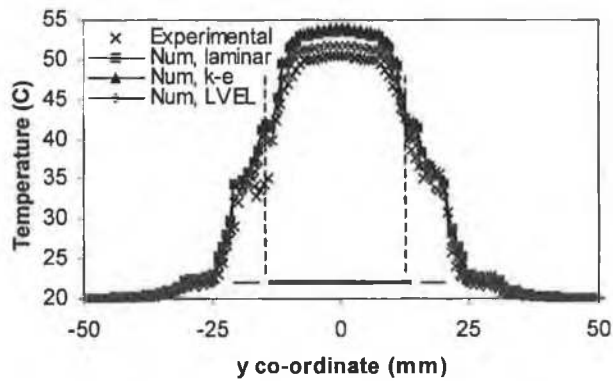
To investigate this aspect, measured and predicted component-PCB surface temperature profiles are compared in Figure 7.1 for component H on the Stage 2 PCB. Both at 2 and 4 m/s, the magnitude and shape of the predicted surface temperature profiles over the package



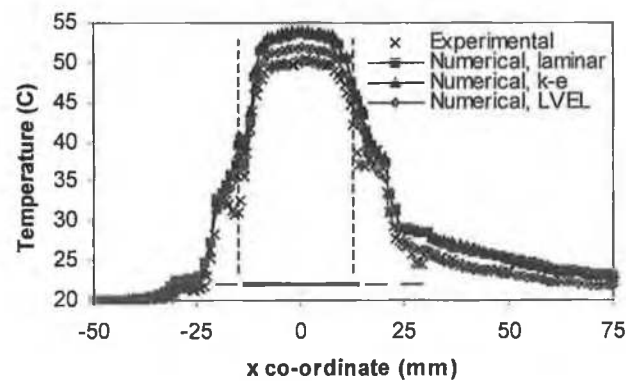
(a) Temperature profile in the span-wise direction in a 2 m/s airflow



(b) Temperature profile in the stream-wise direction in a 2 m/s airflow



(c) Temperature profile in the span-wise direction in a 4 m/s airflow



(d) Temperature profile in the stream-wise direction in a 4 m/s airflow

**Note:** Origin of x- and y- axes corresponds to the package centre. (—) denotes component body location, (—) denotes copper tracking location. Uncertainty in temperature measurement,  $\pm 1.4^\circ\text{C}$ .

**Figure 7.1** Comparison of measured and predicted component-PCB surface temperature profiles for component H individually powered on the Stage 2 PCB in forced convection.

compare well with measurement, indicating that internal package heat spread is correctly modelled. The measured and predicted board surface temperature profiles are in good agreement in the span-wise direction, Figures 7.1(a) and 7.1(c), indicating that PCB heat spread is well captured. While the same PCB modelling methodology was employed in the stream-wise direction, Figures 7.1(b) and 7.1(d), discrepancies exist, more pronounced downstream of the component. In this region, the board surface temperature is overpredicted by on average 2°C for both airflow velocities. Such discrepancies were highlighted downstream of the single board-mounted PQFP 160 and PQFP 208 devices in Figures 5.2 and 5.12 respectively, and were attributed to inaccurate prediction of the advected air temperature adjacent to the board in this region [35]. However, the corresponding PQFP 160 and PQFP 208 analyses did not show predictive discrepancies upstream of the component. Whereas laminar and turbulent flow model predictions of the board surface temperature downstream of the component are similar, Figure 7.1(b,d), discrepancies between flow model predictions are evident upstream of the component. This suggests that inaccurate prediction of the board surface temperature in this region is more likely attributable to inaccurate prediction of the local convective heat transfer coefficient. The discrepancies in Figures 7.1(b) and 7.1(d) are therefore clearly attributable to the impact of upstream aerodynamic disturbance generated by the passive leading row devices on component H heat transfer not being accurately captured. The decay in junction temperature prediction accuracy from Stages 1 to 2, Tables 5.1 and 7.1, is therefore linked to the increased complexity of the flow phenomena shown in Figure 3.33. The impact of such discrepancies on predictive accuracy for more densely populated PCB applications will be discussed for the Stage 3 configurations.

### **7.2.2 Stage 3, Individually Powered Components**

Non-insulated PCB. In Tables 7.2 and 7.3, the laminar and k- $\epsilon$  flow models predictions are similar at 2 m/s, with greater differences at 4 m/s. For both flow models, the greatest prediction errors occur at the first two leading edge component rows, indicating a weakness of the code to predict the leading edge flows, visualised at 2 m/s in Figure 3.34. In this region, the k- $\epsilon$  model displays better accuracy, particularly at 4 m/s. In free convection conditions, however, the operating temperature of the leading edge individually powered components was accurately predicted, to within 2°C (3%) of measurement, Table 6.1. For forced convection, the predictive discrepancies at the leading edge are therefore not related to component sample, but its location on the board.

**Table 7.2** Comparison of measured and predicted component junction temperatures for individually powered components on the non-insulated Stage 3 PCB in a 2 m/s airflow.

Component location	Measured (°C)	Prediction discrepancy (°C)		
		Laminar	k-ε	LVEL
A	61.4	+7.7 (19%)	+6.3 (15%)	+3.1 (7.5%)
F	61.2	+7.3 (18%)	+6.1 (15%)	+2.9 (7.0%)
G	62.6	+7.1 (17%)	+6.6 (15%)	+2.8 (6.6%)
H	64.4	+4.8 (11%)	+5.1 (12%)	+1.4 (3.2%)
I	64.3	+4.3 (9.7%)	+4.3 (9.7%)	+1.7 (3.8%)
J	64.9	-0.9 (2.0%)	-0.8 (1.8%)	-2.9 (6.5%)
K	61.6	+6.9 (17%)	+5.6 (13%)	+2.3 (5.5%)

**Note:** (A,F,K) and J are leading and trailing edge components respectively. Measurement uncertainty, ±0.4°C. Percentage prediction error in parenthesis ( ) is calculated based on the measured component junction temperature rise above ambient air temperature. Component power dissipation = 3W. Ambient air temperature = 20°C.

**Table 7.3** Comparison of measured and predicted component junction temperatures for individually powered components on the non-insulated Stage 3 PCB in a 4 m/s airflow.

Component location	Measured (°C)	Prediction discrepancy (°C)		
		Laminar	k-ε	LVEL
A	53.0	+9.3 (28%)	+6.6 (20%)	+4.5 (14%)
F	52.9	+8.7 (26%)	+6.6 (20%)	+4.3 (13%)
G	54.6	+6.7 (19%)	+6.3 (18%)	+3.5 (10%)
H	56.6	+3.9 (11%)	+3.7 (10%)	+1.7 (4.6%)
I	55.6	+4.7 (13%)	+4.9 (14%)	+3.0 (8.4%)
J	56.1	+0.4 (1.1%)	+0.4 (1.1%)	-1.2 (3.3%)
K	52.9	+8.6 (26%)	+6.7 (20%)	+4.2 (13%)

**Note:** (A,F,K) and J are leading and trailing edge components respectively. Measurement uncertainty, ±0.4°C. Percentage prediction error in parenthesis ( ) is calculated based on the measured component junction temperature rise above ambient air temperature. Component power dissipation = 3W. Ambient air temperature = 20°C.

Insulated Stage 3 PCB. In Tables 7.4 and 7.5, the greatest prediction errors occur for component G using the k-ε flow model, which is located in a region identified as aerodynamically sensitive by flow visualisation, Figure 3.35. As previously described, the flow separates upstream of the insulated PCB leading edge and re-attaches in a region just downstream of the leading row components A, F and K, with unsteady characteristics at 2 m/s. The flow models therefore display different sensitivities to the aerodynamic conditions on the insulated PCB, with the laminar model being more accurate. The poor accuracy of the k-ε model for component G is attributed to the limited applicability of the wall functions used for the prediction of wall shear stress, hence heat transfer in re-attaching flow conditions [67]. It should also be noted that the k-ε model is not suited to the analysis of the unsteady flow over the insulated board at 2 m/s, as it does not capture flow unsteadiness. This is due in this instance to an overprediction of the turbulent viscosity damping out any transient flow features (Section 4.6.1.2). However, the k-ε model was assessed to reflect normal design scenarios, where there is no *à priori* knowledge of the flow regime, and whether it is steady or unsteady. Though the k-ε predictions should therefore be considered with reservation, this model yields an accuracy

similar to that of the laminar model for the downstream components H to J.

**Table 7.4** Comparison of measured and predicted component junction temperatures for individually powered components on the insulated Stage 3 PCB in a 2 m/s airflow.

Component location	Measured (°C)	Prediction discrepancy (°C)		
		Laminar	k-ε	LVEL
A	74.1	+5.6 (10%)	+6.2 (12%)	+3.3 (6.1%)
F	75.2	+2.6 (4.7%)	+4.1 (7.4%)	+1.4 (2.5%)
G	73.3	+4.1 (7.7%)	+11.9 (22%)	+6.7 (13%)
H	75.7	+2.9 (5.2%)	+5.9 (11%)	+3.0 (5.4%)
I	76.6	+1.5 (2.7%)	+3.0 (5.3%)	+0.7 (1.2%)
J	75.8	-2.1 (3.8%)	-2.0 (3.6%)	-4.8 (8.6%)
K	73.4	+4.9 (9.2%)	+6.6 (12%)	+3.8 (7.1%)

**Note:** (A,F,K) and J are leading and trailing edge components respectively. Measurement uncertainty,  $\pm 0.5^\circ\text{C}$ . Percentage prediction error in parenthesis ( ) is calculated based on the measured component junction temperature rise above ambient air temperature. Component power dissipation = 3W. Ambient air temperature =  $20^\circ\text{C}$ .

**Table 7.5** Comparison of measured and predicted component junction temperatures for individually powered components on the insulated Stage 3 PCB in a 4 m/s airflow.

Component location	Measured (°C)	Prediction discrepancy (°C)		
		Laminar	k-ε	LVEL
A	62.3	+5.8 (14%)	+6.7 (16%)	+5.3 (13%)
F	61.8	+4.5 (11%)	+6.6 (16%)	+4.6 (11%)
G	63.0	+4.8 (11%)	+9.6 (22%)	+7.3 (17%)
H	64.6	+3.4 (7.6%)	+5.5 (12%)	+3.3 (7.4%)
I	65.4	+3.4 (7.5%)	+3.3 (7.3%)	+1.3 (2.9%)
J	64.6	-1.1 (2.5%)	-1.4 (3.1%)	-4.0 (9.0%)
K	62.3	+6.7 (16%)	+7.1 (17%)	+4.9 (12%)

**Note:** (A,F,K) and J are leading and trailing edge components respectively. Measurement uncertainty,  $\pm 0.4^\circ\text{C}$ . Percentage prediction error in parenthesis ( ) is calculated based on the measured component junction temperature rise above ambient air temperature. Component power dissipation = 3W. Ambient air temperature =  $20^\circ\text{C}$ .

### 7.2.3 Stage 3, Simultaneously Powered Components

Non-insulated PCB. In Table 7.6, predictive accuracy for both flow models decays for the downstream components H to J, relative to the corresponding individually powered configurations in Table 7.3. This is attributed to inaccurate prediction of the downstream component temperature rise between the individually- and simultaneously powered configurations. This rise is solely due to component thermal interaction, and is referred to as the component powered-off temperature rise. Measurements and predictions of this variable are compared in Figure 7.2(a). The laminar model overpredicts downstream component powered-off temperature rise by on order 40%, whereas the k-ε model overpredicts by 25%. Therefore, the predictive accuracy obtained for the simultaneously powered PCB in Table 7.6 are only net values, and a function of component power dissipation. Overall, the laminar and k-ε flow model component operating temperature predictions would only be sufficient for the early design phase.

**Table 7.6** Comparison of measured and predicted component junction temperatures for simultaneously powered components on the non-insulated Stage 3 PCB in a 4 m/s airflow.

Component location	Measured (°C)	Prediction discrepancy (°C)		
		Laminar	k-ε	LVEL
A	54.4	+8.8 (26%)	+6.0 (17%)	+3.7 (11%)
B	51.6	+8.9 (28%)	+6.9 (22%)	+2.1 (6.6%)
C	55.4	+8.4 (24%)	+5.5 (16%)	0
D	57.1	+7.4 (20%)	+4.7 (13%)	-0.7 (1.9%)
E	57.8	+5.5 (15%)	+4.0 (11%)	-2.1 (5.6%)
F	55.2	+7.9 (22%)	+5.4 (15%)	+2.8 (8.0%)
G	60.0	+8.8 (22%)	+7.7 (19%)	+2.2 (5.5%)
H	64.2	+7.3 (17%)	+5.7 (13%)	-0.2 (0.5%)
I	64.6	+8.8 (20%)	+7.2 (16%)	+0.8 (1.8%)
J	65.8	+4.5 (10%)	+2.9 (6.3%)	-3.3 (7.2%)
K	54.3	+8.6 (25%)	+6.3 (18%)	+3.5 (10%)
L	51.9	+8.0 (25%)	+7.2 (23%)	+1.4 (4.4%)
M	---	---	---	---
N	55.2	+7.7 (22%)	+6.7 (19%)	+1.4 (4.0%)
O	57.1	+5.5 (15%)	+4.6 (12%)	-1.4 (3.8%)

**Note:** (A,F,K) and (E,J,O) are leading and trailing edge components respectively. Measurement uncertainty,  $\pm 0.4^\circ\text{C}$ . Percentage prediction error in parenthesis ( ) is calculated based on the measured component junction temperature rise above ambient air temperature. Component power dissipation = 3W. Ambient air temperature =  $20^\circ\text{C}$ .

To investigate these discrepancies, measured and predicted component-PCB surface temperature profiles are compared on the board component- and non-component sides in Figures 7.3(a) and 7.3(b) respectively. Considering first the board non-component side, measurements and predictions of the surface temperature distribution agree well, both qualitatively and quantitatively for the laminar and k-ε models, with the exception of localised discrepancies. This agreement indicates that the numerical models accurately predict heat loss from the board non-component side, which is predicted to account for 39% of total power dissipation for all three flow models. Considering the importance of this heat transfer path, this agreement indicates that component-board thermal interaction is accurately captured. As the k-ε model predicts slightly lower surface temperature than the laminar model, but same convective heat loss from this surface, it is likely to predict higher wall shear stress, hence heat transfer coefficients.

On the board component side, Figure 7.3(a), the shape of the predicted surface temperature distributions over the component bodies agree well with measurement, with the magnitude of discrepancies reflecting those of corresponding junction temperature prediction errors in Table 7.6.

Based on these analyses, it is suspected that overprediction of component junction temperature for individually powered components, using the laminar and k-ε models, is related to an underprediction of the heat transfer coefficient. Unlike the k-ε turbulent flow model, the laminar model does not rely on the use of wall functions to calculate this

variable. Since both models yield similar temperature predictive discrepancies, inaccurate prediction of the heat transfer coefficient must essentially be related to inaccurate flow field modelling. For the simultaneously powered cases, inaccurate flow field prediction also impacts on the prediction of fluid mixing, hence advected air temperature adjacent to the board. Both factors combine to amplify junction temperature prediction errors. This explains the decay in accuracy from individually to simultaneously powered configurations in Stage 3.

Insulated Stage 3 PCB. When account is taken of measurement uncertainty, prediction accuracy in Tables 7.7 and 7.8 ranges from +3°C to +22°C (up to 35%) depending on component location, airflow velocity and flow model. Neither flow model yields best accuracy for all components. For example, the laminar model more accurately predicts the junction temperatures of the first two leading edge row component rows, whereas the k- $\epsilon$  predictions are more accurate for the downstream components, I and J.

As evident from Figures 7.2(a) and 7.2(c), overprediction of the downstream component powered-off temperature rise is much more pronounced than on the non-insulated PCB, which results from the adiabatic boundary condition imposed on the board non-component side. These errors are more pronounced for the laminar flow model for devices H to J, and result in junction temperature errors increasing with distance from the PCB leading edge. These trends are reflected in the corresponding surface temperature profile predictions in Figures 7.3(c) and 7.3(d). Although unlikely, to assess potential uncertainties in the insulation thermal conductivity, hence its effectiveness as an adiabatic boundary condition, the nominal value for this parameter was doubled. Junction temperature predictions decreased by a worst-case 1.3°C for the 2 m/s case, indicating that the adiabatic boundary condition was correctly represented in the model. Potential uncertainties in other modelling parameters were found to have minimal impact on the predictions (Section 5.2.1).

The results for the non-insulated and insulated Stage 3 PCBs combined clearly show a weakness of the code to predict downstream component thermal interaction. This is in line with Anderson's results [163] for an air-cooled array of heated blocks. Using the same turbulence modelling and CFD code, the predicted superposition kernel functions<sup>3</sup> were significantly overestimated. This was attributed to underprediction of fluid flow mixing, as good agreement between predicted and measured adiabatic heat transfer coefficient was found. Inaccurate prediction of the component powered-off temperature rise is a

---

<sup>3</sup> Ratio of the passive module adiabatic temperature rise above channel inlet fluid temperature, to the bulk mean temperature rise of the fluid. Indicates the level of thermal mixing.

significant limitation as many PCB applications are densely packed multi-component boards, with more than one component having significant power dissipation.

**Table 7.7** Comparison of measured and predicted component junction temperatures for simultaneously powered components on the insulated Stage 3 PCB in a 2 m/s airflow.

Component location	Measured (°C)	Prediction discrepancy (°C)		
		Laminar	k-ε	LVEL
A	79.4	+7.4 (13%)	+7.8 (13%)	+3.9 (6.6%)
B	74.4	+9.9 (18%)	+14.4 (27%)	+10.5 (19%)
C	81.4	+12.4 (20%)	+9.3 (15%)	+7.2 (12%)
D	85.8	+13.6 (21%)	+5.7 (8.7%)	+2.5 (3.8%)
E	84.4	+13.5 (21%)	+2.5 (3.9%)	-2.2 (3.4%)
F	81.2	+6.5 (11%)	+11.0 (18%)	+5.5 (9.0%)
G	84.0	+12.2 (19%)	+22.4 (35%)	+14.3 (22%)
H	92.1	+13.2 (18%)	+15.6 (22%)	+10.2 (14%)
I	95.7	+15.5 (21%)	+12.4 (16%)	+7.3 (9.6%)
J	94.9	+12.8 (17%)	+5.5 (7.3%)	-0.3 (0.4%)
K	77.0	+8.4 (15%)	+14.6 (26%)	+8.7 (15.3%)
L	72.7	+10.3 (20%)	+18.2 (35%)	+12.1 (23%)
M	---	---	---	---
N	82.2	+13.6 (22%)	+12.4 (20%)	+9.3 (15%)
O	82.5	+13.5 (22%)	+7.9 (13%)	+4.5 (7.2%)

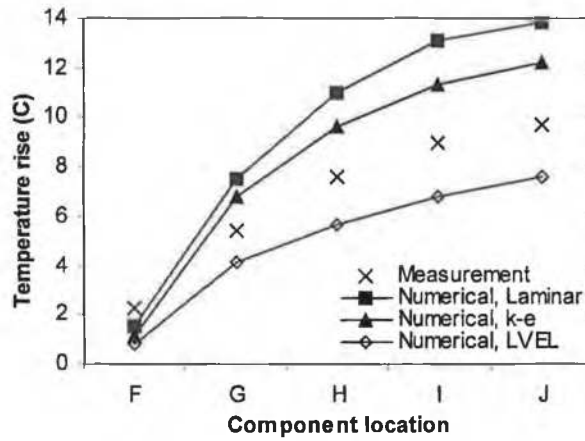
**Note:** (A,F,K) and (E,J,O) are leading and trailing edge components respectively. Measurement uncertainty,  $\pm 0.6^\circ\text{C}$ . Percentage prediction error in parenthesis ( ) is calculated based on the measured component junction temperature rise above ambient air temperature. Component power dissipation = 3W. Ambient air temperature =  $20^\circ\text{C}$ .

**Table 7.8** Comparison of measured and predicted component junction temperatures for simultaneously powered components on the insulated Stage 3 PCB in a 4 m/s airflow.

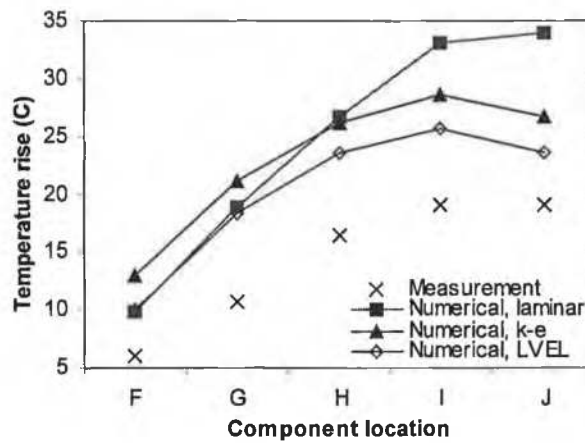
Component location	Measured (°C)	Prediction discrepancy (°C)		
		Laminar	k-ε	LVEL
A	63.7	+6.2 (14%)	+8.9 (21%)	+7.3 (17%)
B	60.0	+7.7 (19%)	+10.0 (25%)	+9.8 (25%)
C	64.1	+10.5 (24%)	+7.4 (17%)	+5.7 (13%)
D	65.8	+12.9 (28%)	+6.1 (13%)	+3.2 (7.0%)
E	63.9	+12.9 (29%)	+4.4 (10%)	+0.4 (0.9%)
F	64.2	+7.6 (17%)	+11.2 (25%)	+7.6 (17%)
G	68.0	+10.9 (23%)	+16.7 (35%)	+12.6 (26%)
H	73.6	+12.2 (23%)	+12.1 (23%)	+7.7 (14%)
I	75.8	+14.5 (26%)	+10.1 (18%)	+5.5 (9.9%)
J	74.1	+13.3 (25%)	+5.5 (10%)	+0.4 (0.7%)
K	63.0	+8.8 (21%)	+12.4 (29%)	+9.1 (21%)
L	59.6	+8.0 (20%)	+12.5 (32%)	+8.4 (21%)
M	---	---	---	---
N	65.3	+12.3 (27%)	+9.1 (20%)	+6.8 (15%)
O	66.0	+12.1 (26%)	+5.4 (12%)	+2.8 (6.1%)

**Note:** (A,F,K) and (E,J,O) are leading and trailing edge components respectively. Measurement uncertainty,  $\pm 0.4^\circ\text{C}$ . Percentage prediction error in parenthesis ( ) is calculated based on the measured component junction temperature rise above ambient air temperature. Component power dissipation = 3W. Ambient air temperature =  $20^\circ\text{C}$ .

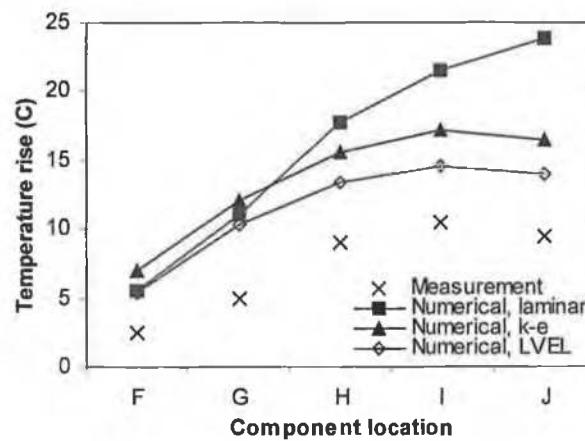




(a) Non-insulated Stage 3 PCB in a 4 m/s airflow



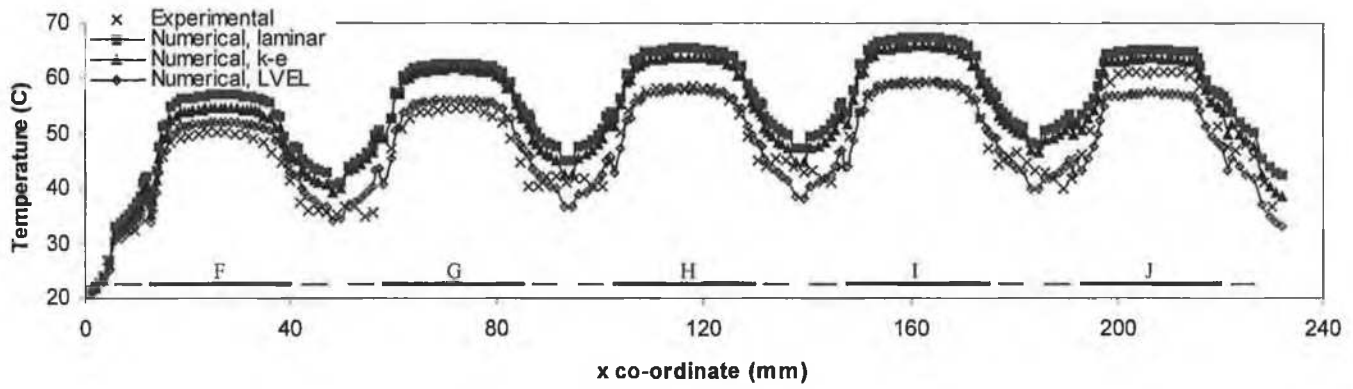
(b) Insulated Stage 3 PCB in a 2 m/s airflow



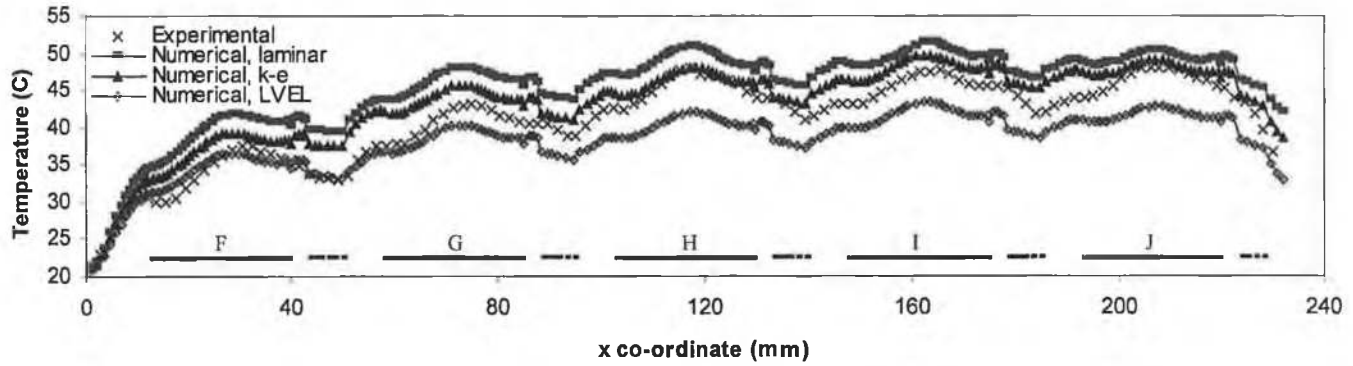
(c) Insulated Stage 3 PCB in a 4 m/s airflow

**Note:** Measurement uncertainty in powered-off component temperature rise,  $\pm 0.8^\circ\text{C}$  and  $\pm 0.6^\circ\text{C}$  in 2 and 4 m/s airflows respectively.

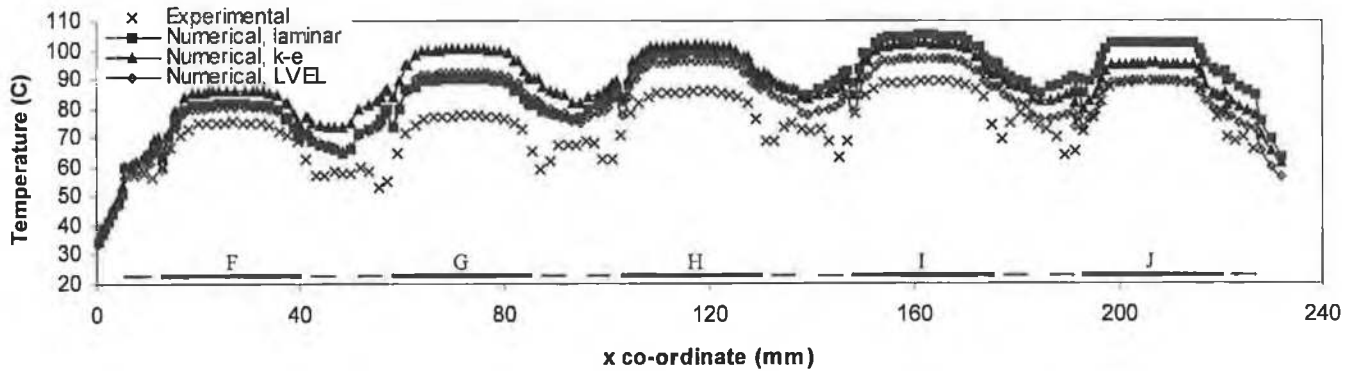
**Figure 7.2** Comparison of measured and predicted component junction temperature rise between the individually- and simultaneously powered configurations for the central stream-wise row components (F - J) on the Stage 3 PCB in forced convection.



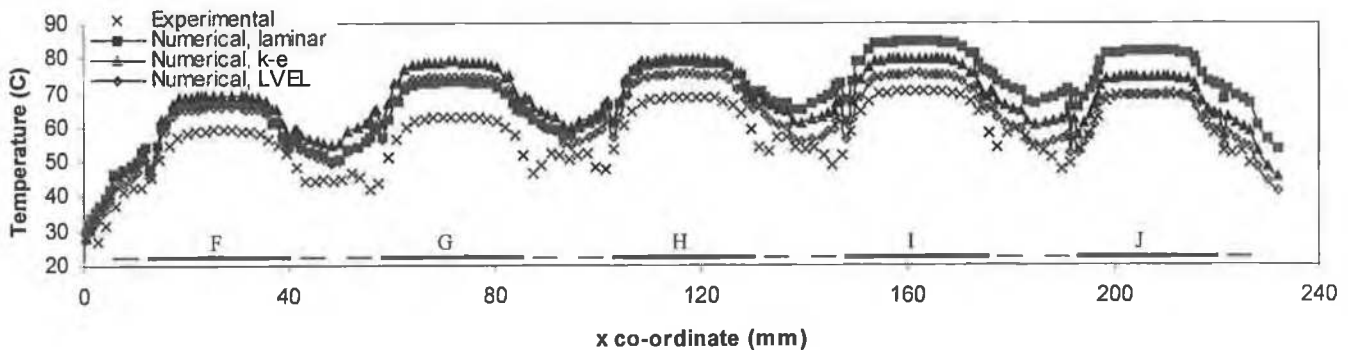
(a) Non-insulated Stage 3 PCB at 4 m/s, component side



(b) Non-insulated Stage 3 PCB at 4 m/s, non-component side



(c) Insulated Stage 3 PCB at 2 m/s, component side



(d) Insulated Stage 3 PCB at 4 m/s, component side

Note: Analysis Plane X-X, Figure 3.19. (—) denotes component body location, (---) denotes copper tracking location on the board component side, and (----) denotes copper tracking location on the board non-component side. Uncertainty in temperature measurement,  $\pm 1.4^\circ\text{C}$ .

**Figure 7.3** Comparison of measured and predicted component-PCB surface temperature profiles in the stream-wise airflow direction on the Stage 3 PCB in forced convection.

Although the  $k$ - $\epsilon$  predictions form the *a priori* results for turbulent flow analysis, a practical observation can be made regarding the LVEL model performance. For the simultaneously powered Stage 3 configurations, the LVEL model predictions are consistently lower than  $k$ - $\epsilon$ 's by on average 5°C (10%). Rodgers et al. [35] reported a similar trend for another PCB topology. The discrepancy between the flow models is due to LVEL predicting higher values of fluid turbulent viscosity in the near-wall region, thereby artificially increasing both convective heat transfer and fluid flow mixing. Despite yielding slightly larger prediction errors than for the  $k$ - $\epsilon$  flow model, LVEL was shown to maintain its predictive accuracy using lower grid densities, unsuitable for the  $k$ - $\epsilon$  model. This result suggests the greater applicability of the LVEL model for system level turbulent flow analysis, where grid density is constrained by computational limits.

#### **7.2.4 Summary of Results**

A systematic assessment of predictive accuracy was presented for PCB-mounted component heat transfer, using a CFD code dedicated to the thermal analysis of electronic systems.

Component operating temperature prediction accuracy ranged from +3°C to +22°C (up to 35%) of measurement, depending on component location on the board, airflow velocity and flow model applied. Such an accuracy would only be sufficient for the early design phase, and represents a significant decay relative to corresponding predictions for free convection, Chapter 6.

The inability of either the laminar or turbulent  $k$ - $\epsilon$  flow models to resolve the complete forced airflows over the board suggests the need for a flow model capable of modelling transition.

Flow visualisation was shown to be an efficient means of identifying aerodynamically sensitive regions on populated boards, where temperature prediction accuracy must be viewed with caution.

### **7.3 Alternative Flow Modelling Strategies**

To investigate if the prediction of both aerodynamic and thermal factors that influence component operational temperature could be improved, a range of candidate, turbulent flow modelling approaches are evaluated using Fluent, which were developed for the prediction of low-Reynolds number, wall-bounded flows. These models are the one-equation Spalart-Allmaras (SA) model, a two-layer zonal model and Shear Stress Transport (SST)  $k$ - $\omega$  model. Their characteristics were outlined in Section 4.3.2.

Improvements in predictive accuracy are assessed for the non-insulated Stage 3 PCB, characterised in a 4 m/s airflow, and the motivation for selecting this test configuration was given in Section 4.4. Repeating the benchmark methodology applied in Section 7.2, the single board-mounted component (Stage 1) configuration is firstly considered, so as to provide a base-line accuracy for each flow model. Any decay in predictive accuracy for the populated board would be attributable to a weakness of the turbulence flow model employed to predict the more complex flows and their impact on component-PCB heat transfer. Predictive accuracy is again assessed in two steps, from individually powered components, to a simultaneously powered configuration, so as to isolate the impact of aerodynamic conditions and component thermal interaction on predictive accuracy respectively.

Candidate turbulence model performance is evaluated against that of the standard high-Reynolds  $k-\epsilon$  model, Tables 7.3 and 7.6, which is considered as the base line accuracy.

### 7.3.1 Stage 1 PCB

In Table 7.9, component junction temperature predictive accuracy is overall within  $\pm 3^\circ\text{C}$  of measurement when account is made of experimental error, with the two-layer zonal model predictions slightly outside this band. The Flotherm and Fluent laminar flow model predictions are within  $1.4^\circ\text{C}$  of each other, which is in line with previous studies that compared the software predictions for single component board heat transfer [148,255]. As outlined in Section 4.3, meaningful comparison of the high-Reynolds number  $k-\epsilon$  flow model [234,235] predictions between the codes could not be made due to differences in wall functions formulations. The impact of wall function formulation on predictive accuracy will be illustrated in Section 7.3.3. However, the similarity in laminar predictions between codes indicates that differences in numerics do not significantly impact on predictive accuracy.

**Table 7.9** Comparison of measured and predicted component junction temperatures for the Stage 1 PCB in a 4 m/s airflow.

Measured ( $^\circ\text{C}$ )	Prediction discrepancy ( $^\circ\text{C}$ )					
	Flotherm		Fluent			
	Laminar	$k-\epsilon$	Laminar	Spalart- Allmaras	2-layer zonal	SST $k-\omega$
58.6	+1.0 (2.6%)	+0.8 (2.1%)	+2.4 (6.2%)	-1.0 (2.6%)	-3.6 (9.3%)	-2.3 (6.0%)

Note: Measurement uncertainty,  $\pm 0.4^\circ\text{C}$ . Percentage prediction error in parenthesis ( ) is calculated based on the measured component junction temperature rise above ambient air temperature. Component power dissipation = 3 W. Ambient air temperature =  $20^\circ\text{C}$ .

### 7.3.2 Non-insulated Stage 3, Individually Powered Components

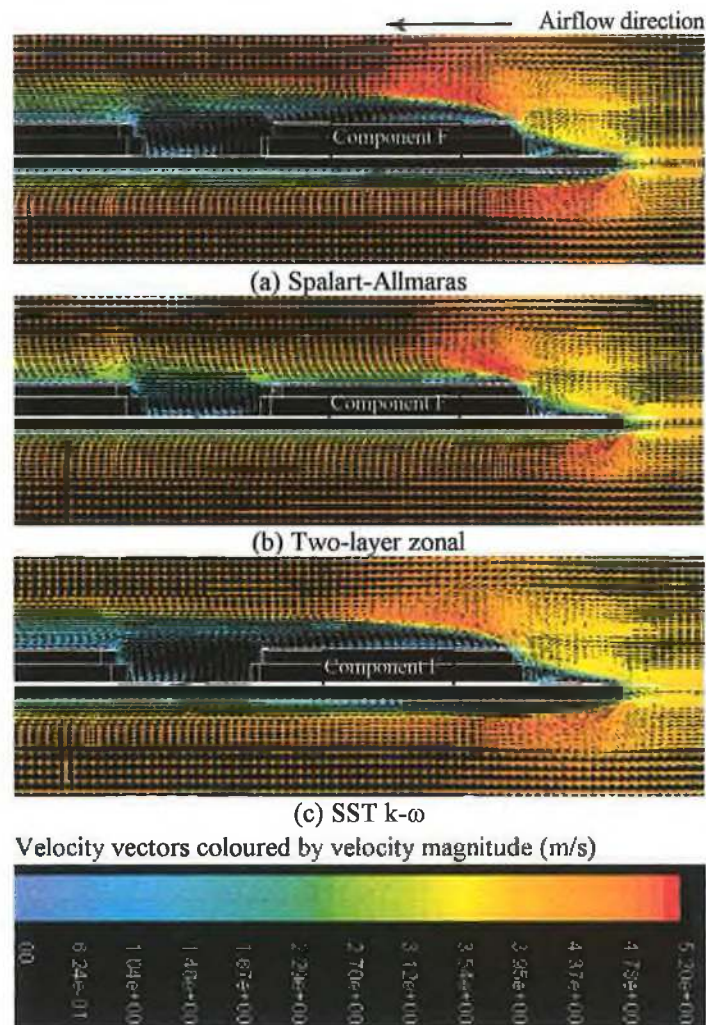
Overall in Table 7.10, the three candidate turbulence models evaluated display improved predictive accuracy relative to the standard  $k-\epsilon$  model. This is most evident for the leading edge components F and G, indicating improved prediction of leading edge flow.

Considering the predictive discrepancy of the two-layer zonal model for the single component-board case, its performance in this instance can be considered fortuitous. This model predicted higher local turbulent viscosity values than with the other turbulence models. This possibly resulted in artificially increasing wall shear stress and hence the convective heat transfer coefficient. Plots of the predicted flow field vectors around the leading edge component F, taken along the board central stream-wise axis are compared in Figure 7.4. Possibly reflecting high values of predicted turbulent viscosity, the two-layer zonal model is seen to predict extremely weak flow separation over the leading edge component. This is in contrast with the extent of flow separation identified by experimental flow visualisation. The SST  $k-\omega$  and Spalart-Allmaras model predictions in Figure 7.4 are more realistic. The thinner hydrodynamic boundary layer predicted by the two-layer zonal model results in higher heat transfer coefficients over the component-board surfaces, to which the lower junction temperature predictions in Table 7.10 are attributable. Based on the above, the SST  $k-\omega$  model is considered to perform best for this test configuration. Predictions for the two-layer zonal model were found to be insensitive to the turbulence model used in the far-field, namely standard  $k-\epsilon$  or RNG  $k-\epsilon$ , suggesting that near-wall treatment may be the determining factor on predictive accuracy in this instance.

**Table 7.10** Comparison of measured and predicted component junction temperatures for individually powered components on the Stage 3 PCB in a 4 m/s airflow.

Component location	Measured (°C)	Prediction discrepancy (°C)			
		* $k-\epsilon$	Spalart-Allmaras	2-layer zonal	SST $k-\omega$
F	52.9	+7.6 (23%)	+4.3 (13%)	+1.0 (3.0%)	+2.8 (8.5%)
G	54.6	+6.5 (19%)	+3.7 (11%)	+0.7 (2.0%)	+2.3 (6.6%)
H	56.6	+3.8 (10%)	+2.2 (6.0%)	-0.5 (1.4%)	+0.8 (2.2%)
I	55.6	+4.9 (14%)	+3.4 (9.6%)	+0.7 (2.0%)	+2.1 (5.9%)
J	56.1	+0.5 (1.4%)	+2.6 (7.2%)	0	+1.6 (4.4%)

**Note:** All predictions generated with the computational model confined to the central stream-wise component row. (\*) Predictions generated with Flotherm. F and J are leading and trailing edge components respectively. Measurement uncertainty,  $\pm 0.4^\circ\text{C}$ . Percentage prediction error in parenthesis ( ) is calculated based on the measured component junction temperature rise above ambient air temperature. Component power dissipation = 3W. Ambient air temperature =  $20^\circ\text{C}$ .



**Figure 7.4** Predicted flow field vectors at the leading edge of the Stage 3 PCB, taken along the board central stream-wise axis (Plane X-X, Figure 3.19).

### 7.3.3 Non-insulated Stage 3, Simultaneously Powered Components

In Table 7.11, when account is taken of measurement uncertainty, prediction accuracy improves from a worst-case +7.9°C (20%) for the k- $\epsilon$  model, to +1.7°C (4.8%) for the SST k- $\omega$  model. This improvement is attributed to better prediction of both leading edge heat transfer, as previously highlighted, and downstream temperature rise due to component thermal interaction.

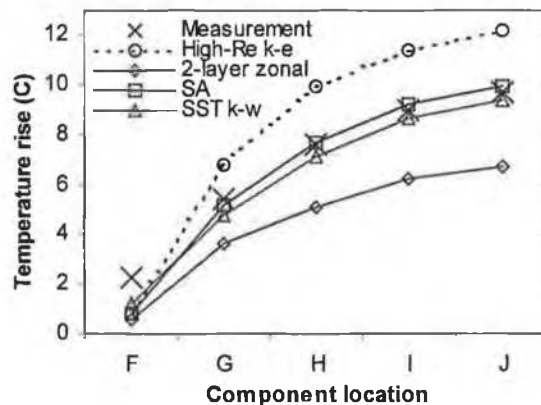
Measurements and predictions of downstream component temperature rise between the individually- and simultaneously powered configurations are compared in Figure 7.5. This temperature rise is solely due to component thermal interaction. Whereas the k- $\epsilon$  model overpredicts downstream component temperature rise by on order 25%, the SST k- $\omega$  and Spalart-Allmaras model predictions are both within 4% of measurement. However, the

two-layer zonal model underpredicts component thermal interaction by up to 30%, which results in junction temperature discrepancies increasing with distance from the PCB leading edge, Table 7.11. Therefore, predictive accuracy for this model in Table 7.11 are net values, and a function of component power dissipation.

**Table 7.11** Comparison of measured and predicted component junction temperatures for simultaneously powered components on the Stage 3 PCB in a 4 m/s airflow.

Component location	Measured (°C)	Prediction discrepancy (°C)			
		*k-ε	Spalart-Allmaras	2-layer zonal	SST k-ω
F	55.2	+6.1 (17%)	+2.8 (8.0%)	-0.7 (2.0%)	+1.7 (4.8%)
G	60.0	+7.9 (20%)	+3.5 (8.8%)	-1.1 (2.8%)	+1.7 (4.3%)
H	64.2	+6.1 (14%)	+2.3 (5.2%)	-3.0 (6.8%)	+0.3 (0.7%)
I	64.6	+7.3 (16%)	+3.6 (8.1%)	-2.1 (4.7%)	+1.7 (3.8%)
J	65.8	+3.0 (6.6%)	+2.8 (6.1%)	-3.0 (6.6%)	+1.3 (2.8%)

**Note:** All predictions generated with the computational model confined to the central stream-wise component row. (\*) Predictions generated with Flotherm. F and J are leading and trailing edge components respectively. Measurement uncertainty, ±0.4°C. Percentage prediction error in parenthesis ( ) is calculated based on the measured component junction temperature rise above ambient air temperature. Component power dissipation = 3W. Ambient air temperature = 20°C.



**Note:** Measurement uncertainty in powered-off component temperature rise, ±0.6°C. k-ε flow model predictions generated with Flotherm.

**Figure 7.5** Comparison of measured and predicted component junction temperature rises between the individually- and simultaneously powered configurations for the central stream-wise row components (F - J) on the Stage 3 PCB.

Although no flow field measurements are presented to assess flow field predictive accuracy, energy balance analyses of component heat transfer were undertaken to assess the sensitivity of the component heat transfer paths to the modelling of the convective domain. The predicted energy balances for the simultaneously powered Stage 3 PCB are presented for all turbulent flow models considered in Table 7.12. The net heat flux through each heat transfer path is presented as a percentage of the total dissipated power. Despite differences

in component junction temperature predictions between turbulence models in Table 7.11, the predicted component heat transfer paths for all flow models are found to be very similar in Table 7.12. This indicates that the component internal conductive domain is relatively flow model independent, with component junction temperature prediction accuracy being therefore related to the flow field prediction. Therefore, improvements in component junction temperature accuracy relative to the standard high-Reynolds number  $k-\epsilon$  model, obtained using the SST  $k-\omega$  flow model, are related to the representation of the convective domain. Thus in this instance, energy balance analyses of component heat transfer help link junction temperature prediction errors to flow field prediction errors.

The predicted energy balances also highlight that the component heat transfer paths are weakly sensitive to component location on the board and convective environment. Thus, when comparing the  $k-\omega$  predictions for a 4 m/s airflow, with corresponding predictions for free convection, Table 6.4, component heat loss to the board only diminishes by on average 7%, to 62%. This again highlights the predominance of board construction as a design parameter for lowering component operating temperature.

**Table 7.12** Numerical component energy balances on the simultaneously powered non-insulated Stage 3 PCB in a 4 m/s airflow.

Component location	Heat path (%)															
	* $k-\epsilon$				Spalart-Allmaras				2-layer zonal				SST $k-\omega$			
	Top	Base	Leads	Sides	Top	Base	Leads	Sides	Top	Base	Leads	Sides	Top	Base	Leads	Sides
F	32	14	50	4	33	14	49	4	34	14	48	4	33	14	49	4
G	33	15	48	4	34	14	48	4	36	14	46	4	35	14	47	4
H	34	14	48	4	34	14	48	4	36	14	46	4	35	14	47	4
I	34	15	47	4	34	14	48	4	36	14	46	4	35	14	47	4
J	33	14	49	4	33	14	49	4	34	14	48	4	33	14	49	4

Note: Laminar and  $k-\epsilon$  flow model energy balance analyses within 1%. Component power dissipation = 3W.

This study highlights the value of using turbulence models more suited to low-Reynolds number flows than a standard  $k-\epsilon$  model, for the analysis of multi-component board heat transfer. Whereas component operating temperature prediction accuracy would only be sufficient for the early design phase using the standard  $k-\epsilon$  model, it would qualify for the intermediate to final design phase using the SST  $k-\omega$  model in this study. The Spalart-Allmaras model performance was comparable despite its simpler calculation strategy. This suggests its potential applicability to engineering calculations in terms of lower computational expense.

It should be noted that using the standard  $k-\epsilon$  flow model in Fluent, which can only be applied with a wall function formulation constrained to  $y^+$  values greater than 30, predicted junction temperatures were on average 10°C (20 to 25%) underestimated relative to



corresponding  $k-\omega$  predictions for the simultaneously powered components, using the same computational mesh. This highlights the impact of near wall meshing for wall functions that are  $y^+$  constrained.

While the present improvements in predictive accuracy may seem modest, it is anticipated that greater improvements could be obtained for more complex flow conditions, to which the limitations of a standard high-Reynolds number  $k-\epsilon$  model with wall functions would be more exposed. Such flow conditions are proposed in future work programmes outlined in Section 8.2.

#### **7.4 Summary**

A systematic assessment of CFD predictive accuracy was presented for PCB-mounted component heat transfer.

Using a CFD code dedicated to the thermal analysis of electronic systems, component operating temperature prediction accuracy ranged from  $+3^\circ\text{C}$  to  $+22^\circ\text{C}$  (up to 35%) of measurement, depending on component location on the board, airflow velocity and flow model applied. Such an accuracy would only be sufficient for the early design phase, and represents a significant decay relative to corresponding predictions for free convection, Chapter 6.

Using turbulence models more suited to the modelling of low-Reynolds number flows, prediction accuracy for component operating temperature improved by up to 15% relative to a standard high-Reynolds number  $k-\epsilon$  flow model. Such improvements are attributed to better prediction of both leading edge heat transfer and component thermal interaction.

Using an SST  $k-\omega$  model, component junction temperature predictions were within  $+2^\circ\text{C}$  (5%) of measurement. Such an accuracy would enable parametric analysis of product thermal performance to be undertaken with greater confidence. Such improvements could also contribute to the generation of more accurate temperature boundary conditions for use in Physics-of-Failure based reliability prediction methods.

It is anticipated that the value of applying such flow models would be more evident for the analysis of more complex flow conditions than considered in this study, where the limitations of a standard high-Reynolds number  $k-\epsilon$  model would be more exposed.

Based on the results presented, the case is made for vendors of CFD codes dedicated to the thermal analysis of electronic equipment to consider the adoption of turbulence models more suited to detailed board level analysis.

Until such flow modelling is incorporated into dedicated CFD codes, the use of flow visualisation on mock-up prototypes in the early design phase can help identify aerodynamically sensitive regions on the board, where temperature predictions should be considered with caution.

## **8.0 Conclusions and Recommendations**

An assessment of Computational Fluid Dynamics (CFD) predictive accuracy for board-mounted electronic component heat transfer was presented in this Thesis. Both standard flow modelling approaches, typically employed for the thermal analysis of electronic systems, and alternative flow modelling strategies were evaluated. Apart from the prediction of component operational temperature in application environments, the applicability of CFD analysis to the design of electronic component reliability screens and convective solder reflow temperature profiles was also investigated. The prominent findings of the research are summarised in this chapter, which closes with recommendations and proposals for future work programmes.

### **8.1 Conclusions**

#### **8.1.1 Experimental Benchmarks**

- A set of experimental benchmarks was presented for both steady-state and transient component heat transfer. High measurement accuracy and reproducibility, combined with minimal thermal resistance variation between samples, established confidence in the experimental data. Further confidence was gained from component structural analysis, which served to eliminate potential numerical modelling uncertainties.
- The use of measured component junction and surface temperature, with supporting experimental flow visualisation, was shown to be effective in isolating sources of numerical prediction error.
- Incrementing test case complexity in controlled steps, from single board-mounted components, to simultaneously powered multi-component configurations, was shown to be efficient in enabling both the numerical modelling methodologies and solver capability to be carefully evaluated. Using this approach the impacts of both aerodynamic and thermal factors on predictive accuracy were quantified.

#### **8.1.2 Component Steady-State Heat Transfer**

Focusing on the Stage 3 PCB configurations, which represent realistic electronic component-board applications, the following conclusions were drawn on CFD predictive accuracy for component operational temperature. Results for the other test configurations will only be used to explain the findings.

### *Standard flow modelling*

- In laminar free convection, component junction temperature predictions were found to be overall within  $\pm 5^{\circ}\text{C}$  or 7% of measurement, independently of component location on the board. In forced airflows, component operating temperature prediction accuracy decayed up to  $+22^{\circ}\text{C}$  (35%) of measurement, depending on component board location, airflow velocity and flow model applied. This decay reflects a weakness of the flow models to deal with the more complex forced airflows over the boards. By contrast, component junction temperature predictions for single board-mounted components were typically within  $\pm 3^{\circ}\text{C}$  or 5% of measurement, demonstrating the suitability of the component and PCB numerical modelling methodologies.
- While for free convection, predictive accuracy for component operational temperature in multi-component board applications would qualify for the intermediate phase of a thermal design process, it would only be sufficient for the early design phase in forced airflows. As prediction accuracy could decay in real electronic systems, where both more complex flow conditions and modelling uncertainties would exist, component junction temperature would ultimately need to be experimentally measured when used for strategic product design decisions, and performance and reliability predictions. This dependency on experimental prototyping diminishes the potential of CFD analysis, as a design method, to reduce electronic product development cycle times.
- The level of predictive accuracy obtained in this study suggests that CFD can only be used with confidence to refine a product thermal design by parametric analysis, on the premise that qualitative predictions can be relied upon. Such an assumption should be considered on a case-by-case basis.
- The inability of either the laminar or high-Reynolds number turbulent k- $\epsilon$  flow model to resolve the complete forced airflows over the populated boards, with greatest prediction error and discrepancy between flow models occurring in aerodynamically sensitive regions, suggests the need for a flow model capable of modelling transition. By contrast, predictions were weakly sensitive to flow model on single component board topologies, reflecting a lower degree of aerodynamic disturbance.
- Downstream component thermal interaction was found to be inaccurately captured using either the laminar or turbulent k- $\epsilon$  flow model. This is a critical limitation considering the combined trends of rising Integrated Circuit (IC) power dissipation and component packing density in electronic systems, which act to amplify component thermal interaction.

- Prediction error for the k- $\epsilon$  model in regions of strong flow re-attachment are primarily attributed to the limited applicability of the wall functions when the local flow conditions deviate significantly from boundary layer flow. This limitation would be critical for the prediction of component operational temperature on PCBs exposed to upstream fan flows, over which multiple attaching, separating and recirculating flow features would exist. Overall, using the k- $\epsilon$  model, prediction accuracy for component-PCB surface convective heat transfer will depend both on how far the flow conditions deviate from boundary layer flow, and on the sensitivity of heat transfer to these conditions. In addition, wall function formulations constrained to having near-wall cell  $y^+$  values greater than 30 are not suitable for detailed analysis of component-PCB heat transfer.
- The k- $\epsilon$  model was shown to be unsuitable for the analysis of unsteady flows as it does not capture flow unsteadiness. This limitation could be critical depending on the sensitivity of component operating temperature to such flow conditions.
- The LVEL model predictions were consistently lower than k- $\epsilon$ 's by on average 5°C (10%). However, this model was shown to maintain its predictive accuracy using lower grid densities, unsuitable for the k- $\epsilon$  model. This suggests LVEL's greater applicability for system level turbulent flow analysis, where grid density is constrained by computational limits.
- In almost all instances, using either the laminar or k- $\epsilon$  flow model, component operating temperature was overpredicted, leading to a conservative thermal design. However, qualitative trends may not be correctly predicted, in terms of identifying the hottest operating components on the board.
- The application of experimental flow visualisation was demonstrated to help identify the complex flow phenomena that develop over forced air-cooled PCBs. Flow visualisation enabled the location of aerodynamically sensitive regions on the boards to be both identified and associated with significant prediction error in component operating temperature.

#### *Alternative flow modelling approaches*

- Using turbulence models more suited to the analysis of low-Reynolds number flows, prediction accuracy for component operating temperature improved by up to 15% relative to a standard high-Reynolds number k- $\epsilon$  flow model. Such improvements are associated with improved prediction of both board leading edge heat transfer and component thermal interaction.

- Numerical energy balance analyses of component heat transfer showed that the component internal conductive domain was weakly sensitive to flow model. Hence improvements in junction temperature accuracy were related to the representation of the convective domain, that is the flow field prediction.
- Using the SST  $k-\omega$  model, component junction temperature predictions were within  $+2^{\circ}\text{C}$  (5%) of measurement. Such an accuracy would enable parametric analysis of product thermal performance to be undertaken with greater confidence. Such improvements could also contribute to the generation of more accurate temperature boundary conditions for use in Physics-of-Failure based reliability prediction methods.
- Despite its simpler calculation strategy, the Spalart-Allmaras model performance was found to be comparable to that of the SST  $k-\omega$  model in this study.

### **8.1.3 Component Transient Heat Transfer**

- Conjugate transient heat transfer from a single board-mounted electronic component was found to be accurately predicted. This suggests that CFD analysis could play an important role in providing critical thermal boundary conditions for component electrical performance and thermo-mechanical behaviour analyses, which at present are obtained using non-conjugate methods.
- CFD analysis could also aid in the design of component reliability screens and convective solder reflow temperature profiles. Component thermal behaviour in such environments can be difficult, if not impossible to experimentally characterise accurately.

### **8.1.4 Numerical Modelling**

- The robustness of the component and board modelling methodologies employed, which are based on nominal component dimensions and material thermo-physical properties, was demonstrated for both steady-state and transient heat transfer. The level of predictive accuracy obtained for single component applications ( $\pm 3^{\circ}\text{C}$  or 5%) was maintained for individually powered components on the non-insulated Stage 3 PCB in free convection, demonstrating that the modelling methodologies transferred to multi-component board applications.
- The predictive performance of resistor network-based component compact thermal models (CTMs) implemented in a CFD environment was found to decay by 7% to 20% relative to the corresponding detailed component models. Errors in the prediction of component-board thermal interaction were highlighted and the coupling of the CTM to

the board was shown to impact on predictive accuracy. The results suggest that improved accuracy could be obtained by modelling component heat transfer using four CTMs, each representative of a quarter geometry detailed model. However, the level of predictive accuracy achievable with detailed modelling should bring balanced expectations from component compact thermal modelling.

- The value of CFD analysis in providing insights into complex multi-mode, three-dimensional heat transfer in electronics systems was highlighted. For example, energy balance analyses of component heat transfer showed that heat transfer to the PCB was the dominant component heat transfer path at on order 70%, mainly by lead conduction. This results in component junction temperature being highly sensitive to board construction. CFD codes can therefore be used as diagnostic tools to evaluate thermal design options for lowering component operating temperature.
- The computational expenses associated with the use of unstructured meshing considerably constrains the analysis of component/PCB heat transfer. The use of a structured Cartesian mesh allowed the grid volume to be increased by a factor of three, in this instance up to 6 million cells. Nevertheless, grid refinement analyses suggested that even finer grids may be required to more accurately resolve the flow fields over the boards, which would be incompatible with typical computational resources. This highlights considerable difficulties to undertake meaningful system level analysis in a design environment.
- Significant man-power and solution time resources are required for the thermal analysis of electronics, to build the CFD models, define the grid and obtain both well-converged and grid-independent solutions. This is at odds with the current requirement for efficient analysis.

## **8.2 Recommendations**

- The benchmarks presented in this Thesis could be used in subsequent studies to assess the performance of other turbulence models or computational techniques for the prediction of electronic component heat transfer. The benchmarks could also serve to evaluate other component and board numerical modelling methodologies.
- Based on the findings of this research, a more robust thermal design methodology should also aim at improved predictive accuracy. While design productivity enhancements, through improved CFD code pre- and postprocessing, respond to the electronics industry's current demand, the success of virtual prototyping methods in the long-term, will depend upon their accuracy. Such a change in philosophy would be

required to enable critical product design decisions or reliability predictions to be made with confidence. The electronics industry should therefore allow vendors of CFD codes dedicated to the thermal analysis of electronic equipment to re-deploy some of their resources, often focused on developing pre- and post processing capabilities, to improve predictive accuracy through improved numerics and fluid flow modelling.

- The adoption of eddy-viscosity turbulence models more suited to the analysis of low-Reynolds number, wall-bounded flows in dedicated CFD codes should be considered so as to enable more accurate prediction of electronic component operational temperature relative to a standard high-Reynolds number  $k-\epsilon$  flow model. Based on the results presented in this study, the SST  $k-\omega$  and Spalart-Allmaras models represent potentially good candidate models. The implementation of such models in CFD codes having a structured Cartesian grid system would reduce computational expenses relative to those incurred in this study with an unstructured grid system.
- Until improved flow modelling is incorporated into dedicated CFD codes, the use of flow visualisation on mock-up prototypes should be considered as a valuable design tool early in the design phase, in terms of identifying aerodynamically sensitive regions, where predictions should be viewed with caution, and helping with the selection of a numerical flow modelling strategy.
- Using either a structured grid system or increased computational power, future work could assess the performance of the SST  $k-\omega$  and Spalart-Allmaras models for the insulated Stage 3 PCB configurations, which represent the most challenging test cases in this study. This would not only permit their capability to model transition to be further evaluated, but also their full potential for improved accuracy to be determined relative to the standard  $k-\epsilon$  flow model.
- While experimental flow visualisation helped isolate sources of prediction error in component junction temperature in this study, in subsequent benchmark studies the use of quantitative flow field and heat transfer measurements combined would enable the impact of flow field prediction error on heat transfer prediction to be more accurately assessed.
- Future benchmark studies on component heat transfer should consider fan-cooling conditions for a range of fan operating points representing different swirling flow conditions.
- Benchmarks should also be undertaken for radiation heat transfer, which is an important heat transfer mechanism in natural convection. The test cases should include multiple sinks and sources of radiation over a range of temperatures.

- The prediction of component transient heat transfer should be studied for multi-component board applications so as to assess the impact of both aerodynamic and thermal interaction prediction errors on the PCB assembly's thermal time constant. There is a need for accurate benchmark data to further assess the potential of CFD to aid in the design of convective solder reflow profiles.
- To fully identify sources of CTM predictive errors, factors such as inclusion of a Side node in the resistor network topology, and the coupling of the CTM to the board should be further examined. The impact of modelling component thermal wakes using CTMs on downstream component thermal interaction should also be evaluated.
- With ever-rising heat fluxes, component miniaturisation and emerging technologies, such as Micro-Electro-Mechanical Systems (MEMs), the modelling of micro- (1-1000  $\mu\text{m}$ ) and nano- (sub-micron) scale heat transfer will become an increasingly important area of development for both the design of microelectronics, and the integration of micro cooling systems at chip level. This will require new physical models and computational techniques.



## References

- [1] CALCE, 1999, "Overview of EPSC Graduate Program," CALCE Electronic Products and Systems Center, University of Maryland, College Park, MD 20742, USA.
- [2] PRC, 1997, Vision and Strategy, Packaging Research Center, Georgia Institute of Technology, 813 Fest Drive, NW Atlanta, Georgia 30332-0560.
- [3] Moore, G.E., 1975, "Progress in Digital Integrated Electronics," Proceedings IEEE International Electron Meeting, pp. 11-13.
- [4] Azar, K., 2002, "Advanced Cooling Concepts and Their Challenges," Invited talk given at the Eighth International Workshop on Thermal Investigations of ICs and Systems (THERMINIC), Madrid, Spain, October 1-4.
- [5] Azar, K., 2000, "The History of Power Dissipation," Electronics Cooling, Vol. 6, No. 1, pp. 42-50.
- [6] Azar, K., and Morabito, J., 2000, "Managing Power Requirements in the Electronics Industry," Electronics Cooling, Vol. 6, No. 4, pp. 12-25.
- [7] Schmidt, R. and Cruz, E., 2002, "Raised Floor Computer Data Center: Effect on Rack Inlet Temperatures of Chilled air Exiting both the Hot and Cold Aisles," pp. 580-594.
- [8] SEMATECH 2002, "International technology Roadmap for Semiconductors - Assembly and Packaging," ITRS 2002 Update, [www.sematech.org](http://www.sematech.org).
- [9] Bar-Cohen, A., 1999, "Thermal Packaging for the 21st Century: Challenges and Options," Invited talk given at the Fifth International Workshop on Thermal Investigations of ICs and Microstructures (THERMINIC), October 3-6, Rome, Italy.
- [10] Lall, P., Pecht, M., and Harkim, E., 1997, "Influence of Temperature on Microelectronics and System Reliability," CRC Press, New York.
- [11] Kirschman, R.K., 1990, "Low Temperature Electronics," IEEE Vol. 6, Part 2, pp. 12-24.
- [12] Davies, M.R.D., Cole, R., and Lohan, J., 2000, "Factors Affecting the Operational Thermal Resistance of Electronic Components," Transactions of the ASME, Journal of Electronic Packaging, Vol. 122, September 2000, pp. 185-191.
- [13] Mahajan, R., Nair, R., Wakharkar V., Swan, J., Tang, J., and Vandentop, G., 2002, "Emerging Directions For Packaging Technologies," Intel Technology Journal - Semiconductor Technology and Manufacturing, Volume, 6 Issue 02, pp. 62 - 75.
- [14] The Uptime Institute, 2000, "White Paper - Heat Density Trends in Data Processing, Computer Systems, and Telecommunications Equipment," Version 1.0, [www.upsite.com/TUIpages/tuihome.html](http://www.upsite.com/TUIpages/tuihome.html).
- [15] Versteeg, H.K., and Malalasekera, W., 1995, "An Introduction to Computational Fluid Dynamics - The Finite Volume Method," Longman Scientific and Technical, London.
- [16] Prakash, C., 1990, "Application of Computational Fluid Dynamics for Analyzing Practical Electronic Cooling Problems," Heat Transfer in Electronic and Microelectronic Equipment, Editor, Bergles, A. E., Hemisphere, New York.
- [17] Lee, T., Chambers, B., and Mahalingam, M., 1994, "Application of CFD Technology to Electronic Thermal Management," Proceedings of the 44th Electronics Components and Technology Conference, pp. 411-420.

- [18] Nakayama, W., and Bergles, A. E., 1990, "Cooling Electronic Equipment: Past, Present and Future," in: *Heat Transfer in Electronic and Microelectronic Equipment*, Editor, Bergles, A. E., Hemisphere, New York, pp. 3-40.
- [19] Pecht, M., Lall, P., and Hakim, E.B., 1992, "The Influence of Temperature on Integrated Circuit Failure Mechanisms," *Quality and Reliability Engineering International*, Vol. 8, pp. 167-175.
- [20] Das, D., and Pecht, M., 1996, "The Role of Heat Transfer Analysis in Avionics Equipment Development," *Proceedings of the 31st ASME National Heat Transfer Conference, HTD-Vol. 329, Volume 7*, pp. 197 - 210.
- [21] Mahajan, R., 2002, "Thermal Management of CPUs: A Perspective on Trends, Needs and Opportunities," Invited talk given at the Eighth International Workshop on Thermal Investigations of ICs and Systems (THERMINIC), Madrid, Spain, October 1-4.
- [22] Hutchings, B., and Iannuzzeli, R., 1987, "Taking the Measure of Fluid Dynamics Software," *Mechanical Engineering*, May Edition, pp. 72-76.
- [23] Lasance, C.J.M., 1997, "Status and Challenges in Thermal Design of Electronic Parts and Systems," *Proceedings of Eurotherm Seminar 58: Thermal Management of Electronic Systems III*, Editors, Bardon, J.P., Beyne, E., Saulnier, J. B., Elsevier, Paris, pp. 91-107.
- [24] Baelmans, M., Meyers, J., and Nevelsteen, K., 2003, "Flow Modeling in Air-Cooled Electronic Enclosures," *Proceedings of the Nineteenth Annual IEEE Semiconductor Thermal Measurement and Management Symposium (SEMI-THERM XIX)*, pp. 27-34.
- [25] Nakayama, W., 2001, "Emerging New Roles of CFD Simulation in Competitive Market Environment," *Proceedings of the Seventh International Workshop on Thermal Investigations of ICs and Systems (THERMINIC)*, pp. 223-229.
- [26] Nakayama, W., 2001, "An Approach to Fast Thermal Design of Compact Electronic Systems: a JSME Project," *Advances in Electronic Packaging; Proceedings of The PACIFIC RIM/ASME International, Intersociety Electronic Packaging Technical/Business Conf & Exhibition (IPACK'01)*, Paper No. IPACK2001-15532.
- [27] Nakayama, W., Behnia, M., and Soodphakdee, D., 2001, "A Novel Approach to the Design of Complex Heat Transfer Systems: Portable Computer Design – A Case Study," *IEEE Transactions on Components and Packaging Technology (CPT)*, Vol. 24, No. 2, pp. 199-206.
- [28] Shapiro, B., 2002, "Creating Reduced-Order Models for Electronic Systems: An Overview and Suggested Use of Existing Model Reduction and Experimental System Verification Tools," *Proceedings of the International Conference on Thermal Challenges in Next Generation Electronic Systems (THERMES 2002)*, pp. 299-306.
- [29] Cullimore, B., 2002, "Nonlinear Programming Applied to Thermal and Fluid Design Optimization," *Proceedings of the Eighth Intersociety Conf on Thermal and Thermomechanical Phenomena in Electronics Systems (ITHERM 2002)*, pp. 54-60.
- [30] Parry, J., Bornoff, R., Stehouwer, P., Driessen, L., Stinstra, E., 2003, "Simulation-based Design Optimization Methodologies applied to CFD," *Proceedings of the Nineteenth Annual IEEE Semiconductor Thermal Measurement and Management Symp, (SEMI-THERM XIX)*.
- [31] Cullimore, B., 2001, "Dealing with Uncertainties and Variations in Thermal Design," *Proceedings of IPACK'01: The Pacific Rim/ASME International Electronic Packaging technical Conference and Exhibition*, Paper No. IPACK2001-15516.

- [32] Moffat, R.J., 2002, "Getting the Most Out of Your CFD Program," Proceedings of the Eighth Intersociety Conf on Thermal and Thermomechanical Phenomena in Electronics Systems (ITHERM 2002), pp. 9-14.
- [33] Minichiello, A., and Belady, C., 2002, "Thermal Design Methodology for Electronic Systems," Proceedings of the Eighth Intersociety Conference on Thermal and Thermomechanical Phenomena in Electronics Systems (ITHERM 2002), pp. 696-704.
- [34] Lasance, C.J.M., 2001, "The conceivable Accuracy of Experimental and Numerical Thermal Analysis of Electronic Systems," Proceedings of the Seventeenth IEEE Semiconductor Thermal Measurement and Management Symp (SEMI-THERM XVII), pp.180-198.
- [35] Rodgers, P., Eveloy, V., and Davies, M., 2003, "An Experimental Assessment of Numerical Predictive Accuracy for Electronic Component Heat Transfer in Forced Convection: Parts I and II," Transactions of the ASME, Journal of Electronic Packaging, Vol. 125, No. 1, pp. 67-83.
- [36] Mack, B., and Venus, T., 2000, "Thermal Challenges in the Telecom and Networks Industry," Electronics Cooling, Vol. 6, No. 2, pp. 44-49.
- [37] Pecht, M., 1996, "Why Traditional Reliability Prediction Models Do Not Work – Is there an Alternative," Electronics Cooling, Vol. 2, No. 1, pp. 10-12.
- [38] Das, D., 1999, "Use of Thermal Analysis Information in Avionics Equipment Development," Electronics Cooling, Vol. 5, No. 3, pp. 28-34.
- [39] Osterman, M., 2001, "We Still Have A Headache With Arrhenius," Electronics Cooling, Vol. 7, No. 1, pp. 53-54.
- [40] Dasgupta, A., 2002, "The Physics-of-Failure Approach at the University of Maryland for the Development of Reliable Electronics," Proceedings of the Third International Conference on Thermal and Mechanical Simulation in (Micro)Electronics (EuroSimE), pp. 10-17.
- [41] Lasance, J.M., 1995, "The need for a Change in Thermal Design Philosophy," Electronics Cooling, Vol. 1, No. 2, pp. 24-26.
- [42] Tucker, P.G., 1997, "CFD Applied to Electronic Systems: A Review," IEEE Transactions on Components, Packaging and Manufacturing Technology - Part A, Vol. 20, No. 4, pp. 518-529.
- [43] Tang, L. and Joshi, Y.K., 1999, "A Multi-Scale Conjugate Thermal Modeling Approach for Air Cooled Electronic Enclosures," Advances in Electronic Packaging; Proceedings of The PACIFIC RIM/ASME International Intersociety Electronic & Photonic Packaging Conference (InterPACK'99), EEP-Vol. 26-1, pp. 295-304.
- [44] Grimes, R., Davies, M., Punch, J., Dalton, T., and Cole, R., 2001, "Modeling Electronic Cooling Axial Fan Flows," Transactions of the ASME, Journal of Electronic packaging, Vol. 123, No. 2, pp. 112-119.
- [45] Nevelsteen, K., Baelmans, De Troch, K., Mesbah, M. and Nelemans, W., 2003, "Screen Characterization Under Fan Induced Swirl Conditions," Proceedings of the Nineteenth Annual IEEE Semiconductor Thermal Measurement and Management Symposium (SEMI-THERM XIX), pp. 1-7.
- [46] Lasance, C.J.M., Rosten, H., and Parry, J., 1997, "The World of Thermal Characterization According to DELPHI-Parts I and II: Experimental and Numerical Methods," IEEE Transactions on Components, Packaging & Manufacturing Technology, Part A, Vol. 20, No.4, pp. 392-398.

- [47] Lasance, C.J.M., den Hertog, D., and Stehouwer, P., 1999, "Creation and Evaluation of Compact Models for Thermal Characterisation Using Dedicated Optimisation Software," Proceedings of the Fifteenth IEEE Semiconductor Thermal Measurement and Management Symposium (SEMI-THERM XV), pp. 189-200.
- [48] Ortega, A., Aranyosi, A., Griffin, R.A., West, S., and Edwards, D., 1999, "Compact Thermal Models of Conduction Cooled Packages," Proceedings of the Fifteenth IEEE Semiconductor Thermal Measurement and Management Symp (SEMI-THERM XV), pp. 221-230.
- [49] Aranyosi, A., Ortega, A., Griffin, R.A., West, S., and Edwards, D., 2000, "Compact Thermal Models of Packages used in Conduction Cooled Applications," IEEE Transactions on Components and Packaging Technology (CPT), Vol. 23, No. 3, pp. 470-480.
- [50] Lasance, C.J.M., 2000, "Two Benchmarks to Facilitate the Study of Compact Thermal Modeling Phenomena," IEEE Transactions on Components and Packaging Technology (CPT), Vol. 24, pp.559-566.
- [51] Bosch, E.G.T., 2001, "Thermal Compact Models: An Alternative Approach," Proceedings of the Seventh International Workshop on Thermal Investigations of ICs and Systems (THERMINIC), Paris, France, September 24-27, pp. 197-202.
- [52] Boyalakuntla, D.S., and Murthy, J.Y., 2001, "COBRA-Based Compact Models for Simulation of Electronic Chip Packages," Proceedings of The Pacific Rim/ASME International Electronic Packaging Technical Conference and Exhibition (IPACK'01), July 8-13, 2001, Kauai, Hawaii, USA, Paper Number IPACK2001-15534.
- [53] Gerstenmaier, Y.C., Pape, H., and Wachutka, G., 2001, "Rigorous Model and Network for Static Thermal Problems," Proceedings of the Seventh International Workshop on Thermal Investigations of ICs and Systems (THERMINIC), Paris, France, September 24-27, pp. 203-208.
- [54] Sabry, M.N., 2001, "Compact Thermal Models for Electronic Systems," Proceedings of Seventh International Workshop on Thermal Investigations of ICs and Systems (THERMINIC), Paris, France, September 24-27, pp. 197-202.
- [55] Sabry, M.N., 2002, "Dynamic Compact Thermal Models: An Overview of Current and Potential Advances," presented at the Eighth International Workshop on Thermal Investigations of ICs and Systems (THERMINIC), Madrid, Spain, October 1-4.
- [56] Lau, J., Wong, C.P., Prince, J.L. and Nakayama, W., 1998, "Electronic Packaging Design, Materials Process and Reliability," McGraw-Hill, New York, pp. 162-165.
- [57] Sathe, S.B., and Sammakia, B.G., 1996, "A Numerical Study of the Thermal Performance of a Tape Ball Grid Array (TGBA) Package," 31st ASME National Heat Transfer Conference, HTD-Vol. 329, pp. 83-93.
- [58] Meinders, E.J., and Hanjalic, K., 1998, "Experimental Evaluation of the Local Convective Heat Transfer from Configurations of Wall-Mounted Cubes in a Channel Flow," Electronics Cooling, Vol. 4, No. 1, pp. 34-38.
- [59] Azar, K., and Rodgers, P., 2001, "Visualization of Air Flows in Electronic Systems," Electronics Cooling, Vol. 7, No. 2, pp. 26-33.
- [60] Schofield, W.H., and Logan, E., 1990, "Turbulent Shear Flow Over Surface Mounted Obstacles," Transactions of the ASME, Journal of Fluids Engineering, Vol. 112, pp. 376-385.

- [61] Boyle, M.T., and Asante, K.A., 1990, "Detailed Film Coefficient Measurement of a Simple Large-Scale Semiconductor Package Geometry," Proceedings of the Sixth IEEE Semiconductor Thermal and Temperature Measurement Symposium (SEMI-THERM VI), pp. 89-94.
- [62] Meinders, E.R., 1998, "Experimental Study of Heat Transfer in Turbulent Flows over Wall-Mounted Cubes," Ph.D. Thesis, Faculty of Applied Physics, Delft University of Technology, The Netherlands, pp. 19-36.
- [63] Saulnier, J.B., 1995, "The Numerical Modelling of Heat Transfer in Electronic Systems: Challenges and Ideas for Answer," Proceedings of EURO THERM Seminar 45: Thermal Management of Electronic Systems II, Editors, Beyne, E., Lasance C.J.M., and Berghmans, J., Kluwer Academic Publishers, Dordrecht, pp. 3-15.
- [64] Lau, J., Wong, C.P., Prince, J.L. and Nakayama, W., 1998, "Electronic Packaging Design, Materials Process and Reliability," McGraw-Hill, New York, pp. 162-165.
- [65] Speziale, C., and So, R.M.C., 1998, "Turbulence Modeling and Simulation," in: The Handbook of Fluid Dynamics, Edited by Johnson, R. W., CRC Press and Springer, Chapter 14.
- [66] Heyerichs, K., and Pollard, A., 1996, "Heat Transfer in Separated and Impinging Turbulent Flows," International Journal of Heat and Mass Transfer, Vol. 39, No. 12, pp. 2385-2400.
- [67] Ferziger, J.H., and Peric, M., 1997, "Computational Methods for Fluid Dynamics," Springer, Berlin, pp. 276-279.
- [68] Garimella, S.V., 1997, "Flow Visualization Methods and their Application in Electronic Systems," in Thermal Measurement in Electronic Cooling, Azar, K., Ed., CRC Press LLC, New York, pp. 349-385.
- [69] Flotherm, Version 3.2 Reference and User Manuals, Flomerics Limited, Bridge Road, Hampton Court, Surrey, KT8 9HH, United Kingdom, 2001, [www.flomerics.com](http://www.flomerics.com).
- [70] Fluent, Version 6.1 Documentation, 2003, Fluent Inc., 10 Cavendish Court, Labanon, NH 03766, USA, [www.fluent.com](http://www.fluent.com).
- [71] Parry, J., Rantala, J., and Lasance, C.J.M., 2001, "Enhanced Electronic System Reliability – Challenges for Temperature Prediction," Proceedings of the Seventh International Workshop on Thermal Investigations of ICs and Systems (THERMINIC), pp. 29-35.
- [72] MIL-HDBK-217F, 1991, "Reliability Prediction of Electronic Equipment," U.S. Department of Defense, Washington D.C., USA.
- [73] Lasance, C.J.M., 2001, "The European Project Profit: Prediction of Temperature Gradients Influencing the Quality of Electronic products," Proceedings of the Seventeenth IEEE Semiconductor Thermal and Temperature Measurement Symposium (SEMI-THERM XVII), pp. 120-125.
- [74] Warner, M., Parry, J., Bailey, C., Marooney, C., Reeves, H., and Pericleous, K., 2001, "Flo/Stress: An Integrated Stress Solver for the CFD Tool Flotherm," Proceedings of IPACK'01: The Pacific Rim/ASME International Electronic Packaging technical Conference and Exhibition, Paper No. IPACK2001-15740.
- [75] Wakil, J., and Ho, P.S., 2000, "Nonuniform Temperature and Strain Fields in a Powered Package," IEEE Transactions on Components and Packaging Technologies, Vol. 23, No 3.

- [76] Down, W.H., 1991, "Achieving Consistency in IR Reflow," *Electronic Packaging and Production*, 110-113.
- [77] Lohan, J. and Davies, M., 1994, "Transient Thermal Behaviour of a Board-Mounted 160-Lead Plastic Quad Flat Pack," *Proceedings of the Fourth Intersociety Conf. on Thermal Phenomena in Electronic Systems (ITHERM'94)*, Washington D.C., USA, May 4-7, pp. 108-116.
- [78] Second European Lead-Free Soldering Technology Roadmap, Soldertech, Kingston Lane, Uxbridge, UB8 3PJ, UK, <http://www.lead-free.org>.
- [79] Nimmo, K., 2001, "Lead-Free Trends and Requirements and the Need for Global Co-Operation," *The International Journal of Microcircuits and Electronic Packaging*, Vol. 24, No. 4, (2001), pp. 304-315.
- [80] Garimella, S.V., 1997, "High-Performance Cooling Techniques for Electronic Systems," *Proceedings of EURO THERM Seminar 58: Thermal Management of Electronic Systems III*, Editors, Bardon, J. P., Beyne, E., Saulnier, J. B., Elsevier, Paris, pp. 3-15.
- [81] Kim, S.J., and Lee, S.W., (Editors), 1996, "Air Cooling Technology for Electronic Equipment," CRC Press, New York.
- [82] Moffat, R.J., and Ortega, A., 1988, "Direct Air-Cooling of Electronic Components," *Advances in Thermal Modeling of Electronic Components and Systems*, Editors, Bar-Cohen, A., and Kraus, A. D., Hemisphere Publishing Corporation, New York, 1, pp. 129-282.
- [83] Incropera, F.P., 1988, "Convection Heat Transfer in Electronic Equipment Cooling," *Transactions of the ASME, Journal of Heat Transfer*, 110, pp. 1097-1111.
- [84] Azar, K., and Russell, E.T., 1990, "Effect of Component Layout and Geometry on the Flow Distribution in Electronic Circuit Packs," *Proceedings of the Sixth IEEE Semiconductor Thermal and Temperature Measurement Symposium (SEMI-THERM VI)*, Phoenix, Arizona, pp. 1-9.
- [85] Boyle, M.T., and Asante, K.A., 1990, "Detailed Film Coefficient Measurement of a Simple Large-Scale Semiconductor Package Geometry," *Proceedings of the Sixth IEEE Semiconductor Thermal and Temperature Measurement Symposium (SEMI-THERM VI)*, pp. 89-94.
- [86] Boyle, M.T., and Leclair, S.E., 1997, "The Effects of Secondary Flows on the Convective Heat Transfer from a Heated Block in an Airstream," *32<sup>nd</sup> ASME National Heat Transfer Conference, HTD-Vol. 343, Vol. 5*, pp. 35-47.
- [87] Smith, T.F., Beckermann, C., Weber, S.W., 1991, "Combined Conduction, Natural Convection, and Radiation Heat Transfer in an Electronic Chassis," *Transactions of the ASME Journal of Electronic Packaging*, Vol. 113, pp. 382-390.
- [88] Ortega, A., 1996, "Conjugate Heat Transfer in Forced Air Cooling of Electronic Components," In: *Air Cooling Technology for Electronic Equipment*, Editors, Kim, S. J., and Lee, S.W., CRC Press, New York, pp. 104-171.
- [89] Buller, M.L., and Kilburn, R.F., 1981, "Evaluation of Surface Heat Transfer Coefficients For Electronic Module Packages," Presented at the ASME, Heat Transfer in Electronic Equipment, Winter Meeting, Washington, D.C., pp. 25-28.
- [90] Wirtz, R.A., and Dykshoorn, P., 1984, "Heat Transfer From Arrays of Flat Packs in a Channel Flow," *Proceedings of IEPS*, pp. 318-326.

- [91] Moffat, R.J., Arivizu, D.E., and Ortega, A., 1985, "Cooling Electronic Components: Forced Convection Experiments with an Air Cooled Array," 23rd ASME National Heat Transfer Conference, Denver, Colorado, pp. 17-27.
- [92] Sridhar, S., Faghri, M., Lessmann, R.C., and Schmidt, R., 1990, "Heat Transfer Behaviour Including Thermal Wake Effects in Forced Air Cooling of Arrays of Rectangular Blocks," ASME HTD, Thermal Modelling and Design of Electronic Systems and Devices, Vol. 153, pp. 15-26.
- [93] Lehmann, G.L., and Pembroke, J., 1991, "Forced Convection Air Cooling of Simulated Low Profile Electronic Components: Part 1 - Base Case," Transactions of the ASME, Journal of Electronic Packaging, March, Vol. 113, pp. 21-26.
- [94] Arabzadeh, M., Ogden, E.L., and Ghajar, A.J., 1993, "Conduction Heat Transfer Measurements for an Array of Surface Mounted Heated Components," Enhanced Cooling Techniques for Electronic Applications, ASME HTD-Vol. 263, pp.69-78.
- [95] Wirtz, R.A., and McAuliffe, W., 1989, "Experimental Modelling of Convection Downstream From an Electronic Package Row," Transactions of the ASME, Journal of Electronic Packaging, Vol. 111, pp. 207-212.
- [96] McEntire, A.B., and Webb, B.W., 1990, "Local Forced Convective Heat Transfer From Protruding and Flush-Mounted Two-Dimensional Discrete Heat Sources," International Journal Heat and Mass Transfer, Vol. 33, No. 7, pp. 1521-1533.
- [97] Kang, S.S., 1994, "The Thermal Wake Function for Rectangular Electronic Modules," Transactions of the ASME, Journal of Electronic Packaging, Vol. 116, March, pp. 55-59.
- [98] Ortega, A., Wirth, U., and Kim, S.J., 1994, "Conjugate Forced Convection from a Discrete Heat Source on a Plane Conducting Surface: a Benchmark Experiment," ASME HTD-292, - Heat Transfer in Electronic Systems, ASME, New York, pp. 25-36.
- [99] Lohan, J., Davies, M., and Cole, R., 1997, "Thermal Superposition on a Populated Printed Circuit Board," Proceedings of the 32nd ASME National Heat Transfer Conference, HTD-343, Vol. 5, pp. 73-82.
- [100] Anderson, A.M. and Moffat, R.J., 1990, "A New Type of Heat Transfer Correlation for Air Cooling of Regular Arrays of Electronic Components," ASME HTD Thermal Modelling and Design of Electronic Systems and Devices, Vol. 153, pp. 27-39.
- [101] King, D.E. and Wright, N.T., 1999, "Survey of Forced Convection Correlations for Cooling of Electronic Components Mounted on Printed Circuit Boards," Proceedings of the 33rd ASME National Heat Transfer Conference, Paper Number NHTC99-137.
- [102] Graham, K., and Witzman, S., 1988, "Analytical Correlation of Thermal Design of Electronic Packages," Cooling Technology for Electronic Equipment, Editor, Aung, W., Hemisphere Publishing Corporation, New York, pp. 249-264.
- [103] Rosten, H., Parry, J., Addison, J., Viswanath, R., Davies, M., and Fitzgerald E., 1995, "Development, Validation and Application of a Thermal Model of a PQFP," Proceedings of the 45th Electronic Components Technology Conference (ECTC), pp. 1140.
- [104] Nakayama, W., and Park, S.H., 1996, "Conjugate Heat Transfer from a Single Surface-Mounted Block to Forced Convection Air Flow in a Channel," Journal of Heat Transfer, Vol. 118, pp. 301-309.
- [105] Tang, W. and Ghajar, A.J., 1997, "Experimental Study of Conjugate Heat Transfer In a Horizontal Channel with Discrete Heated Cubic Blocks," 32nd ASME National Heat Transfer Conference, HTD-Vol. 343, Vol. 5, pp. 91-102.

- [106] Lohan, J., and Davies, M., 1996, "Thermal Interaction Between Electronic Components," Proceedings of the 31st ASME National Heat Transfer Conference, HTD-329, Vol. 7, pp. 73 - 82.
- [107] Cole, R., Dalton, T., Punch, J., Davies, M.R. and Grimes, R., 2001, "Forced Convection Board Level Thermal Design Methodology for Electronic Systems," Transactions of the ASME, Journal of Electronic packaging, Vol. 123, No. 2, June 2001.
- [108] SEMI International Standards, 1992, "G38-87 Test Method - Still- and Forced Air Junction-to-Ambient Thermal Resistance Measurements of Integrated Circuit Packages," SEMI International Standards, Packaging Volume, pp. 173-177.
- [109] JESD51-2 JEDEC Standard 51, Addendum No. 2, Integrated Circuits Thermal Test Method Environment Conditions -Natural Convection (Still Air), Electronic Industries Association, Engineering Department, [www.jedec.org](http://www.jedec.org).
- [110] JESD51-6 JEDEC Standard 51, Addendum No. 6, Integrated Circuit Thermal Test Method Environmental Conditions - Forced Convection (Moving Air), Electronic Industries Association, Engineering Department, [www.jedec.org](http://www.jedec.org).
- [111] Bosch, E., and Lasance, C.J.M., 2000, "Accurate Measurement of Interface Thermal Contact Resistance by means of a Transient Method," Proceedings of the Sixteenth IEEE Semiconductor Thermal and Temperature Measurement Symposium (SEMI-THERM XVI), pp. 167-173.
- [112] Szekely, V., Farkas, G., Nikodemusk, E., Rencz, M., Ress, S., Torok, S., 2000, "New Procedures for Thermal Transient Testing," Proceedings of the Sixth International Workshop on Thermal Investigations of ICs and Systems (THERMINIC), Budapest, Hungary, pp. 15-19.
- [113] Rencz, M., Szekely, V., and Kollar, E., 2000, "Measuring Dynamic Thermal Multiport Parameters of IC Packages, Proceedings of the Sixth International Workshop on Thermal Investigations of ICs and Systems (THERMINIC), Budapest, Hungary pp. 244-250.
- [114] Schweitzer, D., and Pape, H., 2002, "Thermal Transient Modelling and Experimental Validation of Power Packages," Proceedings of the Eighth International Workshop on Thermal Investigations of ICs and Systems (THERMINIC), Madrid, Spain, October 1-4, pp. 17-22.
- [115] Davies, M., Lohan, J., Punch, J., and Moore, T., 1993, "The Thermal Characteristics of a Board-Mounted 160 Lead Plastic Quad Flat Pack," Proceedings of EURO THERM Seminar 29, Editors, Hoogendoorn, C. J., Henkes, R. A. W. M., and Lasance, C. J. M., Kluwer Academic Publishers.
- [116] Castro, I.P., and Robins, A.G., 1977, "The Flow Around a Surface Mounted Cube in Uniform and Turbulent Streams," Journal of Fluid Mechanics, Vol. 79, Part 2, pp. 307-335.
- [117] Hunt, J.C.R, Abell, C.J., Peterka, J.A., and Woo, H., 1978, "Kinematical Studies of the Flows Around Free or Surface-Mounted Obstacles; Applying Topology to Flow Visualisation," Journal of Fluid Mechanics, Vol. 86, Part 1, pp. 179-200.
- [118] Garimella, S.V., and Eibeck, P.A., 1992, "Onset of Transition in the Flow over a Three-Dimensional Array of Rectangular Obstacles," Transactions from the ASME Journal of Electronic Packaging, Vol. 114, pp. 251-255.
- [119] Sparrow, E.M., Vemuri, S.B., and Kadle, D.S., 1983, "Enhanced and Local Heat Transfer, Pressure Drop and Flow Visualisation for Arrays of Block-Like Electronic Components," Int. Journal of Heat and Mass Transfer, Vol. 26, No. 5, May, pp. 689-700.



- [120] Schmidt, R.R., 2001, "Use of Naphthalene Sublimation Technique for Obtaining Accurate Heat transfer Coefficients in Electronic Cooling Applications," *Electronics Cooling*, Vol. 7, No. 3, pp. 26-32.
- [121] Newport, D., Dalton, T., Davies, M., and Whelan, M., 1999, "An Optical Investigation into the Temperature and Velocity Fields about an Enclosed PCB with an Array of Simulated 2D Components in Free Convection," *Proceedings of the fifth International Workshop on Thermal Investigations of ICs and Systems (THERMINIC)*, pp. 200-206.
- [122] Newport, D.T., Dalton, T.M., Davies, M.R.D., Whelan, M., and Forno, C., 2001, "On the Thermal Interaction Between an Isothermal Cylinder and Its Isothermal Enclosure for Cylinder Raleigh Numbers of Order  $10^4$ ," *Transactions of the ASME, Journal of Electronic Packaging*, Volume 123, No. 4, pp. 1052-1061.
- [123] Grimes, R., and Davies, M., 2001, "Aerodynamic and Thermal Investigation into Axial Flow Fan Cooling of Electronic Systems, Parts I and II," *Proceedings of the 35th National Heat Transfer Conference*, Anaheim, USA, June 10-12, Paper Numbers NHTC01-14110 and 14111.
- [124] Kehoe, E., Grimes, R., and Davies, M., 2001, "A Mixed Thermal Convection Criteria for a Printed Circuit Board," Paper EPP-24711, *Proceedings of the International Mechanical Engineering Congress and Exposition*, New York, USA, November 11-16.
- [125] Cole, R., Davies, M., and Punch, J., 2001, "A Board Level Study of an Array of Ball Grid Components Part I: Aerodynamic measurements," Paper NHTC01-1418, *Proceedings of the 35th National Heat Transfer Conference*, Anaheim, USA, June 10-12.
- [126] Wirtz R.A., and Mathur, A., 1993, "Convective Heat Transfer Distribution on the Surface of an Electronic Package," *ASME National Heat Transfer Conference*, August, Atlanta, Georgia.
- [127] Davies, M., Cole, R., and Punch, J., 2001, "A Board Level Study of an Array of Ball Grid Components Part II: Thermal Measurements," Paper NHTC01-1419, *Proceedings of the 35th National Heat Transfer Conference*, Anaheim, USA, June 10-12.
- [128] Evely, V., Lohan, J., and Rodgers, P., 2000, "A Benchmark Study of Computational Fluid Dynamics Predictive Accuracy for Component-Printed Circuit Board Heat Transfer," *IEEE Transactions on Components and Packaging Technology (CPT)*, Vol. 23, No. 3, pp.568-577.
- [129] Ota, T. and Kon, N., 1980, "Turbulent Heat Transfer of Momentum and Heat in a Separated and Reattached Flow over a Blunt Flat Plate," *Transactions of the ASME, Journal of Heat Transfer*, Vol. 102, pp. 749-754.
- [130] Fokkelman, W.F., Meinders, E.R., and Hanjalic, K., 1997, "The Backward-Facing Step Flow in the Transitional Regime," *Proceedings of EURO THERM Seminar 58: Thermal Management of Electronic Systems III*, Editors, Bardon, J. P., Beyne, E., Saulnier, J. B., Elsevier, Paris, pp. 37-43.
- [131] Abe, K. Kondoh, T., and Nagano, Y., 1994, "A New Turbulence Model for Predicting Fluid Flow and Heat Transfer in Separating and Reattaching Flows – I. Flow Field Calculations," *International Journal of Heat and Mass Transfer*, Vol. 37, No. 1, pp.139-151.
- [132] Abe, K. Kondoh, T., and Nagano, Y., 1995, "A New Turbulence Model for Predicting Fluid Flow and Heat Transfer in Separating and Reattaching Flows – II. Thermal Field Calculations," *International Journal of Heat and Mass Transfer*, Vol. 38, No. 8, pp.1467-1481.

- [133] Freitas, C.J., 1995, "Selected Benchmarks from Commercial CFD codes," Transactions of the ASME, Journal of Fluids Engineering, Vol. 117, pp. 208-218.
- [134] Cokljat, D., Kim, S.E., Iaccarino, G., and Durbin, P. A., 2003, "A Comparative Assessment of the V2F Model for Recirculating Flows," AIAA-2003-0765.
- [135] Hanjalic. K., and Obi, S. (Editors), 1997, Proceedings of the Sixth ERCOFTAC/IAHR/COST Workshop on Refined Flow Modelling, Delft University of Technology, The Netherlands.
- [136] Azar, K., and Manno, V.P., 1992, "Using a Thermal Simulation Model to Interpret Test Data," Proceedings of the Eight IEEE Semiconductor Thermal Measurement and Management Symposium (SEMI-THERM VIII), pp. 4-10.
- [137] Rhee, J., and Moffat, R.J., 1993, "Considerations in the Numerical Simulation of Experimental Electronics Cooling Studies," Solutions to CFD Benchmark Problems in Electronics Packaging, ASME HTD-Vol. 255, pp.1-9.
- [138] Ghosh, P., 1998, "Software Tools for Concurrent Design of Electronic Systems," Proceedings of the Sixth Intersociety Conference on Thermal and Thermomechanical Phenomena in Electronic Systems (ITHERM'98), pp. 378-385.
- [139] Holt, B.R., Ghosh, P. and Wyatt, W.G, 1997, "Thermal Design of Mobile Computers," 32nd ASME National Heat Transfer Conference, HTD-Vol. 343, No. 5, pp.9-15.
- [140] Remsburg, R., 1998, "Advanced Thermal Design of Electronic Equipment," Chapman and Hall, New York, pp. 9-20.
- [141] Linton, R.L., and Agonafer, D., 1993, "Benchmark Problems for System-Level Electronics Cooling," Solutions to CFD Benchmark Problems in Electronics Packaging, ASME HTD-Vol. 255, pp. 37-43.
- [142] Kathir, Z. and Lefebvre, S., 2001, "Thermal Analysis of Power Cycling Effects on High Power IGBT Modules by the Boundary Element Method," Proceedings of the Seventeenth IEEE Semiconductor Thermal Measurement and Management Symposium (SEMI-THERM XVII), pp. 27-34.
- [143] Igc, P.M., Mawby, P.A., Towers, M.S. and Batcup, S., 2001, "Dynamic Electro-Thermal Physically Based Compact Models of the Power Devices for Device and Circuit Simulations," Proceedings of the Seventeenth IEEE Semiconductor Thermal Measurement and Management Symposium (SEMI-THERM XVII), pp. 35-42.
- [144] Wen, S., and Lu, G.Q., 2000, "Finite Element Modeling of Thermal and Thermomechanical Behavior for Three-dimensional Packaging of Power Electronics Modules," Proceedings of the Seventh Intersociety Conference on Thermal and Thermomechanical Phenomena in Electronic Systems (ITHERM'2000), Vol. II, pp. 303-309.
- [145] Sarvar, F. and Whalley, D.C., 2000, "IGBT Package Design for High Power Aircraft Electronic Systems," Proceedings of the Seventh Intersociety Conference on Thermal and Thermomechanical Phenomena in Electronic Systems (ITHERM'2000), Vol. II, pp.391-397.
- [146] Adams, V., Blackburn, D., Joshi, Y., and Berning, D., "Issues in Validating Package Compact Thermal Models for Natural Convection Cooled Electronics Systems," 1997, IEEE Transactions on CPMT - Part A, Vol. 20, No. 4, pp. 420-431.

- [147] Ramakrishna, K., Thomas, T.R., Tom Lee, T.-Y., Trent, J.R. and Hause, J.V., 1998, "Thermal Performance of an Air-Cooled Plastic Ball Grid Array Package in Natural and Forced Convection," Proceedings of the Sixth Intersociety Conference on Thermal and Thermomechanical Phenomena in Electronic Systems (ITHERM'98), pp. 27-34.
- [148] Zahn, B.A., 1998, "Evaluating Thermal Characterisation Accuracy Using CFD Codes - A Package Level Benchmark Study of IcePaK and Flotherm," Proceedings of the Sixth Intersociety Conference on Thermal and Thermomechanical Phenomena in Electronic Systems (ITHERM'98), pp. 322-329.
- [149] Lohan, J., Tiilikka, P., Rodgers, P., Fager, C.M., and Rantala, J., 2000, "Experimental and Numerical Investigation into the Influence of Printed Circuit Board Construction on Component Operating Temperature in Natural Convection," IEEE Transactions on Components and Packaging Technology (CPT), Volume 23, Number 3, pp. 578-586.
- [150] Peng, G. and Ishizuka, M., 2002, "Numerical Analysis of Heat Transfer in a Compact Plastic Ball Grid Array Package Air Cooling Model," Proceedings of the Eighth Intersociety Conference on Thermal and Thermomechanical Phenomena in Electronic Systems (ITHERM'02), pp. 29-35.
- [151] Kim, S.H., Anand, N.K., and Fletcher, L.S., 1991, "Free Convection Between Series of Vertical Parallel Plates with Embedded Line Heat Sources," Transactions of the ASME, Journal of Heat Transfer, Vol. 113, Feb., pp. 108-115.
- [152] Di Perna, C., Evangelisti, A., Paroncini, M., and Ricci, R., 1994, "Natural Convection in a Rectangular Enclosure with an Array of Chips Mounted on a Vertical Wall," in Thermal Management of Electronic Systems, Editors, Hoogendoorn, C. J., Henkes, R. A. W. M., and Lasance, C. J. M., Kluwer Academic Publishers, Dordrecht, pp. 97-106.
- [153] Heindel, T.J., Ramadhyani, S., and Incropera, F.P., 1995, "Laminar Natural Convection in a Discretely Heated Cavity: 1 – Assessment of Three-Dimensional Effects," Transactions of the ASME, Journal of Heat Transfer, Vol. 117, Nov., pp. 902-909.
- [154] Heindel, T.J., Ramadhyani, S., and Incropera, F.P., 1995, "Laminar Natural Convection in a Discretely Heated Cavity: II – Comparisons of Experimental and Theoretical Results," Transactions of the ASME, Journal of Heat Transfer, Vol. 117, Nov., pp. 910-917.
- [155] Wang, H.Y., Penot, F., and Saulnier, J.B., 1997, "Numerical Study of a Buoyancy-Induced Flow along a Vertical Plate with Discretely Heated Integrated Circuit Packages," Int. J. Heat Mass Transfer, Vol. 40, No. 7, pp. 1509-1520.
- [156] Drabbels, J.P.A., 1997, "Natural Convection Heat Transfer of Metal Cuboids Flush Mounted in a Horizontal Plate," in Thermal Management of Electronic Systems II, Editors, Beyne, E., Lasance C. J. M., and Berghmans, J., Kluwer Academic Publishers, Dordrecht, pp. 273-280.
- [157] Behnia, M., and Nakayama, W., 1998, "Numerical Simulation of Combined Natural Convection-Conduction Cooling of Multiple Protruding Chips on a Series of Parallel Substrates," Proceedings of The Sixth Intersociety Conference on Thermal and Thermomechanical Phenomena in Electronic Systems (ITHERM'98), pp. 135-142.
- [158] Rosten, H.I. and Viswanath, R., 1994, "Thermal Modelling of the Pentium™ Processor Package," Proceedings of the 44th Electronics Components and Technology Conference, pp. 1140-1150.
- [159] Teng, S., Lee, T.-Y.T., Mahalingam, M., and Joiner, B., 1997, "Thermal Model of a Component Package for System Level Applications," Journal of Electronics Manufacturing, Vol. 7, No.2, pp. 115-127.

- [160] Adams, V.H., Ramakrishna, K., Tom Lee, T.-Y., Hause, J.V., and Mahalingam, M., 1999, "Design-Based Thermal Performance Evaluation of a GaAs MMIC Device in a Plastic Ball Grid Array Package," Proceedings of The PACIFIC RIM/ASME International Intersociety Electronic & Photonic Packaging Conference (InterPACK'99), EEP-Vol. 26-1, pp. 277-285.
- [161] Chiriac, V.A., and Lee, T.-Y.T., 1999, "Thermal Strategy for Modelling The Wirebonded PBGA Packages," Advances in Electronic Packaging; Proceedings of The PACIFIC RIM/ASME International Intersociety Electronic & Photonic Packaging Conference (InterPACK'99), EEP-Vol. 26-1, pp. 287-293.
- [162] Ramakrishna, K. and Tom Lee, T.-Y., 2002, "Prediction of Thermal Performance of Flip Chip - Plastic Ball Grid Array (FC-PBGA) Packages: Effect of Substrate Physical Design," Proceedings of the Eighth Intersociety Conference on Thermal and Thermomechanical Phenomena in Electronic Systems (ITHERM'02), pp. 528-537.
- [163] Anderson, A., 1997, "A Comparison of Computational and Experimental Results for Flow and Heat Transfer from an Array of Heated Blocks," Transactions of the ASME, Journal of Electronic Packaging, Vol. 119, March, pp. 32-39.
- [164] Rodgers, P., Lohan, J., Evely, V., Fager, C.M., and Rantala, J., 1999, "Validating Numerical Predictions of Component Thermal Interaction on Electronic Printed Circuit Boards in Forced Convection Air Flows by Experimental Analysis," Advances in Electronic Packaging; Proceedings of The PACIFIC RIM/ASME International Intersociety Electronic & Photonic Packaging Conference (InterPACK'99), EEP-Vol. 26-1, pp. 999-1009.
- [165] Deb, P., and Majumdar, P., 1999, "Numerical Investigation of Fluid Flow and Heat Transfer over Distributed Heated Modules with the Standard k- $\epsilon$  Model and a Low Reynolds Number Model, Proceedings of the 33<sup>rd</sup> ASME National Heat Transfer Conference, NHTC99-311.
- [166] Hellsten, A. and Rautahaimo, P. (Editors), 1999, Proceedings of the Eighth ERCOFTAC/IAHR/COST Workshop on Refined Turbulence Modelling, Helsinki University of Technology, Finland.
- [167] Rosten, H., Parry, J., Lasance, C., Vinke, H., Temmermann, W., Nelemans, W., Assouad, Y., Gautier, T., Slattery, O., Cahill, C., O'Flattery, M., Lacaze, C., and Zemlianoy, P., 1997, "Final Report to SEMITHERM XIII on the European-Funded Project DELPHI - the Development of Libraries and Physical Models for an Integrated Design Environment," Proceedings of the Thirteenth Annual IEEE Semiconductor Thermal Measurement and Management Symposium (SEMI-THERM XIII), pp. 73-91.
- [168] Pape, H., and Noebauer, G., 1999, "Generation and Verification of Boundary Independent Compact Thermal Models According to DELPHI/SEED Methods," Proceedings of the Fifteenth Annual IEEE Semiconductor Thermal Measurement and Management Symposium (SEMI-THERM XV), pp. 201-211.
- [169] Parry, J., Rosten, H., and Kromann, G.B., "The Development of Component-Level Thermal Compact Models of a C4/CBGA Interconnect Technology: The Motorola PowerPC 603 and PowerPC604 RISC Microprocessors," Transactions on Components, Packaging & Manufacturing Technology – Part A, Vol. 21, No.1, 1998.
- [170] Pashaie-Rad, S., Hermanson, J.C., and Rences, J.J., 1998, "Development of Component-Level Thermal Models of a Ceramic Pin Grid Array," Proceedings of the Sixth Intersociety Conference on Thermal and Thermomechanical Phenomena in Electronic Systems (ITHERM 1998), pp. 512-519.

- [171] Yu, E., and Przekwas, A., 1999, "Reduced Thermal Models of Electronic Packages For System Level Design Applications," *Advances in Electronic Packaging*, Proceedings of the Pacific RIM/ASME International Intersociety Electronic & Photonic Packaging Conference (InterPACK'99), EEP-Vol. 26-1, pp. 75-82.
- [172] Shidore, S., and Tom Lee, T.Y., 1999, "A Comparative Study of the Performance of Compact Model Topologies and their Implementation in CFD for a Plastic Ball Grid Array Package," *Advances in Electronic Packaging*; Proceedings of The PACIFIC RIM/ASME International Intersociety Electronic & Photonic Packaging Conference (InterPACK'99), EEP-Vol. 26-1, pp. 97-104.
- [173] Shidore, S., Adams, V., and Lee, T.-Y. T., 2001, "A Study of Compact Thermal Model Topologies in CFD for a Flip Chip Ball Grid Array Package," *IEEE Transactions on Components and Packaging Technology (CPT)*, Vol. 24, No. 2, pp. 191-198.
- [174] DeVoe, J., Ortega, A., and Mulugeta, B., 2003, "On the Performance of Compact Thermal Models of Electronic Chip Packages in Conjugate Board Level Simulation," *Proceedings of the Nineteenth Semiconductor Thermal Measurement and Management Symposium (SEMI-THERM XIX)*, pp. 313-318.
- [175] DeVoe, J., and Ortega, A., 2002, "An Investigation of Board Level Effects on Compact Thermal Models of Electronic Chip Packages," *Proceedings of the Eighteenth Semiconductor Thermal Measurement and Management Symp (SEMI-THERM XVIII)*.
- [176] DeVoe, J., and Ortega, A., 2002, "An Assessment of the Behavior of Compact Thermal Models of Electronic Packages in a Printed Circuit Board Level Environment," *Proceedings of the Eighth Intersociety Conference on Thermal and Thermomechanical Phenomena in Electronic Systems (ITHERM 2002)*, San Diego, CA, USA, May 30-June 1, pp. 69-76.
- [177] Lasance, C.J.M., 1994, "Thermal Management of Air-Cooled Electronic Systems: New Challenges for Research," in: *Thermal Management of Electronic Systems*, Proceedings of EURO THERM Seminar 29, Editors, Hoogendoorn, C. J., Henkes, R. A. W. M., and Lasance, C. J. M., Kluwer Academic Publishers, pp. 3-24.
- [178] Gartner Dataquest, 2000, "Commercial CFD Software Revenues," Corporate Headquarters, Gartner Inc., 56 Top Gallant Road, Stamford, CT 06904, USA, [www.gartner.com](http://www.gartner.com).
- [179] Flomerics, 1999, "Maximizing Productivity in Thermal Design of Electronic Systems," Flomerics Limited, 81 Bridge Road, Hampton Court, Surrey, KT8 9HH, United Kingdom, [www.flomerics.com](http://www.flomerics.com).
- [180] Flomerics, 2002, "Flomerics Confirms No. 1 Position in Electronics Thermal Analysis," Flomerics Limited, 81 Bridge Road, Hampton Court, Surrey, KT8 9HH, United Kingdom, [www.flomerics.com](http://www.flomerics.com).
- [181] Marrs, R., Molnar, R., Lynch, B., Mescher, P., and Olachea, G., 1995, "Recent Technology Breakthroughs achieved with the new SuperBGA® Package," *Proceedings of the International Electronics Packaging Conference*, pp. 565-576.
- [182] Guenin, B.M., Marrs, R.C., and Molnar, R.J., 1995, "Analysis of a Thermally Enhanced Ball Grid Array Package," *IEEE Transactions on Components, Packaging and Manufacturing Technology – Part A*, Vol. 18, No. 4, pp. 458-468.
- [183] Guenin, B., 2001, "Future Challenges in Microelectronics Packaging," Invited Presentation given at the Seventh International Workshop on Thermal Investigations of ICs and Systems (THERMINIC), Paris, France, September 26, 2001.

- [184] Guenin, B., 1997, "Packaging: Designing for Thermal Performance," *Electronics Cooling*, Vol.3, No.2, pp. 14-19.
- [185] JEDEC Solid State Technology Association, Engineering Department, 2500 Wilson Blvd, Arlington VA 22201-3834, USA, <http://www.jedec.org/>
- [186] Semiconductor Equipment and Materials International (SEMI), Global Headquarters, San Jose, 3081 Zanker Road, San Jose, CA 95134 USA, <http://www.semi.org/>
- [187] Amkor, 2002, "Small Outline IC Packages: Data Sheet," Operations Headquarters, 1900 South Price Road, Chandler, AZ 85248-1604, USA, [www.amkor.com](http://www.amkor.com).
- [188] Amkor, 2002, "MQFP PowerQuad 2 Packages: Data Sheet," Operations Headquarters, 1900 South Price Road, Chandler, AZ 85248-1604, USA, [www.amkor.com](http://www.amkor.com).
- [189] "Thermal Clad Selection Guide," 2002, The Bergquist Company, 18930 West 78<sup>th</sup> Street, Chanhassen, MN 55317, USA.
- [190] Graebner, J.E. and Azar, K., 1997, "Thermal Conductivity Measurements in Printed Wiring Boards," *Transactions of the ASME, Journal of Heat Transfer*, Vol. 119, No. 3, pp. 401-405.
- [191] Punch, J., and Davies, M., 1997, "Still-air Junction-to-ambient Thermal Resistance of Different Devices as a Function of Effective Thermal Conductivity of Printed Circuit Boards," *Proceedings of EURO THERM Seminar 58: Thermal Management of Electronic Systems III*, Editors, Bardou, J. P., Beyne, E., Saulnier, J. B., Elsevier, Paris, pp. 262-268.
- [192] Sofia, J. W., 1995, "Fundamentals of Thermal Resistance Measurements," *Application Notes from Analysis Tech.*, Wakefield, MA, USA.
- [193] SEMI G32-94, "Guide Line for Unencapsulated Thermal Test Chip," SEMI International Standards, Packaging Volume.
- [194] EIA/JESD51-4, 1997, "Thermal Test Chip Guideline (Wire Bond Type Chip)," *Electronic Industries Association, Engineering Department, 2500 Wilson Boulevard, Arlington, VA 22201-3834, USA.*
- [195] Motta, V., 1995, "New JEDEC Standards for Thermal Measurements: Review and Examples," *Proceedings of EURO THERM Seminar 45: Thermal Management of Electronic Systems II*, Editors, Beyne, E., Lasance C. J. M., and Berghmans, J., Kluwer Academic Publishers, Dordrecht, pp. 293-300.
- [196] Lasance, C.J.M., 1997, "Thermal Resistance: An Oxymoron?," *Electronics Cooling*, Vol. 3, No. 2, pp. 20-22.
- [197] JEDEC JC15.1, "CTM Standardization," JEDEC Thermal Sub-Committee, Meeting # 42, October 21-22, 2003, Palo-Alto, CA, USA.
- [198] Lin, P.C., and Nguyen, L.T., 1993, "Thermal Characteristics of IC Packages," Presented at the EURO THERM Seminar 29: Thermal Management of Electronic Systems, Delft University of Technology, The Netherlands.
- [199] Marrs, R.C., 1994, "Thermal Performance of the 28 x 28 mm QFP PowerQuad2," *Proceedings of the Electronic Components Technology Conference (ECTC)*, pp.429-441.
- [200] SEMI G42-88, 1992, "Thermal Test Board Specification for Standardization for Measuring Junction-to-Ambient Thermal Resistance of Semiconductor Packages," SEMI International Standards, Packaging Volume.

- [201] Cole, R., 1997, "Thermal Interaction between Electronic Components on a Printed Circuit Board," Interim M.Eng. Report, Department of Mechanical and Aeronautical Engineering, University of Limerick, Ireland.
- [202] Micro-BetaCHIP Probe, Betatherm corporation, 910 Turnpike Road, Shrewsbury, Massachusetts, MA 015045, USA.
- [203] Järvinen, T., 1994, "Emissivity Determination of Some Surfaces with Fourier-Transform Infrared Spectrometer," Laboratory of Applied Thermodynamics, Helsinki University of Technology, Espoo, Finland.
- [204] Kline, S.J., and McClintock, F.A., 1953, "Describing Uncertainties in Single Sample Experiments," *Mechanical Engineering*, January, pp. 3-8.
- [205] Moffat, R.J., 1982, "Contributions to the Theory of Single Sample Uncertainty Analysis," *Transactions of the ASME, Journal of Fluids Engineering*, Vol. 104, pp. 250-260.
- [206] Moffat, R.J., 1985, "Using Uncertainty Analysis in the Planning of an Experiment," *Transactions of the ASME, Journal of Fluids Engineering*, Vol. 107, pp. 173-178.
- [207] Moffat, R.J., 1988, "Describing the Uncertainties in Experimental Results," *Experimental Thermal and Fluid Science*, Elsevier Science Publishing, New York, pp. 3-17.
- [208] Moffat, R.J., 1997, "Uncertainty Analysis," in *Thermal Measurement in Electronic Cooling*, Azar, K., Ed., CRC Press LLC, New York, pp. 45-80.
- [209] Sweet, J.N., 1997, "Temperature Measurement in Electronics Cooling," in *Thermal Measurement in Electronic Cooling*, Azar, K., Ed., CRC Press LLC, New York, pp. 167-214.
- [210] Rodgers P., 1992, "Thermal Resistance Measurements of 160 PIN QFPs," Amkor Packages Qualification Report, Analog Devices B. V., Limerick, Ireland.
- [211] Rodgers, P., Eveloy, V., Lohan, J., Fager, C.M., and Rantala, J., 1999, "Experimental Validation of Numerical Heat Transfer Predictions for Single- and Multi-Component Printed Circuit Boards in a Forced Convection Environment: Part I – Experimental and Numerical Modelling," 33rd ASME National Heat Transfer Conference, NHTD99-167.
- [212] Cullity, B. D., 1978, "Elements of X-Ray Diffraction," 2nd edition, Addison-Wesley Publishing Company.
- [213] Haque, S., Lu, G. Q., Goings, J., and Sigmund, J., 2000, "Characterization of Interfacial Thermal Resistance by Acoustic Micrography Imaging," *Journal of Microelectronics Reliability*, Vol. 40, No. 3, pp. 465-476.
- [214] Struers, "About Grinding and Polishing," Valhojs Alle 176, DK-2610 Rodovre, Denmark.
- [215] Pecht, M.G., Nguyen, L., and Hakim, E.B., 1995, "Plastic Encapsulated Microelectronics," John Wiley & Sons, Inc., pp. 361-414.
- [216] Suhir, E., 1993, "Predicted Bow of Plastic Packages of Integrated Circuit (IC) Devices," In: *Thermal Stress and Strain of Microelectronics Packaging*, Editor, Lau, J. H., pp. 385-409.
- [217] Chanchani, R., and Hall, P.M., 1993, "Temperature Dependence of Thermal Expansion of Materials for Electronic Packages," In: *Thermal Stress and Strain of Microelectronics Packaging*, Editor, Lau, J. H., pp. 173-193.
- [218] Matijasevic, G.S., Wang, C.Y., and Lee, C.C., 1993, "Thermal Stress Considerations in Die-Attachment," In: *Thermal Stress and Strain of Microelectronics Packaging*, Editor, Lau, J. H., pp. 194-220.

- [219] Lam, D.C.C., Chong, J.I.T., and Tong, P., 2002, "The Role of Water in Delamination in Electronics Packages: Water Evaporation From Epoxy," IEEE Transactions on Components and Packaging Technology (CPT), Vol. 25, No. 4, pp. 708-712.
- [220] Jensen, F., 1995, "Electronic Component Reliability: Fundamentals, Modelling, Evaluation and Assurance, Wiley, New York, pp. 21-57.
- [221] Chowdhury, A., Guenin, B., Woo, C., Kim, S., and Lee, S., 1998, "The Effect of Die Attach Layer Delamination on the Thermal Performance of Plastic Packages," Proceedings of the Electronic Components Technology Conference (ECTC), May 25-28, Seattle, WA.
- [222] Moore, T.D., 2002, "Design for Control of Stress and Warpage in Laminate Integrated Circuit Multichip Assemblies," PhD Thesis, University of Limerick, Ireland.
- [223] Lohan, J., Evely, V., and Rodgers, P., 2002, "Visualization of Forced Air Flows over a Populated Printed Circuit Board and their Impact on Convective Heat Transfer," Proceedings of the Eighth Intersociety Conference on Thermal and Thermomechanical Phenomena in Electronics Systems (ITHERM 2002), San Diego, CA, May 29-June 1, pp. 501-511.
- [224] Dantec, Safex "Standard" Fog Fluid, Dantec Measurement Technology A/S, Tonsbakken 16-18, PO Box 121, DK-2740 Skovlunde, Denmark.
- [225] Lohan, J., Tiilikka, P., Fager, C.M., and Rantala, J., 2000, "Effect of both PCB Thermal Conductivity and Nature of Forced Convection Environment on Component Operating Temperature: Experimental Measurement and Numerical Prediction," Proceedings of the 16th IEEE Semiconductor Thermal Measurement and Management Symposium (SEMI-THERM XVI).
- [226] EIA/JESD51-3, "Low Effective Thermal Conductivity Test Board for Leaded Surface Mount Components," Electronic Industries Association, Engineering Department, 2500 Wilson Boulevard, Arlington, VA 22201-3834, USA, 1996.
- [227] EIA/JESD51-7, "High Effective Thermal Conductivity Test Board for Leaded Surface Mount Packages," Electronic Industries Association, Engineering Department, 2500 Wilson Boulevard, Arlington, VA 22201-3834, USA, 1999.
- [228] Behnia, M., Nakayama, W., and Wang, J., 1998, "CFD Simulations of Heat Transfer from a Heated Module in an Air Stream: Comparison with Experiments and a Parametric Study," Proceedings of The Sixth Intersociety Conference on Thermal and Thermomechanical Phenomena in Electronic Systems (ITHERM'98), pp. 143-151.
- [229] Kim, S.E., 1996, "Computational Fluid Dynamics for Turbulent Flows: Part II Near-Wall Treatments," Fluent User's Group Meeting, MTG-96-172, Dae-Jeon, Korea. Kim, E., and Choudhury, D., 1995, "A Near-Wall Treatment Using Wall Functions Sensitized to Pressure Gradient," ASME FED Vol. 217, Separated and Complex Flows.
- [230] Rodi, W., 1991, "Experience with Two-Layer Models Combining the k- $\epsilon$  model with a One-Equation Model Near the Wall," Paper Number AIAA 91-0216, Proceedings of the 29th Aerospace Sciences Meeting, January 7-10, Reno, Nevada, USA.
- [231] Patankar, 1990, S.V., "Numerical Heat Transfer and Fluid Flow," Taylor & Francis.
- [232] Spalding, D.B., 1980, "Mathematical modeling of fluid mechanics, heat transfer and chemical reaction processes," CFDU Tech. Rep. HTS/80/1. Mechanical Engineering Department, Imperial College, London, U.K.



- [233] Agonafer, D., Gan-Li, L. and Spalding, D.B., 1996, "The LVEL Turbulence Model for Conjugate Heat Transfer at Low Reynolds Numbers," ASME, Application of CAE/CAD to Electronic Systems, EEP-Vol. 18, pp. 23-26.
- [234] Launder, B. E. and Spalding, D.B., 1974, "The Numerical Computation of Turbulent Flows," Computer Methods in Applied Mechanics and Engineering, Vol. 3, pp. 269-289.
- [235] Launder, B. E., and Spalding, D.B., 1972, "Mathematical Models of Turbulence," Academic Press.
- [236] Burgos, J., Manno, V.P. and Azar, K., 1995, "Achieving Accurate Thermal Characterisation Using a CFD Code – A Case Study of Plastic Packages," IEEE Trans on Components, Packaging, and Manufacturing Technology – Part A, Vol. 18, No. 4, pp. 732-738.
- [237] Mohammadi, B., and Pironneau, O., 1994, "Analysis of the K-Epsilon Turbulence Model," Wiley, Paris.
- [238] Spalding, D.B., 1961, "A Single Formula for the Law of the Wall," Transactions of the ASME, Series A, Journal of Applied Mechanics, Vol. 28, No. 3, pp. 444-458.
- [239] Mathur, S.R., and Murthy, J.Y., 1997, "A Pressure-Based Method for Unstructured Meshes," Numerical Heat Transfer, Vol. 31, pp. 195-215.
- [240] Kim, S.E., Mathur, S.R., Murthy, J.Y., and Choudhury, D., 1998, "A Reynolds-Averaged Navier Stokes Solver Using Unstructured Mesh-Based Finite Volume Scheme," AIAA-Paper 98-0231.
- [241] Spalart, P. and Allmaras, S., 1992, "A One-Equation Model for Aerodynamic Flows," Technical Report AIAA-92-0439, American Institute of Aeronautics and Astronautics.
- [242] Launder, B. E., and Sharma, B. I., 1974, "Application of the Energy Dissipation Model of Turbulence to the Calculation of Flow Near a Spinning Disc," Lett. Heat and Mass Transfer, Vol. 1, pp. 131-138.
- [243] Lam, C.K.G., and Bremhost, K., 1981, "A Modified Form of the k- $\epsilon$  Model for Predicting Wall Turbulence, ASME Journal of Fluids Engineering, Vol. 103, pp. 456-460.
- [244] Yang, Z., and Shih, T. H., 1993, "New Time Scale Based k- $\epsilon$  Model for Near-Wall Turbulence," AIAA Journal, Vol. 31, pp. 1191-1198.
- [245] Wilcox, D.C., 1998, Turbulence Modeling for CFD, DCW Industries, Inc., La Canada, California.
- [246] Menter, F.R., 1994, "Two-Equation Eddy Viscosity Turbulence Models for Engineering Applications," AIAA Journal, Vol. 32, No. 8, pp. 1598-1605.
- [247] Chen, H.C., and Patel V. C., 1988, "Near-Wall Turbulence Models for Complex Flows Including Separation," AIAA Journal, Vol. 26, No. 6, pp. 641-648.
- [248] Madhavan, P., and Joshi, Y., 2002, "Computational Simulations of Server Room Cooling – A Parametric Study," Proceedings of the International Workshop on Thermal Investigations of ICs and Systems, Madrid, Spain, October 1-4, pp. 277-282.
- [249] Wolfshtein, M., 1969, "The Velocity and Temperature Distribution of One-Dimensional Flow with Turbulence Augmentation and Pressure Gradient," International Journal of Heat and Mass Transfer, Vol. 12, pp. 301-318.
- [250] Yahkot, V., and Orszag, S. A., 1986, "Renormalisation Group Analysis of Turbulence. I. Basic Theory," Journal of Scientific Computing, Vol. 1, No. 1.

- [251] Choudhury, D., 1993, "Introduction to the Renormalization Group Method and Turbulence Modeling," Fluent Inc. Technical Memorandum TM-107.
- [252] Chui, E.H. and Raithby, G.D., 1993, "Computation of Radiant Heat Transfer on a Non-Orthogonal Mesh Using the Finite-Volume Method," Numerical Heat Transfer, Part B, Vol. 23, pp. 269-288.
- [253] Icepak, Version 4.0 Documentation, 2002, Fluent Inc., 10 Cavendish Court, Labanon, NH 03766, USA.
- [254] Agonafer, D., and Moffat, D.F., 1990, "Numerical Modelling of Forced Convection Heat Transfer for Modules Mounted on Circuit Boards," Transactions of the ASME, Journal of Electronics Packaging, Vol. 112, pp. 333-337.
- [255] Yang, M. C., 2000, "A Comparison of Using Icepak and Flotherm in Electronic Cooling," Proc of 7th Intersociety Conference on Thermal and Thermomechanical Phenomena in Electronic Systems, Vol. 1, pp. 240-246.
- [256] Aranyosi, A., Ortega, A., Evans, J., Tarter, T., Pursel, J., Radhakrishnan, J., 2000, "Development of Compact Thermal Models for Advanced Electronic Packaging: Methodology and Experimental Validation for a Single-Chip CPGA Package," Proceedings of the Seventh Intersociety Conference on Thermal and Thermomechanical Phenomena in Electronics Systems (ITHERM 2000), Vol. 1, pp. 225-232.
- [257] Rosten, H.I., Krueger, W.B., Bar-Cohen, A., Lasance, C.J.M., and Temmerman, W., 1997, "Thermal Characterization of Electronic Packages," Flomerics Limited, 81 Bridge Road, Hampton Court, Surrey, KT8 9HH, United Kingdom.
- [258] Parry, J., Pape, H., Schweitzer, D., and Janssen, J., 2002, "Transient Performance of Common Modeling Assumptions Used in Detailed Thermal Package Models," Proceedings of the Eighth International Workshop on Thermal Investigations of ICs and Systems (THERMINIC), pp. 283-289.
- [259] Tatchell, T., 1998, "Grid Systems for CFD and Their Application to Electronics Thermal Analysis," Flomerics Limited, Bridge Road, Hampton Court, Surrey, KT8 9HH, United Kingdom.
- [260] Lasance, C.J.M., 2003, "Recent Progress in Compact Thermal Models," Proceedings of the Nineteenth Annual IEEE Semiconductor Thermal Measurement and Management Symposium (SEMI-THERM XIX), pp.290-299.
- [261] Lasance, C.J.M., Vinke, H., and Rosten, H., 1995, "Thermal Characterization of Electronic Devices with Boundary Condition Independent Compact Models," IEEE Transactions on Components, Packaging and Manufacturing Technology - Part A, Vol. 18, No. 4, pp. 723-731.
- [262] Vinke, H., and Lasance, C.J.M., 1997, "Thermal Characterization of Electronic Devices by Means of Improved Boundary Condition Independent Compact Models, In Thermal Management of Electronic Systems II, Editors Beyne, Lasance and Berghmans, Kluwer Academic Publishers, pp. 115-124.
- [263] Flomerics, 2000, "Overview of Compact Component SmartPart, Flotherm Version 3.1," Flomerics Limited, Bridge Road, Hampton Court, Surrey, KT8 9HH, United Kingdom, 2001, [www.flomerics.com](http://www.flomerics.com).
- [264] Jensen, R.H., Andrejack, G. A., Button, D.P., and Bydal, B.A., 1989, "Comparative Thermal Performance of Various Substrate Materials in a Simple Packaging Application: Actual versus Predicted," Proceedings of the 39th Electronic Components Technology Conference (ECTC), pp. 572-576.

- [265] Sarvar, F., Poole, N.J., and Witting, P.A., 1990, "PCB Fiber Glass Laminates: Thermal Conductivity Measurements and Their Effect on Simulation," *Journal of Electronic Materials*, Vol. 19, pp. 1345-1350.
- [266] Incropera, F.P., and De Witt, D.P., 1990, "Fundamentals of Heat and Mass Transfer," Third Edition, Wiley, New York, pp. 481-533.
- [267] Eckert, E.R.G. and Soehngen, E., 1951, "Interferometric Studies on the Stability and Transition to Turbulence of a Free Convection Boundary Layer," *Proc. Gen. Discuss, Heat Transfer ASME-IME*, London.
- [268] Bejan, A., 1993, *Heat Transfer*, Wiley, pp. 335-397.
- [269] Incropera, F.P., and De Witt, D.P., 1990, "Fundamentals of Heat and Mass Transfer," Third Edition, Wiley, New York, pp. 345-418.
- [270] Holman, J.P., 1992, "Heat Transfer," Seventh Edition, McGraw-Hill, London, pp. 418.
- [271] Bejan, A., 1993, *Heat Transfer*, Wiley, pp. 216-289.
- [272] Fitzgerald, E.P. and Davies, M.R.D., 1996, "Thermal Conductivity of Plastic Encapsulants," *Proceedings of the Second International Workshop on Thermal Investigations of ICs and Microstructures (THERMINIC)*, pp. 133-142.
- [273] Lasance, C.J.M., 1997, "Technical Data: Thermal Conductivity," *Electronics Cooling*, Vol. 3, No. 2, pp. 12.
- [274] CINDAS, Center for Information and Numerical data Analysis and Synthesis, Purdue University, Purdue University, West Lafayette, IN 47907 USA, <https://engineering.purdue.edu/IIES/CINDAS/>
- [275] Keltner, N.R., 1998, "Heat Transfer Measurements in Electronic Cooling Applications," *Electronics Cooling*, Vol. 4, No. 3, pp. 30-47.
- [276] Moffat, R. J., 1997, "Notes on Using Thermocouples," *Electronics Cooling*, Vol. 3, No. 1, pp. 12-15.
- [277] Christiaens, F., Beyne, E., Vandeveld, B., Roggen, J., Mertens, R., Van Puymbroeck, J. Heerman, M., and Berghmans, J., 1997, "Compact Transient Thermal Models for the Polymer Stud Grid Array (PSGA) Package," *Proceedings of the 58th Seminar on Thermal Management of Electronics Systems (EUROTHERM) September 24-26, Nantes, France*, pp. 202-209.
- [278] Noebauer, G., 2001, "Creating Compact Models Using Standard Spreadsheet Software," *Proceedings of the Seventeenth IEEE Semiconductor Thermal Measurement and Management Symposium (SEMI-THERM)*, pp. 126-133.
- [279] Schweitzer, D., and Pape, H., 2001, "Thermal Impedance of Packages in Dual Cold Plate Environments," *Proceedings of the Seventh International Workshop on Thermal Investigations of ICs and Systems (THERMINIC)*, pp. 245-249.
- [280] Aihara, T., 1991, "Air Cooling Techniques by Natural Convection," *Cooling Techniques for Computers*, Editor, Aung, W., Hemisphere Publishing Corporation.
- [281] Lasance, C., and Yoshi, Y., 1999, "Thermal Analysis of Natural Convection Electronic Systems: Status and Challenges," in *Advances in Thermal Modeling of Electronic Components and Systems*, Editors, A. Bar-Cohen and A.D. Kraus, ASME PRESS, Vol. 4, pp. 1-177.

- [282] Moffat, R.J., and Ortega, A., 1986, "Buoyancy Induced Forced Convection," Heat Transfer in Electronic equipment, HTD-Vol. 57, pp. 135-144.
- [283] Anderson, A.M., and Moffat, R.J., 1987, "Buoyancy-Induced Forced Convection on an Isolated Plate, Rough and Smooth," Proceedings of the 37<sup>th</sup> Electronic Components Technology Conference (ECTC), pp. 539-544.
- [284] PST5-01 Thermal test die, DELPHI, Kokomo, Indiana 46904-9005, USA, [www.delphi.com](http://www.delphi.com)
- [285] Dacles-Mariani, J, Zilliac, G.G., Chow, J.S., and Bradshaw, P., 1995, "Numerical/Experimental Study of a Wingtip Vortex in the Near Field," AIAA Journal, Vol. 33, No. 9, pp.1561-1568.
- [286] Jongen, T., 1992, "Simulation and Modeling of Turbulent Incompressible Flows," Ph.D. Thesis, EPF Lausanne, Lausanne, Switzerland.

## Appendix A: Thermal Test Components

In this appendix, vendor supplied package external geometry details for the PQFP 160, SO8 and PQFP 208 are given, on the basis of which the component numerical models were constructed. Corresponding component internal architecture was documented in Chapter 3. The thermal test dies layouts and their operating characteristics are also given in this appendix. Additional Scanning Acoustic Microscopy (SAM) images are presented for the PQFP 160 test component, supporting the structural analyses undertaken in Chapter 3.

### A.1 External Component Geometry

The PQFP 160, SO8 and PQFP 208 package external geometry details are given in Figures A.1 to A.3 respectively. Their geometry are in accordance with the appropriate JEDEC standard [185] for each package type.

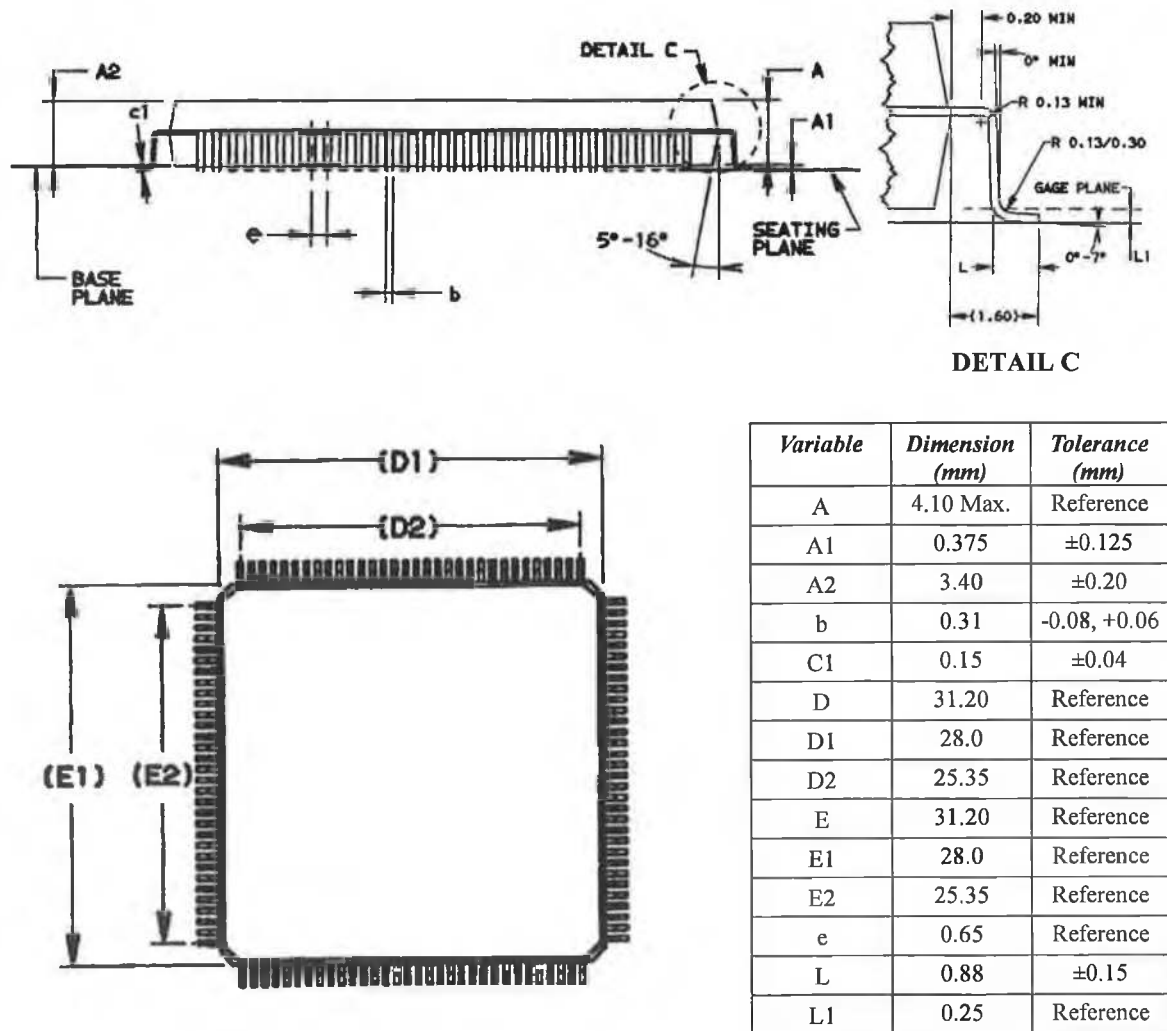
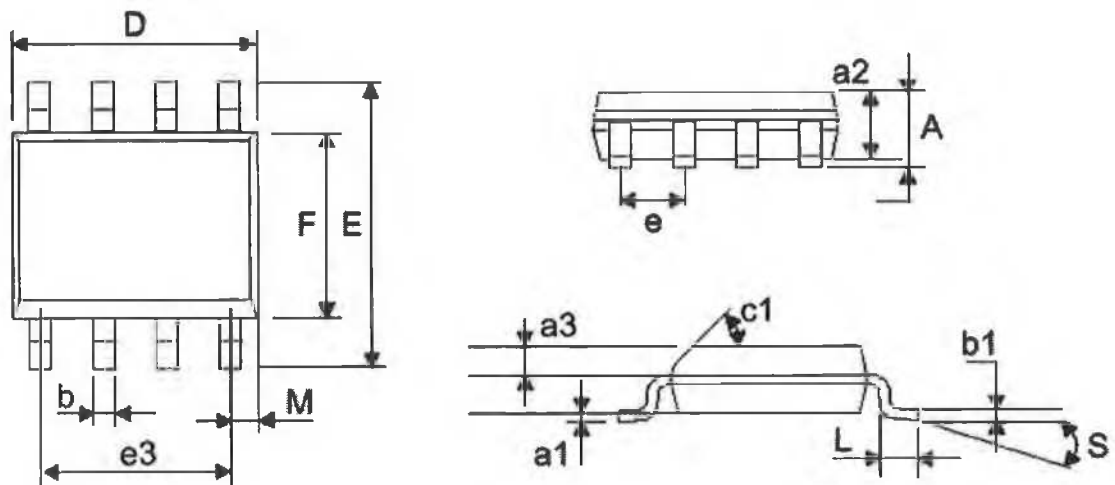


Figure A.1 160-lead PQFP (Amkor) package body geometry details.



<i>Variable</i>	<i>Dimension (mm)</i>	<i>Tolerance (mm)</i>
A	1.75 Max.	Reference
a1	0.2	-0.1
a2	1.45	-0.2
b	0.35	-0.15
b1	0.2	-0.01, +0.05
c1	45°	Reference
D	5.0	-0.2
E	6.0	±0.2
e	1.27	Reference
e3	3.81	Reference
F	4.0	-0.2
L	0.4	+0.8
M	0.6 Max.	Reference
S	8° Max.	Reference

**Figure A.2** SO8 (Infineon) package body geometry details.

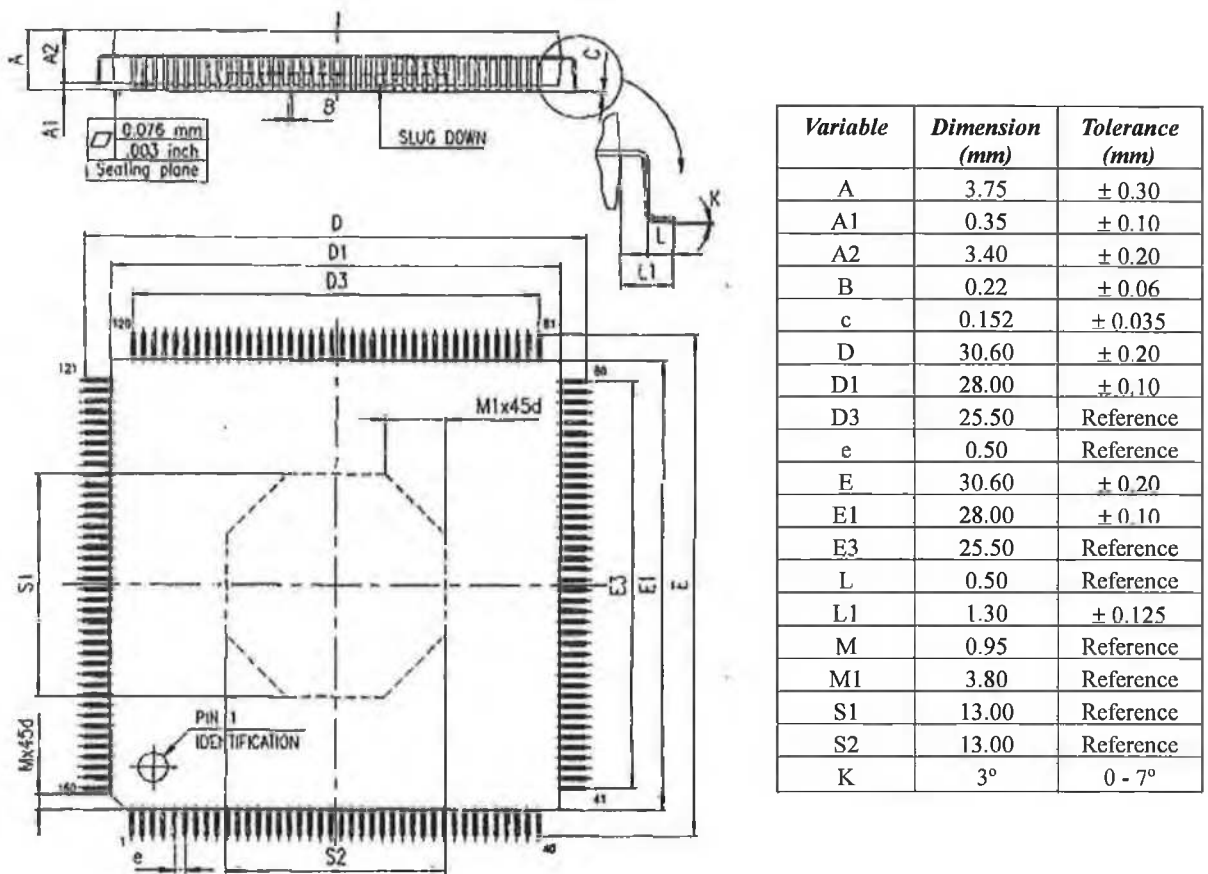
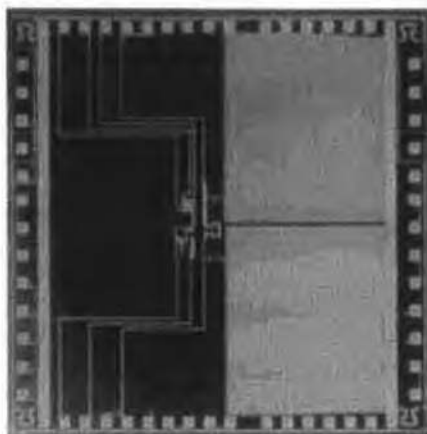


Figure A.3 PQFP 208 (ST microelectronics) package body geometry details.

## A.2 Thermal Test Die

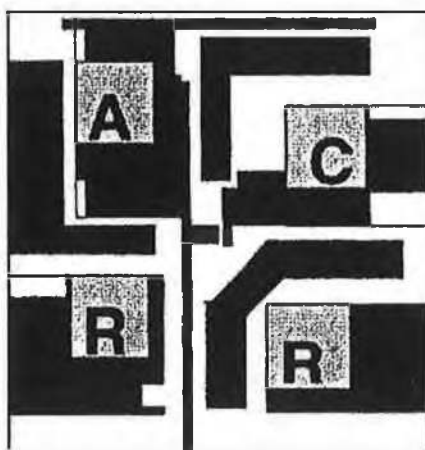
Each component contained an embedded thermal test die with functionality that conformed to SEMI standard G32-94 [193]. The respective thermal test die layouts are shown in Figure A.4.

Component power dissipation was provided by a diffused resistor for all test dies, with centrally located temperature sensitive diodes used for junction temperature measurement. The vendor specified linear coefficients for the PQFP 160, SO8 and PQFP 208 sensing diodes were 10.0, 1.83 and 2.05 mV per °C rise in temperature respectively, at a recommended excitation current of 300, 100 and 100  $\mu$ A respectively. The temperature sensitive diodes on each test die were calibrated to an accuracy of  $\pm 0.4^\circ\text{C}$ ,  $\pm 0.5^\circ\text{C}$  and  $\pm 0.2^\circ\text{C}$  for the PQFP 160, SO8 and PQFP 208 components respectively.



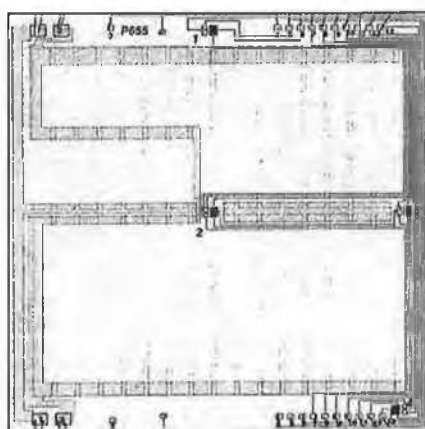
**Note:** Test die dimensions = 7.5 mm square. Nominal thickness = 610 to 660  $\mu\text{m}$ .

(a) PQFP 160: Delphi PST5-01 test pattern [284]



**Note:** Test die dimensions = 0.63 mm square. Nominal thickness = 380  $\mu\text{m}$ . R = Resistor pad, A = Anode pad of the diode, C = cathode pad of the diode.

(b) SO8: Infineon G453A test pattern [168]



**Note:** Test die dimensions = 9.2 mm square. Nominal thickness = 620  $\mu\text{m}$ .

(c) PQFP 208: ST Microelectronics P655 test pattern [195]

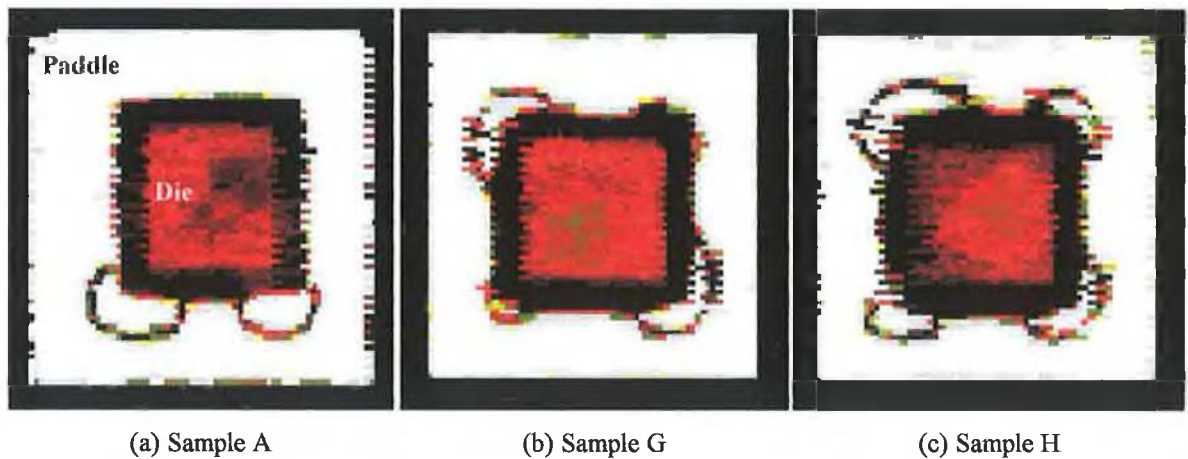
**Figure A.4** Thermal test die layouts.



### A.3 Scanning Acoustic Microscopy

In addition to the Scanning Acoustic Microscopy (SAM) analysis presented in Section 3.3.4 for package designs I and III, Samples G and C respectively, additional scans were performed for package design I, Samples, (A,G,H), using an Ultrasonic Sciences Limited (USL) machine, equipped with a 25 MHz focused probe.

The SAM images shown in Figure A.5 provide supporting evidence of delamination at the die-paddle interface. Although image resolution is not as good as in Figure 3.25(b,i), due to limited equipment resolution, the red coloured regions over the die region, and characteristic patterns at the die corners, clearly indicate delamination over the entire surface area of the die. The patterns at the die corners of sample G, Figure A.5(b) match those obtained for this sample in Figure 3.25(b,i).



**Note:** Red coloured regions indicate delamination.

**Figure A.5** Scanning Acoustic Microscopy (SAM) analysis of the die-paddle interface for the 160-lead PQFP component, package design I.

## Appendix B: Uncertainty Analysis

Estimated uncertainties in the measured variables used to assess numerical predictive accuracy, namely component junction temperature and component/board surface temperature, as well as variables forming numerical boundary conditions, namely component power dissipation and free-stream air velocity, were given in Chapter 3 for the respective test configurations. These estimates were based on an Nth order, single-sample uncertainty analysis [204-208], details of which are given in this appendix.

The Nth order uncertainty represents the overall uncertainty in the measurement, accounting for both process instability as viewed through the instrumentation, and the fixed and random errors in the instrumentation. The single-sample uncertainty in a measured quantity R, calculated from a set of individual measurements or parameters, is given by combining the individual sensitivity times the uncertainty interval for each contributing parameter by a root-sum-square method:

$$\delta R = \left( \sum_{i=1}^n \left( \frac{\partial R}{\partial x_i} \right)^2 \delta x_i^2 \right)^{1/2} \quad (\text{B.1})$$

where the data reduction equation for R is given by  $R = f(x_1, x_2, \dots, x_n)$ ,  $x_i$  are the individual measurements or parameters,  $\delta x_i$  is the uncertainty in  $x_i$ ,  $\partial R / \partial x_i$  is the sensitivity coefficient for R with respect to the measurement of  $x_i$ . The odds are 20/1 that the value of R is within  $\pm \delta R$  of the recorded value, whereby the measurements are assumed to have a “normal” distribution centred around the recorded value, with a standard deviation of  $\delta R / 2$ .

Details of the analysis used to estimate measurement uncertainty in component junction temperature are given in the following section.

### B.1 Uncertainty in Measured Component Junction Temperature

Component junction temperature measurement was deduced from the individual measurements of the thermal test die diode temperature rise above ambient conditions and of the reference (ambient air) temperature, as:

$$T_j = T_{\text{ref}} + \Delta T_j \quad (\text{B.2})$$

where  $T_j$  is the component junction temperature,  $T_{\text{ref}}$  is the measured reference temperature, and  $\Delta T_j$  is the measured diode temperature rise above reference conditions, given by Equation (3.2).

Applying the uncertainty analysis formulated in Equation (B.1), the uncertainty in measured component junction temperature, derived from the data reduction equation for

this variable, Equation (B.2), is expressed as:

$$\delta T_j = \left( (V_{f1} - V_{f2})^2 \delta K^2 + 2K^2 \delta V_f^2 + \delta T_{ref}^2 \right)^{1/2} \quad (B.3)$$

where  $\delta K$ ,  $\delta V_f$ , and  $\delta T_{ref}$  are the uncertainties in the measured linear coefficient for forward voltage change with temperature (K factor), diode forward voltage, and reference temperature respectively. Whereas the latter two uncertainties were directly deduced from instrument calibration, the experimental uncertainty in the K factor was derived from Equation (3.2) as:

$$\delta K = \left( \frac{2}{(V_{f1} - V_{f2})^2} \delta T_{ref}^2 + \frac{2K^2}{(V_{f1} - V_{f2})^2} \delta V_f^2 \right)^{1/2} \quad (B.4)$$

The measured K factors, given in Table B.1, are based on a 80°C diode temperature rise above reference conditions for each test component. For all test configurations, the uncertainty in the K factor is solely related to the uncertainty in the reference temperature, as uncertainty in the voltage measurement is negligible due to high instrument precision.

**Table B.1** Measured parameters and estimated uncertainties.

<i>Parameter and unit</i>	<i>Nominal value</i>		<i>Uncertainty</i>
$V_f$ (V)	All test configurations	---	$\pm 10^{-5}$
I (A)	All test configurations	---	$\pm 10^{-5}$
$T_{ref}$ (°C)	PQFP 160, populated PCB	13 - 20	$\pm 0.3$
	PQFP 160, SEMI PCB	10 - 20	$\pm 0.5$
	SO8, PQFP 208	20	$\pm 0.2$
K (°C/V)	PQFP 160, populated PCB	-100	$\pm 0.6$ (0.6%)
	PQFP 160, SEMI PCB	-100	$\pm 0.9$ (0.9%)
	SO8	-546.4	$\pm 4.8$ (0.9%)
	PQFP 208	-489.5	$\pm 1.7$ (0.4%)

**Note:** The uncertainty in measured K factor is given as both an absolute value, and normalised value (%) in parenthesis ( ). The normalised uncertainty in K factor is the ratio of the absolute uncertainty in K factor to the measured K factor value.

The estimated uncertainties in measured component junction temperature given in Chapter 3, were derived from Equation (B.3) using the uncertainties given in Table B.1 for the measured K factor, diode forward voltage, and reference temperature.

## Appendix C: Fluid Flow Modelling

In this appendix the time-averaged governing equations solved by Computational Fluid Dynamics (CFD) analysis for the prediction of fluid flow and heat transfer are given. In addition, the mathematical formulations of the eddy viscosity turbulence models evaluated in this study are presented.

### C.1 Time-Averaged Conservation Equations

The time-averaged continuity, momentum and energy equations for incompressible flow, whereby the Reynolds stresses and fluxes are modelled by the Boussinesq hypothesis, are [15]:

Continuity:

$$\frac{\partial \rho}{\partial t} + \frac{\partial}{\partial x_i}(\rho u_i) + \frac{\partial}{\partial x_j}(\rho u_j) + \frac{\partial}{\partial x_k}(\rho u_k) = 0 \quad (C.1)$$

X-momentum (y and z momentum similar):

$$\begin{aligned} \frac{\partial}{\partial t}(\rho u_i) + \frac{\partial}{\partial x_k}(\rho u_i u_k) + \frac{\partial}{\partial x_j}(\rho u_j u_i) + \frac{\partial}{\partial x_i}(\rho u_k u_i) - \frac{\partial}{\partial x_i}(\mu_{\text{eff}} \frac{\partial u_i}{\partial x_i}) \\ - \frac{\partial}{\partial x_j}(\mu_{\text{eff}} \frac{\partial u_i}{\partial x_j}) - \frac{\partial}{\partial x_k}(\mu_{\text{eff}} \frac{\partial u_i}{\partial x_k}) = - \frac{\partial p}{\partial x_i} \end{aligned} \quad (C.2)$$

where the effective viscosity,  $\mu_{\text{eff}}$ , is the sum of the molecular viscosity and an apparent viscosity due to turbulent mixing:

$$\mu_{\text{eff}} = \mu + \mu_t \quad (C.3)$$

Energy:

$$\begin{aligned} \frac{\partial}{\partial t}(\rho C_p T) + \frac{\partial}{\partial x_i}(\rho u_i C_p T) + \frac{\partial}{\partial x_j}(\rho u_j C_p T) + \frac{\partial}{\partial x_k}(\rho u_k C_p T) - \frac{\partial}{\partial x_i}(k_{\text{eff}} \frac{\partial T}{\partial x_i}) \\ - \frac{\partial}{\partial x_j}(k_{\text{eff}} \frac{\partial T}{\partial x_j}) - \frac{\partial}{\partial x_k}(k_{\text{eff}} \frac{\partial T}{\partial x_k}) = - \frac{\partial p}{\partial t} \end{aligned} \quad (C.4)$$

where the effective conductivity,  $k_{\text{eff}}$ , is the sum of the molecular conductivity and an apparent conductivity due to turbulent mixing:

$$k_{\text{eff}} = k + k_t \quad (C.5)$$

The turbulent conductivity,  $k_t$ , and the turbulent viscosity,  $\mu_t$ , are related by the turbulent Prandtl number:

$$\frac{\mu_t C_p}{k_t} = Pr_t = 0.9 \quad (C.6)$$

The turbulent viscosity,  $\mu_t$ , is computed using an eddy viscosity turbulence model.

## C.2 Eddy Viscosity Turbulence Models

In this study, both eddy viscosity turbulence models typically employed in CFD codes dedicated to the thermal analysis of electronic equipment, and alternative turbulent flow modelling strategies, available in general-purpose CFD codes, are evaluated for the prediction of electronic component heat transfer. In Flotherm [69], a dedicated CFD code, a zero-equation mixing length model, LVEL [233], and two-equation high-Reynolds number  $k$ - $\epsilon$  model [234] are assessed. The potential for improved predictive accuracy is evaluated using a one-equation Spalart-Allmaras model [241], two-layer zonal model [247] and two-equation Shear Stress Transport (SST)  $k$ - $\omega$  model [246], all of which implemented in Fluent [70], a general-purpose CFD code. The characteristics of these turbulence models were presented in Sections 4.2 and 4.3. Their mathematical formulations, given in the respective CFD code user manuals [69,70], are summarised in this Section to provide an insight into calculation strategies.

### C.2.1 LVEL Model

The zero-equation mixing-length LVEL model [233] automatically calculates a length scale for each fluid cell by solving a Laplacian type differential equation to determine the distance of the cell from all apparent walls. This length scale, together with the locally computed velocity is used to compute a turbulent viscosity.

*Length scale.* The distance from the wall is deduced from the solution of the following differential equation:

$$\nabla\Phi = -1 \quad (C.7)$$

with the boundary condition  $\Phi = 0$  within the fluid domain. The distance to the wall or distance between walls,  $D$ , is deducible from the local value and local gradient of  $\Phi$ :

$$D = \sqrt{|\nabla\Phi|^2 + 2\Phi} \quad (C.8)$$

*Near-wall treatment.* The dimensionless distance from the wall,  $y^+$ , and the

dimensionless velocity parallel to the wall,  $u^+$ , are related through the following wall function formulation [238]:

$$y^+ = u^+ + \frac{1}{E} \left[ e^{\kappa u^+} - 1 - \kappa u^+ - \frac{(\kappa u^+)^2}{2} - \frac{(\kappa u^+)^3}{6} - \frac{(\kappa u^+)^4}{24} \right] \quad (C.9)$$

where the Von Karman's constant,  $\kappa$ , and the wall roughness parameter,  $E$ , are taken as 0.417 and 8.6 respectively.

The dimensionless effective viscosity,  $\nu^+$ , defined as the ratio of the effective viscosity to the laminar viscosity, is computed as:

$$\nu^+ = 1 + \frac{\kappa}{E} \left[ e^{\kappa u^+} - 1 - \kappa u^+ - \frac{(\kappa u^+)^2}{2} - \frac{(\kappa u^+)^3}{6} \right] \quad (C.10)$$

### C.2.2 Standard High-Reynolds Number k- $\epsilon$ Model

The standard two-equation k- $\epsilon$  model [234,235] computes the eddy viscosity by solving additional differential equations for turbulent kinetic energy,  $k$ , and for the rate of dissipation of turbulence energy,  $\epsilon$ :

$$\frac{\partial}{\partial t}(\rho k) + \frac{\partial}{\partial x_i}(\rho u_i k) = \frac{\partial}{\partial x_j} \left( \Gamma_k \frac{\partial k}{\partial x_j} \right) + G_k + G_b - \rho \epsilon - S_k \quad (C.11)$$

and

$$\frac{\partial}{\partial t}(\rho \epsilon) + \frac{\partial}{\partial x_i}(\rho u_i \epsilon) = \frac{\partial}{\partial x_j} \left( \Gamma_\epsilon \frac{\partial \epsilon}{\partial x_j} \right) + (G_k + C_{3\epsilon} G_b) C_{1\epsilon} \frac{\epsilon}{k} - C_{2\epsilon} \rho \frac{\epsilon^2}{k} + S_\epsilon \quad (C.12)$$

where  $G_k$  and  $G_b$  represent the generation of turbulence kinetic energy due to the mean velocity gradients and due to buoyancy respectively;  $S_k$  and  $S_\epsilon$  are user-defined source terms;  $C_{1\epsilon}$ ,  $C_{2\epsilon}$  and  $C_{3\epsilon}$  are constants; and the effective diffusivities,  $\Gamma_k$  and  $\Gamma_\epsilon$ , are given by:

$$\Gamma_k = \mu + \frac{\mu_t}{\sigma_k} \quad (C.13)$$

and

$$\Gamma_\epsilon = \mu + \frac{\mu_t}{\sigma_\epsilon} \quad (C.14)$$

where  $\sigma_k$  and  $\sigma_\epsilon$  are the turbulent Prandtl numbers for  $k$  and  $\epsilon$  respectively.

The eddy viscosity,  $\mu_t$ , is computed by combining  $k$  and  $\epsilon$  as:

$$\mu_t = C_\mu \frac{\rho k^2}{\varepsilon} \quad (\text{C.15})$$

The production of turbulence kinetic energy is modelled as:

$$G_k = -\rho u_i' u_j' \frac{\partial u_j}{\partial x_i} \quad (\text{C.16})$$

where  $G_k$  is expressed as  $G_k = \mu_t S^2$ ,  $S$  being the modulus of the mean rate-of-strain tensor, defined as  $S = \sqrt{2S_{ij}S_{ij}}$ .

The generation of turbulence due to buoyancy is given by:

$$G_b = \beta g_i \frac{\mu_t}{Pr_t} \frac{\partial T}{\partial x_i} \quad (\text{C.17})$$

where  $Pr_t$  is the turbulent Prandtl number for energy and  $g_i$  is the component of the gravitational vector in the  $i$ th direction. The default value of  $Pr_t$  is 0.9 and 0.85 in Flotherm and Fluent respectively. The coefficient of thermal expansion,  $\beta$ , is defined as:

$$\beta = -\frac{1}{\rho} \left( \frac{\partial \rho}{\partial T} \right)_p \quad (\text{C.18})$$

For ideal gases, Equation (C.17) reduces to:

$$G_b = -g_i \frac{\mu_t}{\rho Pr_t} \frac{\partial \rho}{\partial x_i} \quad (\text{C.19})$$

It can be seen from the transport equation for  $k$ , Equation (C.11), that turbulence kinetic energy tends to be augmented ( $G_b > 0$ ) in unstable stratification. For stable stratification, buoyancy tends to suppress the turbulence ( $G_b < 0$ ).

By default in both Flotherm and Fluent, the buoyancy effects on  $\varepsilon$  are neglected simply by setting  $G_b$  to zero in the transport equation for  $\varepsilon$ , Equation (C.12). However, if the buoyancy effects on  $\varepsilon$  are included, the value of  $G_b$  given by Equation (C.17) is used in the transport equation for  $\varepsilon$ . The degree to which  $\varepsilon$  is affected by the buoyancy is determined by the constant  $C_{3\varepsilon}$ . In Flotherm,  $C_{3\varepsilon}$  is specified as 1.0. In Fluent,  $C_{3\varepsilon}$  is calculated according to the following relation:

$$C_{3\varepsilon} = \tanh \left| \frac{v}{u} \right| \quad (\text{C.20})$$

where  $v$  is the component of the flow velocity parallel to the gravitational vector and  $u$  is

the component of the flow velocity perpendicular to the gravitational vector.  $C_{3\varepsilon}$  will become unity for buoyant shear layers for which the main flow direction is aligned with the direction of gravity. For buoyant shear layers that are perpendicular to the gravitational vector,  $C_{3\varepsilon}$  will become zero.

The model constants defined in Flotherm and Fluent are given in Table C.1.

**Table C.1** Model constants for the high-Reynolds number k- $\varepsilon$  model implemented in Flotherm [69] and Fluent [70].

	$C_{1\varepsilon}$	$C_{2\varepsilon}$	$C_{3\varepsilon}$	$C_{\mu}$	$\sigma_k$	$\sigma_\varepsilon$
<b>Flotherm</b>	1.44	1.92	= 1.0	0.09	1.0	1.217
<b>Fluent</b>	1.44	1.92	$\tanh  v/u $	0.09	1.0	1.3

*Near-wall treatment.* In this study the k- $\varepsilon$  model was employed in conjunction with wall functions in Flotherm, and a two-layer zonal model in Fluent. Near-wall treatment for the two-layer zonal model is given in Section C.2.4.

Two wall functions formulations are available for use in conjunction with the k- $\varepsilon$  model in Flotherm, referred to as standard and revised [69]. Both are based on the formulation of Launder and Spalding [235]. The performance of the standard model is limited if the near-wall fluid grid cell is within the viscous sub-layer, as wall skin friction and heat transfer can be considerably overestimated as shown in this study. To remedy this issue, the revised formulation incorporates proprietary corrections blending together turbulent viscosity in the near-wall region and the bulk flow. This formulation was employed for all computations performed using the k- $\varepsilon$  model implemented in Flotherm in this study, as outlined in Chapter 4. The wall function formulation is given as follows, with the exception of the proprietary corrections made to turbulent viscosity.

To evaluate the surface friction and the surface heat transfer coefficient, the universal logarithmic variation of velocity and temperature profiles in turbulent flow near a solid surface is used. The non-dimensional distance from the wall  $y^+$  is defined as:

$$y^+ = \frac{u_\tau y}{\nu} \quad (C.21)$$

The friction velocity,  $u_\tau$ , is equal to  $(\tau_w / \rho)^{1/2}$ , where  $\tau_w$  is the shear stress evaluated at the wall.

For  $y^+ > 11.5$  (turbulent):

$$u^+ = \frac{u}{u_\tau} = \frac{1}{\kappa} \ln(Ey^+) \quad (C.22a)$$

where the Von Karman's constant,  $\kappa$ , and the wall roughness parameter,  $E$ , are taken as 0.435 and 9 respectively in Flotherm.



For  $y^+ < 11.5$  (laminar):

$$u^+ = \frac{u}{u_\tau} = y^+ \quad (\text{C.22b})$$

From the calculated value of  $u$  at a distance  $y$  from the surface, shear stress is calculated and applied as a source (negative) of momentum at the near-wall cell. The Stanton number  $St$  is used in the application of the heat transfer boundary conditions where:

$$St = \frac{q''_w}{\rho u C_p (T - T_w)} \quad (\text{X.23})$$

with  $q''$  being the wall heat flux and  $C_p$  the specific heat capacity of the fluid. The wall heat transfer coefficient is deduced as:

$$h = St \rho u C_p \quad (\text{C.24})$$

For laminar flow ( $y^+ < 11.5$ ):

$$St = \frac{1}{Re \cdot Pr} \quad (\text{C.25a})$$

For turbulent flow ( $y^+ > 11.5$ ) via generalised form of Taylor-Prandtl analogy (heat flux is proportional to momentum flux):

$$St = \frac{s}{0.9(1 + s^{1/2} P_J)} \quad (\text{C.25b})$$

where  $s = \tau_w / (\rho u^2)$ , 0.9 is the turbulent Prandtl number, and  $P_J$  is Jayatilke's sub-layer resistance function.

From calculated values of  $u$ ,  $P_J$ ,  $\tau_0$  (hence  $s$ ),  $q_w$  is deduced and applied to the near-wall cells.

*Domain inlet boundary conditions.* In Flotherm, the kinetic turbulent energy and dissipation rate of turbulent kinetic energy prescribed at inlet are calculated based on the following guidelines. The kinetic turbulent energy is calculated as:

$$k = 10^{-3} (u_{in} I)^2 \quad (\text{C.26})$$

where  $u_{in}$  is the average inlet velocity and  $I$  is the turbulence intensity at inlet.

The dissipation rate of turbulent kinetic energy is estimated as:

$$\varepsilon = (C_\mu^{3/4} k^{3/2}) / l_{in} \quad (\text{C.27})$$

where  $l_{in}$  is a turbulent length scale arbitrarily calculated as:

$$l_i = 0.1 A_{in}^{1/2} \quad (\text{C.28})$$

where  $A_{in}$  is the nominal inlet area.

As the above estimates represent crude approximations [15], solution sensitivity to the values of  $k$  and  $\epsilon$  at inlet boundaries needs to be assessed.

The specification of turbulent boundary conditions at domain inlet boundaries for the high-Reynolds number  $k$ - $\epsilon$  model implemented in Fluent is outlined in Section C.2.4.

### C.2.3 Spalart-Allmaras Model

The Spalart-Allmaras model [241] is a one-equation model that solves a modelled transport equation for a quantity that is a modified form of the turbulent eddy viscosity. The transported variable,  $\tilde{\nu}$ , is identical to the turbulent kinematic viscosity except in the viscosity-affected near-wall region. The transport equation for  $\tilde{\nu}$  is:

$$\frac{\partial}{\partial t}(\rho \tilde{\nu}) + \frac{\partial}{\partial x_i}(\rho \tilde{\nu} u_i) = G_v + \frac{1}{\sigma_{\tilde{\nu}}} \left[ \frac{\partial}{\partial x_j} \left\{ (\mu + \rho \tilde{\nu}) \frac{\partial \tilde{\nu}}{\partial x_j} \right\} + C_{b2} \rho \left( \frac{\partial \tilde{\nu}}{\partial x_j} \right)^2 \right] - Y_v + S_{\tilde{\nu}} \quad (C.29)$$

where  $G_v$  is the production of turbulent viscosity and  $Y_v$  is the destruction of turbulent viscosity that occurs in the near-wall region due to wall blocking and viscous damping;  $\nu$  is the molecular kinematic viscosity;  $S_{\tilde{\nu}}$  is a user-defined source term; and  $\sigma_{\tilde{\nu}}$  and  $C_{b2}$  are constants having the following values:  $\sigma_{\tilde{\nu}} = 2/3$ ,  $C_{b2} = 0.622$ .

The turbulent viscosity,  $\mu_t$ , is computed from:

$$\mu_t = \rho \tilde{\nu} f_{v1} \quad (C.30)$$

with the viscous damping function,  $f_{v1}$ , given by:

$$f_{v1} = \frac{\chi^3}{\chi^3 + C_{v1}^3} \quad (C.31)$$

where  $\chi = (\tilde{\nu} / \nu)$  and  $C_{v1} = 7.1$ .

The production term,  $G_v$ , is modelled as:

$$G_v = C_{b1} \rho S_v \tilde{\nu} \quad (C.32)$$

where

$$\tilde{S} = S + \frac{\tilde{\nu}}{\kappa^2 d^2} f_{v2} \quad (C.33)$$

and

$$f_{v2} = 1 - \frac{\chi}{1 + \chi f_{v1}} \quad (C.34)$$

$C_{b1}$  and  $\kappa$  are constants equalling 0.1355 and 0.4187 respectively,  $d$  is the distance from the wall, and  $S$  is a scalar measure of the deformation tensor. By default in Fluent, as in the original model proposed by Spalart and Allmaras,  $S$  is based on the magnitude of the vorticity:

$$S = \sqrt{2\Omega_{ij}\Omega_{ij}} \quad (C.35)$$

where  $\Omega_{ij}$  is the mean rate-of-rotation tensor and is defined by:

$$\Omega_{ij} = \frac{1}{2} \left( \frac{\partial u_i}{\partial x_j} - \frac{\partial u_j}{\partial x_i} \right) \quad (C.36)$$

The justification for the default expression for  $S$  is that, for the wall-bounded flows that were of most interest when the model was formulated, turbulence is found only where vorticity is generated near walls. However, it has since been acknowledged that the effect of mean strain on the turbulence production should also be taken into account, and a modification to the model has been proposed [285] and incorporated into Fluent. This modification combines measures of both rotation and strain tensors in the definition of  $S$ :

$$S = |\Omega_{ij}| + C_{\text{prod}} \min(0, |S_{ij}| - |\Omega_{ij}|) \quad (X.37)$$

where  $C_{\text{prod}} = 2.0$ ,  $|\Omega_{ij}| = \sqrt{2\Omega_{ij}\Omega_{ij}}$ , and  $|S_{ij}| = \sqrt{2S_{ij}S_{ij}}$

with the mean strain rate,  $S_{ij}$ , defined as:

$$S_{ij} = \frac{1}{2} \left( \frac{\partial u_j}{\partial x_i} + \frac{\partial u_i}{\partial x_j} \right) \quad (X.38)$$

Including both the rotation and strain tensors reduces the production of eddy viscosity and consequently reduces the eddy viscosity itself in regions where the measure of vorticity exceeds that of strain rate.

The turbulent destruction term is modelled as:

$$Y_v = C_{w1} \rho f_w \left( \frac{\bar{v}}{d} \right)^2 \quad (C.39)$$

where

$$f_w = g \left[ \frac{1 + C_{w3}^6}{g^6 + C_{w3}^6} \right]^{1/6} \quad (C.40)$$

$$g = r + C_{w2}(r^6 - r) \quad (C.41)$$

$$r = \frac{\bar{\nu}}{S\kappa^2 d^2} \quad (C.42)$$

with constants  $C_{w2} = 0.3$ ,  $C_{w3} = 2.0$ , and

$$C_{w1} = \frac{C_{b1}}{\kappa^2} + \frac{(1 + C_{b2})}{\sigma_v} \quad (C.43)$$

and  $\bar{S}$  is given by Equation (C.33). Note that the modification described above to include the effects of mean strain on  $S$  will also affect the value of  $\bar{S}$  used to compute  $r$ .

The model constants are given in Table C.2.

**Table C.2** Model constants for the Spalart-Allmaras model implemented in Fluent [70].

<i>Constant</i>	<i>Value</i>
$C_{b1}$	0.1355
$C_{b2}$	0.622
$\sigma_v$	2/3
$C_{v1}$	7.1
$C_{w1}$	$\frac{C_{b1}}{\kappa^2} + \frac{(1 + C_{b2})}{\sigma_v}$
$C_{w2}$	0.3
$C_{w3}$	2.0
$\kappa$	0.4187

*Wall boundary conditions.* At walls, the modified turbulent kinematic viscosity,  $\bar{\nu}$ , is set to zero. When the mesh is fine enough to resolve the laminar sublayer, the wall shear stress is obtained from the laminar stress-strain relationship given in Equation (C.21). If the mesh is too coarse to resolve the laminar sub-layer, it is assumed that the centroid of the wall adjacent cell falls within the logarithmic region of the boundary layer, and the law-of-the-wall defined in Equation (C.22a) is employed, with the Von Karman constant,  $\kappa$ , and the wall roughness parameter,  $E$ , taken as 0.4187 and 9.793 respectively. The former calculation strategy was employed for this study, whereby no wall functions were relied upon.

*Domain inlet boundary conditions.* Based on the user-specified turbulent viscosity ratio at inlet boundaries, the boundary value for the modified turbulent viscosity,  $\bar{\nu}$ , is computed by combining  $\mu_t/\mu$  with the appropriate values of density and molecular viscosity. As such an estimate represents a crude approximation, solution sensitivity to the prescribed turbulent viscosity ratio at inlet needs to be assessed.

### C.2.4 Two-Layer Zonal Model

The two-layer zonal model [247] is an alternative to the wall function approach for modelling the near-wall region when using a k- $\epsilon$  model, such as standard high-Reynolds number k- $\epsilon$  [235] or RNG k- $\epsilon$  [250,251]. In the two-layer zonal model, the viscosity-affected near-wall region is resolved all the way to the viscous sublayer. The fluid domain is subdivided into a viscosity-affected region and a fully-turbulent region. The demarcation of the two regions is determined by a wall-distance-based, turbulent Reynolds number,  $Re_y$ , defined as:

$$Re_y = \frac{\rho y \sqrt{k}}{\mu} \quad (C.44)$$

where  $y$  is the normal distance from the wall at the cell centres, interpreted as the distance to the nearest wall:

$$y = \min_{\vec{r}_w \in \Gamma_w} \|\vec{r} - \vec{r}_w\| \quad (C.45)$$

where  $\vec{r}$  is the position vector at the field point,  $\vec{r}_w$  is the position vector on the wall boundary, and  $\Gamma_w$  is the union of all wall boundaries involved.

In the fully turbulent region ( $Re_y > 200$ ), a k- $\epsilon$  model is employed. In the viscosity-affected near-wall region ( $Re_y < 200$ ), the one-equation model of Wolfshtein [249] is applied. This model solves the same transport equation for momentum and the turbulent kinematic energy as for the standard high-Reynolds k- $\epsilon$  model (Section C.2.2), but the turbulent viscosity,  $\mu_{t\_2\text{-layer}}$ , is computed from:

$$\mu_{t\_2\text{-layer}} = \rho C_\mu l_\mu \sqrt{k} \quad (C.46)$$

where the length scale,  $l_\mu$ , is computed from:

$$l_\mu = y C_1 (1 - e^{-Re_y/A_\mu}) \quad (C.47)$$

where  $A_\mu$  is a constant equalling 70 [247]. The two-layer formulation for turbulent viscosity described above is smoothly blended with the high-Reynolds-number  $\mu_t$  definition from the outer region, as proposed by Jongen [286]:

$$\mu_t = \lambda_\epsilon \mu_{t\_outer\_region} + (1 - \lambda_\epsilon) \mu_{t\_2\text{-layer}} \quad (C.48)$$

where  $\mu_{t\_outer\_region}$  is the high-Reynolds number definition described in Section C.2.2 for the

k- $\varepsilon$  model, and  $\lambda_\varepsilon$  is a blending function defined in such a way that it is equal to unity far from walls and is zero very near to walls. The blending function is:

$$\lambda_\varepsilon = \frac{1}{2} \left[ 1 + \tanh \left( \frac{\text{Re}_y - 200}{A} \right) \right] \quad (\text{C.49})$$

where the constant A determines the width of the blending function. By defining a width such that the value of  $\lambda_\varepsilon$  will be within 1% of its far-field value given a variation of  $\Delta\lambda_\varepsilon$ , the result is:

$$A = \frac{|\Delta \text{Re}_y|}{\tanh(0.98)} \quad (\text{C.50})$$

Typically,  $\Delta \text{Re}_y$  would be assigned a value that is between 5% and 20% of the  $\text{Re}_y$  value of 200. The main purpose of the blending function is to prevent solution convergence from being impeded when the k- $\varepsilon$  solution in the outer layer does not match with the two-layer formulation.

The  $\varepsilon$  field is computed from:

$$\varepsilon = \frac{k^{3/2}}{l_\varepsilon} \quad (\text{C.51})$$

where the length scale  $l_\varepsilon$  is computed from Chen and Patel [247] as:

$$l_\varepsilon = y C_1 (1 - e^{-\text{Re}_y/A_\varepsilon}) \quad (\text{C.52})$$

where  $C_1 = \kappa C_\mu^{-3/4}$  and  $A_\varepsilon = 2 C_1$ . If the whole flow domain is inside the viscosity-affected region ( $\text{Re}_y < 200$ ),  $\varepsilon$  is not obtained by solving the transport equation, but instead obtained algebraically from Equation (C.51).

A procedure similar to that employed for  $\mu_t$  is used to ensure a smooth transition between the algebraically-specified value of  $\varepsilon$  in the inner region and the value of  $\varepsilon$  obtained from solution of the transport equation in the outer equation.

*Wall boundary conditions.* When the mesh is fine enough to resolve the laminar sublayer, the wall shear stress is obtained from the laminar stress-strain relationship given in Equation (C.21). This calculation strategy was employed for this study, whereby no wall functions were relied upon.

*Domain inlet boundary conditions.* The kinetic turbulent energy is calculated from the user-prescribed turbulence intensity as:

$$k = 3/2 (u_{in} I)^2 \quad (C.53)$$

where  $u_{in}$  is the average inlet velocity and  $I$  is the turbulence intensity at inlet.

The value of  $\varepsilon$  is obtained from the user-specified turbulent viscosity ratio,  $\mu_t/\mu$ , and  $k$  using the following relationship:

$$\varepsilon = \rho C_\mu \frac{k^2}{\mu} \left( \frac{\mu_t}{\mu} \right)^{-1} \quad (C.54)$$

As the above estimates represent crude approximations [15], solution sensitivity to the prescribed values of  $k$  and  $\varepsilon$  at inlet needs to be assessed.

### C.2.5 Shear Stress Transport (SST) $k$ - $\omega$ Model

The SST  $k$ - $\omega$  model [246] blends a standard  $k$ - $\omega$  model [245] in the inner region of the boundary layer, and a high-Reynolds number  $k$ - $\varepsilon$  model [235] in the outer part. To achieve this, the  $k$ - $\varepsilon$  model is converted into a  $k$ - $\omega$  model formulation. The standard  $k$ - $\omega$  model is based on modelled transport equations for the turbulence kinetic energy ( $k$ ) and the specific dissipation rate ( $\omega$ ), which represents the frequency of the vorticity fluctuations. The  $k$ - $\omega$  model is essentially a direct translation of the low-Reynolds number  $k$ - $\varepsilon$  model, with the addition of transition specific closure coefficients [66]. In the SST  $k$ - $\omega$  model, the definition of the turbulent viscosity is modified to account for the transport effects of the principal turbulent shear stress. It also incorporates a damped cross-diffusion term in the  $\omega$  equation.

The turbulence kinetic energy,  $k$ , and the specific dissipation rate,  $\omega$ , are obtained from the following transport equations:

$$\frac{\partial}{\partial t}(\rho k) + \frac{\partial}{\partial x_j}(\rho u_j k) = \frac{\partial}{\partial x_j}(\Gamma_k \frac{\partial k}{\partial x_j}) + G_k - Y_k + S_k \quad (C.55)$$

and

$$\frac{\partial}{\partial t}(\rho \omega) + \frac{\partial}{\partial x_j}(\rho \omega u_j) = \frac{\partial}{\partial x_j}(\Gamma_\omega \frac{\partial \omega}{\partial x_j}) + G_\omega - Y_\omega + D_\omega + S_\omega \quad (C.56)$$

where  $G_k$  represents the generation of turbulence kinetic energy due to mean velocity gradients;  $G_\omega$  represents the generation of  $\omega$ ;  $\Gamma_k$  and  $\Gamma_\omega$  represent the effective diffusivities of  $k$  and  $\omega$  respectively;  $Y_k$  and  $Y_\omega$  represent the dissipation of  $k$  and  $\omega$  due to turbulence;  $D_\omega$  represents the cross-diffusion term; and  $S_k$  and  $S_\omega$  are user-defined source terms.

The effective diffusivities are given by:

$$\Gamma_k = \mu + \frac{\mu_t}{\sigma_k} \quad (\text{C.57})$$

$$\Gamma_\omega = \mu + \frac{\mu_t}{\sigma_\omega} \quad (\text{C.58})$$

where  $\sigma_k$  and  $\sigma_\omega$  are the turbulent Prandtl numbers for  $k$  and  $\omega$  respectively. The turbulent viscosity is computed as:

$$\mu_t = \frac{\rho k}{\omega} \frac{1}{\max\left[\frac{1}{\alpha^*}, \frac{\Omega F_2}{a_1 \omega}\right]} \quad (\text{C.59})$$

where

$$\Omega = \sqrt{2\Omega_{ij}\Omega_{ij}} \quad (\text{C.60})$$

$$\sigma_k = \frac{1}{F_1 / \sigma_{k,1} + (1 - F_1) / \sigma_{k,2}} \quad (\text{C.61})$$

$$\sigma_\omega = \frac{1}{F_1 / \sigma_{\omega,1} + (1 - F_1) / \sigma_{\omega,2}} \quad (\text{C.62})$$

where  $\Omega_{ij}$  is the mean rate-of-rotation tensor, and the coefficient  $\alpha^*$  damps the turbulent viscosity causing a low-Reynolds number correction:

$$\alpha^* = \alpha_\infty^* \left( \frac{\alpha_0^* + \text{Re}_t / R_k}{1 + \text{Re}_t / R_k} \right) \quad (\text{C.63})$$

where  $R_k = 6$ ,  $\alpha_0^* = \beta_i / 3$ ,  $\beta_i = 0.072$  and

$$\text{Re}_t = \frac{\rho k}{\mu \omega} \quad (\text{C.64})$$

The blending functions,  $F_1$  and  $F_2$ , are given by:

$$F_1 = \tanh(\Phi_1^4) \quad (\text{C.65})$$

$$\Phi_1 = \min \left[ \max \left( \frac{\sqrt{k}}{0.09\omega y}, \frac{500\mu}{\rho y^2 \omega} \right), \frac{4\rho k}{\sigma_{\omega,2} D_\omega^+ y^2} \right] \quad (\text{C.66})$$



$$D_{\omega}^+ = \max \left[ 2\rho \frac{1}{\sigma_{\omega,2}} \frac{1}{\omega} \frac{\partial k}{\partial x_j} \frac{\partial \omega}{\partial x_j}, 10^{-20} \right] \quad (C.67)$$

$$F_2 = \tanh(\Phi_2^2) \quad (C.68)$$

$$\Phi_2 = \max \left[ 2 \frac{\sqrt{k}}{0.09\omega y}, \frac{500\mu}{\rho y^2 \omega} \right] \quad (C.69)$$

where  $y$  is the distance to the next surface and  $D_{\omega}^+$  is the positive portion of the cross-diffusion term (Equation C.80).

The production of turbulence kinetic energy is defined as:

$$G_k = -\rho u_i' u_j' \frac{\partial u_j}{\partial x_i} \quad (C.70)$$

where  $G_k$  is expressed as  $G_k = \mu_t S^2$ ,  $S$  being the modulus of the mean rate-of-strain tensor, defined in the same way as for the standard  $k$ - $\epsilon$  model,  $S = \sqrt{2S_{ij}S_{ij}}$ .

The production of  $\omega$  is given by:

$$G_{\omega} = \frac{\alpha}{\nu_t} G_k \quad (C.71)$$

where  $G_k$  is given by Equation (C.70) and the coefficient  $\alpha_{\omega}$  is given by:

$$\alpha_{\omega} = F_1 \alpha_{\omega,1} + (1 - F_1) \alpha_{\omega,2} \quad (C.72)$$

where

$$\alpha_{\omega,1} = \frac{\beta_{i,1}}{\beta_{\omega}^*} - \frac{\kappa^2}{\sigma_{\omega,1} \sqrt{\beta_{\omega}^*}} \quad (C.73)$$

$$\alpha_{\omega,2} = \frac{\beta_{i,2}}{\beta_{\omega}^*} - \frac{\kappa^2}{\sigma_{\omega,2} \sqrt{\beta_{\omega}^*}} \quad (C.74)$$

where  $\kappa = 0.41$ ,  $\beta_{i,1} = 0.075$  and  $\beta_{i,2} = 0.0828$ .

The dissipation of turbulence kinetic energy is given by:

$$Y_k = \rho \beta^* k \omega \quad (C.75)$$

where

$$\beta^* = \beta_i^* [1 + \xi^* F(M_t)] \quad (C.76)$$

with  $\xi^* = 1.5$ ,  $R_\beta = 8$  and  $\beta_\infty^* = 0.09$ , and

$$\beta_i^* = \beta_\infty^* \left( \frac{4/15 + (Re_t/R_\beta)^4}{1 + (Re_t/R_\beta)^4} \right) \quad (C.77)$$

where  $Re_t$  is given by Equation (C.64).

The dissipation of  $\omega$  is given by:

$$Y_\omega = \rho \beta_i \omega^2 \quad (C.78)$$

where

$$\beta_i = F_1 \beta_{i,1} + (1 - F_1)\beta_{i,2} \quad (C.79)$$

with  $\beta_{i,1} = 0.075$ ,  $\beta_{i,2} = 0.0828$  and  $F_1$  is obtained from Equation (C.65).

To blend the standard k- $\omega$  and SST k- $\omega$  models together, the standard k- $\epsilon$  model has been transformed into equations based on k and  $\omega$ , which leads to the introduction of a cross-diffusion term,  $D_\omega$ , in Equation (C.56).  $D_\omega$  is defined as:

$$D_\omega = 2(1 - F_1)\rho \sigma_{\omega,2} \frac{1}{\omega} \frac{\partial k}{\partial x_j} \frac{\partial \omega}{\partial x_j} \quad (C.80)$$

The model constants are given in Table C.3.

**Table C.3** Model constants for the SST k- $\omega$  model implemented in Fluent [70].

Constant	$\sigma_{k,1}$	$\sigma_{k,2}$	$\sigma_{\omega,1}$	$\sigma_{\omega,2}$	$a_1$	$\beta_{i,1}$	$\beta_{i,2}$	$\alpha_\infty^*$	$\alpha_\infty$	$\alpha_n$	$\beta_\infty^*$	$R_\beta$	$R_k$	$R_\omega$	$\xi^*$	$M_{10}$
Value	1.176	1.0	2.0	1.168	0.31	0.075	0.0828	1.0	0.52	1/9	0.09	8	6	2.95	1.5	0.25

*Wall boundary conditions.* When the mesh is fine enough to resolve the laminar sublayer, the wall shear stress is obtained from the laminar stress-strain relationship given in Equation (C.21). This calculation strategy was employed for this study, whereby no wall functions were relied upon.

*Domain inlet boundary conditions.* The kinetic turbulent energy is calculated from the user-prescribed turbulence intensity using Equation (C.53). The value of  $\omega$  is obtained from the prescribed turbulent viscosity ratio,  $\mu_t/\mu$ , and k using the following relationship:

$$\omega = \rho \frac{k}{\mu} \left( \frac{\mu_c}{\mu} \right)^{-1} \quad (\text{C.81})$$

As the above estimates represent crude approximations, solution sensitivity to the prescribed values of  $k$  and  $\varepsilon$  at inlet needs to be assessed.

## **Appendix D: Publication Work**

### **D.1 Conference Proceedings**

Eveloy, V., Rodgers, P., and Lohan, J., 2001, "Numerical Heat Transfer Predictive Accuracy for an In-Line Array of Board-Mounted PQFP Components in Forced Convection," Proceedings of The PACIFIC Rim/ASME International Electronic Packaging Technical Conference & Exhibition (IPACK'01), Paper Number IPACK2001-15690.

Eveloy, V., Rodgers, P., and Lohan, J., 2001, "On Numerical Predictive Accuracy for Electronic Component Heat Transfer in Forced Convection," Proceedings of the Seventh International Workshop on Thermal Investigations of ICs and Systems (THERMINIC), pp. 36-42.

Eveloy, V., Rodgers, P., and Lohan, J., 2002, "Numerical Heat Transfer Predictive Accuracy for an In-Line Array of Board-Mounted PQFP Components in Free Convection," Proceedings of the Third International Conference on Thermal and Mechanical Simulation in (Micro)Electronics (EuroSimE), Paris, France, April 14-16, pp. 101-109.

Eveloy, V., Rodgers, P., and Lohan, J., 2002, "Comparison of Numerical Predictions and Experimental Measurements for the Transient Thermal Behavior of a Board-Mounted Electronic Component," Proceedings of the Eighth Intersociety Conference on Thermal and Thermomechanical Phenomena in Electronics Systems (ITHERM 2002), San Diego, CA, May 29-June 1, pp. 36-45.

Lohan, J., Eveloy, V., and Rodgers, P., 2002, "Visualization of Forced Air Flows over a Populated Printed Circuit Board and their Impact on Convective Heat Transfer," Proceedings of the Eighth Intersociety Conference on Thermal and Thermomechanical Phenomena in Electronics Systems (ITHERM 2002), San Diego, CA, May 29-June 1, pp. 501-511.

Eveloy, V., Rodgers, P. and Hashmi, M.S.J., 2003, "Numerical Prediction of Electronic Component Heat Transfer: An Industry Perspective," Proceedings of the Nineteenth IEEE Semiconductor Thermal Measurement and Management Symposium (SEMI-THERM XIX), San Jose, CA, USA, March 11-13, pp. 14-26.

Eveloy, V., Rodgers, P., DeVoe, J., Ortega, A., and Hashmi, M.S.J., 2003, "An Experimental Assessment of Compact Thermal Models for Board-Mounted Electronic Component Heat Transfer," Proceedings of the Nineteenth IEEE Semiconductor Thermal Measurement and Management Symposium (SEMI-THERM XIX), San Jose, CA, USA, March 11-13, pp. 300-312.

Eveloy, V., Rodgers, P. and Hashmi, M.S.J., 2003, "Application of Numerical Analysis to the Optimisation of Electronic Component Assembly Processes and Reliability Screening," Proceedings of the International Conference on Advanced Materials & Processing Technologies (AMPT), Dublin, Ireland, July 8-11, pp. 643-646.

Eveloy, V., Rodgers, P. and Hashmi, M.S.J., 2003, "An Experimental Assessment of Computational Fluid Dynamics Predictive Accuracy for the Prediction of Electronic Component Operational Temperature," Proceedings of the ASME Summer Heat Transfer Conference (ASME HTC), Las Vegas, Nevada, USA, July 21-23, Paper Number HT2003-47282.

### **D.2 Journals**

Eveloy, V., Rodgers, P., 2002, "Board-Mounted Component Transient Thermal Behavior: Numerical Prediction versus Measurement," The International Journal of Microcircuits and Electronic Packaging, Vol. 25, No. 1, pp. 27-50.

Eveloy, V., Rodgers, P. and Hashmi, M.S.J., "Numerical Prediction of Electronic Component Operational Temperature: A Perspective," accepted for publication in the IEEE Transactions on Component and Packaging Technologies.

Eveloy, V., Rodgers, P. and Hashmi, M.S.J., "Application of Experimental Airflow Visualization to Aid the Numerical Modeling of Electronic Component Convective Heat Transfer," accepted for publication in the International Journal of Microcircuits and Electronic Packaging.

Eveloy, V., Rodgers, P. and Hashmi, M.S.J., "Application of Numerical Analysis to the Optimisation of Electronic Component Assembly Processes and Reliability Screening," accepted for publication in the Journal of Materials Processing Technology.

*In review*

Eveloy, V., Rodgers, P. and Hashmi, M.S.J., "Numerical Heat Transfer Predictive Accuracy for an In-Line Array of Board-Mounted PQFP Components in Free Convection," in review for possible publication in the Transactions of the ASME, Journal of Electronic packaging.

Eveloy, V., Rodgers, P. and Hashmi, M.S.J., "An Experimental Assessment of Computational Fluid Dynamics Predictive Accuracy for Electronic Component Operational Temperature," in review for possible publication in the Transactions of the ASME, Journal of Electronic packaging.